# Shot-peening and low-cycle fatigue of titanium alloys : instrumented indentation and X-ray diffraction

Yugang Li

Thèse
de doctorat
de l'UTT

Yugang LI

# Shot-peening and Low-cycle Fatigue of Titanium Alloys: Instrumented Indentation and X-ray Diffraction

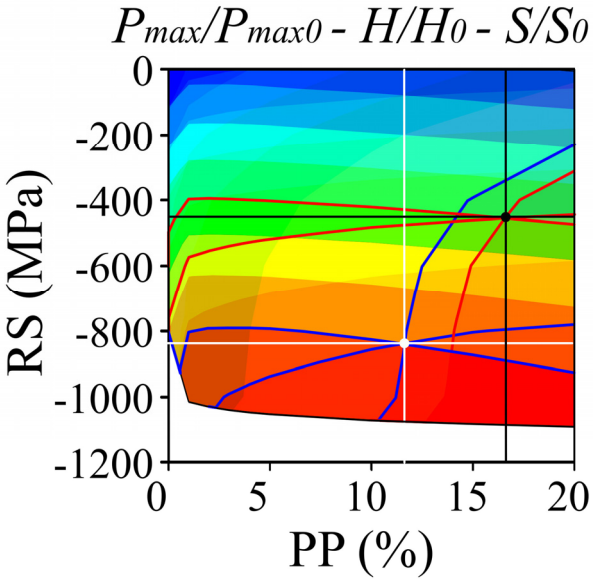


**Spécialité :**
Systèmes Mécaniques et Matériaux

2015TROY0031

Année 2015

utt
université de technologie
Troyes

# THESE

*pour l'obtention du grade de*

## DOCTEUR de l'UNIVERSITE DE TECHNOLOGIE DE TROYES

**Spécialité : SYSTEMES MECANIQUES ET MATERIAUX**

*présentée et soutenue par*

**Yugang LI**

*le 13 novembre 2015*

# Shot-peening and Low-cycle Fatigue of Titanium Alloys: Instrumented Indentation and X-ray Diffraction

## JURY

| | | |
|---|---|---|
| Mme C. LANGLADE | PROFESSEUR DES UNIVERSITES | Président |
| M. M. FRANCOIS | PROFESSEUR DES UNIVERSITES | Directeur de thèse |
| Mme P. KANOUTÉ | INGENIEUR DE RECHERCHE ONERA | Directrice de thèse |
| M. A. KORSUNSKY | PROFESSOR | Examinateur |
| Mme C. MABRU | PROFESSEUR DES UNIVERSITES | Rapporteur |
| M. H. PELLETIER | PROFESSEUR DES UNIVERSITES | Rapporteur |

*To my wife Cunfeng*

*To my parents and my elder sister*

"*I never saw a wild thing sorry for itself. A small bird will drop frozen dead from a bough without ever having felt sorry for itself.*"

- D.H. Lawrence

# Acknowledgements

How time flies. Four years have passed so fast, like a shuttle traveling on the loom. But, these four years are not poems written in water. With the assistances of many people, finally, I finished my doctoral dissertation.

First and foremost, I would like to show my sincere appreciation to my supervisors, Prof. Manuel François and Dr. Pascale Kanouté, for their support and guidance throughout my Ph.D study. Manuel leaded me into the gate of scientific research, taught me many skills and lots of knowledge in materials sciences and engineering, and greatly broadened my horizon. Pascale showed me profound sensibleness on fatigue of metallic materials. Things they passed on to me will definitely become the steady basis of my researching career in the future.

Authentic gratitude will also be expressed to Prof. Pelletier Hervé and Prof. Mabru Catherine for their valuable comments on my thesis, and to Prof. Langlade Cécile and Prof. Korsunsky Alexander for serving as juries in my Ph.D defense committee. Their kind help and frank advices greatly improved the quality of my thesis. I would like to show my special thanks to Mr. Virgil Optasanu, who helped me a lot on the heat treatment of T40, and Ms. Anne Lepied, who supplied us with the bulk of Ti-18 alloy.

Many colleagues in U.T.T, who gave me lots of help in technical support, experimental experiences, specimen preparation, problem discussion, etc., are absolutely worthy of my cordial acknowledgement. They are Mr. Bruno Guelorget, Mr. Laurent Daniel, Mr. Bruno Lesage, Prof. Xiaolu Gong, Prof. Zhidan Sun, Prof. Delphine Retraint, Mr. François Weil, Mr. Donato Gallitelli and Mr. Abdellah Oukkir. Without their assistance I could not have finished my Ph.D work so fluently.

I would like to sincerely appreciate my friends as well. Hongchang Han, Qiong Li, Yingjun Deng, Hui Shang, Xiaowei Lv, Mengyi Zhang and Haibin Zhu helped me a lot in my daily life. Without the help of Fanjuan Meng, Song Chen, Jie Zhang, Huan Wang, Wenjin Zhu, Tian Wang, Jian Zhang, I could not adapt to the life in Troyes so quickly and so well. Kun Jia, Xuan Zhou aided me a lot in experiments. Zhongmeng Wen, Jianqiang Zhou, Weijie liu, Zhenming Yue, Yosr Ghozzi enlightened me from several aspects for numerical simulations. Von Dim Nguyen helped me a lot about the usage of modeFRONTIER.

Last but not least, I would like to show my most sincere appreciation and deepest love to my wife, my parents and my elder sister. It is them who rose me up to more than I can be. Their altruistic love is always the strongest support of my life. I'm so proud of loving and being loved by them.

Yugang Li

Sep. 2015, at Troyes

# Notations

$\sigma_{res}$: Residual stress;

$\sigma_{max}$: Maximum stress;

$\sigma_{min}$: Minimum stress;

$\sigma_{mean}$: Mean stress;

$\sigma_a$: Stress amplitude;

$\Delta\sigma$: Stress range;

$\Delta\varepsilon$: Strain range;

$\Delta\varepsilon_e$: Elastic strain range;

$\Delta\varepsilon_p$: Plastic strain range;

$\Delta\varepsilon/2$: Strain amplitude;

$\Delta\varepsilon_p/2$: Plastic strain amplitude;

R: Load ratio;

$R_\varepsilon$: Strain ratio;

$\lambda$: Wavelength of the electromagnetic radiation;

$d$: Inter-atomic lattice spacing;

$\theta$: Bragg angle;

$\Phi$, $\Psi$, $\eta$: Sample angles;

$\varphi$, $\chi$, $\omega$: Goniometric angles;

$\theta$, $\gamma$: Diffractometric angles;

($S_1$, $S_2$, $S_3$): Specimen reference system;

($G_1$, $G_2$, $G_3$): Goniometer reference system;

($L_1$, $L_2$, $L_3$): Laboratory reference system;

$P$: Load on indenter;

$h$: Penetration depth of indenter;

$h_c$: Actual contact depth of indenter;

$P_{max}$: Maximum indentation load;

$h_{max}$: Maximum indentation depth;

$S$: Contact stiffness;

$H$: Contact hardness;

$A_c$: Projected contact area;

| | |
|---|---|
| $\beta$: | Geometric correction factor; |
| $E$: | Young's modulus; |
| $E^*$: | Reduced Young's modulus; |
| $\sigma_y$, $\sigma_{0.2}$: | Yield stress; |
| $v$: | Poisson's ration; |
| $K$: | Hardening coefficient; |
| $n$: | Hardening exponent; |
| $f$: | Friction coefficient; |
| $C_{str}$: | Structural compliance; |
| $C_f$: | Frame compliance; |
| $C_s$: | Sample compliance; |
| $C^*$: | Composite compliance; |
| $\tau$: | Average penetration depth of X-ray beam; |

# Abbreviations

| | |
|---|---|
| SP: | Shot-peening; |
| RS: | Residual stress; |
| WH: | Work hardening; |
| PP: | Accumulated plastic strain; |
| IIT: | Instrumented indentation test |
| FEM: | Finite element method; |
| X-RD: | X-ray diffraction; |
| EBSD: | Electron backscatter diffraction; |
| CPT: | Commercial pure titanium; |
| RVE: | Representative volume element; |
| *P-h* curve: | Indentation load vs depth curve; |
| AFM: | Atomic force microscope; |
| SMAT: | Surface mechanical attrition treatment; |
| WEDM: | Wire-cutting electric discharge machining; |
| DOE: | Design of experiment; |
| PCC: | Pearson correlation coefficient; |
| MOGA II: | Multi-objective genetic algorithm (improved version) |
| FMOGA II: | Fast multi-objective genetic algorithm (improved version) |
| SOM: | Self organizing maps; |
| MCDM: | Multi-criteria decision making; |
| SD: | Strength differential effect; |
| GIXRD: | Grazing incidence X-ray diffraction |
| LCF: | Low cycle fatigue |
| EDS: | Energy-dispersive X-ray spectroscopy |
| SEM: | Scanning electrical microscope |
| PSD: | Position sensitive detector |

# List of figures

# List of tables

# Shot-peening and low-cycle fatigue of titanium alloys: instrumented indentation and X-ray diffraction

## Abstract

There are two problems when investigating the effects of shot-peening on fatigue process. The first one is characterizing residual stresses (RS) and strain hardening (WH) on the sample surface. The second one is the evolution of RS and WH during fatigue.
In order to solve the first problem, this thesis proposes a “simultaneous function method” to measure RS and WH with nanoindentation. Accumulated plastic strain (PP) is used to represent WH. Then, by establishing functions of normalized indentation responses through a series of finite element method (FEM) simulations, normalized indentation responses obtained from nanoindentation experiments can be used to extract RS and PP values, assuming that the constitutive behavior is known. Although the simultaneous function method shows fairly high accuracy from a pure numerical view point, experiments performed on T40 commercial pure titanium are not completely satisfying. However, if the residual stress profile is known, the method can be used to derive the work hardening profile.
In order to study the second problem, a series of strain-controlled fatigue tests are performed on Ti-18 alloy. Fatigue specimens of 4 material states, including raw, shot-peened, prestrained and prestrained & shot-peened, were tested under 3 different strain amplitudes over 100 cycles. X-ray diffraction tests on the sample surfaces showed that the RS relaxation and the cyclic softening increase together with the strain amplitude. IIT tests showed that shot-peening may induce a softening of the surface of Ti-18 alloy samples.

**Keywords:** Shot Peening, Residual Stresses, Strain Hardening, Titanium alloys, X-rays - Diffraction, Nanoindentation, Fatigue

# Grenaillage et fatigue oligocyclique d'alliages de titane: indentation instrumentée et diffraction des rayons X

## Résumé

Deux problèmes surviennent lorsque nous étudions les effets du grenaillage de précontrainte sur le processus de la fatigue. Le premier est la caractérisation des contraintes résiduelles (CR) et de l'écrouissage. Le second est l'évolution de CR et de l'écrouissage pendant le cyclage.
Pour résoudre le premier problème, cette thèse propose une méthode pour mesurer les contraintes et l'écrouissage par nanoindentation. Ici, l'écrouissage est représenté par la déformation plastique cumulée (PP). A l'aide d'une série de simulations par éléments finis (MEF) en supposant le comportement du matériau connu, les réponses obtenues par indentation permettent d'obtenir simultanément contrainte et déformation plastique. Bien que satisfaisante d'un point vue numérique, les performances expérimentales obtenues sur un alliage de titane temps T40 restent insuffisantes. Cependant, si le profil de contrainte est connu, on peut toutefois obtenir le profil de déformation plastique. Les biais induits par la préparation de la surface ont été analysés en détail.
Pour le second problème, une série d'essais de fatigue ont été effectués sur un alliage Ti-18. Quartre traitement ont été testé sur 100 cycles sous 3 amplitudes différentes de déformation. Des mesures par diffraction des rayons X ont montré que la relaxation des contraintes et l'adoucissement cyclique augmentent avec l'amplitude de déformation. Les essais d'indentation ont montré un adoucissement de la couche grenaillée.

**Mots clés:** Grenaillage de précontrainte, Contraintes Résiduelles, Écrouissage, Titane - Alliages, Rayons X - Diffraction, Nanoindentation, Matériaux - Fatigue

# General introduction

Nearly all of the manufacturing and mechanical processes, such as rolling, deep drawing, cutting, turning, shot-peening, etc., can simultaneously introduce residual stresses and work hardening into components. For some of them, residual stresses and work hardening are inevitable without much useful meaning, for instance for machining process. However, for some other processes, the original intention is the introduction of these two factors, for example deep-rolling and shot-peening.

After the development of the past few centuries, shot peening has already become a fairly mature surface treating method which has been broadly used to treat many components, such as gear parts, cams, clutch springs, turbine blades, thin-gauge skins and so on, for improving their mechanical properties, surface hardness, erosion resistance and fatigue resistance. Thereinto, its fatigue resistance improvement is quite effective. In shot-peening process, high velocity shot impacts the component surface with force sufficient to create a series of continuous layers which are locally plastically deformed. Generally, the plastic deformation are quite severe, may even reach several tens percent in the region near the surface. The incompatibility between those layers can produce fairly high compressive residual stresses, even higher than the yield stress of the material, in the subsurface region of the components, which can effectively retard the propagation of fatigue cracks. Impact of shot may also be able to make the originally existing micro-cracks to be closed, which can obviously prevent the initiation of macroscopic fatigue crack. The comprehensive effect of all these factors is that the fatigue resistance performance of the shot-peened components can be improved obviously (fatigue limit will become higher, at the same time fatigue life will become longer). For components which will be submitted to low cycle fatigue loading, the deformation in each cycle can reach the plastic range, shot-peening treatment is necessary, convenient, and practical.

When we would like to study the effects of shot-peening on the low cycle fatigue tests, two major problems need to be considered. One problem is how to characterize residual stress and work hardening which are simultaneously introduced. Although many conventional characterization methods for residual stresses and work hardening have been developed in the past few decades, some obvious insufficiencies limited their application on fatigue samples. Firstly, they are not capable to accurately measure residual stresses and work hardening in small volumes, especially considering the small dimensions of fatigue test samples and the shallow layers created by shot-peening. Secondly, there is no effective approach to quantitatively characterize work hardening in such a component.

Another problem is the relaxation of residual stress and the evolution of work hardening, which always occur during low cycle fatigue process. The cyclic relaxation of surface compressive residual stresses and the possible cyclic softening phenomenon can weaken the efficiency of shot-peening process. Deeper investigation on these two problems can greatly help to understand the influence of shot-peening process. Important information can be

obtained from this to guide the modification of shot-peening to further improve the low cycle fatigue resistance of mechanical components.

A systemic review is made in Chapter 1 on a series of critical conceptions involved in the present thesis. Current situation and background in relative researching fields have been investigated and illustrated in this chapter. There are two major aims of the present thesis. First, a new characterizing method to simultaneously measure the shot-peening induced residual stresses and work hardening in a small volume will be proposed. Second, the relaxation of residual stress and mean stress and the evolution of work hardening on a titanium alloy under cyclic loading will be studied.

In Chapter 2, a new approach to qualitatively characterize residual stresses and work hardening in small volumes was firstly explored. Since both work hardening and accumulated plastic strain are closely correlated to the movement and pile-up of dislocations, the latter was used to represent to the former in this study. Considering that instrumented indentation test is a localized testing technique, which is sensitive to both residual stresses and work hardening, it has become our ideal candidate. In order to save time, money and material, the preliminary exploration was firstly performed with the finite element method (FEM) simulations. Firstly, a FEM model was built by checking its mesh convergence and adequacy. After that, several influencing factors (such as friction coefficient, material properties, etc.) and indentation responses (including maximum indentation load, contact stiffness, contact hardness and pile-up values) were investigated for finding out some factors which can possibly be used as quantitative indicators of residual stresses and accumulated plastic strain. After several attempts, a “simultaneous function method” was finally proposed. Simulations with two arbitrary combinations of residual stresses and accumulated plastic strain showed fairly high accuracy of this method from a purely numerical point of view.

In Chapter 3, the accuracy and adaptability of the simultaneous function method were investigated together with instrumented indentation tests, both experiments and simulations, on two shot peened T40 specimens which are respectively prepared with mechanical polishing (sample No.3) and electrolytic polishing (reference). However, a significant gap between experimental results and simulated data was obtained. In order to reduce this gap, an inverse method with multi-objective optimization was used. But, when residual stresses and accumulated plastic strain were considered, the simultaneous function method with the optimized parameters still did not work. A limited method can be used to extract the profile of accumulated plastic strain if the residual stresses are known by X-ray diffraction, however, the derived values are generally higher than experimental data. Even if sample disturbance induced by the mechanical polishing process of the sample No.3 was taken into account, the results still had not been obviously improved. Finally, in order to bypass the difference between electrolytic-polishing sample and the mechanical-polishing sample, the reference was set in another way. A position far away enough from the shot-peened surface (900 $\mu$m) on sample No.3, which is supposed to be without the influence of shot-peening induced residual stresses

and work hardening, was set as the new “reference”. After this kind of operation, the accuracy of the limited method was greatly improved.

Then, the relaxation of residual stress and the evolution of work hardening during low cycle fatigue process were studied in Chapter 4. A recently developed high-strength near $\beta$ titanium alloy, Ti-18, was used as the target material, because of its excellent mechanical properties, such as high specific strength, good ductility, etc. Low cycle fatigue tests on twelve fatigue samples of four material states (including raw, shot-peened, prestrained and prestrained & shot-peened) were conducted under three different strain amplitudes (0.7%, 1.0% and 1.4%). Results of fatigue tests and X-ray diffraction tests showed that the relaxations of mean stress and surface residual stresses increase along with the increase of strain amplitude. Shot-peening has little influence on the relaxation behavior of both mean stress and surface residual stresses. However, a proper tensile prestrain procedure can effectively retard the relaxation of both mean stress and residual stresses. Furthermore, results of instrumented indentation tests showed that shot-peening did not introduce work hardening but softening into the surface of the Ti-18 samples, which is in contrast to the results on T40.

At last, in Chapter 5, we conclude the whole thesis and give several perspectives for the relative researches in the future.

# Chapter 1

# Background and research status

In the study of the effects of shot-peening on the low cycle fatigue (LCF) resistance of components, two major problems need to be considered. One problem is how to measure conveniently and quickly residual stress profile in the depth of peened surfaces and how to evaluate quantitatively the work-hardening profiles. One of the aims of the present work is to propose a method to achieve both objectives simultaneously through instrumented indentation. The second problem is the simultaneous evolutions of residual stresses and the applied mean stress during the application of a cyclic strain loading. The respective role of work hardening and residual stresses in the fatigue performance of a shot-peened layer needs to be clarified as well.

Since being able to induce compressive residual stress layer into the surface of sample, shot-peening was proved to be capable to obviously improve fatigue properties of components [1]. However, dimensions and shape of the fatigue test samples caused a stubborn situation when we trying to characterize residual stresses and work hardening induced by shot peening process. Firstly, for economic reason and for saving material, in the dimension range suggested by fatigue test standard (such as ASTM E466-07 [2]), people always tend to use samples as small as possible. Precise measurement of residual stresses, especially in small dimensions, is always troublesome for researchers. Second, until now, there is no effective way to quantitatively characterize accumulated plastic strain in such a sample either. Owning to the reasons mentioned above, an objective problem was presented in front of us: find out a new method which is much more suitable for charactering residual stresses and accumulated plastic strain in shot peened fatigue test samples.

Characterization of residual stresses was investigated by many researchers [3], and a series of characterizing methods were built and developed [4] in the past few decades. No one can deny the merits of these methods, however, their shortcomings cannot be ignored as well, especially when considering the difficulties mentioned above.

Since being sensitive to both residual stresses and work hardening (which is closely correlated with hardness) in a local range [5, 6], instrumented indentation test (IIT) is a possible and interesting way to separate and characterize them along the gradient direction in depth of the layer affected by shot-peening process. However, how to realize it still needs to be discussed in detail. Even if characterizing residual stresses and work hardening through IIT could be realized, accuracy of the results has also to be compared with traditional methods.

In this thesis, we also would like to investigate the influence of shot-peening process on the LCF resistance of titanium alloys, especially the relaxation of residual stresses, the evolution of work hardening and the effects of prestrain process. In the literature, some

researchers proposed that the behavior of residual stresses under fatigue loading is quite similar as mean stress [7]. Thus, the relaxation behavior of mean stress will be one of the concerns in the present work as well. Furthermore, work hardening has direct relationship with accumulated plastic strain, because both of them are considered to be closely correlated with the movement and the piling up of dislocations [8]. Seeing this, accumulated plastic strain will be used in characterizing work hardening and studying the cyclic evolution of work hardening. In the present work, the high-strength near $\beta$-phase titanium alloy Ti-18 is chosen because of its remarkable mechanical properties and its potential use in aerospace applications. Considering all the problems mentioned above, several aspects of background information and research status should be introduced at first.

## 1.1 Basic concepts concerned

### 1.1.1 Shot-peening

Shot-peening is a cold working process used to produce a compressive residual stress layer and modify mechanical properties of metals. In this process, high velocity shot (round metallic, glass, or ceramic particles) impact the surface with a force sufficient to create a local plastic deformation. The process is widely accepted in extending fatigue life and retarding stress corrosion cracking as well as forming or shaping aerodynamic curvatures of aircraft wing skins [9].

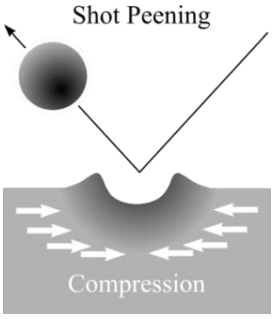


**Fig. 1-1. The scheme of shot-peening process.**

During the shot-peening process, each piece of shot that strikes the material acts as a tiny peening hammer, imparting to the surface a small dimple. Because of the occurrence of the dimple, the surface of the material yields in tension. However, below the surface, the material tries to restore its original shape, thereby producing below the dimple, a hemisphere of cold-worked material highly stressed in compression. After being peened with many shots for many times, the whole surface was full of dimples uniformly distributed. This will produce a surface layer containing compressive residual stress, whereas a core region containing tensile residual stress for equilibrium. Simultaneously, accumulated plastic strain is induced into the surface of components as well. Since many kinds of component failures (such as fatigue failures, corrosion fatigue, stress corrosion cracking, hydrogen assisted cracking, fretting, galling and erosion caused by cavitation, etc.) originated at the surface, the considerable compressive

residual stress in the surface layer can significantly prolong the lifetime and increase the load-carrying ability of components.

Shot-peening is used as a remedy if fatigue problems can be anticipated, for instance in stress concentration areas. As a result of the shot-peening process, compressive residual stresses exist in a thin surface layer. Because residual stresses do not affect cyclic stresses, cyclic slips may still occur. The cyclic slips can even lead to small microcracks, but these cracks cannot easily grow. The compressive residual stresses reduce or prevent crack opening of the microcracks. As a result, the stress concentration at crack tip is much lower and crack growth will be more difficult. It may even be stopped completely. The residual stress zone serves as a barrier for microcrack growth [10].

### 1.1.2 Residual stress

Generally speaking, residual stresses refer to the self-equilibrating internal stresses existing in a free component or structure without any external load applied. It is well known that no material, component or structure in application exists which is free of residual stresses. According to the scale of the inhomogeneity, residual stresses are mainly divided into three classifications, called residual stresses of the $1^{st}$, $2^{nd}$ and $3^{rd}$ kind [11].

-Residual stresses of the $1^{st}$ kind are almost homogeneous in a relatively large range of the materials (about several grains). Internal forces related to residual stresses of $1^{st}$ kind are in an equilibrium with view to any cross-sectional plane throughout the complete body. In addition, the internal moments related to the residual stresses with reference to each axis disappear. When interfering with the equilibrium of force and moments of a volume containing $1^{st}$ kind residual stresses, macroscopic dimension changes will be aroused.

-Residual stresses of the $2^{nd}$ kind are nearly homogenous across microscopic areas of the materials (one grain or parts of a grain). Internal forces and torques related to residual stresses of the $2^{nd}$ kind are equilibrated across a sufficient number of grains. Macroscopic dimension changes of a volume comprising $2^{nd}$ kind of residual stresses may only be observed if distinct disturbance of this equilibrium happens.

-Residual stresses of the $3^{rd}$ kind are inhomogeneous across submicroscopic areas of the materials (about several atomic distances within a grain and the equilibrium is only confined in small parts of a grain). No macroscopic dimension changes will happen if this equilibrium is disturbed.

It can be seen that these definitions are sufficient to describe all residual stress state existing in a component if mechanical effects or non-mechanical influence are absent [11]. Usually, the total residual stresses acting at a particular point of component are determined by a superposition of the $1^{st}$, $2^{nd}$ and $3^{rd}$ kind of residual stresses. Fig. 1-2 illustrate schematically a possible local superposition of the three different kinds of residual stresses.

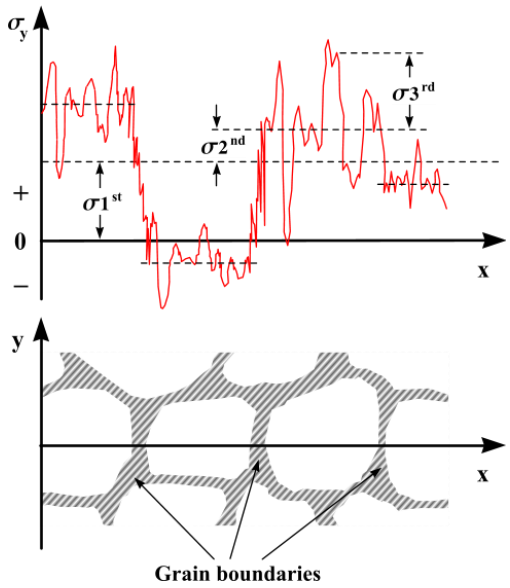


**Fig. 1-2. Total residual stress distribution along several grains of a polycrystal (schematically) and their separation in 1st, 2nd and 3rd kind of residual stresses [11].**

The classification of residual stresses discussed corresponds with the commonly used subdivision of residual stresses into macroscopic residual stresses and microscopic residual stresses. Macroscopic residual stresses usually refer to the 1st kind of residual stresses. In most situations, only this type of residual stresses will be considered if problems and effects related to residual stresses are discussed in engineering disciplines. Microscopic residual stresses, on the other hand, are very often regarded as a combination of residual stresses of the 2nd and 3rd kind.

Generally, macroscopic residual stresses can be induced due to several reasons [12]:

-Nonhomogeneous plastic flow under the action of external treatment (shot-peening, auto-fretting, roller burnishing, hammer peening, shock laser treatment)

-Nonhomogeneous plastic deformation during non-uniform heating or cooling (ordinary quenching, molding of plastics)

-Structural deformation from metalworking (heat treatment)

-Heterogeneity of a chemical or crystallographic order (nitriding or case hardening)

-Various surface treatments (enameling, nickel plating, chrome plating, PVD and CVD coating)

-Differences in expansion coefficients and mechanical incompatibility of the different components of composites (composites with a metallic and organic matrix, ceramic coatings)

In fact, the essentially formative mechanism of residual stresses is the inhomogeneous elastic or plastic deformations existing in a component. In such a permanent manner that incompatibilities of the state of deformation occur [13]. Consequently, any process (such as rolling, bending, shot-peening, etc.) that can induce nonhomogeneous plastic deformation into component will produce residual stresses. This is the reason why residual stresses are always accompanied with non-uniformly distributed plastic strain after the treatment of these processes.

Tensile residual stresses and compressive residual stresses always occur together. Without any external load, residual tensile stresses must be balanced by residual compressive stresses. Take the 1st kind residual stresses as an example, as shown in Fig 1-3, their distribution must satisfy the equilibrium equation:

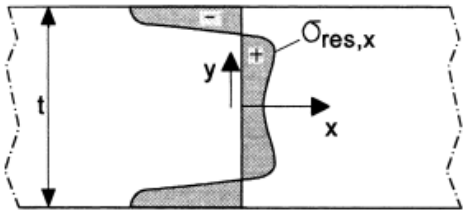


**Fig. 1-3. The distribution of 1st kind of residual stress is an equilibrium distribution [10].**

$$\int_{-t/2}^{t/2} \sigma_x dy = 0 \tag{1-1}$$

$$\int_{-t/2}^{t/2} y \cdot \sigma_x dy = 0 \tag{1-2}$$

The significance of residual stresses for fatigue is important in various practical problems. Unintentional tensile residual stress can have an adverse effect on the fatigue resistance, while compressive residual stress can significantly improve the fatigue behavior [10].

### 1.1.3 Work hardening

Work hardening, also known as strain hardening or cold working, is the phenomenon whereby a ductile metal becomes harder and stronger as it is plastically deformed [14].

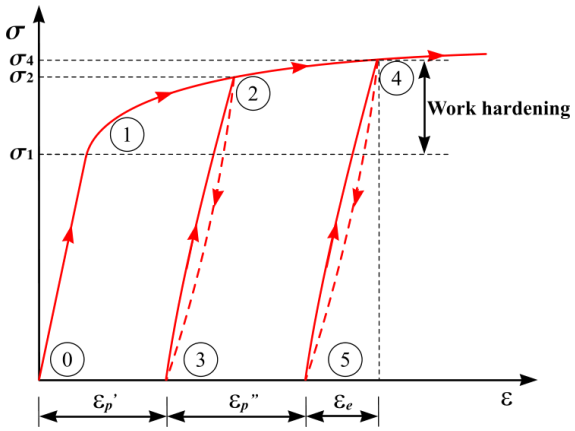


**Fig. 1-4. Loading and unloading cycles in a tensile test demonstrating work hardening.**

Considering a true-stress vs true-strain curve obtained from a uniaxial tensile test with several loading and unloading cycles, as shown in Fig. 1-4. The tensile test begin at ⓪ and then go upwards, elastically, to ①, the stress level corresponding to the apparent elastic limit ($\sigma_1$). Keep loading to ② (yielding occurs) and unloading to ③, plastic strain $\varepsilon_{p'}$ is left. Then load again, elastic behavior (the path of which will be slightly different from the unloading path) is observed again. However, this time the elastic part does not end with the initial elastic

limit $\sigma_1$, but a new elastic limit $\sigma_2$ which is higher. This means that, after a loading-unloading cycle, in order to yield the material again, a higher stress need to be applied. Keep doing this kind of loading-unloading cycles, the elastic limit of each new loading part will keep increasing. This kind of strengthening and hardening performance, when being plastically deformed, of metal material is call work hardening, for it usually happen in the forming process of metal at room temperature.

The forming mechanism of work hardening is closely related to the dislocations. In the metals, plastic deformation occurs through dislocation movement. When dislocations move, they are more likely to encounter and interact with other dislocations or crystalline defects, thereby producing resistance to further motion. In addition, the number of dislocations in a metal during deformation drastically increases (usually by several orders of magnitude), which further enhances the probability of interaction. The more dislocations within a metal, the more they will interact and become pinned or tangled. This will result in a decrease in the mobility of the dislocations and a strengthening of the metal [15]. As the dislocation density increases there is an increase in the flow stress of the material. However, the ductility (rate of elongation or reduction of area) will decrease at the same time as shown in Fig.1-5. Work hardening is usually called cold working because the plastic deformation must occur at a temperature low enough that atoms cannot rearrange themselves.

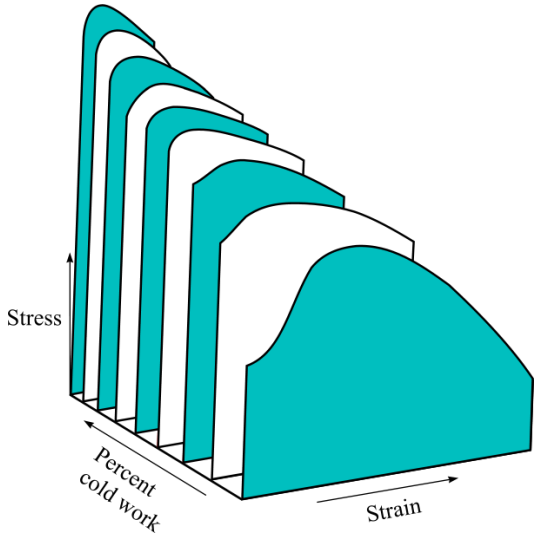


**Fig. 1-5. The influence of cold work on the stress-strain behavior for a low-carbon steel [15].**

### 1.1.4 Fatigue failure in metallic materials

Fatigue or fatigue failure is related to the changes of material properties due to the application of stress or strain cycles, this repeated loading can lead to cracking or fracture [16]. Fatigue failure were already observed and firstly investigated in the 19$^{th}$ century. Inchoate engineering research performed by August Wöhler showed that a single load application, far below the static strength of a structure, did not do any damage to the structure. However, if the same load was repeated many times, it could induce a complete failure.

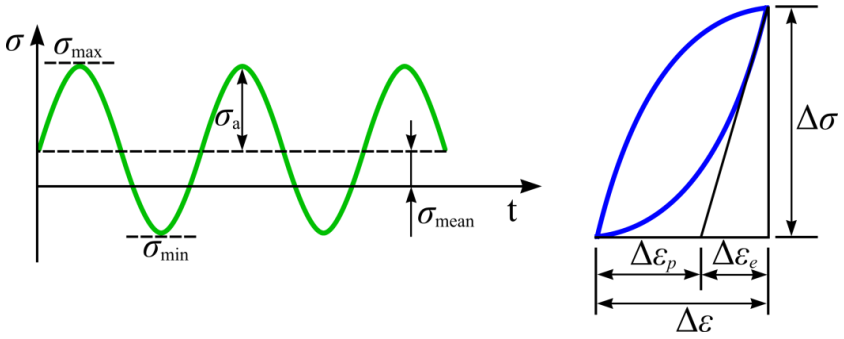


**Fig. 1-6. Scheme of the critical fatigue parameters.**

In a typical fatigue process, there are several critical parameters that affect the lifetime to crack initiation. They can provide lots of important information about fatigue process, which can directly help us to analyze fatigue properties of the target material. These parameters, including maximum stress ($\sigma_{max}$), minimum stress ($\sigma_{min}$), mean stress ($\sigma_{mean}$), stress amplitude ($\sigma_a$), stress range ($\Delta\sigma=2\sigma_a$), strain range ($\Delta\varepsilon$), plastic strain range ($\Delta\varepsilon_p$) and elastic strain range ($\Delta\varepsilon_e$), are sketched in Fig. 4-6. In practice, strain amplitude ($\Delta\varepsilon/2$) and plastic strain amplitude ($\Delta\varepsilon_p/2$) are used more frequently than strain ranges.

The ratio between the minimum load and the maximum load is usually called load ratio ($R$). According to the variations of load ratio and number of cycles, fatigue tests could be classified into several kinds, such as fully reversed low-cycle fatigue, repeated high-cycle fatigue, etc. Fatigue tests can also be classified into stress-fatigue and strain-fatigue according to the types of load controlling the tests. Fatigue failure mainly depends on the number of cycles and less on their frequency, except the cases when environmental and visco-plasticity effects at high temperatures are involved [16]. Fatigue failures occur in many different forms which are usually split into crack initiation stage (in which fatigue is a material surface phenomenon), crack propagation stage (in which fatigue resistance become a bulk property, but not a surface one) and the final failure stage (in the last cycle of the fatigue life, material is broken suddenly). Differentiating between the two periods is of great importance because several surface conditions (such as surface roughness) do affect the initiation stage, but have a negligible influence on the crack propagation stage [10]. In the present thesis, our attention is focused on the cyclic relaxation behavior of residual stress induced by shot-peening which mainly occurs at the very beginning part (hundreds of cycles) of the crack initiation stage.

## 1.2 The influence of RS and WH on fatigue process

### 1.2.1 The influence of residual stress

The practically most important area in which residual stresses influence the service behavior of materials/components/structures is the field of fatigue. Several investigations have confirmed that the presence of compressive (tensile) residual stresses at the surface of cyclically loaded materials/components/structures is beneficial (detrimental) to improve fatigue life [12]. Consequently, to components, which are expected to have a large resistance

against fatigue failure, many designers apply engineering techniques to generate compressive residual stresses at the surface. Frequently used procedures are shot-peening, surface-rolling, induction-hardening, case-hardening, nitriding and suitable combination of these treatments. Actually, all methods mentioned improve the high cycle fatigue (HCF) performance of various metallic materials. The observed increase of the endurance level depends on the process variables and can always be contributed to a certain amount of surface compressive residual stresses. In recent years, remarkable progress was obtained in predicting quantitatively the effects of residual stresses on the fatigue behavior of surface treated steel parts. Nowadays, at least objective concepts can be presented to use residual stresses in optimizing the design of various technical components which are fatigue loaded. A typical result [17] to what extent the bending fatigue strength of a low-alloy steel can be increased by case hardening and subsequent shot-peening is shown in Fig. 1-7. The chemo-thermical treatment yields a fatigue strength which is about 4 times greater than that of the normalized steel. By shot-peening a further increase of 6% is realized.

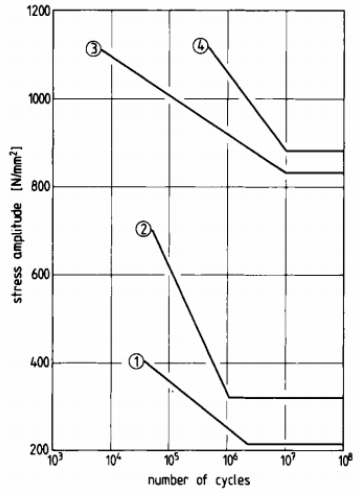


**Fig. 1-7. Woehler-curves of a case hardening steel 16 MoCr5 (1) normalized state, (2) blind hardened state, (3) case hardened state, (4) case hardened and shot-peened state [17].**

## 1.2.2 The influences of work hardening

Experiments also showed that softened and hardened steels represent different residual stress sensitivities. The beneficial influence of compressive residual stresses on bending fatigue strength can increase up to a certain extent with the increasing hardness of the materials [18]. This observation is due to the fact that metals with different hardness have different stability of the initial residual stress state during bending fatigue loading. In higher hardness material state, residual surface stresses are more stable. While in the normalized state, machining induced residual stresses almost completely relax during the fatigue process, they remain stable in the hardness state thus acting as mean stresses during the whole fatigue lifetime [19]. Plain carbon steels with hardness values < 400 HV are unsensitive to residual stresses of the 1$^{st}$ kind, which relax nearly completely in course of fatigue loading. In this particular case, however, residual micro stresses enhance the fatigue behavior. This was

demonstrated for some milled normalized steel specimens [18]. In the work hardened area dislocations have formed and become tangled, increasing the strength and hardness of material. This is profitable for keIIng the original pre-induced compressive residual stresses and improving the fatigue resistance of metal. Moreover, pre-induced work hardening (normally through applying a proper over load) can produce a plastic zone around the front of the fatigue micro cracks, which can further retard their growth, as shown in Fig. 1-8.

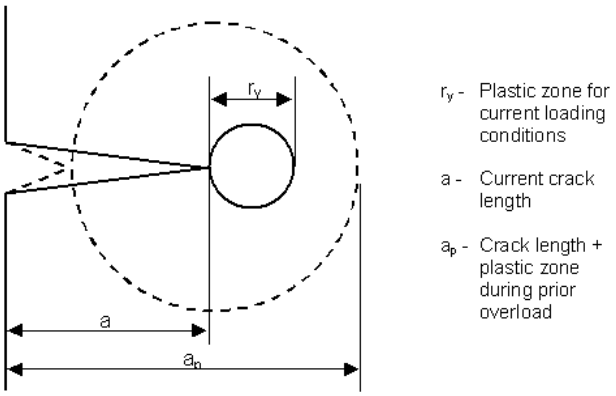


**Fig. 1-8. Plastic zone size parameters used in crack growth retardation models [20].**

## 1.3 Evolution of RS and WH during fatigue process

### 1.3.1 Cyclic relaxation of residual stress

Many researchers have concerned with the variations of residual stresses during the process of fatigue failure. In low cycle fatigue of a rolled HSLA steel, Quesnel *et al.* [21] found that residual stresses changed sign each half cycle, being opposite in sign to the sign of the applied load before load release. Noyan & Cohen summarized investigations on plain carbon steels in high-cycle fatigue [22]. A clear pattern emerges. Below the fatigue limit with annealed specimens, compressive stresses form and saturate. In one study [23] these stresses were found to occur only in deformation markings. Above fatigue limit, these residual stresses develop and then decrease until fracture. For specimens that are shot-peened, relaxation occurs at all stress level and is most rapid in the early stages of fatigue. In tension-tension fatigue of a shot-peened specimen, the stress can even reverse sign and become tensile. Much more work need to be done with various loading histories, because most of the previous work concentrates on bending or torsion. Noyan & Cohen [22] believe that the fading of residual stressrd during fatigue process is often attributed to microcrack formation, although there is as yet little evidence. Another interpretation by Taira's group [24, 25] is that the residual stresses form in annealed specimens due to elongation of the near surface region from excess vacancies formed during cycling. This continues until work hardening saturates, at which time the maximum compressive stress occurs. Additional cycles produce deformation of deeper layer, resulting in relaxation. Thus relaxation of residual stress should only occur in tensile cycles. However, no relaxation is observed in their case. James [26] suggests that stresses can relax owing to microplasticity in the near-surface region. As the surface is initially in compression, the relief

would occur only in a compressive half cycle. However, peened specimens do show stress relief in tensile cycling. Noyan & Cohen [22] proposed that the dominant process causing the compressive stress is micro-plastic elongation occurs in the near-surface region meanwhile the bulk is stretched elastically. A maximum residual stress may occur because the surface can only sustain a certain level of plasticity without void formation, or because of local work hardening. After shot-peening, the observation that relaxation occurs in tensile cycling leads us to believe that the bulk is elongating plastically more than the hardened surface. One thing interesting is that residual stresses could be examined after each half cycle of fatigue, to see when formation and relaxation actually occurs. Residual stresses should be measured in the axial and transverse direction, and in a direction normal to the surface. Such results might lead to an understanding of why in some cases the sign of residual stresses is not important in fading [27], whereas in other cases it is clear that the algebraic sum of applied and residual stress is controlling [28]

### 1.3.2 Cyclic relaxation of mean stress

For mechanical components subjected to asymmetric cyclic loading leading to plastic strain, most materials exhibit the phenomenon of either mean stress relaxation or strain ratchetting, or a combination of the two, depending on the applied load and structure geometry. If the maximum and minimum strains are fixed, then stress relaxation will occur. The initially non-zero mean stress will progressively shift towards zero as cyclic loading is applied, as sketched in Fig. 1-11. Mean stress relaxation, whereby the mean stress in a fatigue specimen subjected to strain-controlled fatigue (with a nonzero mean stress) tends toward zero with the progression of cyclic deformation. This is quite similar to the stress relaxation under monotonic loading with fixed strain, except it is induced by the cyclic loading rather than the elapsed time.

Literature showed that strain amplitude has strong influence on the cyclic relaxation behavior of mean stress [29]. For instance, several studies were conducted on N18 superalloy (which is used for turbine discs applications) for investigating the relaxation behaviors of mean stresses and residual stress, as shown in Fig. 1-9 [29]. Classic nonlinear kinematic hardening (NLK) model was modified by Jung & Chaboche [30] by introducing a threshold in the dynamic recovery term. Comparing with the experimental data obtained by Bussac & Lautridou [31], the modified NLK model with threshold can describe the relaxation behavior of the shot-peening induced residual stress in N18 superalloy very well.

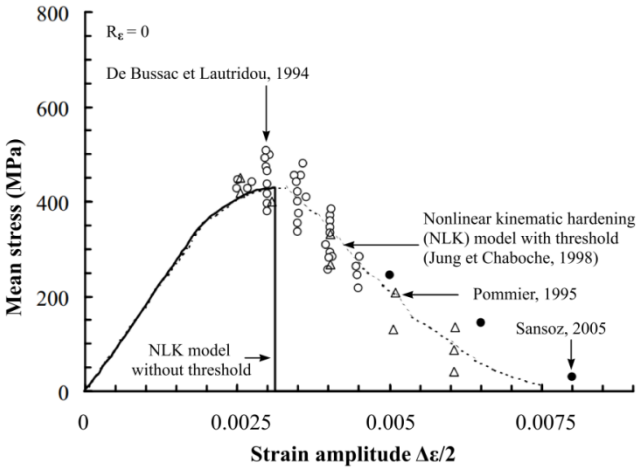


**Fig. 1-9. Evolution of stabilized mean stress for N18 superalloy fatigue samples (at 650°C) under repeated strain load (R$\varepsilon$=0) [29].**

By observing the curve predicted by the modified NLK model (the dash line in Fig. 1-10), a brief understanding about the relationship between mean stress relaxation and strain amplitude can be obtained. Actually, along with the increase of strain amplitude, mean stress will firstly increase to a certain value and then begin to decrease. While, the increasing stage is also divided into two parts: a linear increasing part ($0 \leq \Delta\varepsilon/2 \leq 0.0015$) followed by a nonlinear increasing part ($0.0015 \leq \Delta\varepsilon/2 \leq 0.0031$). The linear increasing part is caused by the fact that elastic cyclic deformation occurs in the whole sample (even if some localized plastic deformation may exist). Beyond the elastic limit, the material will yield. The very beginning part of plastic deformation will caused the increase of mean stress as well, which is the nonlinear increase part. However, the strain amplitude range and the increasing magnitude highly depend on the cyclic hardening/softening behavior of the material. In this nonlinear part, the strain amplitude still remains elastic, even if slight plastification may occur in the first tensile half cycle. Beyond the plastification at the first tensile half cycle, there will be three different situations. First, if cyclic strain amplitude is still below the fatigue limit, no relaxation of mean stress can be observed. Second, if cyclic strain amplitude is slightly above the fatigue limit (limited plastification), only limited relaxation will occur. However, after several numbers of cycles, a stable state can be reached which will leave a non-fully relaxed mean stress. Third, if cyclic strain amplitude is highly above the fatigue limit (high plastification), fully relaxation will occur and the mean stress will become zero.

Two things need to be further explained. First, the mean stress relaxation behavior shown in Fig. 1-9 can be observed under the loading condition that $R_\varepsilon \neq -1$, while, the relaxation of shot-peening induced residuals stress can happen under nearly any cyclic loading condition. The investigations under the loading condition $R_\varepsilon = 0$, which can show the relaxation of both mean stress and surface residual stress, will be quite interesting. It can help us to better understand the similarity and the divergence between the relaxation behavior of mean stress and that of the surface residual stress introduced through shot-peening. Second, all the mean stress levels shown in Fig. 1-10 are obtained from stabilized cycle. Actually, mean stress

relaxation along with the increase of number of cycles exists as well. Literature showed that this kind of relaxation tend to be stable after certain number of cycles.

If supposing that surface residual stress will act similar as mean stress, Fig. 1-10 can be used to under strand the role and the relaxation of residual stresses. If there is no mean stress relaxation in a cyclic softened material, flow stress imposed by the strain load will act as the black curve in Fig. 1-10. When compressive residual stress exists in the material, the black curve will uniformly shift downward as the blue curve. If the cyclic softening behavior exhibits in the material, flow stress at imposed strain level *C* is expected to be lower than that at *A*. The tendency for this kind of softening behavior in compression is not as significant as in tension. Consequently, the shape of the hysteresis loop for the portion *C* and *D* will roughly keep the same as that for *A* and *B*. A progressive reduction in the combination of mean stress and residual stress with increasing strain cycles will occur, as the red curve shown in Fig. 1-10. The decreasing rate progressively diminishes as the stress level of the combination approaches zero.

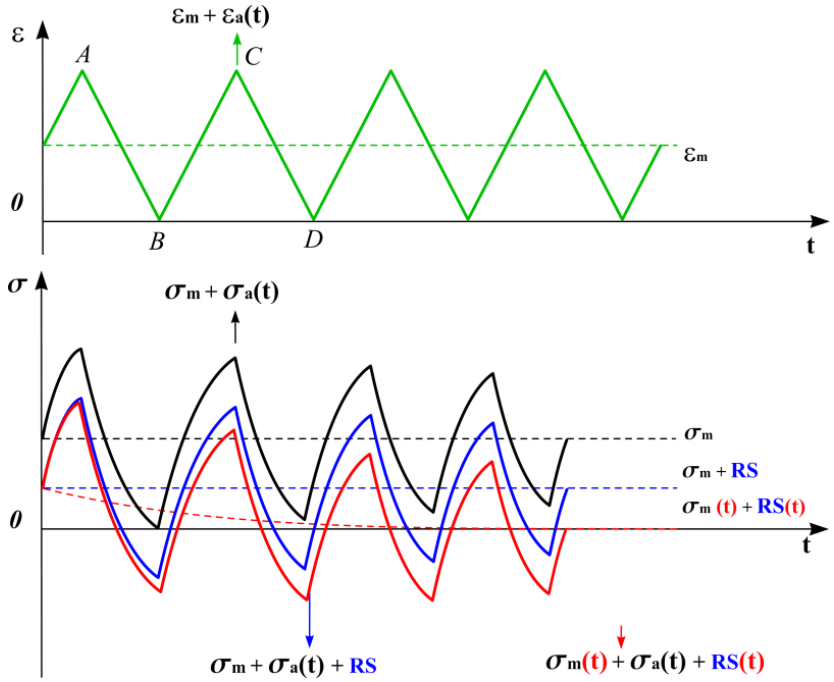


**Fig. 1-10. Relaxation of mean stress and residual stress in a cyclically softening material subjected to strain-controlled fatigue.**

Mean stress relaxation can also occur in cyclically hardening materials [32], although, the mechanisms are not so clear. Cyclic hardening reduces the plastic strain range and increase the stress range for a fixed total strain amplitude. With reference to Fig. 1-10, the material develops a higher flow stress at *C* than at *A*. However, with a tensile mean stress, the material yields more in tension than in compression. This preferential plastic straining alters the shape of the hysteresis loops in such a way that the stress at point *D* is lower that at *B*, although *C* is at a higher stress level that at *A*. The net result is that a relaxation of mean stress occurs in a cyclically hardening material as well.

### 1.3.3 Cyclic evolution of work hardening

Fatigue tests can be done at constant stress amplitude or at constant strain (or plastic strain) amplitude. Schematic diagrams of stress vs accumulated plastic strain for these two cases are shown in Fig 1-11 and Fig 1-12. The stress necessary to maintain a constant plastic strain amplitude increases as the number of cycles increases until it reaches a saturation value, as shown in Fig 1-11, which is called “fatigue hardening”.

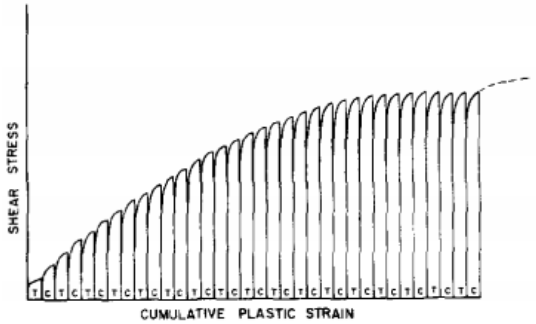


**Fig. 1-11. “Fatigue hardening” (schematic): at constant prescribed plastic strain amplitude, the observed shear stress amplitude increase with increasing number of cycles (solid line). The flow stress as measured in an interposed tensile test may rise even more (dashed line), (T=tension, C=comperssion).**

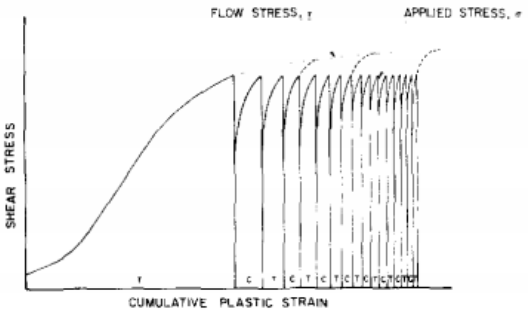


**Fig. 1-12. “Cyclic hardening” (schematic): at constant prescribed shear stress amplitude, the observed plastic strain amplitude decrease with increasing number of cycles (solid line). The flow stress as measured in an interposed tensile test may rise above the applied stress amplitude (dashed line).**

Conversely, in a test done at constant stress amplitude, the plastic strain per half-cycle decrease as the number of cycles increase until it reaches an approximately constant value, as shown in Fig 1-12. In saturation stage, both strain and stress amplitude are constant, no matter which is prescribed. During the initial hardening period, however, there are substantial differences in the material behavior for the two cases, and these differences may have a profound effect on whether or not fatigue failure eventually occurs.

Even in a test under constant applied stress amplitude, hardening still happens in the initial fatigue period. If a tensile test is interposed after a given number of cycles, the flow stress still can become larger than the previously applied stress amplitude. By the way, the larger the number of previous stress cycles the larger the flow stress values until a saturation value is reached. The ratio between the flow stress and the previously applied stress amplitude may be identified as a quantitative measure of “cyclic hardening” which should be carefully distinguished from the “fatigue hardening” shown above. Literature mentioned that is may be reasonable to assume that the dislocation interactions underlying cyclic hardening are similar to those determining work hardening in a tensile test at the same stress level, and thus there should be a correlation between the ratio and the work hardening rate in the material [33].

## 1.4 Characterization of residual stress

The “locked-in” character of residual stresses makes it very challenging to evaluate with high accuracy, no matter which kind of measurement technique is used. However, the various residual stress measurement methods are now quite mature and the accuracy gap is often not very large [4]. In the past few decades, many methods were developed for characterizing residual stresses.

### 1.4.1 Relaxation measurement methods

Many experiments and cases showed that structural deformations that accompany the stress redistribution that occurs when residual stresses are released by cutting or material removal. A linear relationship between the deformation and the released residual stresses is accepted, because that the “release” mentioned above is typically elastic. This provides the basis of the “relaxation” methods for characterizing residual stresses [34-36]. Since all of these methods need to cut or remove the material, they are normally called “destructive” methods. In nearly all cases, the deformation/stress relationship is made complicated, because that the stress is removed from one region of the specimen while the measurement are made on a different region where only partial stress relief occurs. For some simple geometries the deformation/stress relationship can be determined analytically, otherwise, finite element calibrations will be needed.

The hole-drilling method [37] is probably the most widely used relaxation method for the measurement of residual stresses. It involves drilling a small hole in the surface of the specimen. The relief of stress distorts the region around the hole and the stress is obtained from measurement of this distortion with strain gauges or full-field optical techniques. Fig 1-14(a) illustrates this process. This method becomes popular because it can give reliable and rapid results with many specimen types, and creates relatively localized and often tolerable damage. The hole-drilling method is well developed and now standardized as ASTM E837-08 [37]. In this procedure, the drilling speed and angle have strong influences on the value of induced drilling stresses and the accuracy of test. Also, the hole itself is a stress concentrator, which can lead to unwanted local plastic deformation, contributing to the distortion.

An “inside-out” variant of hole-drilling method is the ring-core method, where the “hole” is around the outside and the measurement on the inside, as shown in Fig 1-13. This method has the advantage over the hole-drilling method that it provides much larger surface strains and can identify larger residual stresses. However, it creates much greater specimen damage and it is more difficult to implement in practice.

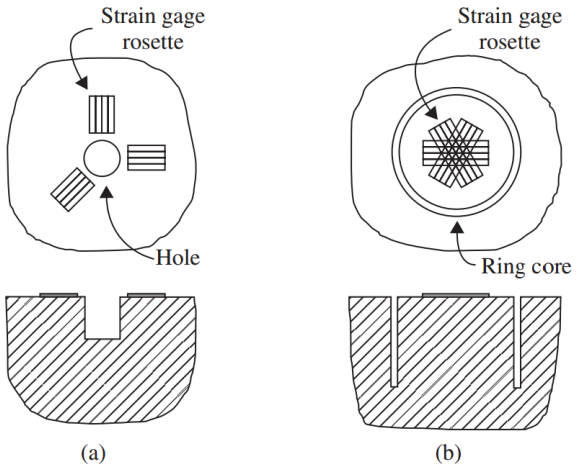


**Fig. 1-13. Hole-drilling method: (a) conventional hole-drilling method, (b) ring-core method [4].**

There are lots of other kinds of relaxation methods as well. Such as the splitting method [38], the sectioning method [39], the layer removal method [40], the deep-hole method [41, 42], the slitting method [43, 44], the contour method [45], and so on. The various relaxation techniques differ greatly in their characteristics, for example their applicable specimen geometry, their cutting procedure, measurement procedure, residual stress components identified, spatial resolution, and so on.

Different relaxation methods have various limits. For instance, hole drilling method is not suitable for the cases that stresses are highly non-uniform or noisy data is strong, layer removal is highly time-consuming and subject to measurement drift, etc.. Normally, volume affected by destructive methods varies from several $mm^3$ (hole drilling method) to few $cm^3$ (layer removal method). This makes them not suitable for our case, because the radius of the fatigue sample is quite small and the layer affected by the shot-peening is fairly thin.

### 1.4.2 Diffraction methods

The diffraction methods provide the possibility of a “non-destructive” procedure to measure residual stresses. There are several diffraction methods, such as X-ray diffraction [46], synchrotron X-ray diffraction [47] and neutron diffraction [48, 49], and so on. These methods mainly concern with the measurement of distance between atomic planes in crystalline or polycrystalline materials using the electromagnetic radiation, typically X-rays and neutrons. The radiation is absorbed and then reradiated with the same frequency such that strong emissions occur at certain orientations and minimal emissions at some other orientations, which flows the Bragg’s law [4]:

$$n\lambda = 2d\sin\theta \tag{1-1}$$

where $n$ is integer, $\lambda$ is the wavelength of the electromagnetic radiation, $d$ is the distance between the diffracting planes (inter-atomic lattice spacing) and $\theta$ is the Bragg angle, as shown in Fig 1-14.

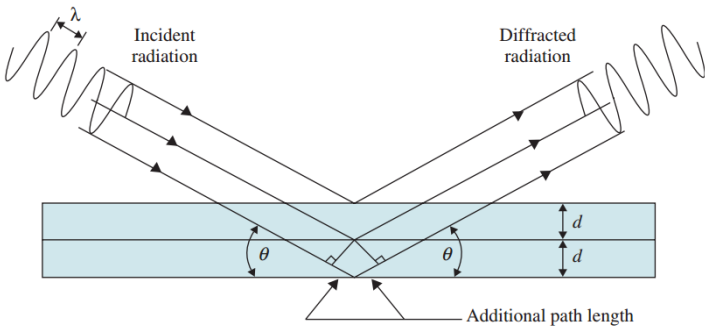


**Fig. 1-14. Radiation diffraction within a crystal structure [4].**

In this study, many X-ray diffraction tests will be performed in order to characterizing residual stresses and work hardening. Thus, here, our attention will be mainly paid to the X-ray diffraction tests. Considering the 4-circle Seifert PTS-3000 X-ray diffractometer used in this thesis, before talking about the measurement of residual stress with X-ray diffraction, the geometrical definition of a common X-ray diffraction system need to be introduced at first.

### 1.4.2.1 Geometrical definition of X-ray diffraction system

The key for describing a diffraction system consistently is to split the useful angles, a set of eight angles usually found in the literature, into three groups corresponding to three different aspects of physical acquisitions. The first group is the 'sample angles', denoted $\Phi$, $\Psi$, $\eta$, which are used to probe the mechanical state of the material at a given depth. The second group is the 'goniometric angles', denoted $\varphi$, $\chi$, $\omega$, which are used to describe the rotation of the goniometer system. The third group is called the 'diffractometric angles', denoted $\theta$ and $\gamma$, which are used to define the direction of the diffracted beam [50], as shown in Fig. 1-15. Similarly, three orthonormal reference systems need to be defined as well. The first is 'the specimen (S) reference system', denoted ($S_1$, $S_2$, $S_3$), as shown in Fig. 1-16. $S_3$ is normal to the specimen surface and directed towards outside. $S_1$ and $S_2$ stay in the plane of the surface and are freely chosen to make the system to be direct. The second reference system called 'the goniometer (G) reference system', denoted ($G_1$, $G_2$, $G_3$) is represented in Fig. 1-16 as well. $G_1$ is the propagation direction of the incident X-ray beam. G2 is the axial direction of the goniometer. $G_3$ is chosen so that the system ($G_1$, $G_2$, $G_3$) is direct. The third reference system is called 'the laboratory (L) reference system', denoted ($L_1$, $L_2$, $L_3$) as shown in Fig. 1-15(a). $L_3$ is normal to the diffracting plane {*hkl*} Directeur de thèse. $L_2$ is the intersection line of the diffracting plane {*hkl*} and the diffraction plane defined by the incident and diffracted beams. $L_3$ is chosen so that the system ($L_1$, $L_2$, $L_3$) is direct. One thing needs to be noticed is that the acquisition modes using a zero- (punctual) or a one-dimensional (position-sensitive) detector can be described by taking $\gamma$=0, which means that everything takes place in the equatorial plane of the diffractometer [50].

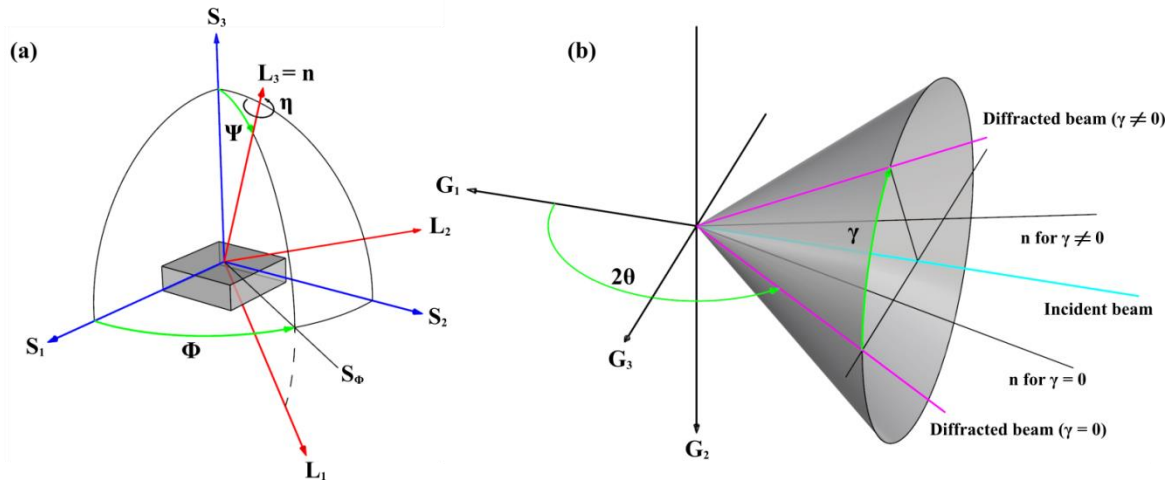


**Fig. 1-15. (a) Definition of the specimen reference system ($S_1$, $S_2$, $S_3$), of the laboratory reference system ($L_1$, $L_2$, $L_3$) and of the sample angles $\Phi$, $\Psi$, $\eta$; (b) Definition of the goniometer reference system ($G_1$, $G_2$, $G_3$) and of the diffractrometric angles $\theta$ and $\gamma$ [50].**

### 1.4.2.2 Standard $\sin^2\Psi$ method

Regarding the residual stress measurement with X-ray diffraction, there is a standard method broadly used, named standard $\sin^2\Psi$ method. The reference position for defining the origin of the angles is shown in Fig. 1-16. In order to determine the residual stresses in the material through X-ray diffraction, the specimen should have two kinds of rotations. One rotation is characterized by the tilt angle $\Psi$ between $S_3$ and $L_3$. This kind of tilt can be accomplished by a rotation about $S_1$ ($\chi$-mode) or $S_2$ ($\omega$-mode) respectively, or by the combined rotation of $S_1$ and $S_2$ (combined tilt mode (mixed mode)). The other rotation is characterized by the azimuth angle $\Phi$ and is executed by rotating around the specimen normal $S_3$.

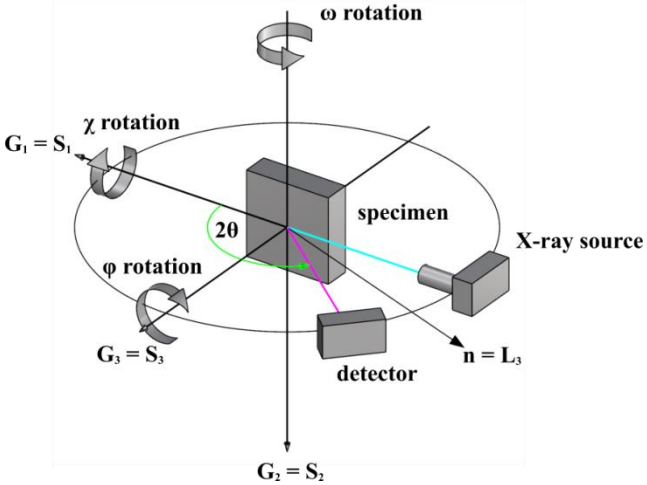


**Fig. 1-16. Reference position ($\varphi$=$\chi$=$\omega$=0), for which the axes $S_1$ and $G_1$, $S_2$ and $G_2$, $S_3$ and $G_3$ are superposed pair wisely [50].**

The residual or applied strain $\varepsilon_{\Phi\Psi}$ ($\{hkl\}$,$\tau$) can be determined from a change in the interplanar spacing $d_{\Phi\Psi}$ of the diffracting planes $\{hkl\}$ as follows:

$$\varepsilon_{\Phi\Psi}(\{hkl\},\tau)=\ln(\frac{d_{\Phi\Psi}\{hkl\}}{d_0})\approx\frac{d_{\Phi\Psi}\{hkl\}-d_0}{d_0} \tag{1-2}$$

where $d_0$ is the interplanar spacing of the unstrained material and $\theta_0$ is the corresponding Bragg angle.$\tau$ is the average penetration depth. Strains calculated from X-ray diffraction data acquired at crystallographic scale $\varepsilon_{\Phi\Psi}$ ($\{hkl\}$,$\tau$) can be correlated to the components of macrostress tensor $\sigma_{ij}(\tau)$ in the sample volume by:

$$\varepsilon_{\Phi\Psi}(\{hkl\},\tau)=F_{ij}\sigma_{ij}(\tau) \tag{1-3}$$

where the $F_{ij}$ are the Generalized X-ray Elasticity Constants (GXEC). When the material is macroscopically isotropic, the $F_{ij}$ depend on the two X-ray Elasticity Constants (XEC) $1/2S_2\{hkl\}$ and $S_1\{hkl\}$. They depend on the elasticity constants of the single crystal and the set of planes $\{hkl\}$ for a given crystal structure.

$$\begin{aligned}
F_{11}&=\frac{1}{2}S_2\{hkl\}\cos^2\Phi\sin^2\Psi+S_1\{hkl\}\\
F_{22}&=\frac{1}{2}S_2\{hkl\}\sin^2\Phi\sin^2\Psi+S_1\{hkl\}\\
F_{33}&=\frac{1}{2}S_2\{hkl\}\cos^2\Phi+S_1\{hkl\}\\
F_{12}&=F_{21}=\frac{1}{2}S_2\{hkl\}\sin 2\Phi\sin^2\Psi\\
F_{13}&=F_{31}=\frac{1}{2}S_2\{hkl\}\cos\Phi\sin 2\Psi\\
F_{23}&=F_{32}=\frac{1}{2}S_2\{hkl\}\sin\Phi\sin 2\Psi
\end{aligned} \tag{1-4}$$

In the above equations, one strain value (the shift of $2\theta$) is considered at each sample orientation ($\Phi$, $\Psi$). This is suitable for stress measurement with the positon-sensitive detectors which will be used in this thesis. By performing X-ray diffraction tests with various $\Phi$ angles and $\Psi$ angles (which means that varying the goniometer angles $\varphi$ and $\chi$ as shown in Fig 1-16), all the six independent components of the stress tensor could be obtained by linear least squares regression on the $\varepsilon_{\Phi\Psi}$ ($\{hkl\}$,$\tau$) vs $\sin^2\Psi$ plot, as shown in Fig 1-17 [51]. If shear stress components are neglect (supposed to be 0), the $\varepsilon_{\Phi\Psi}$ ($\{hkl\}$,$\tau$) vs $\sin^2\Psi$ plot will be a linear equation, as shown in Fig. 1-17(a). In this case, normal stress components can be calculated with the slop $m$ and the constants $F_{ij}$. If shear stress components are taken into account, the $\varepsilon_{\Phi\Psi}$ ($\{hkl\}$,$\tau$) vs $\sin^2\Psi$ plot will be Fig. 1-17(b). In this case, normal stress components can be calculated can be calculated as before. As for the shear stress components, they can be calculated with the slop $b$ of the $\Delta\varepsilon_{\Phi\Psi}$ ($\{hkl\}$,$\tau$) vs $\sin^2\Psi$ plot, as shown in Fig. 1-17(c), and the constants $F_{ij}$. The $\varepsilon_{\Phi\Psi}$ ($\{hkl\}$,$\tau$) vs $\sin^2\Psi$ plot may deviate from a straight line or a parabola-like curve when something, for instance strong texture, stress gradient, composition gradient, etc. exist in the material.

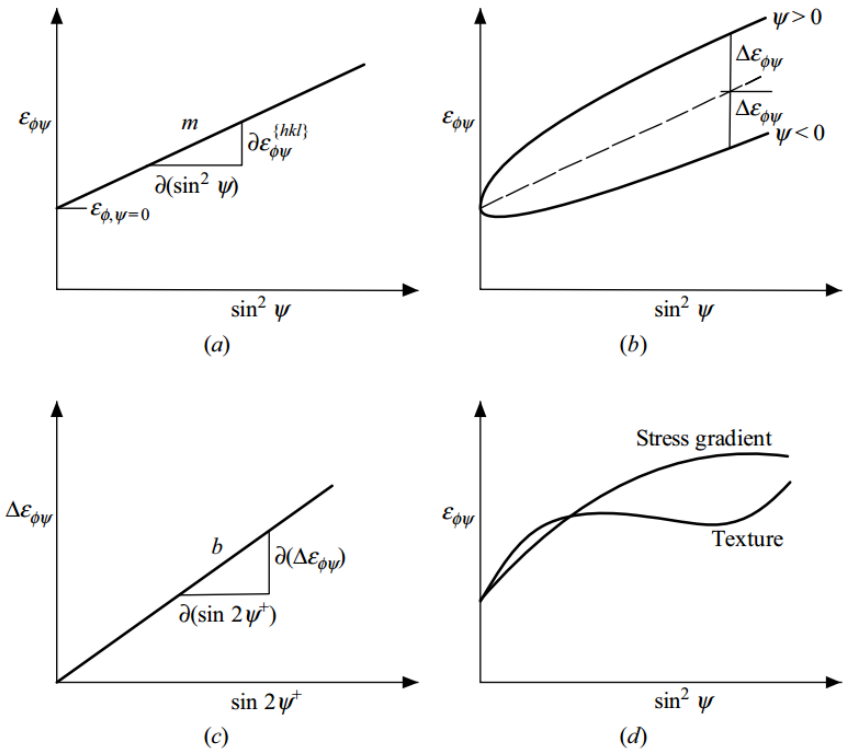


**Fig. 1-17. Stress measurement from the $\varepsilon_{\Phi\Psi}$ ($\{hkl\},\tau$) vs $\sin^2\Psi$ plot: (a) linear when $\tau_\Phi=0$; (b) $\Psi$-split due to $\tau_\Phi\neq0$; (c)plot of $\Delta\varepsilon_{\Phi\Psi}$ ($\{hkl\},\tau$) vs $\sin^2\Psi$; (d) curved due to texture, stress gradient, or composition gradient [51].**

Two major problems limited the application of X-ray diffraction for our case. Firstly, the beam size of X-ray diffraction, normally several $mm^2$, is too large comparing with the radius of the fatigue samples. Secondly, using X-ray diffraction on small cylindrical component is always troublesome, because that the sample surface curvature can severely decrease the quality of the diffraction patterns. This can directly affect the accuracy of the stress values extracted.

### 1.4.3 Instrumented indentation methods

The destructive or semi-destructive nature of the relaxation methods limits their application in the cases that the completeness of the sample need to be highly kept As for diffraction methods, it is always difficult to separate intrinsic microstructural effects on the physical parameters from the effects of a residual stress, and hence the methods require the preparation of stress-free reference sample for comparison purposes. Additionally, the physical methods, such as magnetic [52] and ultrasonic [53] methods, cannot be directly applied to amorphous/glass materials that do not have a long-range ordered atomic structures [6]. In the past two decades, one more technique has been added into the list of residual stress measurement methods. It is the instrumented indentation test.

Instrumented indentation test (IIT), also known as depth-sensing indentation or nanoindentation, allows the application of a specified force or displacement which could be controlled and measured simultaneously and continuously over a complete loading cycle.

Many material properties, such as Young's modulus [53, 54], hardness [53, 54], yield strength [55, 56], work-hardening exponent [57], fracture toughness [58], small-scale mechanical behavior (for instance, indentation size effect, pressure-induced phase transformation of semiconductors, inhomogeneous deformation of amorphous alloys) [6], and so on, can be derived from this test. Recently, much attention has been paid to instrumented indentation as a new way for characterizing residual stresses, because it may overcome the limitations of conventional methods.

After applying uniaxial or biaxial stresses into component, variation of hardness was observed through conventional Vickers [59] and Rockwell [60] hardness tests, which became the original motivation of measuring residual stress with instrumented indentation technique. Results showed that tensile stress tends to decrease the apparent hardness and compressive stresses increase it [60]. Based on this phenomenon, several empirical relationships were built for trying to extract residual stresses value from hardness tests.

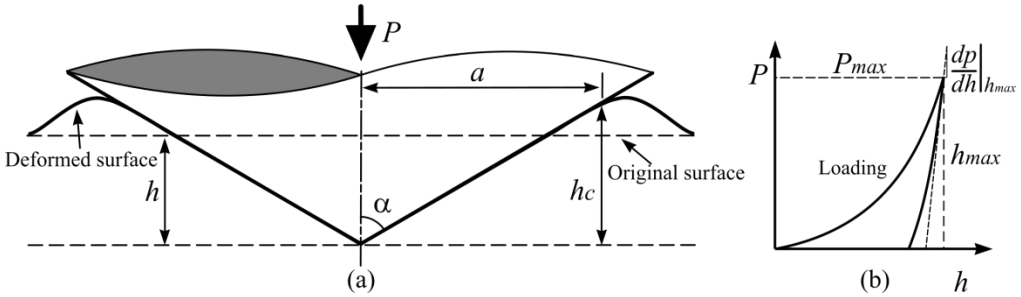


**Fig. 1-18. Scheme of equivalent conical indenter and the *P-h* curve derived from it [61].**

Since its commercialization in the middle of 1980s, instrumented indentation has become a powerful tool for measuring small-scale mechanical properties of materials. Considering a conical indenter equivalent to a Berkovich indenter as shown in Fig. 1(a), for which the semi apex angle $\alpha$ is equal to 70.3º , the evolution of the indentation load ($P$) regarding the penetration depth ($h$) (called *P-h* curve) is shown in Fig. 1-18(b). Different from conventional hardness tests, mechanical properties can be obtained only through analyzing the *P-h* curve during the whole loading and unloading sequence.

In a typical instrumented indentation process, contact stiffness ($S$), contact hardness ($H$) and projected contact area ($A_c$) are respectively defined as:

$$S = \left.\frac{dP}{dh}\right|_{h\max} = 2E^{*}a \tag{1-5}$$

$$H = \frac{P_{\max}}{A_c} \tag{1-6}$$

$$A_c = \pi a^2 \tag{1-7}$$

where $a$ is the projected contact radius, $dp/dh|_{hmax}$ is the initial slope of the unloading curve as shown in Fig. 1-18(b), $P_{max}$ is the maximum load and $E^*$ is the reduced modulus which is expressed as:

$$\frac{1}{E^{*}} = \frac{(1-\nu^2)}{E} + \frac{(1-\nu'^2)}{E'} \tag{1-8}$$

$E$ and $v$ are the Young's modulus and the Poisson's ratio of the tested material and $E$' and $v$' are the Young's modulus and the Poisson's ratio of the indenter, respectively. One thing needs to be noticed is that the projected contact area can also be expressed as a function of the actual contact depth $h_c$, because the shape of the indenter tips is usually a regular geometry (such as cone, triangular pyramid, sphere, etc.). For example, $A_c=24.5h_c^2$ for an ideal Berkovich tip. According to the most popular method proposed by Oliver and Pharr [54], the actual contact depth can be given by:

$$h_c = h_{\max} - \omega \frac{P_{\max}}{S} \tag{1-9}$$

Based on the IIT processes, several theoretical models were built for correlating the residual stresses and the instrumented indentation responses and then to try to realize the measurement of residual stresses. Some of them tried to build the relationship between contact hardness and residual stresses, like the model of LaFontaine *et al.* [62]. Some other models tried to connect residual stress with the projected contact area, such as the model proposed by Suresh and Giannakopoulos [63], the model by Lee *et al.* [64, 65] and the model by Carlsson & Larsson [66, 67]. Some other models also need the assistance of some material properties, like yield strength, Young's modulus, such as the model of Swadener *et al.* [68].

Besides the theoretical models mentioned above, numerical simulation techniques have also been used to establish the influences of residual stresses on instrumented indentation responses. Finite element simulations of sharp tip indentation were performed by Chen *et al.* [69] to analyze both the ratio of the in-plane residual stress to the yield strength ($\sigma_R/\sigma_Y$) and the reciprocal yield strain ($E/\sigma_Y$) on the contact hardness ($H$), the contact stiffness ($S$) and the work of plastic deformation ($W_p = \int_0^{h_{\max}} Pdh$). Based on the results, Chen *et al.* [69] proposed a method of reverse analysis to extract $\sigma_R$, $\sigma_Y$ and $E$ from only the $P$-$h$ curve. Based on the numerical simulation results, Xu & Li [70] proposed a coupled instrumented indentation simulation on bending test for determining the residual stress in a mechanically polished fused quartz beam.

Some more explanation need to be made on Eq.(1-5). Since the indenter tip (normally is diamond) is always much harder than the tested materials, thus, the mathematical foundations of indentation problem began from the contact analysis between a rigid punch and an elastic half-space [71]. Love firstly succeeded in finding a solution for conical [72] and cylindrical indenter [73]. Later on, Harding and Sneddon established an analytical procedure for deriving loading-displacement relations for an indenter of arbitrary axisymmetric shape [74]. And, this solution procedure was further simplified by Sneddon with the method of Hankel transforms [75].

Based on Sneddon's solution, a modification of Eq.(1-5) was obtained as:

$$E^* = \frac{1}{\beta} \cdot \frac{\sqrt{\pi}}{2} \cdot \frac{S}{\sqrt{A_c}} \tag{1-10}$$

In this formula, there is a correction factor $\beta$ which is correlated with the geometric shape of the indenter. The value of $\beta$ is taken to be 1 for axisymmetric indenters (e.g. conical and

spherical indenters). This is the reason why we cannot see $\beta$ in the Eq.(1-5). As for Berkovich indenter, the value of $\beta$ was recommended to be 1.304 [76].

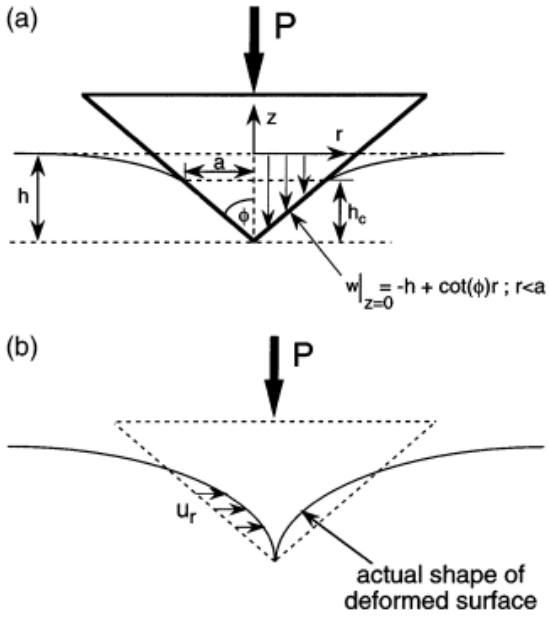


**Fig. 1-20. (a) Geometry used by Sneddon to describe indentation of an elastic half-space by a right circular cone. (b) Schematic representation of the actual shape of the deformed surface predicted by Sneddon's analysis when the radial displacements are taken into account [71].**

Another study performed by Hay *et al*. [71] showed that there should be another correction factor $\gamma$ in the Eq.(1-5), which is not negligible. Hay *et al*. [71] pointed out that one subtlety of Sneddon's solution was overlooked. Indeed, in Sneddon's solution for indentation of elastic half-space by a rigid cone, radial inward displacements of surface points inside the circle of contact are present and must be taken into account. The schema of radial inward displacements of surface points inside the circle of contact is shown in Fig. 1-19.

An important thing is that the correction factor $\gamma$ is suitable only for rigid indenters, which is meaningful for our later simulations (with rigid conical indenter). Hay *et al*. [71] suggested that for conical indenter, the value of correction factor $\gamma$ can be approximately calculated with:

$$\gamma = \pi \cdot \frac{\pi/4 + 0.15483073 cot\phi \dfrac{(1-2\nu)}{4(1-\nu)}}{(\pi/2 - 0.83119312 cot\phi \dfrac{(1-2\nu)}{4(1-\nu)})^2} \tag{1-11}$$

The results of Hay *et al*. [71] were further proved by Troyon *et al*. [77]. And, Troyon *et al*. [77] showed that in a general case, both $\beta$ and $\gamma$ should be taken into account, and the general form of Eq.(1-5) should be like this:

$$E^* = \frac{1}{\beta\gamma} \cdot \frac{\sqrt{\pi}}{2} \cdot \frac{S}{\sqrt{A_c}} \tag{1-12}$$

## 1.5 Characterization of Work Hardening

The characterization of work hardening is not easy. Several methods have been proposed based on different influences and mechanisms of work hardening. The mechanism of work hardening always accompany with microstructure evolutions in materials, such as dislocation movements, the tangle and pile-up of dislocations, missorientation of grains, the formation of microtwins, and so on. The testing techniques sensible to these microstructure evolutions could provide several ways for characterizing work hardening indirectly.

### 1.5.1 Hardness indentation

For a perfectly plastic-rigid solid the theory of hardness indentation is relatively simple. An important conclusion of the theory is that the hardness (the average pressure under the indenter), is a constant factor of the yield stress [78, 79] When Knoop or Vickers diamond indenter is used, this factor, known as the Tabor relation, is very close to three. However, several researches showed strong deviation of this factor [80]. Gerk [81] pointed out that the deviation of the behavior of the material from the Tabor relation is the result of the appreciable work-hardening which occurs during the initial stages of plastic deformation under the indenter.

The fact that the work-hardening influences the measured hardness value of a well annealed high purity of *fcc* metal was suggested by many researchers, such as Gilman [79]. Tests on nickel-free austenitic stainless steel made by Mirza and Khamdi [82] showed that the degree of deformation variation applied in cold-rolling process for the amount of 15%, 30%, 45% and 54%, is able to change the grain structure and increase the material hardness significantly without changing the phases. Similar hardness variation was observed on AISI 304 stainless steel as well by Milad *et al.* [83], however martensitic phase transformation occurred during the cold-rolling process.

Numerical simulation has also been used for calibrating the relationship between hardness and work hardening. Fazil & Ahmet [84] established an analytical relation between hardness and effective strain induced in a metal during cold working. The aim of the work of Fazil & Ahmet [84] is to determine hardness value from numerically obtained plastic strain without producing samples and making measurements, however their results showed a way for characterizing work hardening quantitatively by using their method reversely.

Hardness indentation test is simple and easy to perform. In most situations, residual stresses will normally be induced together with work hardening. However, hardness was proved to be sensitive to both of them, which severally limited applying hardness for measuring work hardening.

### 1.5.2 Electron backscatter diffraction (EBSD)

Mechanical twinning was proved to improve work hardening. This so called twinning induced plasticity (TWP) effect is considered to be resulted from a dynamical Hall-Petch effect [85-87]. Allain *et al.* [87] suggested that the high strain hardening of Fe-Mn-C TWIP steels is

mainly due to mechanical twinning. Bouaziz *et al.* [88] also proved the strong contribution of kinematical hardening to the mechanical behavior, which is closely linked to the TWIP effect. Electron backscatter diffraction (EBSD) analysis gives new possibilities for characterizing the microstructure evolution during plastic deformation [89].

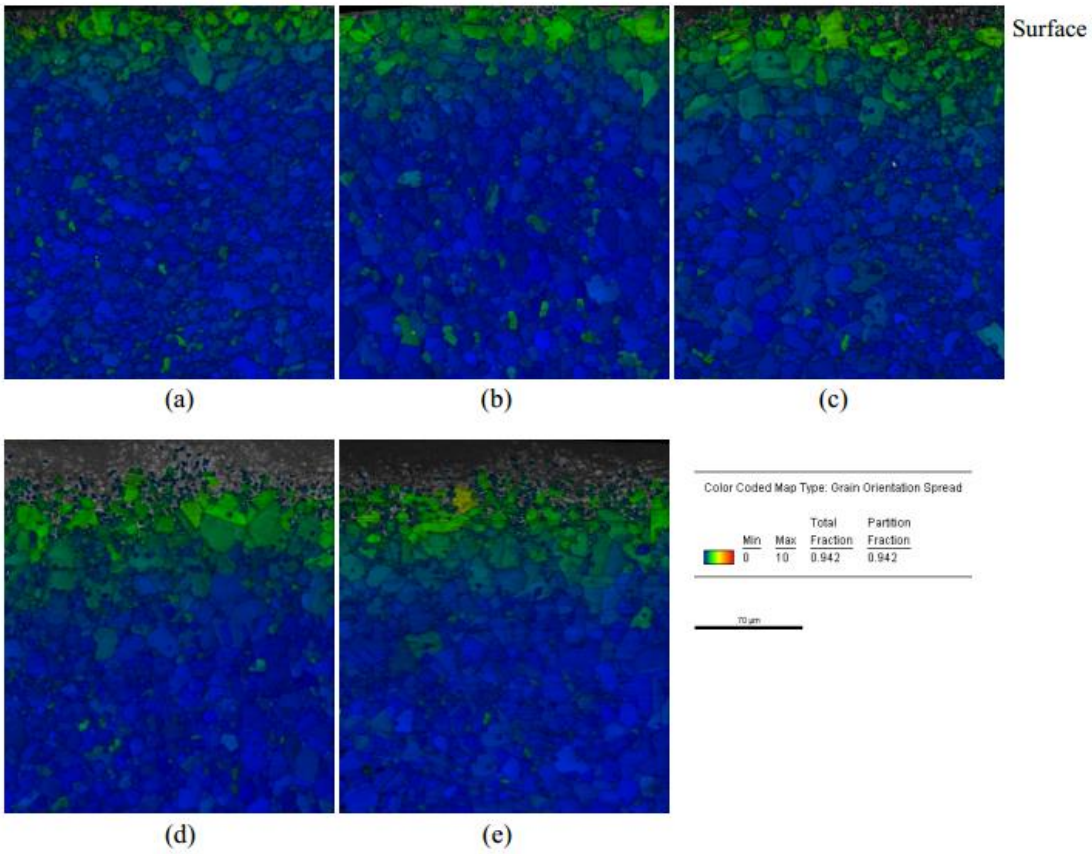


**Fig. 1-21. Maps of grain orientation spread (colour) and image quality (greyscale) for five shot peen intensities: (a) 4-6 A; (b) 5-7 A; (c) 6-8 A; (d) 7-9 A; (e) 8-10 A, applied to nickel-based alloy 720Li, showing the effects of surface deformation at the exposed sample edge (top) [92].**

Wilkinson *et al*. [90] go further in quantifying strain, using cross-correlation measurements of small shifts in EBSD patterns with a sensitivity of $10^{-4}$. Deformation assessments have been achieved as well by measuring an image quality parameter. Image quality describes the quality of an EBSD pattern by measuring the integrity of the crystal lattice in the diffracting volume. More strained microstructures are prone to increase dislocation interference resulting in reduced image quality during data collection. This phenomenon also provides a reasonable estimation of microstructural strain as shown by Yoda *et al*. [91], although it is dependent on the material type, absolute grain orientation and sample preparation procedure of the diffracting volume. Yoda *et al*. [91] also proposed an improved way to measure strain differences between grains using a parameter called average misorientation per grain which measures orientation within a grain on a kernel-by kernel basis, averaging the mismatch between adjacent kernels and assigning this as the average misorientation for that grain. Based

on this kind of feature, EBSD was used by Child *et al*. [92] to characterize the effect of shot-peening on work hardening at various shot-peening intensities.

The EBSD technique discussed above provide a more reliable method (high resolution) of assessing grain orientation due to induced strain hardening, comparing with hardness, which includes the contribution of residual stresses [93]. However, it can only give a qualitative characterization of work hardening, such as comparing the hardened zone and level with different conditions. It cannot provide a quantitative measurement of the amount of the work hardening.

### 1.5.3 X-ray diffraction

X-ray diffraction peak broadening analysis is proved to be a quite convenient approach to study the microstructural evolution of crystalline material. The peak broadening increases as the crystalline size is reduced and microstrain increases during the work hardening process [94].

The method of quantifying the level of work hardening in components by correlating the X-ray diffraction peak broadening to the equivalent true plastic strain has been studied and discussed in literature [95-97]. An example is shown in Fig. 1-22. If the level of work hardening is correlated to the amount of the equivalent true plastic strain, then it is accumulative and independent of the mode of deformation [96]. The peak width increases as the crystallite size is reduced and microstrain increases with the accumulated work hardening. As a metal is work hardened, the dislocation density increases which directly reduces the size of the perfectly crystalline regions or crystallites (coherent diffracting domains) and increases the average (standard deviation) microstrain in the crystal lattice. The reduced crystallite size and increased microstrain both produce broadening of diffraction peaks which can be conveniently measured as a mean of quantifying the degree to which the material has been cold worked [96].

The close relationship between the dislocation density in material and the peak broadening in X-ray diffraction had been discussed by several researchers. Wilkens [98, 99] first developed the theory about symmetrical X-ray diffraction lines broadened by dislocation, which was successfully verified by the experimental study of tensile deformed Cu-single crystals oriented for single slip [100]. The first theory for the diffraction peak broadening was proposed by Warren & Averbach [101]. They assumed that the broadening is caused by the size effect and strain effect. Groma & Ungar [102, 103] have discussed how the peak broadening in X-ray diffraction is closely related to the dislocation density in metallic materials. They built an effective model to correlate statistically stored dislocation (SSDs) density with local plastic strain. The plastic zone size and plastic strain distribution are determined quantitatively by Yang *et al*. [104] through measuring the full width at half the maximum (FWHM) of the peak in the magnitude of the discrete Fourier fransform (DFT) of backscattered electron (BSE) images of the microstructure around a fatigue crack tip in a commercially pure titanium (Ti) specimen. According to the results of a calibration made from images collected during an *in*

*stiu* tensile test, the peak width has a close relationship with strain for images of multi-grain patches. On the basis of this calibration, a plastic strain distribution map around the crack tip has been produced [105].

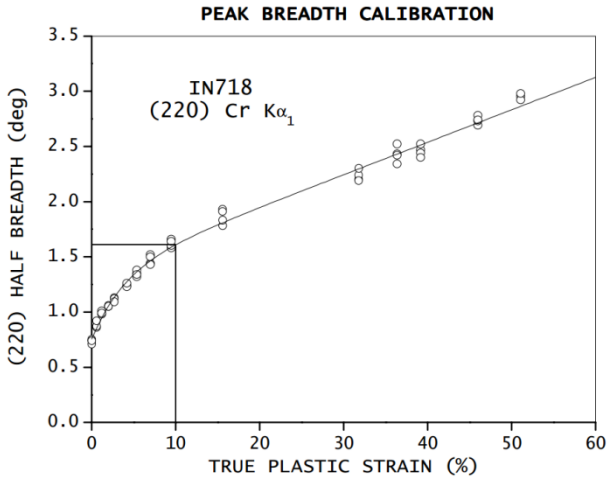


**Fig. 1-22 Dependence of (220) peak breadth on "work hardening" expressed as true plastic strain. Samples were prepared in compression with multiple measurements shown (the K*α*1 peak breadth corresponding to 10% work hardening is indicated) [94].**

The observed diffraction peak width is actually the convolution of broadening due to the work hardening present in the specimen and instrumental broadening. These two components may be separated using Stokes'method [96], however, this approach requires extensive data collection to completely define the diffraction peak profile and a reference specimen without work hardening [96]. With conventional X-ray diffractometer, as configured in Section 1.4.2, the beam size (normally can reach several $mm^2$) and the sample edge effect will make it impossible to characterize work hardening in a relatively small sample.

## 1.6 Titanium and its alloys

Titanium was named after the powerful sons of the earth–Titans, for representing its hard to extract ore. Many attempts were made to isolate the metal from the titanium ore using titanium tetrachloride ($TiCl_4$) as an intermittent step. The production of ductile, high purity titanium still proved to be difficult, because of the strong tendency of titanium to react with oxygen and nitrogen [106]. This is also the main reason why the cost of titanium and its alloy cannot be reduced remarkably and cannot be extensively used as substitute for steel.

### 1.6.1 Crystal structure

Like many other metals, titanium can crystalize in various crystal structures. Pure titanium as well as the majority of titanium alloys, crystallizes at low temperatures in a modified ideally hexagonal close packed structure, called $\alpha$ titanium. At high temperatures, however, the body-centered cubic structure is stable and is referred to as $\beta$ titanium. The phase transformation temperature is 882°C. The atomic unit cells of the hexagonal close packed (hcp) $\alpha$ titanium

and the body-centered cubic (bcc) $\beta$ titanium are schematically shown in Fig. 1-23 with their most densely packed planes and directions highlighted.

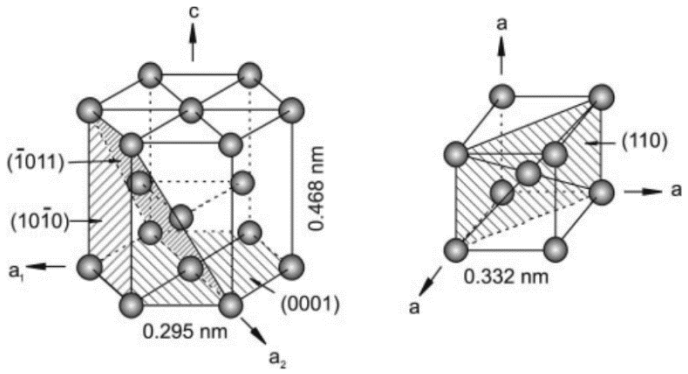


**Fig. 1-23. Crystal structure of hcp $\alpha$ and bcc $\beta$ phase [107].**

The existence of the two different crystal structures and the corresponding allotropic transformation temperature is of central importance since they are the basis for the large variety of properties achieved by titanium alloys.

Both plastic deformation and diffusion rate are closely connected with the respective crystal structure. In addition, the hexagonal crystal lattice causes a distinctive anisotropy of the mechanical behavior for the $\alpha$ titanium. The elastic anisotropy is particularly pronounced. The Young's modulus of titanium single crystal consistently varies between 145 GPa for a load vertical to the basal plane whereas it is only 100 GPa parallel to this plane.

### 1.6.2 Classification of titanium alloys

Commercial titanium alloys are classified conventionally into three different categories ($\alpha$, $\alpha$+$\beta$, and $\beta$ alloys) according to their position in a pseudo-binary section through a $\beta$ isomorphous phase diagram, schematically shown in Fig. 1-24 [106]. The group of $\alpha$ alloys consists various grades of CP titanium and $\alpha$ alloys, which upon annealing while below the $\beta$ transus, contain only small amounts of $\beta$ phase (2~5 vol%) stabilized by iron.

The group of $\alpha$+$\beta$ alloys has a range in the phase diagram (Fig. 1-24) from the $\alpha$/$\alpha$+$\beta$ phase boundary up to the intersection of the MS-line (martensite start line) with room temperature, thus $\alpha$+$\beta$ alloys transform martensitically upon fast cooling from the $\beta$ phase field to room temperature.

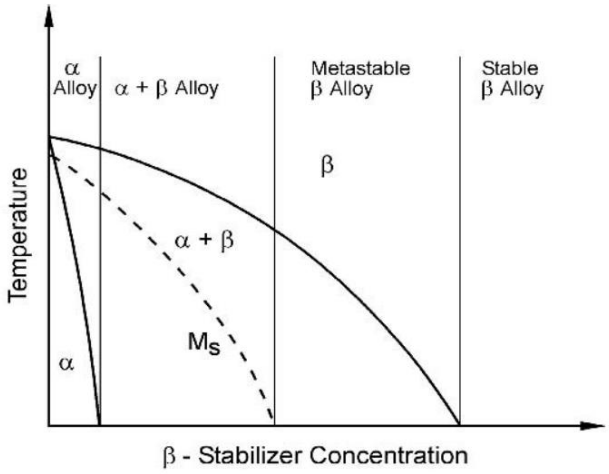


**Fig. 1-24. Pseudo-binary section through a *β* isomorphous phase diagram (schematically) [107].**

The *α* alloys generally have creep resistance superior to *β* alloys, and are preferred for high-temperature applications. The absence of a ductile-to-brittle transition, a feature of *β* alloys, makes *α* alloys suitable for cryogenic applications. Unlike *β* alloys, *α* alloys cannot be strengthened by heat treatment. They are most often used in the annealed or recrystallized condition to eliminate residual stresses caused by working [108].

### 1.6.3 Application of titanium and its alloys

In recent years, titanium and its alloys have been broadly used in lots of fields, such as satellites, rockets, power generating plants, offshore installations, deep drilling, automotive industry, and so on. However, the initial application field of titanium alloys, aerospace, still is the largest and most important one.

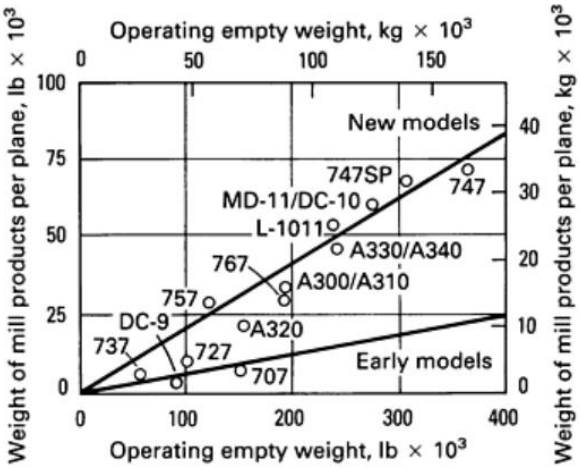


**Fig. 1-25. Increase of titanium consumption on commercial aircraft for both airframe and engine applications [109].**

High-strength-to-density ratio, good resistance and creep life, and good fracture toughness are characteristics that make titanium a preferred metal for aerospace application. The earliest production of titanium started in 1952, for the nacelles and firewalls of the Douglas DC-7

airliner. Since that time, titanium and its alloys have been used for structural components on aircraft ranging from the Boeing 707, to the supersonic SR-71. Titanium fan disks, turbine blades and vanes are commonly used in aircraft turbine engines. Researches concern with titanium is an important aspect which drives the increase of aerospace engine efficiencies [108]. Titanium-base intermetallic compounds are another class of materials which can increase the thrust-to-weight ratios of engines. Using precision titanium castings in jet engines, such as inlet cases or compressor frames, is a rising application [108].

Another major application of titanium is corrosion resistance. Although titanium alloys are still vital to the aerospace industry for their distinguished mechanical properties, recognition of the excellent resistance of titanium to many highly corrosive environments, particularly oxidizing and chloride-containing process streams, has led to widespread on aerospace (industrial) applications [108]. The excellent corrosion resistance of titanium alloys results from the formation of very stable, continuous, highly adherent, and protective oxide films on metal surfaces. Because titanium metal itself is highly reactive and has an extremely high affinity for oxygen, these beneficial surface oxide films form spontaneously and instantly when fresh metal surface are exposed to air and or moisture. Commercially pure titanium is more commonly used than titanium alloys for corrosion applications, especially when high-strength is not a requirement.

## 1.6.4 Our target materials

In this study, there will be two kinds of target materials: T40-CP grade2 and Ti-18 alloy. From alloying elements, fabrication processes, mechanical properties to applications, they are quite different from each other. However, fatigue property is quite important for both of them.

### 1.6.4.1 T40 grade 2 commercial pure titanium

Commercial pure titanium (CPT) has minimum titanium contents ranging from about 98.635 to 99.5 wt%. According to ASTM B 348-06 and ASTM B 265, grade 2 commercial pure titanium should fulfill the chemical requirements shown in Table 1-1. And, its tensile properties need to fulfill the requirements shown in Table 1-2.

**Table. 1-1 Chemical requirements of grade 2 CPT [110, 111]**

| Elements | C | Fe | N | O | H | Ti |
|---|---|---|---|---|---|---|
| Wt% | ≤0.08 | ≤0.20 | ≤0.03 | ≤0.18 | ≤0.015 | Bal |

**Table. 1-2 Tensile requirements of grade 2 CPT [110, 111]**

| Tensile strength | Yield strength, 0.2% offset | | Elongation in 50 mm | Bend test (Radius of Mandrel) | |
|---|---|---|---|---|---|
| min | min | max | min | Under 1.8 mm | 1.8 – 4.75 mm |
| MPa | MPa | MPa | % | in thickness | in thickness |
| 345 | 275 | 450 | 20 | 2T | 2.5T |

At room temperature, commercial pure titanium is typically a 100% $\alpha$ crystal structure. As amounts of impurity elements increase (primarily iron), small but increasing amount of $\beta$ phase are observed metallographically, usually at $\alpha$ grain boundaries. Annealed unalloyed titanium

may have an equiaxed or acicular $\alpha$ microstructure. The former can only be produced through recrystallization of material that has been extensively worked in the $\alpha$ phase, which occurs during $\beta$-to-$\alpha$ transformation during cooling through the transformation temperature range [112].

Commercial pure titanium has excellent resistance to corrosion, high-strength to weight ratio and good ductility as temperature decrease [113]. It is used at temperature below 350 ℃ (below 500℃ if there are no mechanical stresses). If serving at temperatures above these values, it will be under the risk to get severe surface oxidation. Higher temperatures are possible only under protective atmosphere or under vacuum. At low temperatures, tensile and yield strength of CPT goes up. However, contrary to what happens with steels, T40-CP grade 2 does not show any fragile rupture at very low temperatures.

T40 is a standard material in chemical engineering where it is placed in contact with numerous corrosive media (nitric acids, chloride and hypochlorite solutions, humid chlorine, organic acids) [107]. It has also been used frequently for heat exchangers in power stations, reacting containers in various chemical plants [113] and implant components [113]. In such aggressive environments, materials and components normally will undergo cyclical plastic deformation. Thus, stress corrosion and corrosion fatigue, which can be considered as environment sensitive nucleation and growth of subcritical cracks [114], will be their major failure formats. Since shot-peening has primarily an influence on the surface of materials and components, it could be one impede to stress corrosion and corrosion fatigue failure. It is important to know that shot-peening neither is a panacea for all stress corrosion and corrosion fatigue problems, nor is useless in most cases [115]. So, investigating the influences of shot-peening process on commercial pure titanium has its own importance in practical uses.

#### 1.6.4.2 Ti-18 high-strength near-$\beta$ titanium alloy

Along with the development of aerospace introductory, high-strength titanium alloys have been used more and more broadly to replace conventional structural materials, such as high-strength steels for reaching some special requirements, such as reducing weight, avoiding problematic coatings, lowering maintenance requirements, and so on. High-strength near-$\beta$ titanium alloys are mainly used for the landing gear, of which the serving condition is complex and the requirement of mechanical performance is high.

Inchoate high-strength near-$\beta$ titanium alloy is Ti-10-2-3 (Ti-10V-2Al-3Fe) who had the forging applications on the Boeing 777 main landing gear. However, later on, Ti555 has evolved into the baseline alloy for numerous high-strength applications. Comparing with Ti-10-2-3 alloy, Ti555 has many advantages, such as less prone to segregation (because of the content of Fe is lower), less sensitive to forging and heat treatment parameters (because that it is processed further below the $\beta$ phase transformation temperature), air-hardenable in large sections which avoids the need for water-quenching.

The TIMETAL 18 (here after called Ti-18) has been recently designed as a new bimodal titanium alloy, aiming at providing both an improved combination of ductility and mechanical

resistance in heavy sections, a superior quench capability and less sensitivity to heat treatment parameters when compared with the Ti-555 system [116]. By investigating the periodic table of the elements, the component of the alloying elements of Ti-18 were set as: Ti-5.5Al-5Mo-5V-2.3Cr-0.8Fe-0.15O (wt%). The Mo equivalent has been set at about 14.2 and ranges from about 12.8 to 15.2, and the beta stabilizer ratio has been set at about 1.4, according to the equilibrium conditions shown in Eq.(1-13) and Eq.(1-14). The kinetics are affected by the relative amounts of $\beta_{EUT}$ [116].

$$Mo_{eq} = Mo + \frac{V}{1.5} + \frac{Cr}{0.65} + \frac{Fe}{0.35} \tag{1-13}$$

$$\frac{\beta_{ISO}}{\beta_{EUT}} = \frac{Mo + \frac{V}{1.5}}{\frac{Cr}{0.65} + \frac{Fe}{0.35}} \tag{1-14}$$

Direct comparison of tensile properties of Ti-18 and Ti555 were shown in Fig 1-26. For now, the evaluation of production-scale material is still continuing. However, Ti-18 has already shown the dawn of the incremental property improvements over current near-beat alloys.

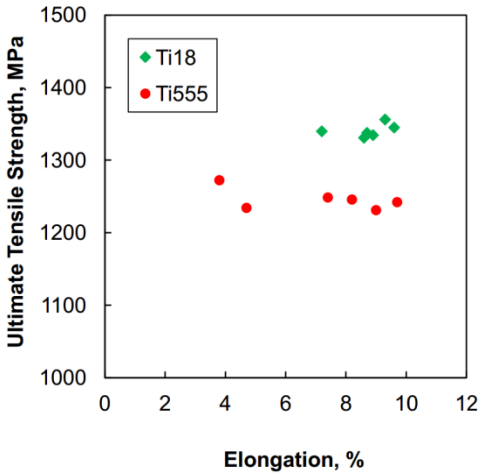


**Fig. 1-26. Comparison of Ti18 and Ti555 L strength-ductility combinations for 250mm diameter billet solution treated at T$_\beta$-44C, 2hrs, air cooled, then aged at 621C for 8hrs, air cooled [117].**

## 1.7 The Aim of This Thesis

During the last decades, the conventional residual stress characterizing methods have already become quite mature. However, the existence of practical difficulties in some special situations still has not been eliminated.

-First, the affected area of conventional residual stress characterizing methods is quite large. For diffraction methods, the beam size normally stays in the range of several square millimeters. As for destructive methods, the affected area can be even larger. This kind of limitation makes it nearly impossible to apply these methods on a relatively small component.

-Second, although some methods have been promoted for characterizing work hardening. However, some of them are quite trivial in practice, and some others can only be used

qualitatively. There is no method which can be easily and conveniently used to realize the quantitative characterization of work hardening.

Third, shot-peening will simultaneously induce residual stresses and work hardening into component. Sometimes, their influences are mixed together, which will be quite troublesome when trying to measure them respectively.

In order to overcome these limitations, developing a new method to quantitatively characterize shot-peening induced residual stresses and work hardening through instrumented indentation techniques will be the first aim of this thesis. The most ideal situation is that we will figure out a pure experimental way which can simultaneously obtain both residual stresses and work hardening levels easily and conveniently. If pure experimental way cannot be reached, a semi-experimental method, which might be assisted by numerical simulations, will be attempted. However, insensitive to both constitutive model and error range of the experimental data will be the expectant properties of the semi-experimental method. How to construct the new approach will firstly be studied with the assistance of finite element method (FEM). From the view point of saving time and materials, FEM simulation is a good choice for exploring new mechanical experimental methods. Once the new method is successfully built, its accuracy and stability will then be tested with FEM simulations as well. This part of work will be discussed in Chapter 2 in detail.

When the new characterizing approach has been proved to be reliable from a pure numerical point of view, it will be used in real experiments to characterize shot-peening induced residual stresses and work hardening in T40. The obtained results will be compared with the results extracted from conventional methods (probably X-ray diffraction). The possible problems that might be met during the application will be solved as well for improving the performance of the new method. This will be the major content of Chapter 3.

As a new branch of high-strength near $\beta$-phase titanium alloys, Ti-18 has great potential to be used in aerospace industry in the future. Thus, investigating its fatigue property will be meaningful. Furthermore, as one of the most broadly utilized surface-treating and manufacturing procedure of aerospace materials, shot-peening process can surely benefit the fatigue resistance of Ti-18 alloy with both imposed compressive residuals stresses and work hardening. Therefore, exploring the relaxation of residual stresses and the evolution of work hardening during low cycle fatigue process is significant for Ti-18 alloy. This will be second aim of this thesis which will be mainly investigated in Chapter 4. This part of work can finally guide the optimization of shot-peening parameters for improving the performance of Ti-18.

# Chapter 2

# Characterization of RS and PP with FEM simulations of IIT

As introduced in Chapter 1, since characterizing residual stresses and accumulated plastic strain in small round bar (such as fatigue test samples) is not easy with conventional methods, we would like to attempt to use instrumented indentation test to solve this problem because of its advantages in local material properties characterization.

Finite element method (FEM) is a convenient and low-cost way for simulating experimental process, which is especially useful in exploring the possibility and demonstrating the feasibility of a new experiment method at the very beginning stage. Thus, in this chapter, FEM will be applied for probing a new method that is suitable to characterize residual stresses and work hardening with instrumented indentation technique.

In Chapter 1, we explained that work hardening can hardly be measured directly. Considering the close relationship between work hardening and accumulated plastic strain, the later will be used as a parameter to represent the former in this study. Both residual stresses and accumulated plastic strain will be manually induced into a FEM model simulating the instrumented indentation test (IIT). Then, the indentation responses will be explored for building a method to obtain, as accurate as possible, the values of the residual stresses and accumulated plastic strain initially induced.

## 2.1 FEM model

Normally, shot-peening process will generate a continuous gradient distribution of RS and PP along the depth. In order to simplify the problem, discretization of the original continuous gradient was conducted. Results of some literatures showed that during IIT simulation process with residual stresses, parameters which will significantly influence the result is the hydrostatic stress in the region beneath the indenter tip, but not each individual component of residual stress [63]. Considering the two points mentioned above, we take a cylindrical representative volume element (RVE) under the shot-peened surface for our investigation, assuming that the values of RS and PP in such a volume are homogeneous. By applying an initial stress or hardening field, an equi-biaxial pre-stress or pre-strain field could be added into the RVE, as shown in Fig. 2-1. Many studies showed that because Berkovich indenter tip is geometric self-similar, it could be represented by a conical indenter with an apex angle which is equal to 70.3°, which gives the same projected contact area as Berkovich indenter tip at the same depth [118].

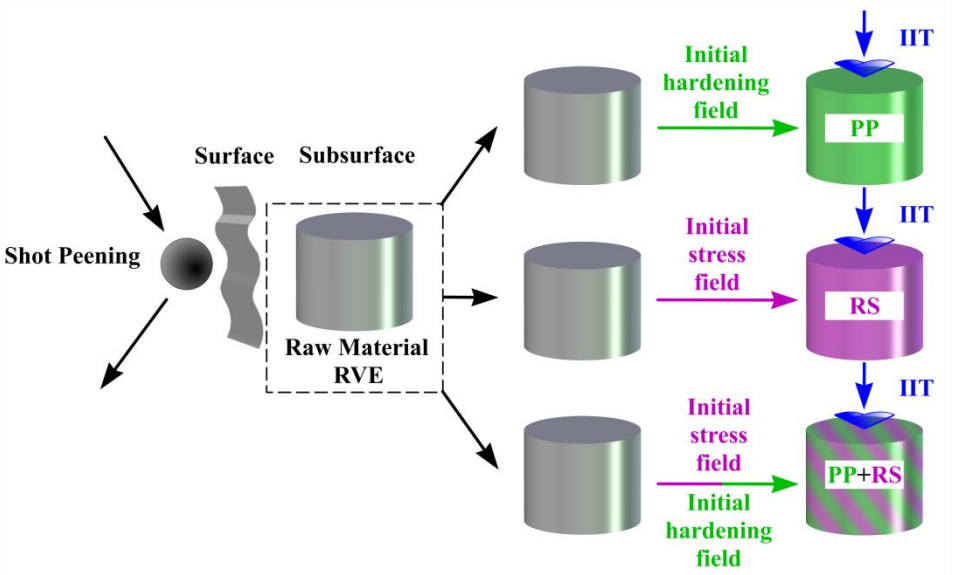


**Fig. 2-1. Schema of the RVE and the way for inducing PP and RS into the model.**

Considering that the whole problem is axisymmetric, an axisymmetric two-dimensional RVE model was built. Compared with a three-dimensional model, the total number of variables in an axisymmetric two-dimensional model will be considerably reduced for the same accuracy. Poon *et al.* [119] showed that loading/unloading curves may be obtained accurately if the RVE size satisfies the following convergence condition:

$$\frac{r_s}{h_s} \geq 1; \quad \frac{h_s}{h_{\max}} \geq 100 \tag{2-1}$$

where $r_s$ and $h_s$ are the radius and height of the cylindrical RVE, which are equal to 50 $\mu$m respectively in this study. These values are assumed to be large enough to approximately represent a semi-infinite body and to acquire the load vs displacement (*P*-*h*) curves accurately without the influences of the boundary effect, considering with the maximum penetration depth ($h_{max}$) equals to 0.5 $\mu$m along with the condition given by Eq.(2-1). Besides, considering the distributions of stress and strain fields in both depth and width direction, and the $h_{max}$ value, the mesh in the zone beneath the indenter (5 $\mu$m×5 $\mu$m) was refined to guarantee the precision of the model. The mesh near the contact area is specially refined, which will be discussed later on.

All the numerical simulations in the study were performed with commercial FEM framework ABAQUS®6.11.2. In ABAQUS®, initial stress and hardening field could be conveniently added into model by using the keyword *INITIAL CONDITIION [120]. However, as for initial stress, a step without any external load should be needed to let the stress field in the whole model reach self-equilibrium. This means that if without a proper boundary condition, the pre-stress induced by using the initial stress field will be released during this step. Considering the feature of the whole problem, boundary conditions as shown in Fig. 2-2 were used. This kind of boundary condition can both represent the real state of the RVE (all

the edges are surrounded by the rest of the material except the top edge) and keep the initial stress field.

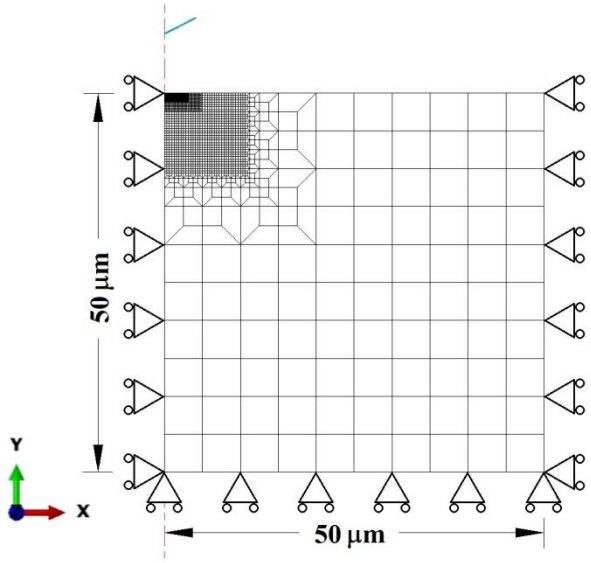


**Fig. 2-2. The axisymmetric model used in this study.**

Seeing the large difference between the Young's modulus of target material and that of the indenter material (normally in diamond), the indenter was represented by an analytical rigid surface. In view of the strong nonlinear stiffness in contact problems, linear quadrilateral elements are used to get convergent results [121]. Considering a metallic material could be assumed as an incompressible material, a four-node bilinear axisymmetric quadrilateral, reduced integration, hybrid element (CAX4RH) in ABAQUS® was used. Since a very small change in displacement for incompressible material produces extremely large changes in pressure, a purely displacement-based solution is too sensitive to be useful numerically. ABAQUS® removes this singular behavior in the system by using hybrid elements, which are mixed formulation elements, using a mixture of displacement and stress variables with an augmented variational principle to approximate the equilibrium equations and compatibility conditions. The hybrid elements also remedy the problem of volume strain locking [121]. The geometry and boundary condition of the whole model with a conical indenter tip is shown in Fig. 2-3. Concerning the feature of the numerical treatment of contact problem, the master surface should make contact with and penetrate the slave surface [120]. So, the indenter tip is defined as the master surface while the target material is defined as the slave surface. Literature showed that the friction coefficient between diamond and metal material is normally in the state between 0.1 and 0.15 [122]. Thus, the interaction between the indenter tip and the target material is assumed to be finite-sliding, surface-to-surface with a friction coefficient of 0.15. The normal contact behavior is defined as "HARD" pressure-overclosure relationship. In this case, the formulation of the normal contact is used as a constraint for non-penetration which treats the normal contact as a unilateral constraint problem. The normal contact pressure cannot be calculated from a contact constitutive equation, but is then obtained as a reaction force in

penetration direction (RF2 in ABAQUS®) in the contact area and, hence, can be deduced from the constraint equations with the Penalty method [120]. Displacement-controlled load was applied on the indenter tip to reach the maximum penetration depth, because it always shows better convergence property than force-controlled load [120]. All the simulations were performed with ABAQUS®/Standard.

As for the constitutive model, a Ludwick type isotropic hardening behavior is used to describe the plastic true-stress/true-strain response of the target material, which is written as follows:

$$\sigma = \sigma_y + K(PP)^n \tag{2-2}$$

where $\sigma_y$ is the initial yield strength of the material, $PP$ is the accumulated plastic strain, $K$ is the hardening coefficient and $n$ is the hardening exponent. All the parameters in the constitutive model and their values are shown in Table 2-1. And, all the corresponding tensile true stress vs true plastic strain curves are shown in Fig. 2-3.

**Table 2-1 Material properties considered in the numerical simulation.**

| | Copper [123] | A | B | C |
|---|---|---|---|---|
| Young's modulus $E$ (GPa) | 122 | 122 | 122 | 122 |
| Poisson's ratio $v$ | 0.33 | 0.33 | 0.33 | 0.33 |
| Yield strength $\sigma_y$ (MPa) | 240 | 800 | 240 | 800 |
| Hardening coefficient $K$ (MPa) | 340 | 340 | 340 | 340 |
| Hardenig exponent $n$ | 0.57 | 0.1 | 0.1 | 0.57 |

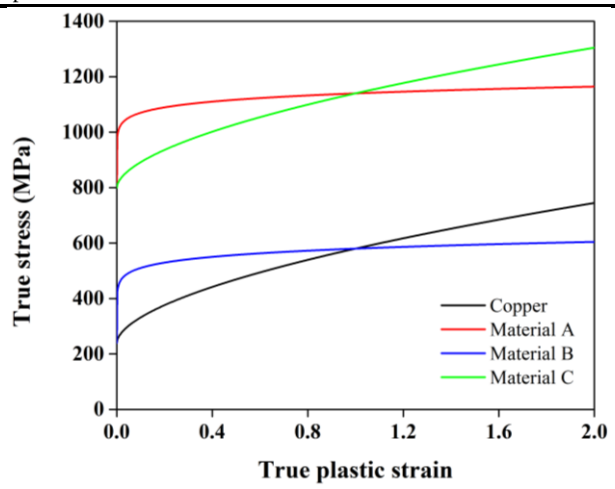


**Fig. 2-3. The tensile true stress vs true plastic strain curves for all the four materials.**

Ludwick hardening behavior was obtained by an adequate choice of parameters in the Johnson-Cook behavior already implemented in ABAQUS®.

## 2.2 Mesh convergence investigation

The first thing that needs to be done with a FEM model is to investigate the convergence of the mesh. In FEM modeling, a finer mesh typically results in a solution with higher accuracy. However, as a mesh is refined, more computing resources (e.g. physical memory, disk space

and CPU time) will be needed to accomplish the simulation. In order to get a mesh that can satisfy the balance between accuracy and computing costs, mesh convergence study has to be done.

In theory, for each successive level of mesh refinement in the convergence study, all elements in the model should be split in all direction. In fact, it is not necessary to carry this out on the whole model. According to St Venant's Principle, local stresses in one region of a structure do not affect the stresses far away enough. From a physical point of view, it should be possible to test convergence of a model by only refining the mesh in the regions of interest, and retain the unrefined (and probably unconverged) mesh elsewhere. In order to avoid abrupt change of mesh, transition regions are needed between the coarse mesh zone and the fine mesh zone.

**Table 2-2 Model information of different mesh strategies.**

| | Total number of elements | Smallest element size | Total number of nodes | Total CPU time | Total number of variables in the model |
|---|---|---|---|---|---|
| | - | nm | - | s | - |
| *Coarse4* | 1512 | 1875.0 | 1456 | 42.7 | 4657 |
| *Coarse3* | 1884 | 937.5 | 1817 | 73.9 | 5822 |
| *Coarse2* | 2350 | 468.8 | 2270 | 133.7 | 7283 |
| *Coarse* | 3519 | 234.4 | 3622 | 292.8 | 11216 |
| *Middle* | 4583 | 117.2 | 4720 | 680.2 | 14728 |
| *Fine* | 6618 | 58.6 | 6817 | 1813.1 | 21433 |
| *Super_fine* | 10572 | 29.3 | 10890 | 5622.6 | 34465 |
| *Super_fine2* | 18387 | 14.6 | 18937 | 9681.2 | 60210 |
| *Local_super_fine3* | 11702 | 7.3 | 11360 | 4986 | 37061 |

In the mesh convergence study, models with 9 different mesh sizes in the interesting region were built. Model information about different mesh strategies are listed in Table 2-2. For the first 8 strategies, elements in the whole contact area were gradually refined until 14.6 nm for the smallest element. For the 9$^{th}$ strategy, most elements in the contact area kept the same size as in the *Coarse* strategy. Only two parts of elements were specially refined. The first part is the elements in the upper left corner, which kept the same size as in the Fine strategy. It is because that this part will make contact with the peak point of the indenter tip and generate very high field gradient, especially at the beginning of the contact. The second part concerns the elements near the boundary of the contact zone between the indenter and the material, which kept the half size as in the *Super_fine2* strategy. One important parameter we would like to get from the IIT simulation is the contact hardness ($H$), which is directly decided by the projected contact area ($A_c$). During the IIT process, pile-up/sinking-in phenomenon often occurs, which will significantly affect the value of $A_c$. In order to take pile-up/sinking-in phenomenon into account for obtaining the value of $A_c$ precisely enough, without increasing too much computing costs, we designed the 9$^{th}$ meshing strategy. Elements in the interesting region of different mesh strategies are shown in Fig. 2-4.

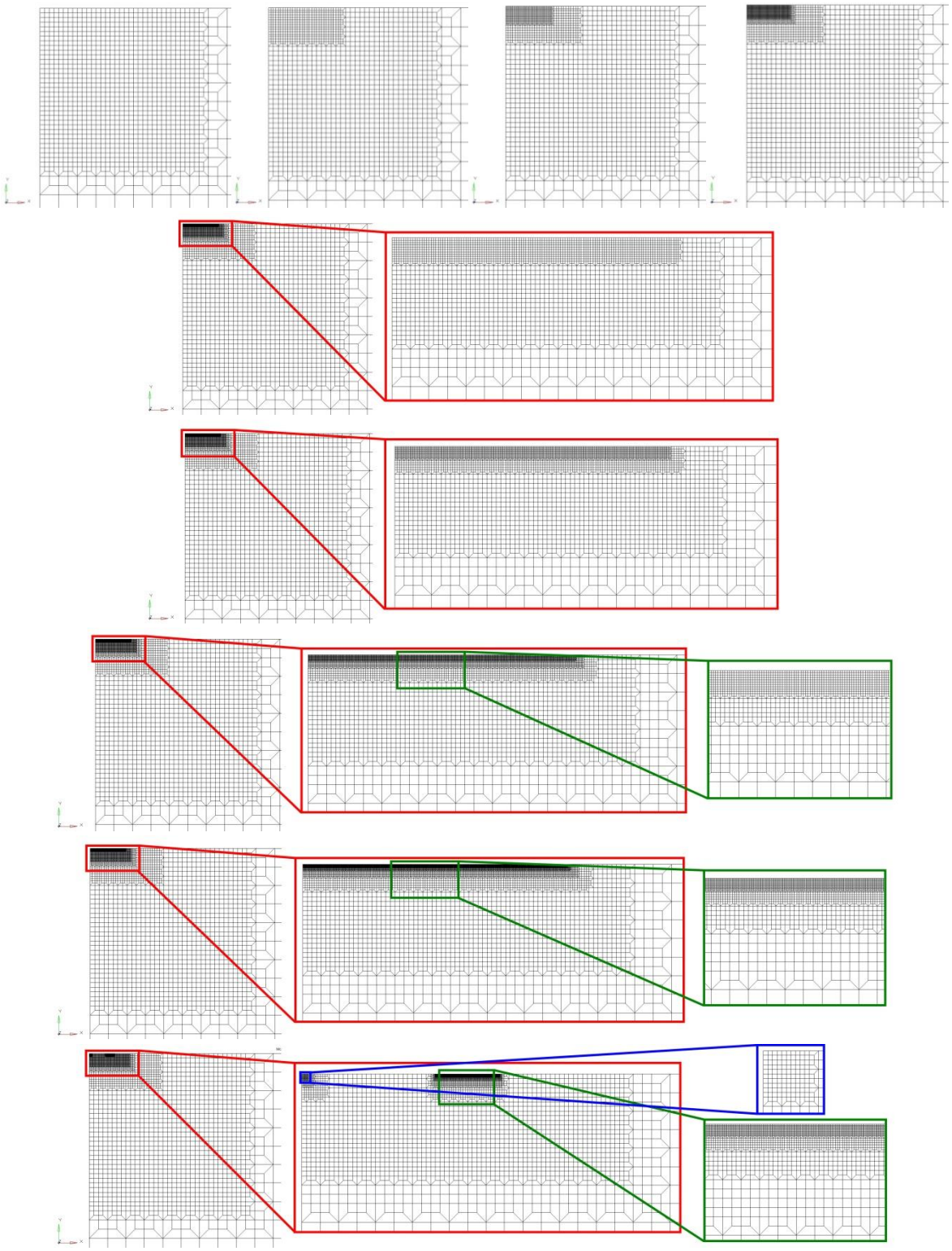

**Fig. 2-4. Elements in the interesting region of different mesh strategies: (a)*Coarse4*; (b)*Coarse3*; (c) *Coarse2*; (d) *Coarse*; (e)*Middle*; (f)*Fine*; (g)*Super_fine*; (h)*Super_fine2*; (i)*Local_super_fine3*.**

With the constitutive behavior of material A, the mesh convergence of different mesh strategies were studied. In the simulations of IIT, there are three key parameters which are

mostly cared about: maximum penetration force ($P_{max}$), contact hardness ($H$) and contact stiffness ($S$). And, $H$ is directly derived from $P_{max}$ and $A_c$. So, in this study, the convergence of mesh will be evaluated on these four parameters. The values of each parameter vs the numbers of element are respectively shown in Fig. 2-5. We could see that after several fluctuations, all the parameters tend to converge. One thing needs to be noticed is that for the *Local_super_fine3* strategy, we can reach nearly the same mesh convergence trend as the *Super_fine2* strategy for all the four parameters, however with much fewer elements and much less CPU time. This is quite profitable for our study which means that by using this kind of mesh, we can get high accuracy without so much computing costs.

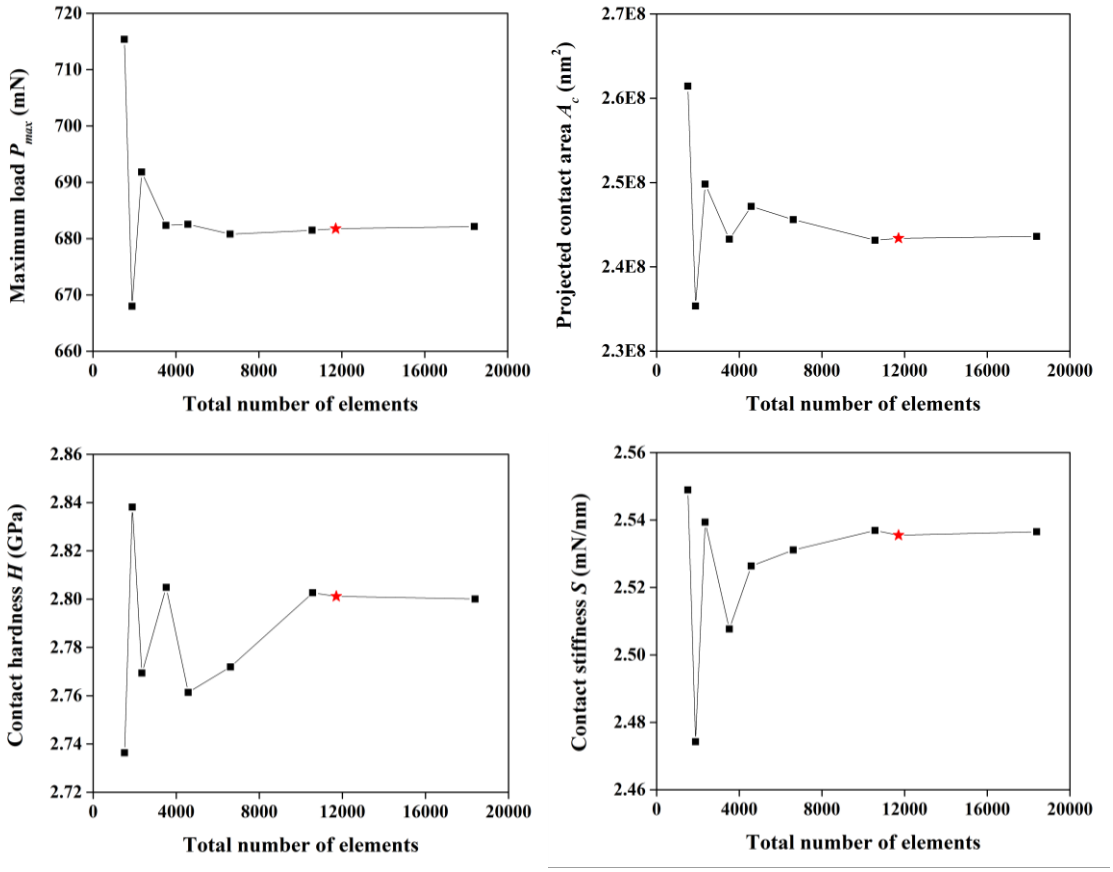


**Fig. 2-5. Mesh convergence investigation for different parameters: (a) maximum load $P_{max}$; (b) projected contact area $A_c$; (c) contact hardness $H$; (d) contact stiffness $S$ (The red star in each figure represents the meshing strategy *Local_super_fine3*.).**

## 2.3 Model adequacy investigation

After several fluctuations, the mesh convergence is obtained for the *Local_super_fine3* mesh strategy, when considering around 12000 elements (as shown in Fig. 2-5). However, before using the FEM model, its adequacy still needs to be checked.

According to classic elastic contact mechanics, the elastic solution of the contact problem between a sharp cone and a semi-infinite body was obtained by Sneddon [75]. This solution is the so called Sneddon's solution. Considering the geometry and stiffness of the indenter tip,

modification coefficients need to be added in Sneddon's solution, as shown in Eq.(1-12). In order to verify the adequacy of the discretization scheme adopted in the FEM model, indentation simulations on a pure-elastic material with $E$ = 122 GPa and $\nu$ = 0.33 were performed, for which the values of the correction factor $\beta$ and $\gamma$ should be 1 and 1.059 respectively. Comparison between the load vs depth ($P$-$h$) curve obtained from the pure-elastic simulation and that obtained from the theoretical elastic solutions was made. The results were listed in Fig. 2-6, from which we could see that the simulation result fits quite well with the modified Sneddon's solution, which shows the adequacy of the FEM model in the elastic range.

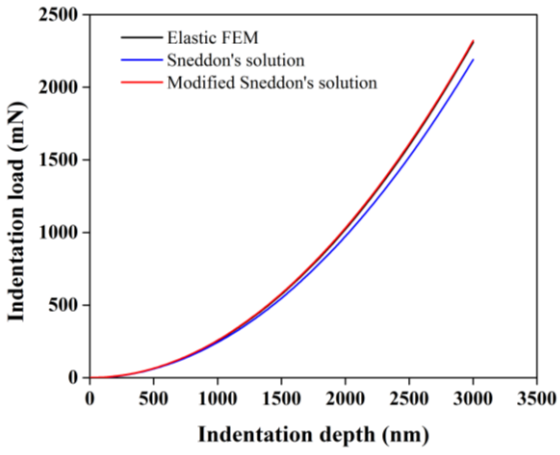


**Fig. 2-6. Comparison among the *P-h* curve obtained from the FEM simulations on a pure-elastic material with a rigid conical indenter and those obtained from theoretical elastic solutions.**

## 2.4 Attempting to measure RS with IIT

Before trying to characterize RS and PP induced by shot-peening process simultaneously, we first attempted to only measure the RS with IIT. As mentioned in Chapter 1, several strategies have been built for characterizing RS with IIT technique during the last few decades. There are many problems with them, however, if some of them can work well, even if through some modifications, RS values could be obtained. Furthermore, if PP could be measured with some further modifications of the same method or using some other ways, half of our problem will be solved.

It has long been recognized that there are some correlations between the hardness of a metallic material measured by conventional hardness techniques and the stress state of the material [124]. This was firstly demonstrated by Kokubo *et al*. [59] when studying the influence of applied bending stress on Vickers hardness measurement in a wide variety of commercial metals and alloys. Then, the further investigation of Sines & Carlson [60] showed that tensile and compressive residual stresses influence the Rockwell B hardness of high carbon steel in different way, as shown in Fig. 2-7.

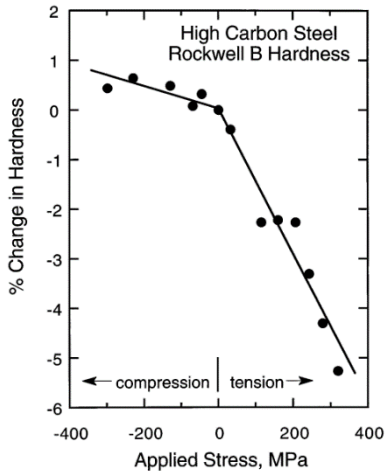


**Fig. 2-7. Changes in Rockwell B hardness produced by uniaxial stresses in a high carbon steel bend bar [60].**

Enlightened by the results of Sines & Carlson, the work of Tsui *et al*. [124] and Bolshakov *et al*. [76] demonstrated that the shape of the indentation curve and the 'apparent' hardness are indeed affected by a residual stress in a manner that might be useful in characterizing the stress. This led Suresh & Giannakopoulos [63] to propose a simple methodology for estimating residual stress through instrumented indentation with a sharp indenter. Their model is based on two assumptions: first, the elastic equi-biaxial residual stress at the surface is uniform over the depth of influence of the indenter; second, an equi-biaxial residual stress state at the indented surface would be equivalent to a hydrostatic stress plus a uniaxial stress component that can induce a differential indentation force. Then, they considered the influence of a residual stress on the shape of indentation curve and thus estimated the residual stress by taking the variation in the projected contact area into account. In the case of a tensile residual stress, they suggested the following equation:

$$\frac{A_c}{A_{c(RS)}} = (1 - \frac{\mathrm{RS}}{H}) \tag{2-3}$$

As for compressive residual stress, they suggested another equation:

$$\frac{A_c}{A_{c(RS)}} = (1 - \frac{\mathrm{RS}\sin\gamma}{H}) \tag{2-4}$$

where $\gamma$ is the inclination of a sharp indenter to the surface, which is 19.7° for the equivalent conical indenter of a Berkovich indenter, $H$ is the contact hardness, $A_c$ is the projected contact area in the case without any residual stress, $A_{c(RS)}$ is the projected contact area in the case with certain level of residual stress. In FEM simulation, contact area can be directly obtained. Then, by using contact area and maximum load, both projected contact area and contact hardness can be conveniently obtained.

One requirement of Eq. (2-3) and Eq. (2-4) is that the indentation hardness $H$ is kept constant as mentioned in some other studies [1]. However, our study showed that $H$ varies. Both RS and PP could impact it, which will be discussed in detail in Section 2.6. Another problem is that the term RS$sin\gamma$ is the component force of RS normal to the surface of conical

indenter, but not the component force normal to the projected contact area. The component force normal to the contact area should be RS*sinγcosγ*, as shown in Fig. 2-8.

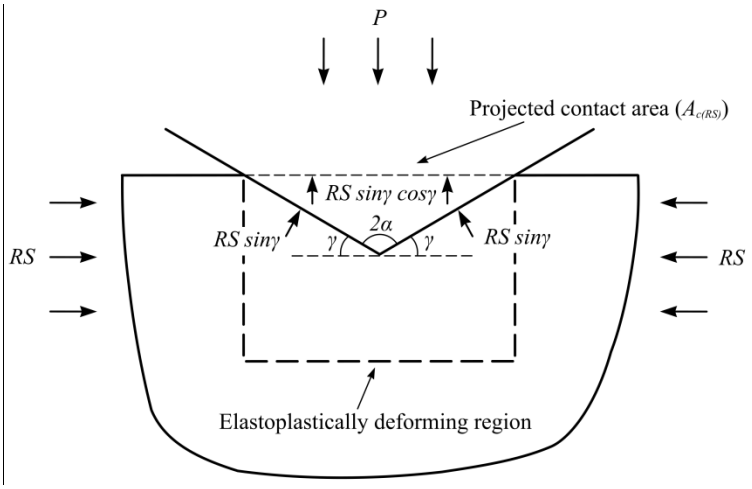


**Fig. 2-8. Schematic of the role of compressive residual stress at the indented surface and the associated nomenclature [63].**

Considering these two problems, we propose to modify the two equations into this form:

$$\frac{A_c}{A_{c(PP/RS)}} = (1 - \frac{RS}{H_{(PP/RS)}}) \quad (2\text{-}5)$$

$$\frac{A_c}{A_{c(PP/RS)}} = (1 - \frac{RS \sin\gamma \cos\gamma}{H_{(PP/RS)}}) \quad (2\text{-}6)$$

where $H_{(PP/RS)}$ is the hardness taking into account residual stresses and plastic deformation. The study on material A with equivalent conical indenter for different levels of RS and PP was made. Both the formulas of Suresh and our modification were examined and the results were shown in Fig. 2-9.

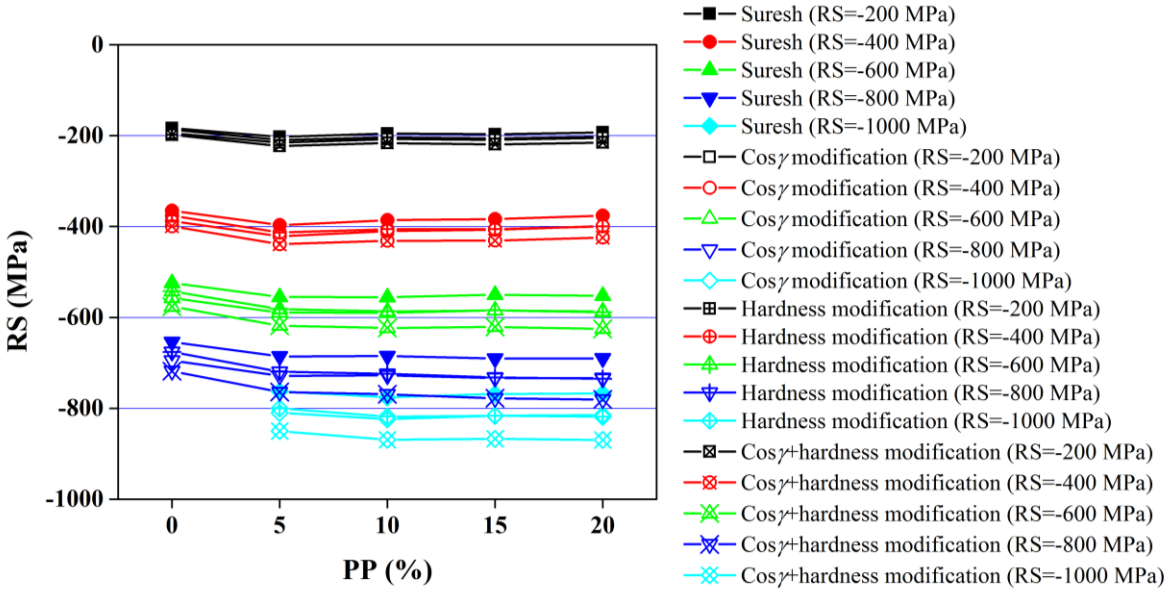


**Fig. 2-9. RS values calculated with both Suresh method and different modifications.**

From Fig. 2-9 we could see that, when RS=-200 MPa, all the methods give nearly the same accurate results. When RS=-400 MPa and RS=-600 MPa, results obtained with cos$\gamma$ modification and hardness modification are still quite good, except the first point (PP=0%). Suresh method underestimated a little bit the RS value and cos$\gamma$ & hardness modification overestimated a little bit. For the point PP=0%, all methods underestimated the RS level. However, the results are still acceptable. As for RS=-800 MPa and RS=-1000 MPa, all the methods give much lower results than the actual RS value. For the case RS=-1000 MPa, the calculated values of original Suresh method were even lower than -800 MPa. However, our modification still worked much better than original Suresh method.

Results in From Fig. 2-9 showed that, for the virtual material A, our modification on the original Suresh method works correctly when the absolute value of RS≤600 MPa. Furthermore, the curves also showed that the existence of PP will directly influence the deduced results. And, along with the increase of RS level, this kind of influence becomes larger.

## 2.5 Separating RS and PP with the shape of the *P-h* Curve

During an IIT process, a continuous load (force or displacement controlled) will be applied on the indenter tip to penetrate into the surface of the target material. Meanwhile, the displacement of the tip will be continuously reported as well. This means that by identifying the contact point properly, the penetration depth can be recorded consecutively. Based on this kind of feature, load vs depth (*P-h*) curves become the data which can be most directly and conveniently obtained from IIT. In the present work, we are interested in the local mechanical state (RS and PP) induced by the shot-peening process. The goal is thus to use *P-h* curve to characterize RS and PP versus depth.

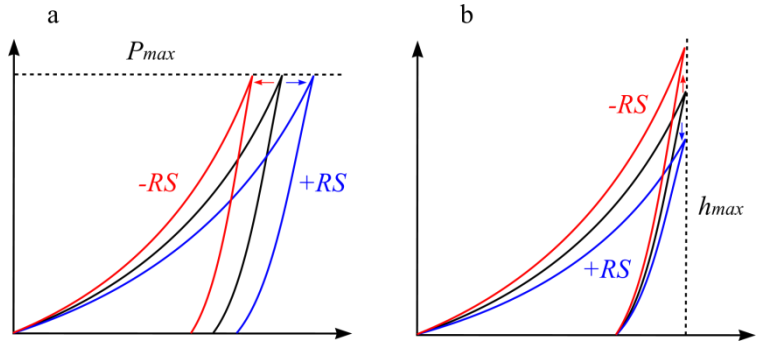


**Fig. 2-10. Shift of *P-h* curve caused by positive or negative RS: (a) force controlled IIT, (b) displacement controlled IIT.**

Literature showed that surface RS in the target material, tensile or compressive, will cause shifts of the *P-h* curve [63, 125]. If the IIT process is force controlled to reach a given maximum force, compressive RS will make the *P-h* curve shift to the left direction towards more shallow penetrations, and tensile RS will produce the opposite. If the IIT process is displacement controlled in order to reach a given maximum penetration depth, compressive RS will make the *P-h* curve shift upwards to higher penetration forces, and tensile RS will

induce the opposite behavior. This phenomenon is shown schematically in Fig. 2-10. If the shift caused by the work-hardening associated to PP is different from that caused by RS, the shape of *P-h* curve may have some kind difference which might make it possible to separate RS and PP.

Based on the idea above, a series of displacement-controlled IIT simulations were made on copper (as shown in Table 2-1) to check its feasibility. It should be noted that, although the present research work is devoted to the shot-peening of titanium alloys, copper was chosen here to allow comparisons with previous indentation work performed in LASMIS laboratory on this material.

First, an accumulated plastic pre-strain (PP) of 2% was induced into the model and the indentation response was simulated. Then a compressive (equi-biaxial) residual stress (RS) was applied on the raw material and its value was varied until the same maximum force ($P_{max}$) as for the case of PP= 2% was obtained. The same $P_{max}$ value was obtained for a stress of -100 MPa. IIT simulations with other situations (raw material, RS=+100 MPa, the combination of PP=2% and RS=-100 MPa and the combination of PP=2% and RS=+100 MPa) were conducted as well. *P-h* curves obtained from these simulations are shown in Fig. 2-11 [126].

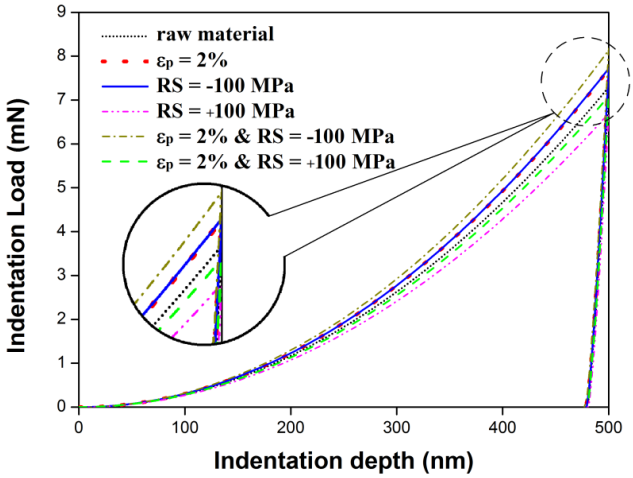


**Fig.2-11. *P-h* curves for various combinations of RS and PP on copper [126].**

In Fig. 2-11, the shift of *P-h* curves mentioned in the literature, were observed. However, the *P-h* curve for the case PP=2% and that for RS=-100 MPa are almost entirely superposed. This important result, which was confirmed by simulations on materials A, B and C, means that RS and PP cannot be separated only from the shape of *P-h* curves. To our knowledge, this result was never mentioned in the literature.

Although *P-h* curves are superposed, one interesting thing was observed from the process. It is that the pile-up values (both at maximum loading and after unloading) for the case PP=2% and those for the case RS=-100 MPa are different, even if their *P-h* curves are completely superposed, as shown in Table 2-3 and Fig. 2-12.

**Table 2-3 Pile-up values of different simulations on copper.**

| | Pile-up value at maximum load | $\Delta 1^*$ (nm) | Pile-up value after unloading | $\Delta 2^*$ (nm) |
|---|---|---|---|---|

| | (nm) | | (nm) | |
|---|---|---|---|---|
| PP = 2% | 36.4 | 7.0 | 51.1 | 6.9 |
| RS = -100 MPa | 43.4 | | 58.0 | |

* Δ1 is the difference in pile-up values between PP and the corresponding RS after loading, Δ2 is the difference in pile-up values between PP and the corresponding RS after unloading.

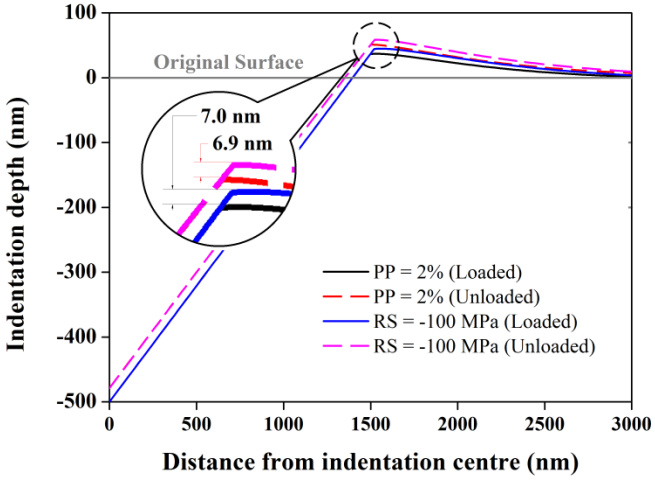


**Fig. 2-12. Indentation dimple profiles of cooper with PP=2% and RS=-100 MPa.**

The difference of pile-up values would give us another possibility to separate RS and PP. However, considering that $h_{max}$=500 nm, the difference value (7.0 nm at maximum load and 6.9 nm after unloading) is quite small, which will be quite difficult to measure experimentally, especially that, with a Berkovitch indenter, the pile-up is not distributed evenly around the triangular dimple produced. In order to fully understand the factors that affect the pile-up values, a series of further simulations were made.

## 2.6 Investigating the influencing factors for IIT simulation

As mentioned above, it is not possible to separate RS and PP based on the shape of *P-h* curves alone, however it was found that RS and PP may have a different influence on pile-up values. In present section, the shape of *P-h* curve, maximum load ($P_{max}$), contact hardness ($H$), contact stiffness ($S$) and the pile-up value are investigated. $S$ and $H$ were studied because they are closely linked to the projected contact area ($A_c$), which, in turn, depends on the pile-up value. These aspects will be discussed in Section 2.7.

Several correlated parameters were studied: constitutive behavior, friction coefficient ($f$), PP and RS. The aim of this part of study is to find out two or more parameters which might be used to separate RS and PP.

### 2.6.1 Constitutive behavior of the tested material

First, the effects of the constitutive behavior of the material were studied. The two controlling parameters are the yield stress and the hardening exponent. All the four materials listed in Table 2-1 were studied and the corresponding *P-h* curves for a given penetration depth

of 500 nm are shown in Fig. 2-13. As expected, for materials with lower yield stress (copper and material B), the $P_{max}$ values are much lower than those of materials with higher yield stress (material A and C). On the opposite, the trends of the unloading curve are inverse, which can be seen more clearly from contact stiffness $S$ in Table 2-4. For copper and material B, the contact stiffness values (considered to be the initial unloading slope) are obviously higher than those of material A and C. As the Young's modulus of the 4 materials is the same, the observed differences can only be attributed to the contact surface and thus to the pile-up phenomenon. As for the amount of pile-up, a similar trend could be observed as well which shows that lower yield stress will cause a higher pile-up value. Hardness values indicated that higher yield stress and lower hardening exponent will produce a higher hardness. This shows that the constitutive behavior of the studied material will significantly affect all the indentation responses that we would like to investigate and should thus be known accurately.

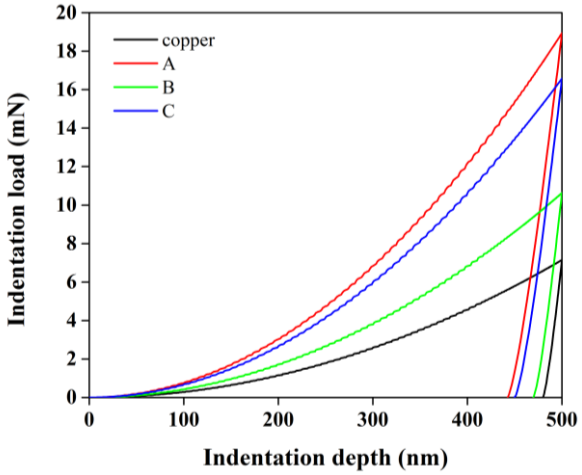


**Fig.2-13. *P-h* curves for various constitutive behaviors.**

**Table 2-4 Values of indentation responses for simulations with different constitutive behaviors.**

| | Copper | A | B | C |
|---|---|---|---|---|
| Contact hardness $H$ (GPa) | 1.03 | 3.14 | 1.54 | 2.66 |
| Contact stiffness $S$ (mN/nm) | 0.440 | 0.406 | 0.438 | 0.412 |
| Maximum load $P_{max}$ (mN) | 7.15 | 18.99 | 10.64 | 16.59 |
| Pile-up value (nm) | 32.5 | -5.7 | 30.7 | 2.4 |

## 2.6.2 Friction coefficient

The effects of friction coefficient ($f$) were investigated as well. Friction coefficient values respectively equal to 0 (frictionless), 0.05, 0.1, 0.2, 0.3 and 0.45 were chosen. *P-h* curves for different materials with various $f$ values are shown in Fig. 2-14. For all the four materials, variation of friction coefficient values will cause a shift of the *P-h* curves. However, this kind of shift is a little more pronounced for material A and C who have higher yield strength.

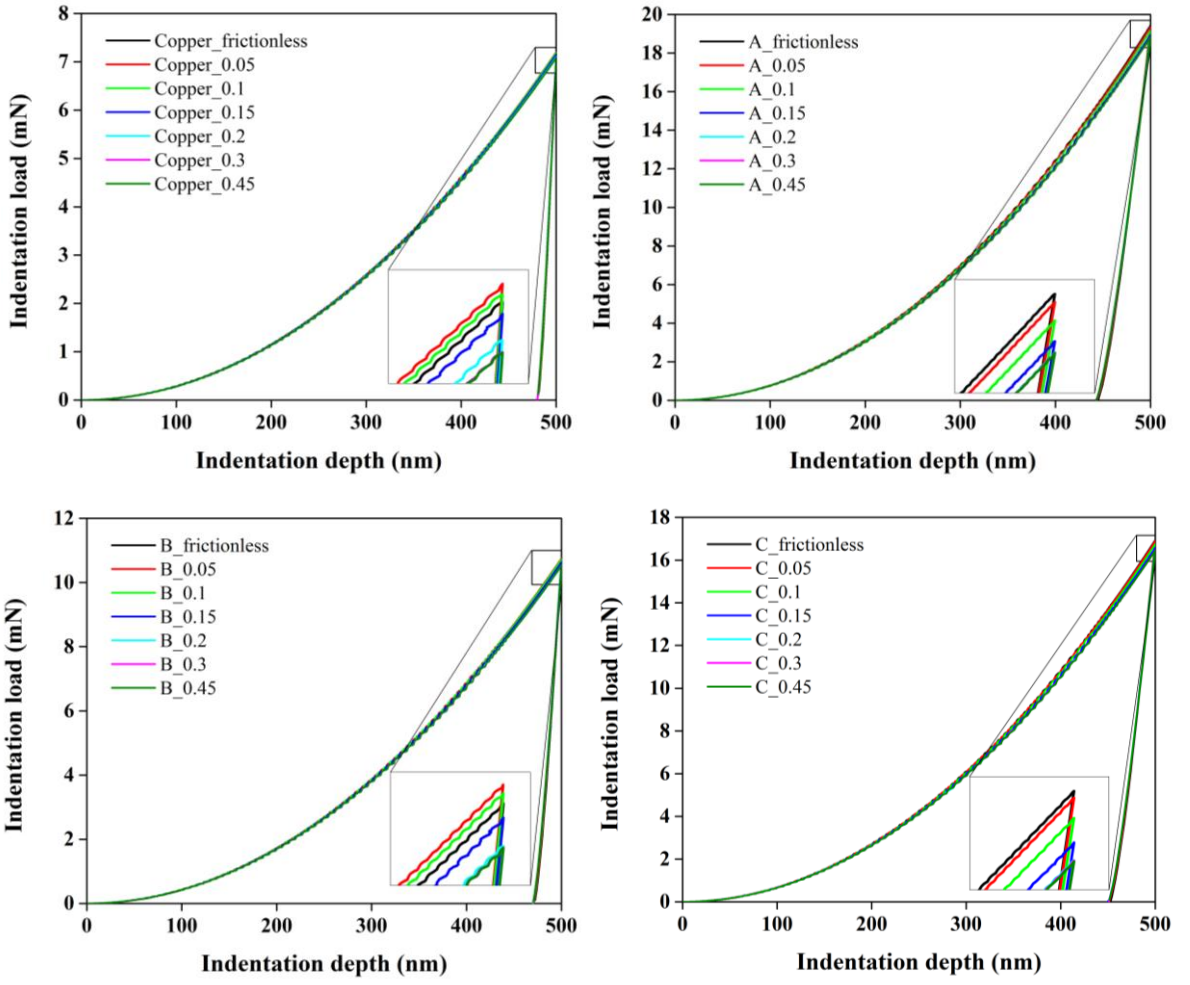


**Fig. 2-14. *P-h* curves for different constitutive behaviors with various friction coefficients: (a) Copper; (b) Material A; (c) Material B; (d) Material C.**

The others analyzed quantities are shown in Fig. 2-15. An increase of the friction coefficient will cause a slight decrease of the maximum load, which is consistent with the observation from *P-h* curves. In contrast, contact hardness values increase. Both contact stiffness and pile-up decreased obviously. It can be seen that their trends are quite similar. This could be explained with Eq.(1-5) which shows the relationship between contact stiffness $S$ and projected contact area $A_c$. And, considering the geometric relation of indentation tip, there is a direct relation between pile-up values and projected contact area $A_c$. The most interesting thing is that for all the materials and all parameters, a saturation phenomenon will occur when $f$ values reach a threshold of about 0.2.

In the literature, some researchers indicate that $f$ has no influence on indentation responses (usually only *P-h* curves and $P_{max}$ were considered), and so their FEM models are logically supposed to be frictionless [123, 127]. However, some other researchers showed that the effects of $f$ depend on material properties [128], indentation depth [129] and so on. And, they could influence the *P-h* curve and the contact hardness [130] as well. Our study showed that the value of $f$ can affect all the indentation responses investigated, which is nearly independent

on material properties. Although the influences on $H$ and $P_{max}$ of copper are not so obvious, the influences on $S$ and pile-up are still not negligible. From Fig. 2-15 it could also be seen that the black line will cross the green line in for both $S$ and pile-up. This means that the influence of $f$ on contact stiffness and pile-up values is not independent. It is mixed with the influence of other factors.

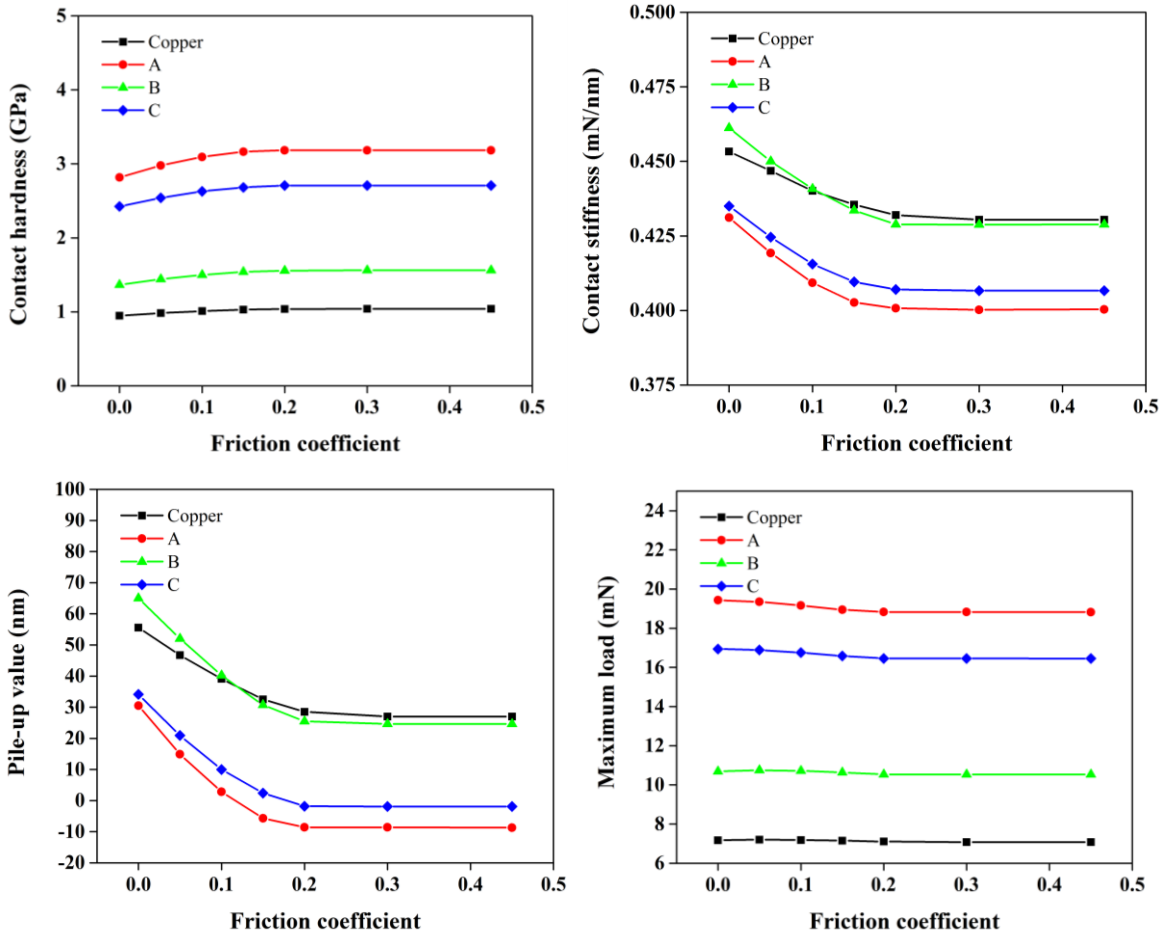


**Fig. 2-15. The influences of friction coefficient on different indentation responses: (a) Contact hardness; (b) Contact stiffness; (c) Maximum load; (d) Pile-up values.**

## 2.6.3 RS and PP

For the purpose of finding out the influences of PP and RS, for each material, four different levels of PP were chosen to be introduced into the model. The corresponding RS levels were determined by the way mentioned in Section 2.5, in order to reach exactly the same $P_{max}$ values.

*P-h* curves of all the situations are shown in Fig. 2-16, from which we could see that, for each given level of PP, a corresponding level of RS which gives exactly the same *P-h* curve can always be found. This means that the exploitation of *P-h* curves cannot give a unique solution as shown before. However, the regularities of distribution of the *P-h* curves for each material are not the same. The PP levels for all the four materials are chosen uniformly.

However, Fig. 2-16 showed that for all the four materials, the gap between the *P-h* curve of each PP level become smaller and smaller along with the uniform increase of PP levels.

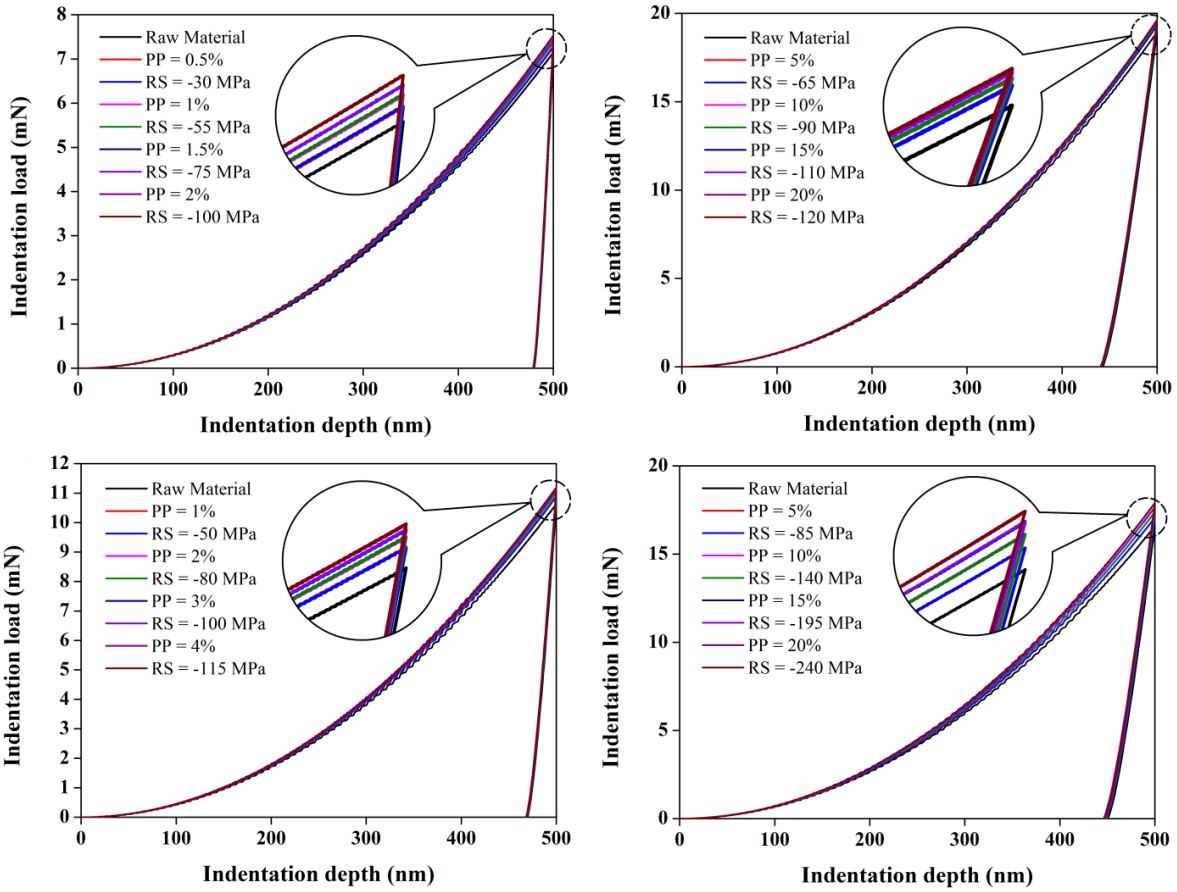


**Fig. 2-16. *P-h* curves of different materials with various levels of PP and the corresponding levels of RS: (a) copper; (b) material A; (c) material B; (d) material C.**

Contact hardness (*H*), contact stiffness (*S*) and maximum load ($P_{max}$) values for all the situations are listed in Table 2-5, Table 2-6, Table 2-7 and Table 2-8. Some studies showed that the hardness obtained from indentations on a certain material (with or without residual stress) shows a kind of invariance [131]. Our results showed that contact hardness values increase when both PP and RS levels are increased, especially for material A and C who has a higher yield stress. As for copper and material B, the increase of *H* values is quite small, which is similar as the invariance phenomenon mentioned in literature. However, the increment of *H* values for certain PP level is lower than that for the corresponding RS level, especially for material A and C. This means that the influences of both PP and RS, on contact hardness *H*, are not the same. The contact stiffness *S* also increases along with the increase of both PP and RS levels. And, the influence (on *S*) of PP level is smaller than that of the corresponding RS level as well. However, copper and material B showed larger difference this time. Results indicated that compressive RS has more influences than PP on all the three

**Table 2-5 *H*, *S* and *Pmax* values of different PP and RS levels for copper.**

| | Contact hardness *H* (GPa) | Contact stiffness *S* (mN/nm) | Maximum load *Pmax* (mN) |
|---|---|---|---|
| Raw Material | 1.03 | 0.440 | 7.15 |
| PP = 0.5% | 1.04 | 0.441 | 7.27 |
| RS = -30 MPa | 1.04 | 0.445 | 7.28 |
| PP = 1% | 1.05 | 0.442 | 7.37 |
| RS = -55 MPa | 1.05 | 0.448 | 7.38 |
| PP = 1.5% | 1.06 | 0.443 | 7.45 |
| RS = -75 MPa | 1.07 | 0.450 | 7.45 |
| PP = 2% | 1.07 | 0.443 | 7.53 |
| RS = -100 MPa | 1.08 | 0.453 | 7.53 |

**Table 2-6 *H*, *S* and *Pmax* values of different PP and RS levels for material A.**

| | Contact hardness *H* (GPa) | Contact stiffness *S* (mN/nm) | Maximum load *Pmax* (mN) |
|---|---|---|---|
| Raw Material | 3.14 | 0.406 | 18.95 |
| PP = 5% | 3.20 | 0.407 | 19.33 |
| RS = -65 MPa | 3.21 | 0.409 | 19.31 |
| PP = 10% | 3.23 | 0.407 | 19.47 |
| RS = -90 MPa | 3.26 | 0.411 | 19.45 |
| PP = 15% | 3.24 | 0.407 | 19.56 |
| RS = -110 MPa | 3.29 | 0.411 | 19.56 |
| PP = 20% | 3.26 | 0.407 | 19.64 |
| RS = -120 MPa | 3.31 | 0.411 | 19.63 |

**Table 2-7 *H*, *S* and *Pmax* values of different PP and RS levels for material B.**

| | Contact hardness *H* (GPa) | Contact stiffness *S* (mN/nm) | Maximum load *Pmax* (MPa) |
|---|---|---|---|
| Raw Material | 1.54 | 0.438 | 10.63 |
| PP = 1% | 1.56 | 0.441 | 10.90 |
| RS = -50 MPa | 1.56 | 0.446 | 10.88 |
| PP = 2% | 1.57 | 0.442 | 11.03 |
| RS = -80 MPa | 1.57 | 0.450 | 11.03 |
| PP = 3% | 1.58 | 0.443 | 11.11 |
| RS = -100 MPa | 1.58 | 0.452 | 11.12 |
| PP = 4% | 1.58 | 0.443 | 11.20 |
| RS = -115 MPa | 1.59 | 0.454 | 11.19 |

**Table 2-8 *H*, *S* and *Pmax* values of different PP and RS levels for material C.**

| | Contact hardness *H* (GPa) | Contact stiffness *S* (mN/nm) | Maximum load *Pmax* (MPa) |
|---|---|---|---|
| Raw Material | 2.66 | 0.412 | 16.58 |
| PP = 5% | 2.73 | 0.412 | 17.07 |
| RS = -85 MPa | 2.78 | 0.418 | 17.07 |
| PP = 10% | 2.82 | 0.412 | 17.38 |
| RS = -140 MPa | 2.86 | 0.419 | 17.38 |
| PP = 15% | 2.88 | 0.411 | 17.65 |
| RS = -195 MPa | 2.92 | 0.421 | 17.68 |
| PP = 20% | 2.92 | 0.411 | 17.90 |
| RS = -240 MPa | 2.98 | 0.423 | 17.90 |

**Table 2-9 Pile-up values of different simulations for copper.**

| | Pile-up value after loading (nm) | $\Delta 1^*$ (nm) | Pile-up value after unloading (nm) | $\Delta 2^*$ (nm) |
|---|---|---|---|---|
| Raw Material | 32.5 | - | 46.5 | - |
| PP = 0.5% | 34.3 | 2.4 | 48.4 | 2.3 |
| RS = -30 MPa | 36.7 | | 50.7 | |
| PP = 1% | 35.0 | 4.1 | 49.4 | 4.0 |
| RS = -55 MPa | 39.1 | | 53.4 | |
| PP = 1.5% | 35.7 | 5.5 | 50.2 | 5.4 |
| RS = -75 MPa | 41.2 | | 55.6 | |
| PP = 2% | 36.4 | 7.0 | 51.1 | 6.9 |
| RS = -100 MPa | 43.4 | | 58.0 | |

**Table 2-10 Pile-up values of different simulations for material A.**

| | Pile-up value after loading (nm) | $\Delta 1^*$ (nm) | Pile-up value after unloading (nm) | $\Delta 2^*$ (nm) |
|---|---|---|---|---|
| Raw Material | -5.7 | - | 34.4 | - |
| PP = 5% | -4.5 | 1.8 | 36.3 | 1.7 |
| RS = -65 MPa | -2.7 | | 38.0 | |
| PP = 10% | -4.8 | 4.0 | 36.4 | 3.3 |
| RS = -90 MPa | -0.8 | | 39.7 | |
| PP = 15% | -4.5 | 4.3 | 36.8 | 4.1 |
| RS = -110 MPa | -0.2 | | 40.9 | |
| PP = 20% | -5.3 | 5.0 | 36.5 | 4.7 |
| RS = -120 MPa | 0.3 | | 41.2 | |

**Table 2-11 Pile-up values of different simulations for material B.**

| | Pile-up value after loading (nm) | $\Delta 1^*$ (nm) | Pile-up value after unloading (nm) | $\Delta 2^*$ (nm) |
|---|---|---|---|---|
| Raw Material | 30.7 | - | 51.6 | - |
| PP = 1% | 34.4 | 1.9 | 55.7 | 1.7 |
| RS = -50 MPa | 36.3 | | 57.4 | |
| PP = 2% | 35.8 | 3.7 | 57.2 | 3.5 |
| RS = -80 MPa | 39.5 | | 60.7 | |
| PP = 3% | 36.8 | 4.1 | 58.2 | 4.1 |
| RS = -100 MPa | 40.9 | | 62.3 | |
| PP = 4% | 37.1 | 5.7 | 58.8 | 5.4 |
| RS = -115 MPa | 42.8 | | 64.2 | |

**Table 2-12 Pile-up values of different simulations for material C.**

| | Pile-up value after loading (nm) | $\Delta 1^*$ (nm) | Pile-up value after unloading (nm) | $\Delta 2^*$ (nm) |
|---|---|---|---|---|
| Raw Material | 2.4 | - | 36.8 | - |
| PP = 5% | 2.4 | 5.1 | 37.5 | 5.4 |
| RS = -85 MPa | 7.5 | | 42.9 | |
| PP = 10% | 1.9 | 8.7 | 38.0 | 8.0 |
| RS = -140 MPa | 10.6 | | 46.0 | |
| PP = 15% | 1.2 | 12.5 | 37.9 | 11.7 |
| RS = -195 MPa | 13.7 | | 49.6 | |
| PP = 20% | 0.1 | 16.6 | 37.7 | 15.0 |
| RS = -240 MPa | 16.7 | | 52.7 | |

subjects investigated. As for contact hardness *H*, higher yield stress makes the difference between the impact of PP and that of RS become larger. However, for contact stiffness *S*, the

difference is smaller. It is quite possible that PP and RS mixed together could be separated by getting and analyzing *H*, *S* values.

Pile-up values at maximum load and after unloading for all the situations are listed in Table 2-9, Table 2-10, Table 2-11 and Table 2-12. The difference between pile-up value of certain PP level and that of the corresponding RS level, as mentioned above, could be observed likewise for all the materials. Along with the increase of the RS and PP levels, this kind of difference became larger and larger. The increase of the difference is distinct among the four materials. For material A and material B, the difference of pile-up values are obviously smaller than those for copper and material C. It might because that the hardening exponent *n* for material A and B ($n$ = 0.1) is much lower than that for copper and material B ($n$ = 0.57). The influence of yield stress is not obvious on the materials with lower *n* values (material A and material B), however much more obvious on the materials with higher *n* values (copper and material C). Especially, on material C which has both high yield stress and high hardening exponent, the difference of pile-up values are nearly two times larger than those on material A and material B. This proved that the higher yield stress and hardening exponent, the larger the difference between the pile-up value obtained from certain PP level and that obtained from the corresponding RS level.

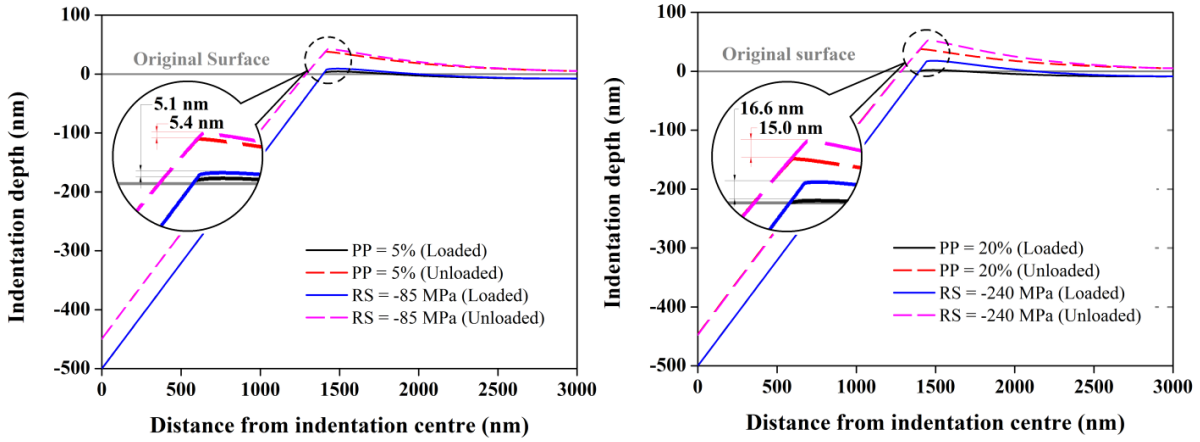


**Fig. 2-17. Indentation dimple profiles of material C: (a) PP= 5%, RS=-85 MPa; (b) PP= 20%, RS= -240 MPa.**

From Table 2-9 to Table 2-12 we can also notice that the pile-up values of different PP levels do not present much difference for all the four materials. This means that PP nearly cannot affect pile-up values. The only exception is that for materials with lower yield stress (copper and material B), along with the increase of PP level, pile-up values will increase a little bit. While, for materials with higher yield stress (material A and material C), the increase of PP will cause a little bit decrease of the pile-up value. On the contrary, RS level shows notable influences into the pile-up value. This can be observed directly and clearly from the indentation dimple profiles of material C, as shown in Fig. 2-17. This kind of phenomenon indicated that pile-up value might be a good parameter for separating RS and PP, because it is quite sensitive to RS but relatively insensitive to PP. This kind of feature could be utilized for characterizing RS and PP simultaneously induced by shot-peening process.

## 2.7 Characterizing RS and PP with simultaneous functions method

### 2.7.1 Principles of the simultaneous functions method

The study above showed that the introduction of a given level of PP or a corresponding level of RS in copper leads to *P-h* curves almost superposed during the loading stage, however, the amount of pile-up is different. However it has been shown that pile-up value is quite sensitive to RS, but insensitive to PP, which could help to separate RS and PP. During this process, some other parameters were investigated as well. Results indicated that maximum load ($P_{max}$), contact hardness ($H$) and contact stiffness ($S$) could be affected by RS and PP as well. The unknowns are RS and PP and the values that can be measured are $P_{max}$, $H$, $S$ and the pile-up. At least two of these values must be measured to obtain RS and PP.

Before discussing in detail the method, several remarks can be done. First, the four parameters which could be used as an input can also be influenced by factors other than RS and PP, like material properties, friction coefficient and so on. Second, although pile-up is the main differentiating factor, its amount is quite low and will be difficult to measure practically. Third, from the definition of $H$ given in Eq.(1-6), it can be seen that $H$ cannot be directly obtained from experiment. To tackle these three problems, several things need to be done.

First, considering that we cannot get rid of the influences of factors like material properties and friction coefficient, for now the only thing we need to do is just chose a set of values for these factors and keep them constant for investigating other parameters.

Second, when loading *P-h* curves are superposed, the amount of pile-up will vary which means that the projected contact area ($A_c$) will change as well. Considering indentation tip geometry, the variations of $A_c$ could be larger than that of pile-up, as shown in Fig. 2-18.

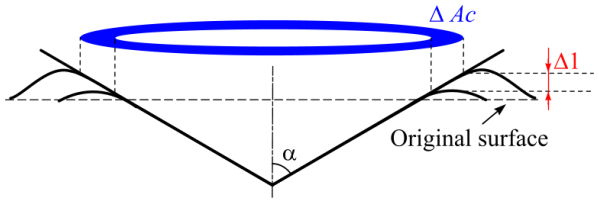


**Fig.2-18. Comparison between pile-up variance and projected contact area variance.**

However, a direct determination of $A_c$, for instance using an Atomic Force Microscope (AFM), is inconvenient in practice as well. In order to overcome this inconvenience, an alternative was considered. The idea proposed is to use contact stiffness $S$ which depends on reduced modulus ($E^*$) and $A_c$ as shown in Eq.(1-5). If shot-peening does not modify the Young's modulus of the specimen, then $E^*$ will be a constant and the variations of $S$ are directly related to the variations of $A_c$. Thus, the value of $A_c$ could be indirectly obtained through $S$, the initial unloading slope of *P-h* curve. Furthermore, according to Eq.(1-10), we can get two equations:

$$E^* = \frac{1}{\beta} \cdot \frac{\sqrt{\pi}}{2} \cdot \frac{S_0}{\sqrt{A_{c0}}} \tag{2-7}$$

$$E^* = \frac{1}{\beta} \cdot \frac{\sqrt{\pi}}{2} \cdot \frac{S}{\sqrt{A_c}} \tag{2-8}$$

where $S_0$ and $A_0$ are respectively the contact stiffness and the projected contact area for the raw (without shot-peening) material, and $S$ and $A$ are the contact stiffness and the projected contact area for the material with some levels of PP and RS. Combining Eq.(2-7) and Eq.(2-8), we can get:

$$\frac{A_c}{A_{c0}} = (\frac{S}{S_0})^2 \tag{2-9}$$

Eq.(2-9) means that, supposing that RS or PP induced by shot-peening cannot affect $E^*$, if a raw material could be prepared, a normalized projected contact area ($A/A_0$) will be obtained very easily and conveniently from the normalized contact stiffness ($S/S_0$).

A similar remark can be made for contact hardness $H$. Considering the definition of contact hardness in Eq.(1-6), if $H$ is normalized by the $H_0$ of the raw material, and taking Eq.(2-9) into account the, following equation can be obtained:

$$\frac{H}{H_0} = \frac{P_{\max 0}}{P_{\max}} \cdot (\frac{S}{S_0})^2 \tag{2-10}$$

Three normalized parameters: $P_{max}/P_{max0}$, $H/H_0$ and $S/S_0$ can thus be defined and obtained conveniently from experiment. Then we need to find a way to use them to separate RS and PP. Although both RS and PP can affect these three normalized parameters, the way and the extent affected for each parameter may not be the same. So, it is possible to obtain three individual mathematic functions, such as $P_{max}/P_{max0}=f$(RS, PP), $S/S_0=g$(RS, PP) and $H/H_0=k$(RS, PP), to build a continuous correlation between each normalized parameter and the set of RS and PP variables. In order to build these functions, the space of variables will be discretized on a grid of N1×N2 points, where N1 is the number of PP levels and the N2 is the number of RS levels. Then, the value of the normalized parameters at each of these discretized points will be obtained from a FEM simulation which contents certain level of PP and RS. Then, by using least squares method, we can use the N1×N2 discretized points to extract the explicit formulation of each function. Seeing that there are two unknowns (RS and PP) for each IIT test, at least two individual functions are needed to extract the two unknowns.

Furthermore, if we plot all the three functions in 3D space, three different spatial quadratic polynomials should be obtained. Projecting the quadratic polynomials onto the plane of the combinations of RS and PP, three different contour plot maps will be built. Any possible combination of RS and PP, will give us a certain value for each normalized parameter, which should correspond to an iso-line on each contour plot map. Based on the difference among the quadric surfaces, the trend of each iso-line will probably be various. Thus, any two iso-lines should generate a cross point, the coordinate of which will directly show the value of RS and PP. If the whole procedure is self-consistent, all the three iso-lines should give only one cross point. The schema about getting the cross point with two quadratic polynomials are shown in Fig.2-17.

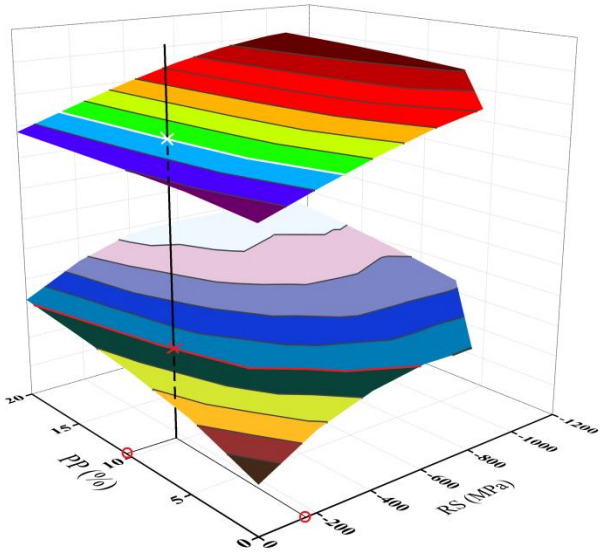


**Fig.2-17. Getting PP and RS values from quadratic polynomials of two normalized parameters vs various combinations of PP and RS.**

Since the basic idea of this separating strategy is to use two functions simultaneously to obtain the RS and PP value which corresponding to the common solution of these two functions, we decided to call this method "the simultaneous function method".

## 2.7.2 Separating RS and PP with simultaneous functions method

Since the principle of the simultaneous function method has already been illustrated, in this part of work, one target material will be studied to testify the feasibility of this method. Material *A* was chosen as the target material, because in former study pile-up values of material *A* showed the least sensibility to both RS and PP. If the simultaneous function method works well on material *A*, it should work well for the other three materials as well. Furthermore, because that the yield stress of material A is relatively high, it enables to explore high levels of residual stresses as observed in shot-peening for practical applications. A series of elastic-plastic IIT simulations on material *A* with different levels of RS and PP were carried out. The levels of PP are respectively 0%, 1%, 5%, 10%, 15% and 20%. The corresponding levels of RS are 0 MPa, -200 MPa, -400 MPa, -600 MPa, -800 MPa -1000 MPa and $-\sigma_y$, where $\sigma_y$ is the yield stress reached for each imposed PP level which is calculated according to Eq.(2-2). Indentation simulation was performed for each possible combination of RS and PP.

Since $H/H_0$ values are obtained indirectly with $S/S_0$ values and $P_{max}/P_{max0}$ values which can be directly obtain from *P-h* curves, the key is to focus on how to obtain $S/S_0$ values. One way mostly used in the literature for getting the contact stiffness was firstly mentioned by Oliver & Pharr [54]. Experiments [5] showed that during an IIT process, unloading curves are distinctly curved and usually well approximated by the power law relation:

$$P = \alpha(h_{\max} - h_f)^m \tag{2-11}$$

where $\alpha$, $m$ and $h_f$ are power law best fitting parameters. Then, the elastic unloading stiffness $S = (dP/dh)_{max}$ could be obtained for the following equation:

$$S = \alpha m (h_{\max} - h_f)^{m-1} \tag{2-12}$$

This method is convenient to use, however, it is purely phenomenological without physics meaning of the unloading process in the indentation test.

Another way for obtaining contact stiffness is more straightforward. Some studies [132, 133] showed that the beginning of the unloading curve presents a quite good linearity, which means that linear fitting of this part can give an approximate value of contact stiffness as well.

Both of these two methods were investigated and the results were compared with the $S$ values calculated according to Eq.(1-5), in which the projected contact area was obtained directly, geometrically, from the FEM model at the end of the loading stage. By analyzing different situations, it has been observed that linearity of the first 5% of the unloading curve is quite good. So, all the linear fittings are conducted on the first 5% of the unload curves. The normalized contact stiffness values, obtained with all the three methods, correspond to each combination of PP and RS were listed in Fig. 2-18. For most of the situations, the normalized contact stiffness values obtained with the linear fitting method showed a much better performance than Oliver-Pharr model. Even if when PP level become high, the results obtained with linear-fitting is always lower than the calculated values, they are still correct.

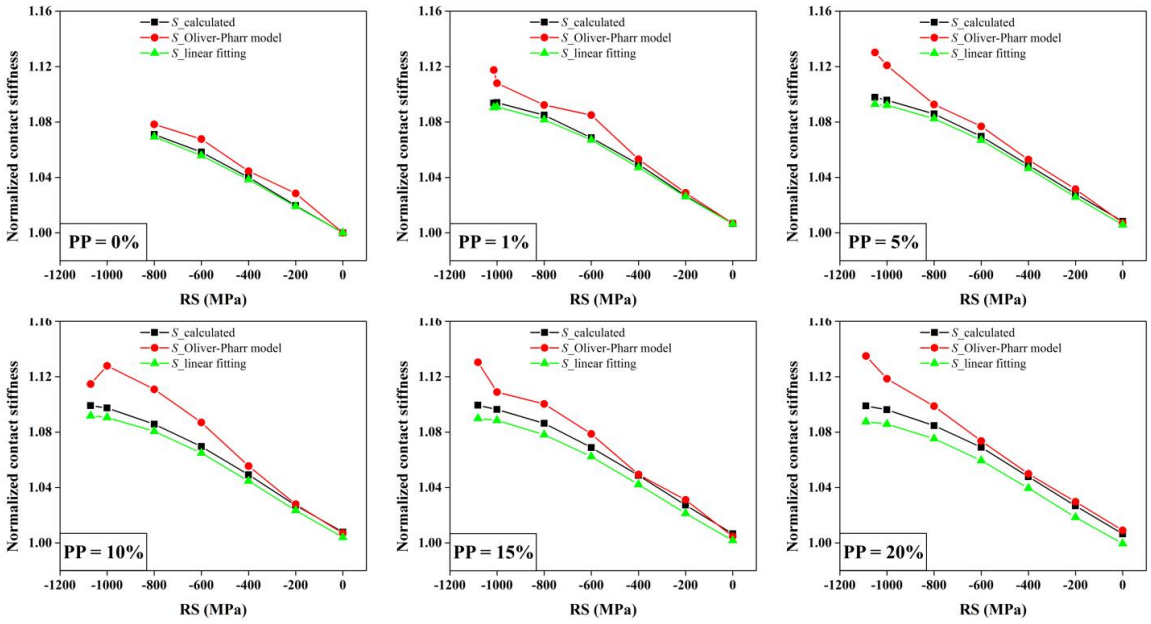


**Fig. 2-18. Comparison between normalized contact stiffness obtained from Oliver-Pharr model and linear fitting.**

From Fig. 2-18 we can see that without RS (no matter with which level of PP), Oliver-Pharr model actually works quite well, even better than linear-fitting at high PP level. However, along with the increase of RS level, the quality of the results obtained with Oliver-Pharr model decrease drastically. As for linear-fitting, it can always obtain exactly the same trend with the calculated $S$ values, only with some shift along with the increase of PP level. Although it has not been carefully studied, we still have the reason to believe that, with some modifications

correlated with PP level, linear-fitting should be able to get the contact stiffness value accurately. Based on the comparison above, we decided to use linear fitting method for getting contact stiffness from the initial unloading part of *P*-*h* curve.

Contour plots of functions *f*(RS, PP), *g*(RS, PP) and *h*(RS, PP) are respectively shown in Fig. 2-19. Several features can be observed from these plots:

- The maximum load $P_{max}$ is the most sensitive parameter because it varies by about 30% between the raw material and the material with the highest RS and PP levels. Corresponding variations for the contact stiffness *S* and the contact hardness *H* are only about 10% respectively.

- After 1% of plastic pre-strain, $P_{max}$ and *S* are mildly influenced by plastic strain PP, however, severely affected by residual stresses RS.

- Contact hardness *H* is affected by both RS and PP. However, for residual stress levels above 600 MPa (in absolute value), contact hardness *H* is almost unaffected by RS but obviously impacted by PP.

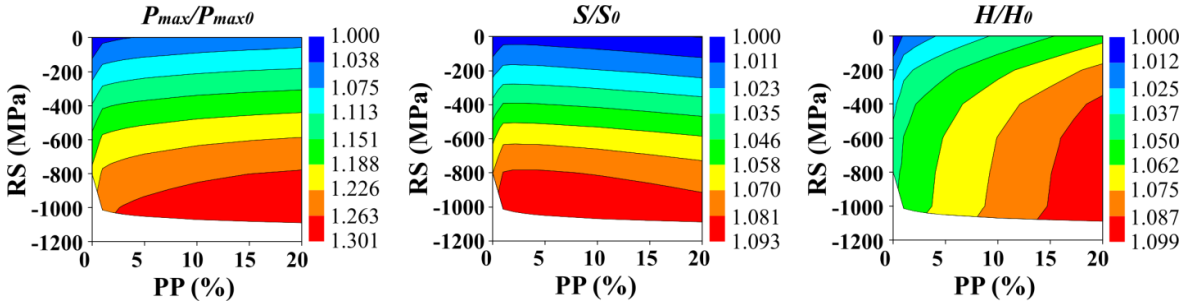


**Fig. 2-19. Contour plots of *f*(RS, PP), *g*(RS, PP) and *h*(RS, PP). (The area in white corresponds to domain beyond-$\sigma_y$, which is impossible to reach elastically.)**

As the responses, in terms of the two quantities RS and PP, of all the three normalized parameters $P_{max}$, *S* and *H* are significantly different from we expected before, an inverse method can be proposed: the knowledge of two of the three indentation parameters, for instance *S* and *H*, may give enough information to obtain the residual stress and the accumulated plastic strain values.

In order to illustrate the method from a purely numerical point of view, simulations of two combinations of RS and PP are performed. Combination 1 ($C_1$) is PP=11.5% and RS=-830 MPa, and combination 2 ($C_2$) is PP=16.5% and RS=-450 MPa. $C_1$ is chosen in the region where contact hardness is almost independent of residual stress. Both $C_1$ and $C_2$ are taken in a range where $P_{max}$ and *S* exhibit a weak dependence to plastic strain. All the normalized indentation responses, $P_{max}/P_{max0}$, $S/S_0$ and $H/H_0$, obtained from the simulations of these two combinations are listed in Table 2-13 [61].

**Table 2-13 Values of parameters obtained from FE simulations of two sets of RS and PP [61]**

| Combinations of PP and RS | PP % | RS MPa | $P_{max}/P_{max0}$ - | $S/S_0$ - | $H/H_0$ - |
|---|---|---|---|---|---|
| $C_1$ | 11.5 | -830 | 1.264 | 1.082 | 1.080 |
| $C_2$ | 16.5 | -450 | 1.189 | 1.047 | 1.085 |

The values of RS and PP derived from the proposed method are listed in Table 2-14. It shows that for both $C_1$ and $C_2$, the derived values of RS and PP from the knowledge of the indentation quantities ($P_{max}/P_{max0}$, $S/S_0$ or $H/H_0$ ) are a little bit higher than the values imposed in the FEM model (less than or about 1%). Fig. 2-20 shows graphically the solution for the three different couples of input values that can be used to determine PP and RS.

**Table 2-14 RS and PP values derived from the simultaneous functions method**

| | $C_1$ (PP=11.5%, RS=-830MPa) | | | $C_2$ (PP=16.5%, RS=-450MPa) | | |
|---|---|---|---|---|---|---|
| | $P_{max}/P_{max0}$ -$S/S_0$ | $P_{max}/P_{max0}$ -$H/H_0$ | $S/S_0$ -$H/H_0$ | $P_{max}/P_{max0}$ -$S/S_0$ | $P_{max}/P_{max0}$ -$H/H_0$ | $S/S_0$ -$H/H_0$ |
| RS (MPa) | -837.9 | -838.3 | -837.6 | -453.4 | -453.1 | -453.8 |
| PP (%) | 11.62 | 11.61 | 11.61 | 16.51 | 16.60 | 16.59 |

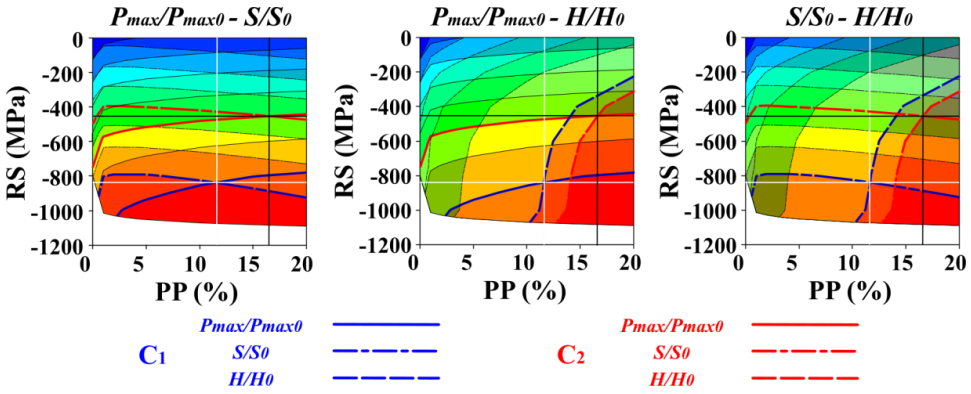


**Fig. 2-20. Identification of RS and PP values through the cross point of isolines of $C_1$ and $C_2$ on the pair-wise superposition of the contour plot of different parameters.**

In order to investigate the stability of the method versus a noise on the input values, a ±0.5% fluctuation was added into each indentation parameter $P_{max}/P_{max0}$, $H/H_0$ and $S/S_0$ listed in Table 2-14. The isolines of different pairs of parameters are shown in Fig. 2-21. With different pairs of parameters, the dispersion range on the RS value for $C_1$ goes from 150 MPa to 200 MPa, while for $C_2$ it goes from 70 MPa to 150 MPa. Concerning the PP, the dispersion range for $C_1$ goes from 5% to 10%, while for $C_2$ it goes from 5% to 15%. For both $C_1$ and $C_2$, the smallest dispersion could be obtained when considering $P_{max}/P_{max0}$ *and* $H/H_0$ as input values. On the contrary a strong dispersion can be observed when the pair $P_{max}$ and $S$ is chosen. This latter case can be explained by the fact that the isovalue lines cross with an acute angle which means that one of the two functions has a weak gradient versus one parameter (PP). When $S$ and $H$ are used, the isovalue lines cross with an angle close to 90 ° but the gradients of the two functions are weak so the sensitivity is decreased.

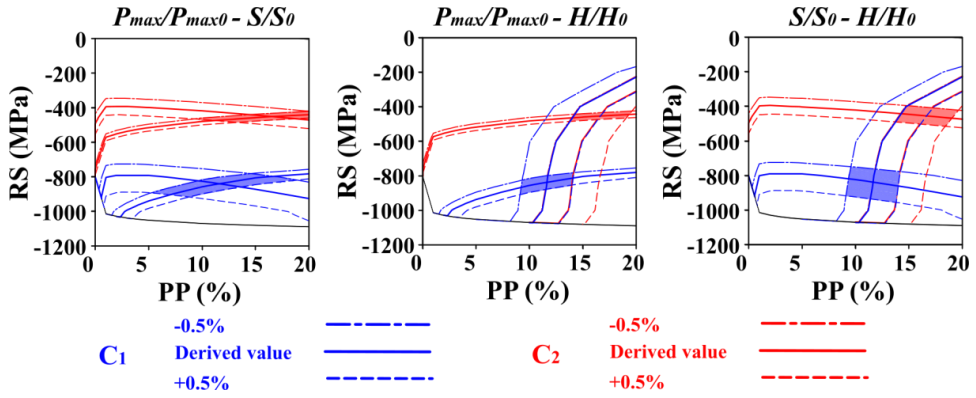


**Fig. 2-21. Dispersion for the three different couples of parameters.**

When all the three parameters are superposed together, PP and RS levels for the two combinations can be obtained as well. The results (both PP and RS) should stay within two small triangles in the superposed contour plot maps. The coordinate of each vertex should be each pair of PP and the corresponding RS values listed in Table 2-14. The triply superposed contour plot and its dispersion figure are shown in Fig. 2-22. Actually, results obtained with this method will not vary much from the results listed in Table 2-14. However, its dispersion will be minimized. Fig. 2-20 also proved that, from a purely numerical point of view, the three normalized parameters should be self-consistent for identifying PP and RS values.

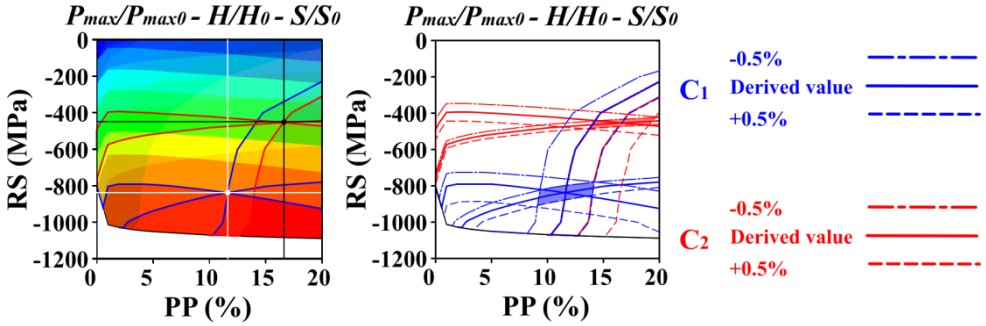


**Fig. 2-22. Identification of RS and PP values through the cross point of isolines of $C_1$ and $C_2$ on the triple superposition of the contour plot of different parameters.**

These two examples show that the sensitivity of the method varies significantly with the region in the (PP-RS) space explored and with the pair of functions ($P_{max}$ and $S$, or $P_{max}$ and $H$, or $S$ and $H$) chosen. This means that, according to the constitutive behavior of the material and the expected magnitude of the residual stress and plastic strain, the functions used in this method must be carefully chosen.

## 2.8 Conclusion

The study in this chapter was performed to investigate the influence of residual stress (RS) and work hardening (PP) on instrumented indentation test (IIT) through a series of numerical simulations, and to figure out an effective way to separate them when they are present simultaneously. The constitutive behaviors of the target materials, copper and three virtual

materials, were described by a Ludwick-type isotropic hardening equation. 2-D axisymmetric finite element simulations with a conical indenter were performed.

In order to satisfy the requirements of both high accuracy and low computing resources, a local refined FEM model was developed. Mesh convergence and model adequacy investigations showed that this model is quite good.

Suresh method and the method of differences between shapes of load vs depth (*P-h*) curves were then studied for trying to measure the RS value and separate it with PP. However, both of them failed. For Suresh method, the influence of RS on the hardness is mixed with that of PP which makes it not suitable for extract RS with the combination of PP. As for the method of differences between shapes of *P-h* curves, simulations showed that exactly the same change in *P-h* curves can be obtained with RS or PP. This makes it impossible to separate them only by analyzing the shapes of the loading *P-h* curves.

However, analysis of the topography of the dimple showed that, even when the *P-h* curves are completely superposed, the pile-up values are different when certain level of PP or the corresponding level of RS is applied. Moreover, this difference increases when PP or RS magnitude increases. This may give a way to estimate residual stresses and work hardening simultaneously, providing that the measurement accuracy is sufficient.

Guided by the former work, a new method based on FE simulation was proposed for characterizing the RS and PP simultaneously induced by shot-peening. Through a series of simulations of instrumented indentation, it was found that, although the loading indentation curves can be affected in the same way by the two quantities, the combination of 2 indentation parameters, obtained from loading/unloading curves can be used to estimate them. These two parameters could be chosen among three: the normalized maximum load ($P_{max}/P_{max0}$), the normalized contact stiffness ($S/S_0$) and the normalized contact hardness ($H/H_0$). The normalization is performed with respect to the values obtained on the untreated material (raw material).

Purely numerical tests were performed and it was found that the smallest dispersion could be obtained for the pair ($P_{max}/P_{max0}$-$H/H_0$). It was also observed that the sensitivity of the method decreases for high residual stress values, close to the compressive yield stress, and that this decrease affects the 3 parameters $P_{max}$, $H$ and $S$.

In the presented study, an equi-biaxial residual stress state was investigated, but according to study of Giannakopoulos [...], indentation is mostly sensitive to the hydrostatic component of the stress tensor, thus the results can be easily transposed to other stress states. Furthermore, the method presented here requires an accurate knowledge of the constitutive behavior of the initial material and does not take into account the effect of kinematic hardening.

In order to verify the practical feasibility of this method, a series of experiments will be conducted. Instrumented indentation tests with Berkovich indenter will be performed on shot-peened samples to test the practicability of this method. X-ray diffraction tests will be performed as well as comparison to check its reliability and precision. Uniaxial tensile test of

samples, with a raw material state, will also be performed as an assistance of X-ray diffraction tests.

# Chapter 3

# Simultaneous characterization of RS and PP induced by shot-peening in practice

In the previous chapter, the possibility of measuring residual stress (RS) and accumulated plastic strain (PP) simultaneously through instrumented indentation test (IIT) was studied from a purely numerical point of view. The method to induce residual stress and accumulated plastic strain was illustrated. Then, mesh convergence and adequacy of the model was checked. The first strategy of separating RS and PP from the shape of load curves failed, because a given level of RS and a corresponding level of PP may show exactly the same loading curve. However, the difference between the pile-up/sinking-in values leads us into proposing a second strategy. By performing a series of simulations on a virtual material (material A), the three functions $P_{max}/P_{max0}=f(\text{RS, PP})$, $S/S_0=g(\text{RS, PP})$ and $H/H_0=h(\text{RS, PP})$ could be obtained, where $P_{max}$, $S$ and $H$ are respectively the maximum load, the contact stiffness and the contact hardness of material with arbitrary RS and PP, while $P_{max0}$, $S_0$ and $H_0$ are respectively the maximum load, the contact hardness and the contact stiffness of reference sample which is supposed to be raw without any RS and PP. From two measured quantities, for instance $P_{max}^{measured}/P_{max0}^{measured}$ and $S^{measured}/S_0^{meaured}$, the value of RS and PP could be obtained by solving a system of two equations with two unknowns:

$$f(\text{RS, PP})=P_{max}^{measured}/P_{max0}^{measured}$$
$$g(\text{RS, PP})= S^{measured}/S_0^{meaured}$$

This method was examined by randomly applying two combinations of RS and PP into the model. Results showed a fairly good accuracy of the RS and PP values.

Since numerical simulations showed a good feasibility and quality of the simultaneous-function method for separating RS and PP, the next step is to apply this method in real experiments. In the present chapter, we will put emphasis on investigating how to characterize RS and PP simultaneously induced through shot-peening process in practice.

## 3.1 Material state

A bar ($\Phi$=50 mm) of T40 alloy, a commercially pure titanium (grade 2 CPT) which contains only $\alpha$ phase, was supplied by CEZUS, a subsidiary of the AREVA group (Ugine, FR). The composition of the material is listed in Table 3-1. The bar was treated through rolling and annealing (650°C, 90 minutes under high vacuum) processes in order to obtain homogeneous micro and macro structures. Ultrasonic inspection showed that the rates of void and defect are qualified.

**Table 3-1 The chemical constituent of the T40 grade 2 CPT.**

| Elements | C | Fe | N2 | O2ppm | H2ppm | Ti | Grain size |
|---|---|---|---|---|---|---|---|
| Wt% | 0.010 | 0.035 | 0.005 | 1050 | 6 | Balance | 50 $\mu$m |

## 3.2 Shot-peening

A piece of material, with a thickness of about 12 mm, was cut off from the bar by a metallographic cut off saw Secotem-15 (Struers International, Ballerip, DK). Then, the top surface of the cut sample was first mechanically polished on a Vector® LC 250 automatic lapping and polishing unit (BUEHLER An ITW International, Lake Bluff, USA), using abrasive discs of 800 grit to remove the layer affected by the cutting process and to obtain good flatness and roughness. Then the sample was fixed on an ultrasonic shot-peening system with a plastic holder. A closed space, the chamber is formed by the sample (on the top), the plastic holder, the die and the sonotrode (on the bottom). A given mass of shot (20 g) is introduced into the chamber. When the sonotrode vibrates, the shot will bounce rapidly and peen the surface of the sample continually until reaching the desired time. The whole process is shown in Fig. 3-1. Several key parameters of the shot-peening process are listed in Table 3-2.

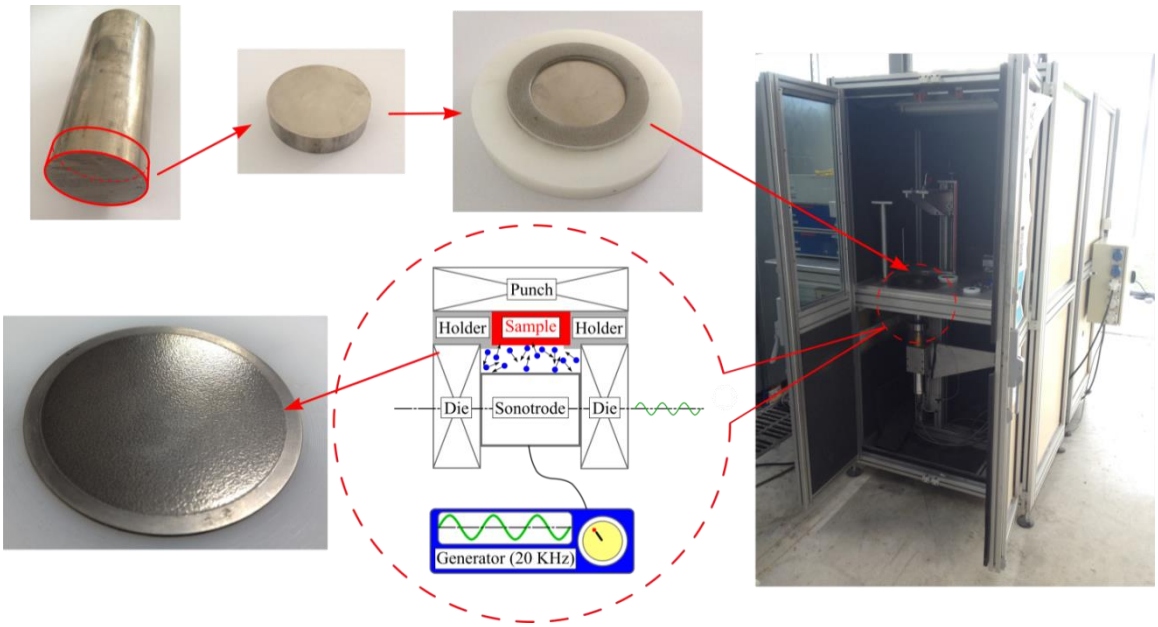


**Fig. 3-1. Scheme of the ultrasonic shot-peening process.**

**Table 3-2 Critical parameters of the shot-peening process.**

| Parameters | Values |
|---|---|
| Diameter of shot (mm) | 3 |
| Mass of shot (g) | 20 |
| Material of shot | 100Cr6 |
| Distance between sample and the sonotrode (mm) | 15 |
| Power (%) | 27 |
| Duration (minutes) | 10, |

After being cut along the depth direction, the metallurgical structure of the cross-section of the shot-peened sample can be observed. On Fig. 3-2 we can see that the grain size of the

sample is about several tens of micrometers. In the layer near the shot-peened surface (depth $\leq 100\ \mu$m), some results of regional metamorphism, such as intersecting and staggering of the slip systems, deformation twinning, etc., could be seen clearly in the grains. However, the grains had not been broken into nanocrystalized structures like in surface mechanical attrition treatment (SMAT) [134, 135]. It is a conventional shot-peening treatment.

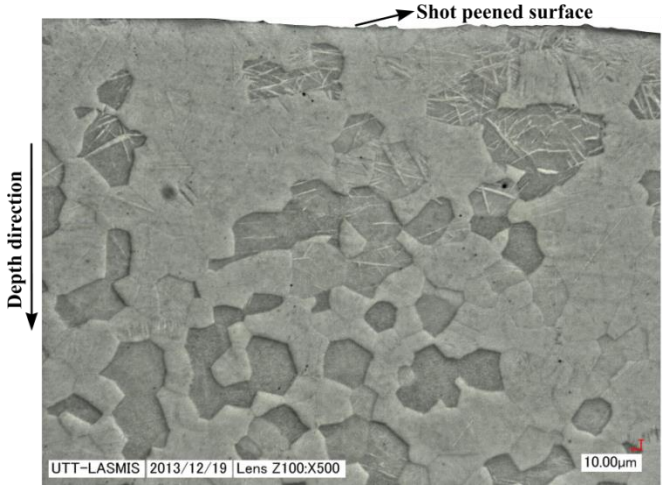


**Fig. 3-2. Metallurgical structure of the cross-section of the shot-peened T40 grade 2 CPT sample.**

## 3.3 Characterizing RS and peak width with X-RD

X-ray diffraction tests were performed with a 4-circle Seifert PTS-3000 X-ray diffractometer (now GE Inspection Technologies GmbH, Hürth, DE), equipped with a copper anode tube (40 kV and 30 mA, $K_\beta$ line is filtered by a Ni filter). Since diffraction peaks with higher angle will be more sensitive to residual stress and lattice distortion, {302} planes of $\alpha$-phase titanium, with peak position at $2\theta_0$ =149.05°, was selected for this study. A Position Sensitive Detector (PSD) which covers 11° was used to collect the diffracted signal. The scanning range was selected from 144° to 154°. The counting time is 220 s/step and the step size is 0.05 °$2\theta$.

As introduced in Chapter 1, for characterizing residual stresses with X-ray diffraction techniques, the $\sin^2\Psi$ method can be used, which means that a series of diffractions with various $\Psi$ angles need to be done. In this study, 13 $\Psi$ angles (-60°, -50°, -40°, -30°, -20°, -10°, 0°, 10°, 20°, 30°, 40°, 50° and 60°) were used. For the Seifert PTS-3000 X-ray diffractometer with a PSD, as shown in Fig. 1-15, the variation of the angles was realized through the rotation of the inclination angles $\chi$ under the goniometer (G) reference system. As shot-peening usually produces an equibiaxial stress state, only one $\Phi$ ($\Phi$=0) direction was necessary.

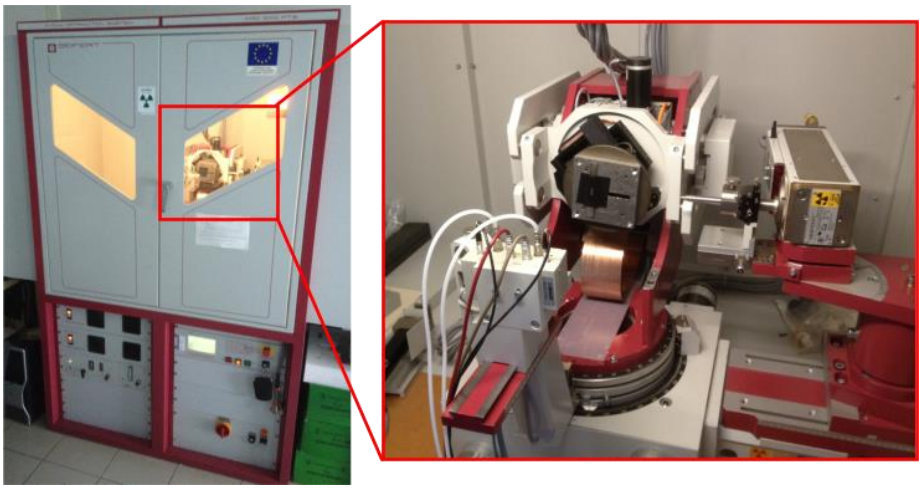

**Fig. 3-3. The configuration of the Seifert PTS-3000 X-ray diffractometer.**

The average penetration depth $\tau$ can be calculated according to:

$$\tau = \frac{\sin\theta}{2\mu} \approx 5\ \mu\text{m} \tag{3-1}$$

where $\mu$ is the linear absorption coefficient which equals to 938.08 cm for titanium and $CuK_\alpha$ radiation. This means that X-ray diffraction performed in this study can only obtain information in a very shallow layer at the top surface of the sample (more precisely, the average of a physical quantity, such as stress, work-hardening, texture, etc., measured by X-rays is taken between the depth 0 and infinity and it corresponds to the value at this penetration depth $\tau$).Thus, in order to get the residual stress profile along the depth into the shot-peened surfaces without introducing additional stresses or work hardening, electrolytic polishing process was conducted on the LectroPol-5 electrolytic polishing unit (Struers International, Ballerip, DK).) with D11 solution (70% ethanol, 20% perchloric acid and 10% *Ethylene glycol monobutyl ether*). The sample was polished with a voltage of 50V and a current of 16 mA for 30 s each time and then cleaned with cold running water. A laser distance detector, of which the uncertainty could reach 3 $\mu$m, was used for monitoring the thickness of the layer removed by the electrolytic polishing process. All the X-ray diffraction tests were strictly controlled to be conducted at the same place of the polished zone (the blue point in the center of the circular, as shown in Fig. 3-5), which guaranteed the consistence of the results.

A script written with the commercial computational software Wolfram Mathematica® was used for extracting the residual stress and peak broadening information from the X-ray diffracting data. The profiles of the residual stress and that of the peak width along with the depth are shown in Fig. 3-4. In this study, the peak was fitted with a Pseudo-Voigt profile which is a linear combination of a Gaussian function G(x) and a Lorentzian function L(x):

$$I_{P-V}(x) = \eta \cdot G(x) + (1-\eta) \cdot L(x) \text{ with } 0<\eta<1 \tag{3-2}$$

$$G(x) = I_0 \cdot exp(-\pi \cdot (\frac{x-x_0}{\beta_G})^2) \tag{3-3}$$

$$L(x) = I_0 \cdot \frac{1}{1+\pi^2\left(\frac{x-x_0}{\beta_L}\right)^2} \tag{3-4}$$

where $x_0$ is the peak position (the centroid position which corresponds to the peak maximum for symmetrical profiles), $I_0$ is the height of the observed line profile, $\beta_G$ and $\beta_C$ are the integral peak widths of the Gaussian function and a Lorentzian function respectively. The background was described by a straight line fitted by least squares on a given number of points taken at each end of the acquisition range. The standard uncertainty is computed from the residual of the least square regression from the non-linear fitting of the peak.

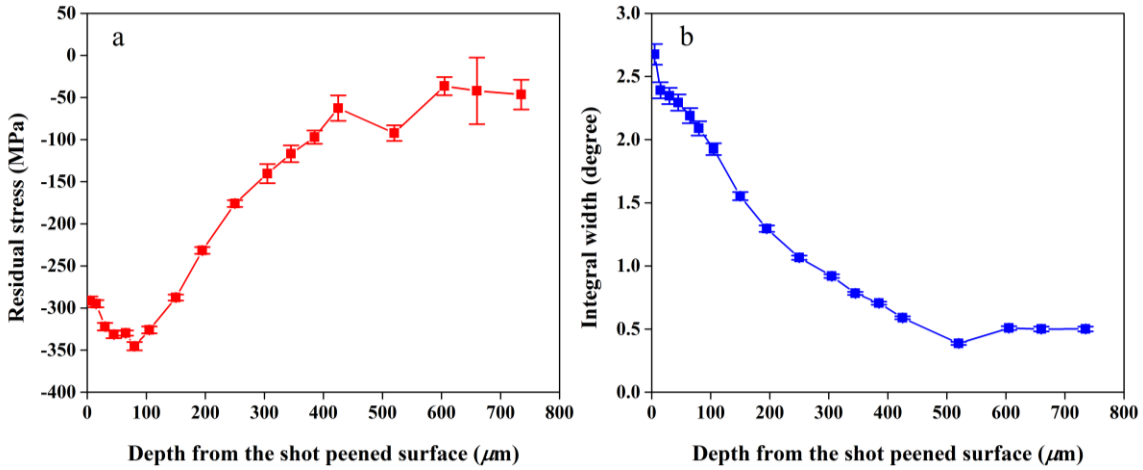


**Fig. 3-4. Results of the X-ray diffraction tests: (a) residual stresses profile along depth; (b) integral width profile along depth.**

The residual stress profile showed in Fig. 3-4 is typical of a shot-peened bulk metal material. Significant compressive residual stress (about -290 MPa) was observed in the top surface layer. The maximum compressive residual stress value (about -350 MPa) is obtained at a depth of about 100 $\mu$m. Then, the residual stress will decrease gradually until it reaches a stable level around -50 MPa with depth ≥500 $\mu$m. As for the integral width, it decreased until also about 500 $\mu$m where a stable peak width around 0.5° was reached. However, the decrease of integral width began from the very top surface but not subsurface layer. The stable level of integral width of 0.5° proved that the material deep enough is quite well crystallized.

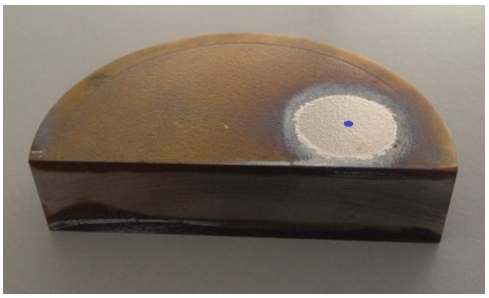

**Fig. 3-5. The sample for X-ray diffraction which went through one increment of electrolytic polishing (the white circular disk is the polished pit and the blue spot is the where the X-ray spot is positioned).**

It should be mentioned that the peak width have not been corrected from the instrumental broadening. . It can also be noticed that the residual stress cannot reach positive value during the depth range investigated in this study. Part of it can be explained by the new equilibrium reached after each layer removal (see below) and the uncertainty could cover another part. However, these arguments are not sufficient to explain the small negative stresses measured beyond 500 $\mu$m. It might be explained by the manufacturing process of the raw material bar: the annealing process may not have thoroughly eliminated the influence of the rolling process.

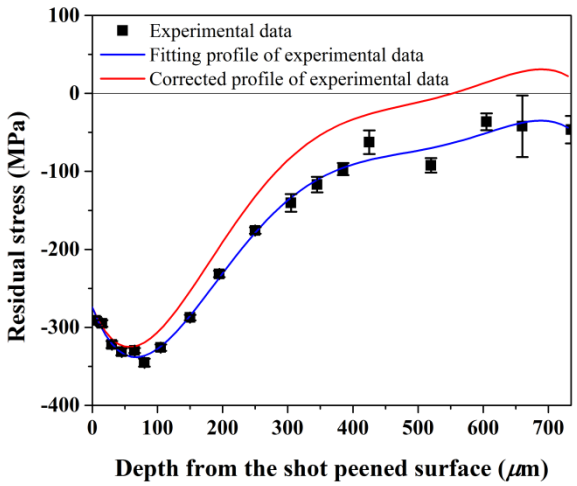


**Fig. 3-6. Residual stress profile along the depth (the blue dots are the measured values, the thin blue line is the fitted profile. The thick red line is the reconstructed profile taking into account the layer removal and assuming that the whole surface of the sample was removed. The actual effect of layer removal should be smaller.**

To check if the removal of successive layer has a significant influence on the measured values, a Mathematica script written by M. Fran ̧ois (UTT, unpublished results) using the eigenstrain theory was used. It assumes that the eigenstrain profile that created the residual stress distribution was not perturbed by successive layer removal, i.e. there is no plasticity due to layer removal. The eigenstrain profile is described by a polynomial of degree 5 up to a depth of 735 $\mu$m and equal to zero beyond. The coefficients of the polynomial are fitted on the measured stress, taking into account the successive removals. The fitted profile is represented by the thin blue curve in Fig. 3-6. Once the coefficients of the polynomial are known, it is easy to recalculate the complete stress profile that existed in the sample before the electrolytic polishing removal. This calculation was performed to estimate the maximum influence of the removal by assuming that the complete surface layer was removed. In fact, as can be seen on Fig. 3.5, removal was performed on a limited area. This means that the actual effects of removal are significantly smaller than what is shown on Fig. 3-6.

## 3.4 Characterizing WH with X-RD

As mentioned in Chapter 1, it is well known that the X-ray diffraction peak broadening analysis is proved to be a convenient approach to study the microstructural evolution of crystalline material. The method of quantifying the level of work hardening in components by

correlating the X-ray diffraction peak broadening to the equivalent true plastic strain has been studied and discussed in the literature [95-97].

In order to realize this kind of calibration on samples cut from a thick ingot, several steps are necessary, including preparing several uniaxial tensile test samples with the raw material state, performing uniaxial tensile tests at various true plastic strain levels and conducting X-ray diffraction tests. The detail concerning the last procedure has already been discussed before. Here, some explanations for the first 2 processes are offered.

### 3.4.1 Preparing the uniaxial tensile test samples

The dimension of the tensile test samples was designed according to the standard ASTM E8/E8M-09 [136], as shown in Fig. 3-7. All the specimens were manufactured by wire-cutting electric discharge machining (WEDM) directly from the bar.

When performing WEDM, the work piece in the sparking zone will go through an extreme fast heating, melting and vaporization followed by a rapid cooling process, during which tremendous changes in both of the surface topography and the surface metallurgy of the work piece will happen. This directly produces a multi-layered heat affected zone, which presents high hardness, high residual stresses, and severe metallurgical transformations at the machined surface of the work piece. Because of the shallow penetration depth of X-rays, this is a serious obstruction for the calibration sought in this study.

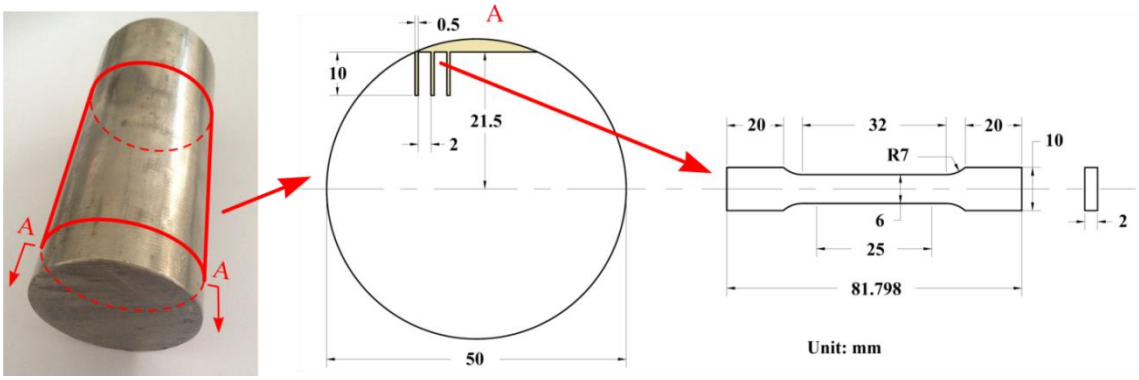


**Fig. 3-7. Dimensions of the uniaxial tensile test specimens.**

In order to get rid of the perturbations introduced by the WEDM process, special polishing procedures were conducted. There are three primary difficulties during the polishing procedure. The first one is how to hold the dog-bone like tensile test samples during the polishing process. The second one is how to keep the dimension accuracy of the specimens and remove the affected layer simultaneously. The last problem is how to get rid of external plastic deformations which will possibly be induced by the mechanical polishing process. Conventional mechanical polishing can keep the dimension accuracy well if being carefully controlled, however, the first and the third problem will become thorny. Electrolytic polishing can overcome the first and the third difficulties easily, but, impossible to assure high dimensional accuracy. As for the vibration polishing process, it has the greatest hope to resolve

all the problems. However, in that case, the material removal speed will be quite low which makes it time consuming.

Considering all of these, a special polishing procedure will be conducted. First, common mechanical polishing process will be conducted by fixing the sample on a specially designed holder which can cover the whole sample. At the end of the common mechanical polishing stage, vibration polishing will be used without any holder or counter balance. If vibration polishing process still cannot provide a surface without external plastic deformation, electrolytic polishing will be finally performed, during which the samples will be under particular protection for keIIng the dimension accuracy.

Mechanical polishing was performed on a Vector® LC 250 automatic lapping and polishing unit (BUEHLER An ITW International, Lake Bluff, USA) using 800-grit and 1200-grit silicon carbide abrasive disc films, (ESCIL Ltd, Chassieu, FR) followed by 10-$\mu$m suspension diamond abrasive paste and 0.05-$\mu$m silica powder (ESCIL Ltd, Chassieu, FR) on special tissues. No abrasive discs of grit smaller than 800 was used, for reducing the possible harmful influences during this process as much as possible.

The samples were attached to the center of a special holder which is made up of a larger steel tensile test sample and two short cylinders. There are several reasons for using such a holder. First, the shape of the large steel tensile test sample is dog-bone like. This kind of geometric shape makes the whole structure much more stable than using a long rectangular holder which can possibly tilt during the rotating polishing process. Second, two cylinders used as the connection part between the holder and the polishing machine is much more stable than using only one cylinder as the rotating axis. If only one cylinder is used, the frictional force between the sample and the abrasive disc will directly make the whole structure tilt to one side, which will severely reduce the dimensional accuracy of the polished tensile test samples. Besides, the T40 grade 2 CPT tensile test samples are dog-bone like as well, which will effectively protect the calibrated part (middle part). Even if the edges of the grip ends will be rounded a little bit during the polishing process, the dimension accuracy of the calibrating part can still be kept very well. Comparison between the two kinds of holders is shown in Fig. 3-8, from which we can see clearly that the holder with two cylinders performed much better than the other one with only one cylinder. Even so, there is still a little tilt that cannot be avoided. So, the only thing we can do is to make it to be uniform on both sides by intermittently (every 5 minutes) reverse the rotating direction.

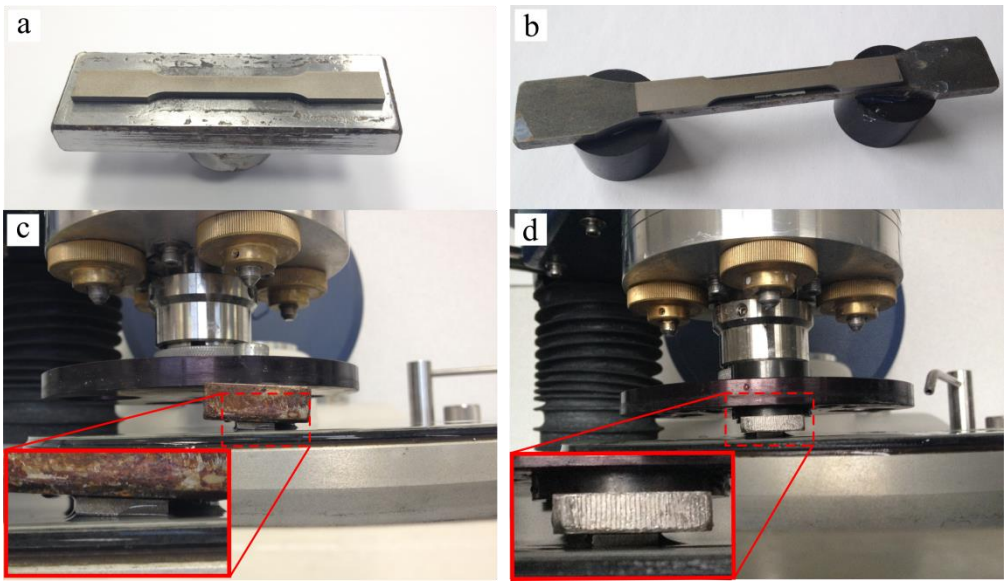


**Fig. 3-8. The polishing sample holders: (a) sample attached on the holder with one cylinder; (b) sample attached on the holder with two cylinders; (c) severe tilt occurred when rotation polishing with the holder with one cylinder; (d) no obvious tilt occurred when rotation polishing with the holder with two cylinders.**

During the whole mechanical polishing process, nothing else than self-weights of the sample holder were put on the sample to reduce the possible external plastic deformation. The total weight of the sample and the sample holder is 180.5 g. The sample was characterized by X-ray diffraction after each 20-minute of polishing in order to monitor the value of the integral peak width. After the mechanical polishing, vibration polishing was performed as well on the VibroMet®2 vibratory polisher (BUEHLER An ITW International, Lake Bluff, USA) with the 0.05-µm silica powder (ESCIL Ltd, Chassieu, FR) on special tissues. During this process, there was no other external load was applied on the sample but its own weight (11.2 g) for further reducing the influences of plastic deformation induced. The sample was tested X-ray diffraction after each 24-hour of polishing for monitoring the value of the integral peak width. When this value reaches the stable value shown in Fig. 3-4 (b), around 0.5°, the sample was considered as well polished.

One thing need to be mentioned is that considering the incident beam size (several $mm^2$) of the copper tube and the size of the calibrated part of the tensile test sample, a special mask made of black rubber adhesive plaster was put on the middle top surface of the sample. This is for preventing unwanted diffraction caused by the sample edges. Similarly, in order to prevent unwanted diffraction caused by the metal sample holder, an adhesive plaster was attached on the holder as well, as shown in Fig. 3-9.

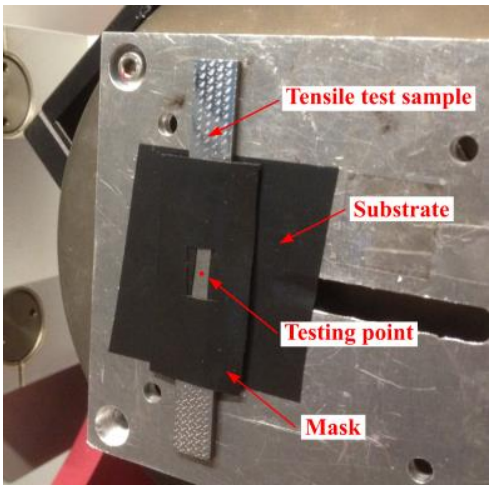


**Fig. 3-9. Mask and substrate used for preventing unwanted diffraction.**

Actually, our results showed that even if the careful vibration polishing process can only reach the integral peak width value around 0.9°, which still cannot fulfil our request of 0.5°. An integral peak width value larger than 0.5° means that there is still some external plastic deformation introduced by the mechanical polishing procedure. Then two strategies were tried to make further decrease of the integral peak width value.

The first strategy used was using annealing process to release the unwanted plastic deformation. Some mechanical polished samples were sent to Institut Carnot de Bourgogne (UMR CNRS 6303, Universit é de Bourgogne) for annealing. The procedures and key parameters of the annealing process were listed as follows:

-(1) Argon gas was first flowed for 1hour to build the protecting environment;

-(2) Heating from room temperature to 650°C with a constant rate of 10°C/min;

-(3) Stay at 650°C for 90 min;

-(4) Cooling to the room temperature naturally;

During the whole process, Argon gas was kept flowing permanently with a speed of 8 L/h.

Although the parameters strictly followed the values in the data sheet of the T40 grade 2 CPT bar provided by the manufacturer (as shown in Appendix 5), the annealing treatment did not succeed. The X-ray diffraction pattern of the raw material (integral peak width ≈ 0.5°) obtained by electrolytic polishing mentioned above and that of the annealed tensile test sample are shown in Fig. 3-10. For the raw material, the quality of the diffraction pattern is quite good. As for the pattern of the annealed tensile test sample, additional peaks occurred. As shown in the local zoom-in of the {302} peak in Fig. 3-10(b), the profile of the noise peak is low but quite broad. The worst thing is that the positions of these noise peaks are superposed with the normal characteristic peaks, which severely affected the accuracy of the determination of the integral peak width values. The reason for this kind of phenomenon might because that the tensile test samples are oxidized during the annealing process, even if they were under the protection of Argon gas environment. The yellow and blue color occurred on the surface of the samples can further prove the existence of the oxidized layer.

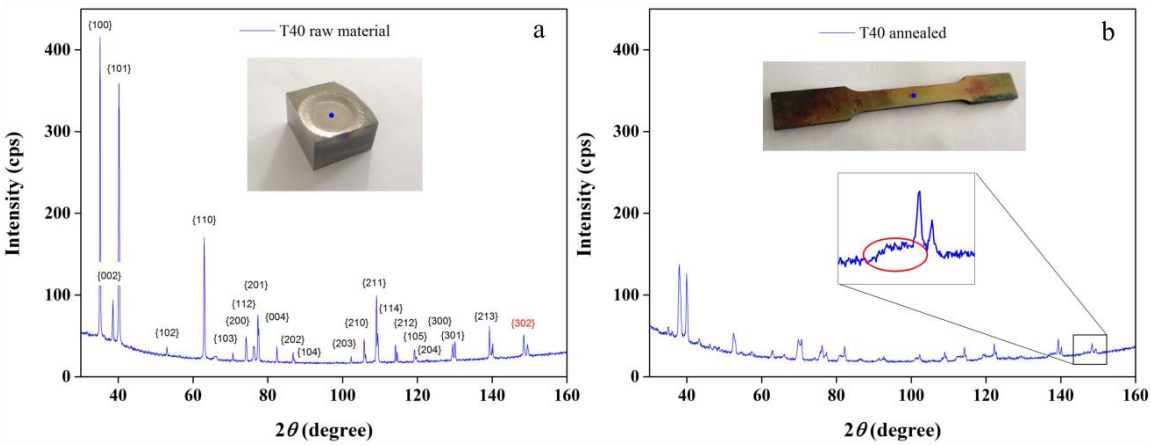


**Fig. 3-10. The X-ray diffraction patterns for the material treated with different methods: (a) raw material electrolytically polished; (b) annealed tensile test sample after mechanical polishing and vibration polishing**

Since the annealing procedure failed, the second strategy, electrolytic polishing, was then performed. Since this procedure is quite prone to round the edges, particular protection needs to be applied on the sample. The black rubber adhesive tape was pasted on the whole sample except two parts. They respectively are the calibrated part on the polished surface and the part on the other side which will make contact with the conductive cantilever of the polishing machine, as shown in Fig. 3-11(a). The final sample after electrolytic polishing was shown in Fig. 3-11(b), from which we can see that the surface of the calibrating part had some little fluctuations. However, the overall dimensions of the sample could be kept accurately enough for making uniaxial tensile test, especially that we do not look for the constitutive behavior (which would need the knowledge of the stress and thus a precise cross-section) but a relationship between the peak width and the plastic strain. This one can be obtained from the lengthening of the specimen. The main requirement is that the plastic strain is homogeneous on the surface irradiated by the X-ray beam.

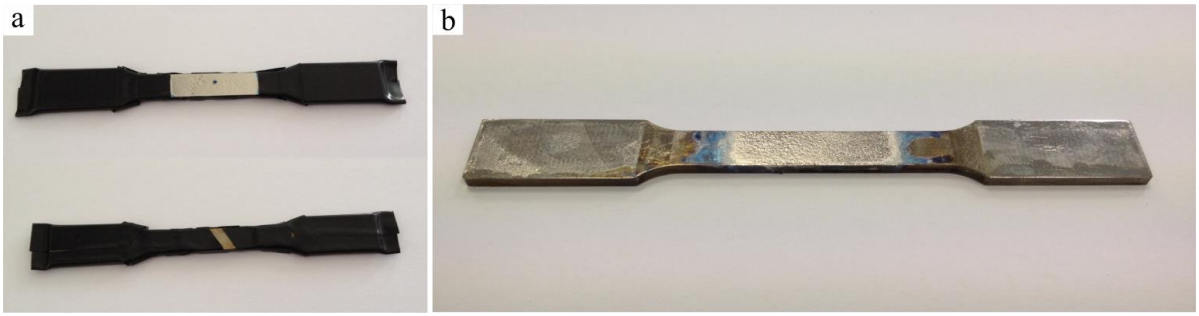


**Fig. 3-11. Particular protected tensile test sample for electrolytic polishing: (a) the protection; (b) the final sample after electrolytic polishing.**

After the careful mechanical polishing (by 800-grit and 1200-grit silicon carbide abrasive disc films followed by 10-$\mu$m suspension diamond abrasive paste and 0.05-$\mu$m silica powder on special tissues with only the self-weight of sample and the sample holder) and vibration polishing (by 0.05-$\mu$m silica powder on special tissues with only the self-weight of the sample) mentioned above, the electrolytic polishing procedure was conducted on LectroPol-5

electrolytic polishing unit (Struers International, Ballerip, DK) with D11 solution (70% ethanol, 20% perchloric acid and 10% *Ethylene glycol monobutyl ether*). The sample was polished with voltage of 45V and current of 15 mA for 15 s each time and then cleaned with cold running water. After three times of electrolytic polishing, integral peak width value of the sample was checked with X-ray diffraction.

Peak width variation during the whole polishing process (including mechanical, vibration and electrolytic polishing procedures) are shown in Fig. 3-12, from which we could see that mechanical polishing had obvious effect in the first 80 min. The integral peak width value decreased quickly from 2.24° to 1.13°. Then some saturation occurs. In the next 80 min, the integral peak width value only decreased 0.05°, among which it did not decrease a bit during the last 60 min. This might because of the weight of the two-cylinder sample holder. Thus, the sample was removed from the holder and put in the vibration polishing machine with only its self-weight. However, the X-ray diffraction results for the sample after 72-h vibration polishing did not seem good enough. The integral peak width values oscillate between 0.9° and 0.8° without further decrease. Finally, after electrolytic polishing had been performed 15 s×3 times, a layer of about 30-$\mu$m thickness was removed and the integral peak width value reached 0.54°. Considering the stable integral peak width values obtained from the former X-ray diffraction tests, we thought that the raw material state was arrived.

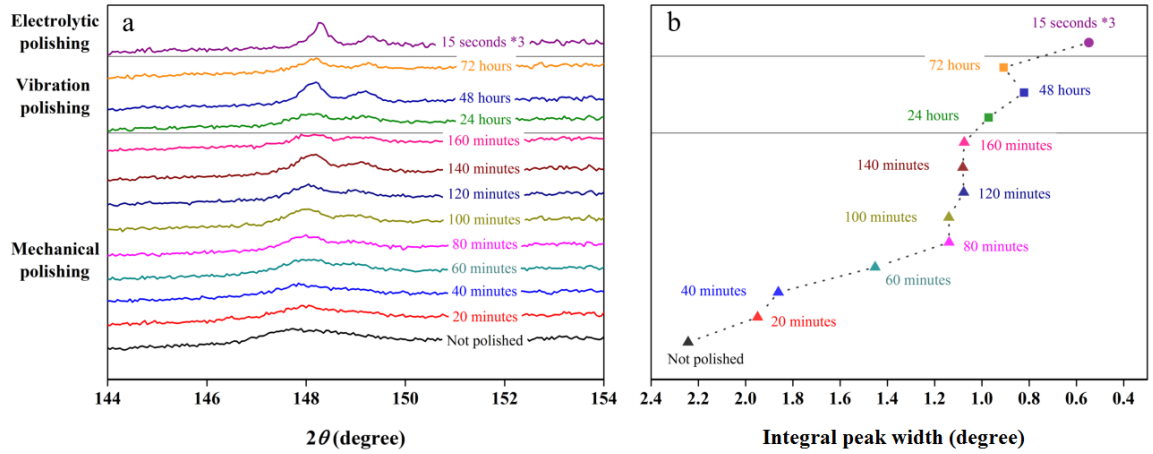


**Fig. 3-12. {302} peak profiles and peak widths corresponding to successive polishing steps: (a) peak profiles; (b) peak widths.**

## 3.4.2 Uniaxial tensile test at various equivalent true plastic strain levels

All the tensile tests were performed on the Instron 4411 5kN electric tension compression testing machine (Instron Ltd., Buckinghamshire, UK). Displacement load was applied with a constant speed of 0.48 mm/min which is calculated from the dimension of the sample according to the standard ASTM E8/E8M-09 [135]. Electronic extensometer was attached on the sample in the middle of the calibrated part for monitoring the local elongation of the calibrated section. The gauge length of the extensometer is 12.5 mm.

For each strain value, the peak width was measured by X-ray diffraction and then the specimen was stretched again. This was repeated until the necking point was reached (it is the highest point on the engineering tensile stress vs strain curve). Our results showed that, for T40 grade 2 CPT, the necking point will be reached around 15% of equivalent true plastic strain. As the cumulated plastic strain reach locally during shot-peening can be significantly higher than this, the fitted curve (a power law) was extrapolated which is, of course, highly debatable. (Since this value is small comparing with the possible PP level induced by shot-peening, the data was extrapolated with a power law which is, of course, debatable.) The results are shown in Fig. 3-13(a). Adjusted *R* squared value showed that the fitting quality is good. The fitted value for true plastic strain equal 0 is 0.57 which is close to the value obtained on the raw material.

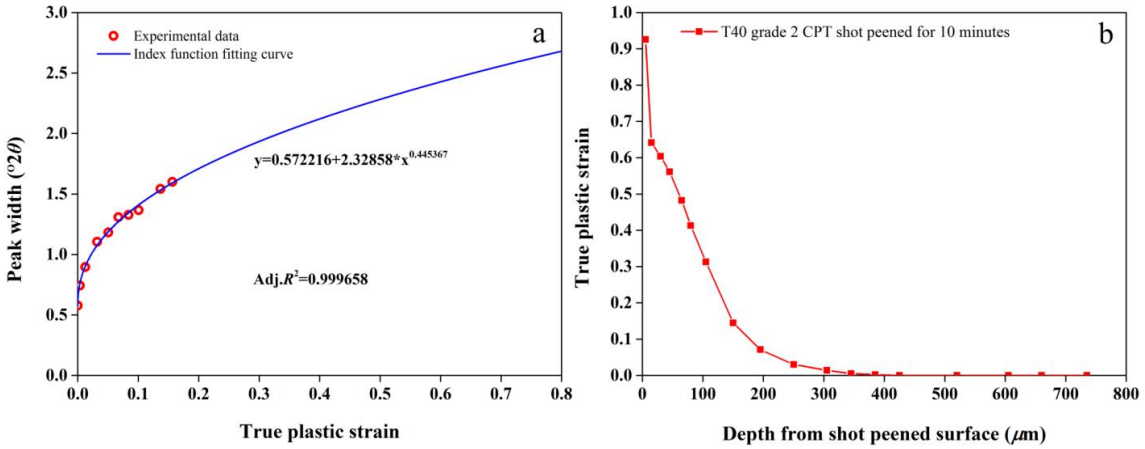


**Fig. 3-13. Relationship between peak width and the equivalent true plastic strain and the profile of equivalent true plastic strain along depth direction: (a) experimental data points and the index fitting function of peak width vs equivalent true plastic strain; (b) profile of equivalent true plastic strain along depth direction extracted from (a).**

By fitting with the power law, showed in Fig. 3-13(a), work hardening introduced by the shot-peening process could be estimated. The profile of work hardening along the depth direction is shown in Fig. 3-13(b), from which we can see that near the shot-peened surface, the level of work hardening can even exceed 60%. Then, it decreases quickly and fades away when depth $\geqslant$ 400 $\mu$m.

So far, the values of residual stresses and equivalent true plastic strain in the shot-peened T40 grade 2 CPT sample were obtained. From these data, an overall perception of the states of residual stresses and work hardening can be obtained, which can be used as references for the later parts of study about characterizing residual stresses and work hardening simultaneously induced by shot-peening process with instrumented indentation tests. The proposed protocol can also be used to define an initial state for fatigue studies, although fatigue tests on T40 grade 2 CPT have not been done in the present study.

## 3.5 Instrumented indentation tests (IIT)

In chapter 2, it was shown that characterizing residual stresses and work hardening simultaneously by instrumented indentation test (IIT) was possible with a reasonable accuracy from a pure numerical view point. In the present section, the method is tested experimentally.

### 3.5.1 Sample preparation

When trying to measure material properties by IIT, the major challenge is the sample preparation. As for our situation that trying to characterize residual stress and work hardening with IIT, it is critical because the preparation should not introduce unwanted residual stress or work hardening. Another challenge is to understand how the sample disturbance can affect the results of IIT. Although surface preparation is of great importance to IIT process, only a few researches focused on this part of study. Furthermore, nearly all of them concentrated on the surface roughness and topography of testing samples. Little attention was paid to the mechanical origin of sample disturbance induced by surface preparation. So, in the following section, the sample preparation process is investigated.

Three little pieces of material were cut off from the shot-peened sample with a metallographic cut off saw Secotem-15 (Struers International, Ballerip, DK) with a low feeding speed (0.01 mm/s) to minimize the influences of the cutting process. Then hot mounting (heating at 180°C for 10 min and then water cooling for 10 min) was performed on the LaboPress-3 hot mounting machine (Struers International, Ballerip, DK) with resin polyester SODY 33 (ESCIL Ltd, Chassieu, FR) for making samples suitable for IIT. Then, one sample was attached on a steel cylinder to increase its self-weight. The self-weight of all the 3 samples are No.1=173.2 g (the one with the steel cylinder), No.2=18.3 g and No.3=6.2 g respectively, as shown in Fig. 3-14.


**Fig. 3-14. Three IIT samples of different self-weights.**

All the samples were then polished to mirror flatness on Vector® LC 250 automatic lapping and polishing unit (BUEHLER An ITW International, Lake Bluff, USA) using abrasive discs of 800-grit and 1200-grit silicon carbide abrasive disc films, (ESCIL Ltd, Chassieu, FR) followed by 10-$\mu$m suspension diamond abrasive paste and 0.05-$\mu$m silica powder (ESCIL Ltd, Chassieu, FR). After that, they were polished on the VibroMet®2 vibratory polisher (BUEHLER An ITW International, Lake Bluff, USA) with the 0.05-$\mu$m silica powder (ESCIL

Ltd, Chassieu, FR). During the whole polishing process, only self-weight of the samples was used for applying pressure, without any other external pressure applied. This polishing procedure bypassed the usage of the abrasive discs of other coarser grit for avoiding their potential harm to the sample surface. Thus the material removing speed in this polishing process is quite low which means that the polishing time was much longer than typical polishing procedure to guarantee that the layer affected by previous polishing steps were fully removed. The polishing time for each of the polishing steps was 2 hours (abrasive discs of 800-grit and of 1200-grit respectively), 3 hours (10-$\mu$m diamond abrasive paste), 10 hours (0.05-$\mu$m silica powder) and 96 hours (vibration polishing with 0.05-$\mu$m silica powder) respectively.

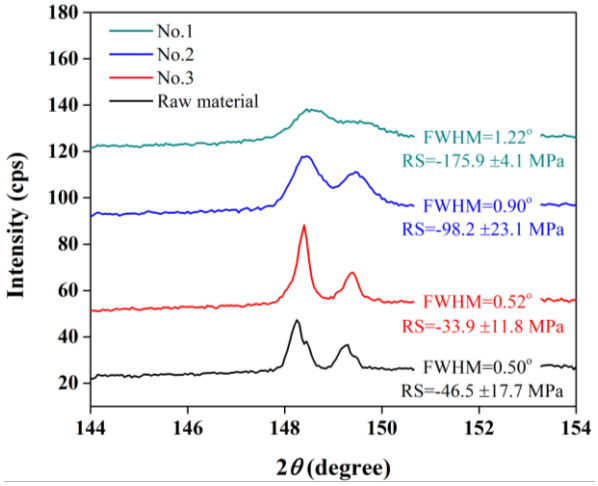


**Fig. 3-15. {302} peak profiles, peak widths and residual stresses corresponding to different polishing protocols of IIT samples.**

The polished sample was checked with X-ray diffraction by comparing with the reference of the electrolytically polished raw material. All the testing points are at the center of the samples. Results of the X-ray diffraction tests are shown in Fig. 3-15. It can be seen clearly that along with the decrease of the self-weight of the samples, the polished surface state will get closer to the reference state. One thing notable is the difference between samples No.2 and No.3. Even if the polishing procedure and parameters are exactly the same, the sample No.2 with a little bit higher weight still cannot fulfil our request of integral peak width equals 0.5°. In order to get close enough to the reference state, the self-weight of the sample needs to be extremely low.

In the literature, differences between various indentation results are mentioned, even if vibration polishing processes were used in all the tests [137-140]. Not much explanation was given about this. Since the preparation protocol of the IIT samples was not explained in detail, based on the results of our study, it is reasonable to supposed that differences in the self-weights of the samples might be one of the main causes.

### 3.5.2 Calibration of the Nano indenter®XP system

All the instrumented indentation tests were performed on the Nano indenter®XP (MTS systems corporation, Eden Praire, USA), as shown in Fig. 3-16, with a Berkovich indenter. Before performing indentation tests on the polished samples, two important calibrations need to be done.

**Fig. 3-16. Nano indenter®XP instrumented indentation system.**

A number of calibration processes, most of which are performed at the factory by the manufacturer and transparent to the user, are required in order to bring an IIT system in operation conditions [141]. However, “frame compliance” and “tip area function” calibrations are distinctive, because they involve making indentations on standard materials. Thus, they are normally the last calibrations which are often conducted by the user. This part of work will be explained in detail in Appendix 4.

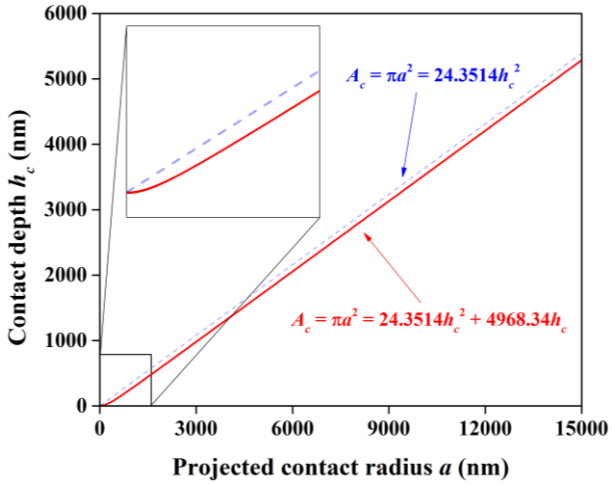


**Fig. 3-17. Calibrated geometric profile of the M128 Berkovich tip on Nano indenter® XP. The blue dush line is the perfect sharp tip and the red line is the tip shape obtained from the calibrated two-term tip area function.**

In fact, the calibrated tip area function represents not only the geometry defect of the tip. It is a comprehensive factor which contains nearly all the facts that may affect the indentation

response in the form of the relationship between $A_c$ and $h_c$, provided that they can be considered identical in the calibration stage and during the measurement. In the present study, the relationship between contact depth $h_c$ and the contact radius $a$, obtained from the two-term tip area function according to Eq.(Appendix 4-6) and the relation shown in Eq.(1-7), is shown in Fig. 3-17. This relationship, as a tip-shape function, will be used to build the "real tip" in FEM mode. This will be explained in detail in the later sections.

### 3.5.3 Instrumented indentation tests on T40 grade 2 CPT

A series of instrumented indentation tests were performed on all the 3 samples following the standard ASTM E 2546-07[142]. Results shown in Fig. 3-15 showed that different levels of work hardening and residual stresses existed in the surface layer of the samples. Although their exact distributions along the indentation depth direction are unknown, we still can have some foresight that the indentation responses on the three samples might be quite different from each other.

Although the results of X-ray diffraction showed the corresponding averaged situations of true plastic strain and residual stress in the depth around 5 $\mu$m, performing indentation tests shallower than 5 $\mu$m is still meaningful. Even if they cannot thoroughly get rid of the influences of true plastic strain and residual stress in top 5-$\mu$m layer, the indentation responses obtained by them still can show something, which might be able to help us to separate residual stress and work hardening induced by shot-peening. This is because that the plastified depth of a indentation is equal to about 7 times of the penetration depth of the tip. From the results shown in Fig.3-4(a) and Fig.3-13(b), we could see that shot-peening process can definitely induce residual stress and of true plastic strain decreasing along the depth from the shot-peened surface. Based on this, we can imagine that it is quite possible that the maximum load $P_{max}$, the contact stiffness $S$ and the contact hardness $H$ may vary along the depth as well, which is profitable for the calibration of RS and PP.

Indentation tests were first made on the sample No.1. Maximum penetration depth $h_{max}$ of 1 $\mu$m was used to control the indenter tip. However, the indentation responses, including $P_{max}$, $S$ and $H$, showed little variances along the depth from the shot-peened surface. This is quite possible that the penetration depth of 1 $\mu$m is not deep enough comparing with the depth influenced by the polishing process. Seeing this, the $h_{max}$ value was increased to 3 $\mu$m. Indentation test were then performed on the reference, sample No.2 and No.3. All the indentation responses are shown in Fig. 3-18. The dark cyan curves are the results of the 1 $\mu$m-deep indentation tests on sample No.1 which had no obvious gradient. Especially, the $H$ curve is much higher than that of the reference (the black curve) which is directly caused by the work hardening and residual stress present in the surface layer of sample No.1. As for the results of the 3 $\mu$m-deep indentation tests on sample No.2, the red curves in Fig. 3-18, for depth far from the shot-peened surface, the $H$ values for large depth got much closer to that of the reference. Since $P_{max}$ and $S$ values highly depend on the $h_{max}$ value, they cannot be used to make comparison between sample No.1 and the reference and sample No.2. However, $H$ which is

supposed to be independent of the $h_{max}$ value can be used to compare. As for 3 $\mu$m-deep indentation tests on sample No.3, the $H$ values for large depth got closest to the hardness of the reference. Comparing with sample No.2, all the three indentation responses, at larger depth from the shot-peened surface of sample, No.3 got even closer to the reference values. Particularly, the $P_{max}$ and $H$ values at large depth were quite close to those of the reference, which shows that sample No.3 was best polished.

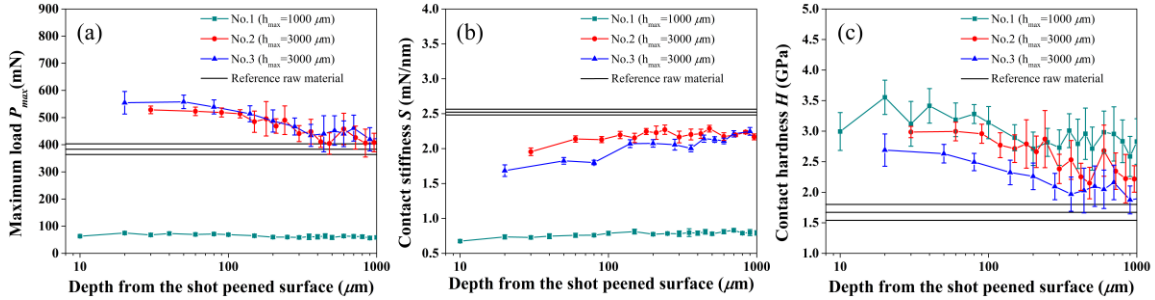


**Fig. 3-18. IIT responses along with depth from the shot-peened surface on reference and on different samples: (a) maximum load $P_{max}$; (b) contact stiffness $S$; (c) contact hardness $H$.**

As for the $S$ curves, two strange things happened. One thing is that as the pure simulation results in Chapter 2 shown, along with the increases of residual stress and of accumulated plastic strain, contact stiffness $S$ values increased as well. However, experimental results of all the 3 samples showed reverse trend as the numerical simulations, even if it was not so obvious for the 1-$\mu$m indentation tests on sample No.1. The other thing is that there were still large differences between the $S$ values of sample No.3 at larger depths and the contact stiffness value of the reference

### 3.5.4 Correction of edge effects

In order to find out the reasons of the strange things happened to contact stiffness $S$ values, some further investigations need to be done. One possible reason should be the edge effects, which are caused by the insufficient distance between indentation and the edge of the sample. In fact, the problem caused by sample edge always exists, even for conventional hardness tests. For instance in Vickers hardness test, an experimental law is that: for steel and copper, indentations have to be spaced with at least 3 diagonal widths and away from the edge at least 2.5 diagonal widths; for lead, zinc, aluminum and tin the indent spacing has to be at least 6 diagonal widths and the edge spacing should be at least 5 diagonal widths [143]. Edge spacing smaller than these values will induce severe edge effects into the results of the tests. Is an indent far away from the edge (more than the above values) safe? Unfortunately, the answer is negative.

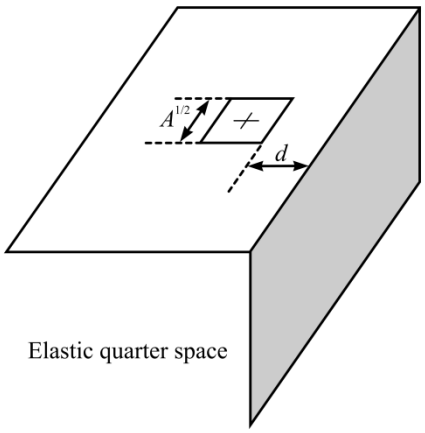


**Fig. 3-19. Geometry of the edge problem solved by Gerber [144] and reanalyzed by Jakes *et al*. [145].**

Gerber [144] worked on the edge effects in elastic contact between a square, rigid punch and an elastic quarter space, as shown in Fig. 3-19. Later on, Jakes *et al*. [145] analyzed Gerber's results in context of King's [146] solution for indentation on an elastic half-space to arrive at an estimate of the structural compliance $C_{str}$ caused by a free edge as:

$$C_{str} = \frac{0.20 + 0.11\nu}{Ed} = \frac{2(0.20 + 0.11\nu)\beta\gamma}{\sqrt{\pi}(1-\nu^2)} \cdot \frac{1}{E^* d} \tag{3-5}$$

In Eq.(3-5), $E$ and $\nu$ are the Young's modulus and the Poisson's ratio of the tested material, $E^*$ is the effective Young's modulus defined in Eq.(1-8), $\beta$ and $\gamma$ are the two correction factors mentioned in Eq.(1-10) and Eq.(1-11), $d$ is the distance from the sample edge to the center of the indent.

In order to determine mechanical properties for indents placed near the edge, the free edge caused structural compliance $C_{str}$ must be considered. Then the composite compliance $C^*$ obtained from the indentation test, as shown in Eq.(Appendix 4-1), should become as:

$$C^* = C_f + C_s + C_{str} \tag{3-6}$$

where $C_f$ is the frame compliance of the indentation system and $C_s$ is the sample compliance. By introducing $C_{str}$, Jakes *et al.* [145] corrected the influences of edge effects from projected contact area $A_c$, effective Young's modulus $E^*$ and contact hardness $H$. [145]. The study of Jakes *et al*. showed that the influences of edge effects on indentation responses are significant and the correction of edge effects is necessary.

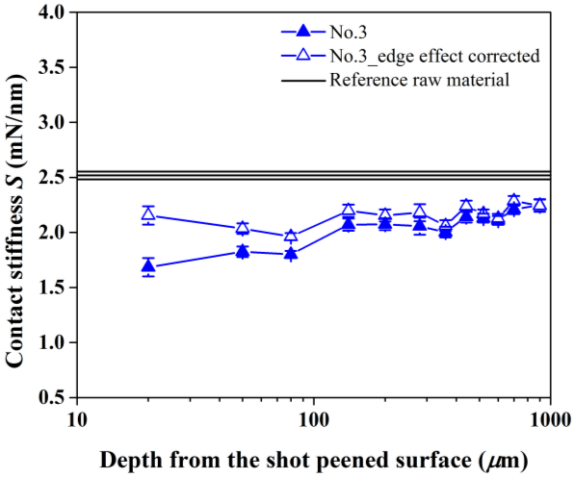


**Fig. 3-20. Comparison between original and corrected *S* values.**

In fact, the foundation of the correction proposed by Jakes *et al.* [145] is to correct contract stiffness *S*, because of the reciprocal relation between sample compliance $C_s$ and contact stiffness *S*:

$$S = \frac{1}{C_s} \tag{3-7}$$

Considering the edge spacing of each group of indents we made on the shot-peened T40 grade 2 CPT sample, edge effects should be one of the reasons which caused the strange trend of contact stiffness *S*. Combining Eq.(3-5), Eq.(3-6) and Eq.(3-7) together, contact stiffness values of sample No.3 was corrected. Comparison between original and corrected *S* values was shown in Fig. 3-20.

## 3.6 FEM simulations of IIT onT40 grade 2 CPT

In Chapter 2, simulations were only performed on several virtual materials for probing the feasibility and method of characterizing RS and PP simultaneously induced by the shot-peening process through IIT technique. In this part of work, FEM simulations using the material property of T40 grade 2 CPT were performed and discussed.

All the configurations of the whole FEM model were explained in Section 2.2. The only difference is that the values of the material property parameters were not virtual but extracted from uniaxial test on T40 grade 2 CPT. Sample dimensions and concrete testing methods were discussed in Section 3.4.1 and Section 3.4.2. Experimental results showed that necking began around PP=10%. Thus, data points beyond this range were not used to do fitting. Experimental true-stress vs true-plastic-strain data and best fitting with the Ludwick model were shown in Fig. 3-21. The parameters obtained from the best fitting curve were directly used in the FEM simulations for describing the material constitutive behavior.

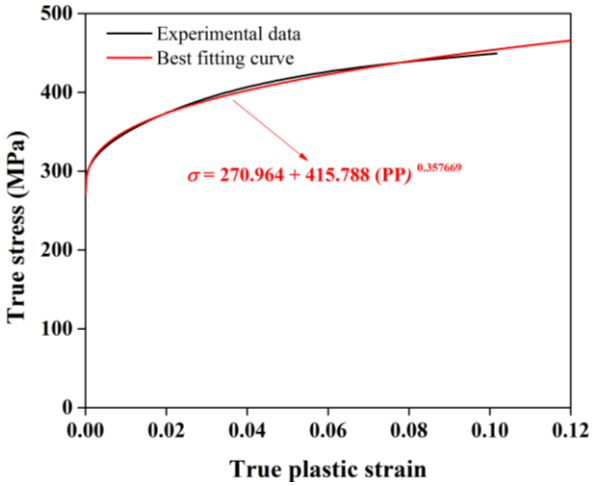


**Fig. 3-21. True-stress vs true-plastic-strain data of uniaxial tensile test and the best fitting curve.**

In order to make sure if the numerical model is precise enough to represent the indentation process of T40 grade 2 CPT, comparisons between the simulated results and the experimental results on the reference sample were made, as shown in Fig. 3-22 and Table 3-3.

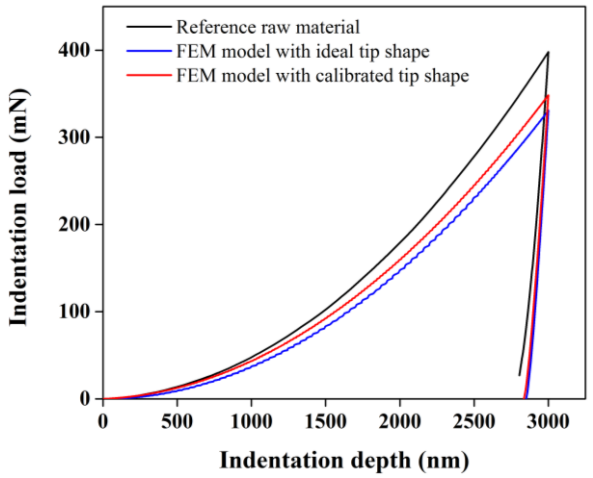


**Fig. 3-22. Comparison between the experimental load vs depth (*P-h*) curve of reference T40 sample and that of the FEM simulation.**

**Table 3-3 Results of the instrumented indentation tests and simulations.**

| Indentation response | Reference | FEM with ideal tip | FEM with calibrated tip |
|---|---|---|---|
| Maximum indentation load $P_{max}$ (mN) | 398.0 ±20.3 | 330.7 | 348.4 |
| Contact stiffness $S$ (mN/nm) | 2.542 ±0.036 | 2.710 | 2.608 |
| Contact hardness $H$ (GPa) | 1.67 ±0.13 | 1.37 | 1.38 |

Data above showed that there are large differences in all the four indentation responses, including load vs depth (*P-h*) curve, maximum indentation load $P_{max}$, contact stiffness $S$ and contact hardness $H$, between the experiment and the simulation. This proved that the FEM model configuration demonstrated in Section 2.2 is not suitable enough to represent the indentation process of a real material, even if it is consistent from a pure numerical point of

view. So, figuring out and modifying the weak points of our existing model will be the aim of the next step of work.

Enlightened by the work of Section 3.5.2.2, the first thing we thought about is the tip defect in real experiment, because in the FEM model, only an equivalent conical indenter with a perfect sharp tip was taken into account. However, literature mentioned that tip defect will strongly influence nearly all kinds of IIT responses [147-150]. Although the maximum penetration depth $h_{max}$ in this study is much deeper than that of conventional IIT tests, the results of Section 3.5.2.2 still showed that the effect of the tip defect may not be negligible.

In order to investigate the effects of tip defect, another FEM model was built. All the configurations of the new model are as the same as in the original one, except the shape of the indenter tip. In the new FEM model, tip shape showed in Fig. 3-17 which was obtained through the tip area function calibration process was used for representing a more realistic indenter.

As shown in Fig. 3-22 and Table 3-3, the obvious differences in all the three indentation responses and the *P-h* curve between the experiment and simulation were decreased in different extents by considering the tip defect, although the differences are still quite large. This confirmed that any further modifications for improving the performance of numerical simulations should be done with the new FEM model.

## 3.7 Improving the accuracy of FEM model with inverse method

Through considering the calibrated tip in the FEM model, the quality of all indentation responses could be improved, but still not enough, which means that there must be some factors which had not been considered properly. By checking the configurations of the model, several possible aspects were considered.

The first possible fact is still the shape of the indenter, although tip area function calibration performed above was supposed to be sufficient to adjust tip defect. However, the two-term tip area function according to Eq.(Appendix 4-6) can only give us a round-tip conical indenter, which may not be the real indenter shape in experiments. In addition, the quality of this calibration procedure highly depends on the precision of the fitting.

Second, material parameters used in the model were extracted from uniaxial a tensile test which may not be precise enough to represent the indentation response of T40 grade 2 CPT. Because it is easy and convenient, uniaxial tensile test is the most basic and important test broadly used in nearly all kinds of numerical simulations for identifying the constitutive behavior of the material. However, for complicated situations, stress-strain results of uniaxial tensile test may not be suitable or enough. During an IIT process, the hard indenter will continuously penetrate the surface of the target material, which makes most of the material beneath the tip under a multi-axial compressive loading path, but not a uniaxial tensile loading path.

Last but not least, although it is an important parameter for contact behavior, friction coefficient during IIT process cannot be effectively measured with an experimental method. The friction coefficient value used in present study was chosen from reference friction values

between diamond and metallic materials from the literature, which are usually obtained with conventional sliding friction experiments. However, the friction behavior of the actual IIT process might be significantly different from the reference values. This makes the friction coefficient values used in our FEM model questionable. Although some researches proved that friction coefficient can hardly influence the indentation response of some materials [], lots of other researches still showed that friction coefficient plays a critical role in the IIT process on many metals [151, 152]. In the former chapter, it had already been shown that friction coefficient can have a significant influence on material A, the constitutive behavior of which was supposed to be similar to a titanium alloy. Thus, we have some reasons to believe the friction coefficient can directly affect the accuracy of IIT simulations for T40 grade 2 CPT.

In fact, many other factors, such as the choice of constitutive model, the setting of contact model between the indenter and the material, can possibly introduce errors into the model as well. However, they are not taken into account here. In fact, identifying which kind of constitutive model and contact behavior is suitable for describing the indentation responses of T40 grade 2 CPT is quite complex, which is far beyond the goal of this thesis. Since the study in Chapter 2 has already shown the possibility and feasibility of our simultaneous function method, even if only from a pure numerical point of view, it means that the constitutive and contact models set in Chapter 2 should be suitable for our problem.

### 3.7.1 Inverse method

The so-called inverse method, a fairly mature way for identifying parameters in models, is performed by combining computing process, such as computer aided design (CAD) or computer aided engineer (CAE), with numerical optimization. In this method, the objective functions are minimized with respect to the model parameters using some numerical optimization algorithms. The parameters of the model are identified as the optimized solution [153, 154].

In this study, commercial multi-objective optimization and design environment ESTECO modeFRONTIER® is used, for it can be easily coupled with almost any CAD or CAE tool (whether commercial or in-house) in a standard workflow which allows the automatic run of a series of computations proposed by a selected optimization algorithm [153, 155]. Since modeFRONTIER is well packaged with abundant optimization algorithms and I/O interfaces, even users with a relatively modest experience, like us, can easily realize optimization process.

Actually, optimization means using some search strategy to find out a set of input variables from a large number of possible options to meet the objectives under the constraints [153, 156]. In modeFRONTIER, a standard optimization workflow is mainly combined with three parts: input variables, the black box and the output variables, as shown in Fig 3-23. Input variables are the free parameters that can be varied or chosen by the designer for constructing the design space. The black box is normally a set of solvers or experiments which can solves the design problems or produces some data. The output variables are a set of measures of the system response or performance.

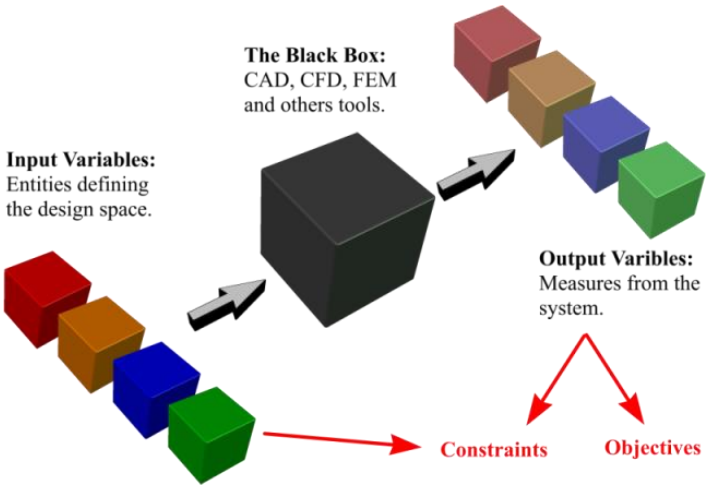


**Fig. 3-23. Schema of the concept behind modeFRONTIER [153].**

Three major possible sources (tip shape, material properties and friction coefficient) that may induce error into the FEM model were considered in this study. Tip shape will be firstly optimized, because it is the basis of other optimizations. When the best tip shape was found, other factors will then be optimized.

Actually, the inverse method is using optimization process to reduce the residual deviation between the FEM results and the experimental data. The combination of input variables which gives the smallest residual deviation will be the optimized solution that is supposed to be the approximate value of the real situation. The schema of the inverse investigating process in present study was shown in Fig. 3-24.

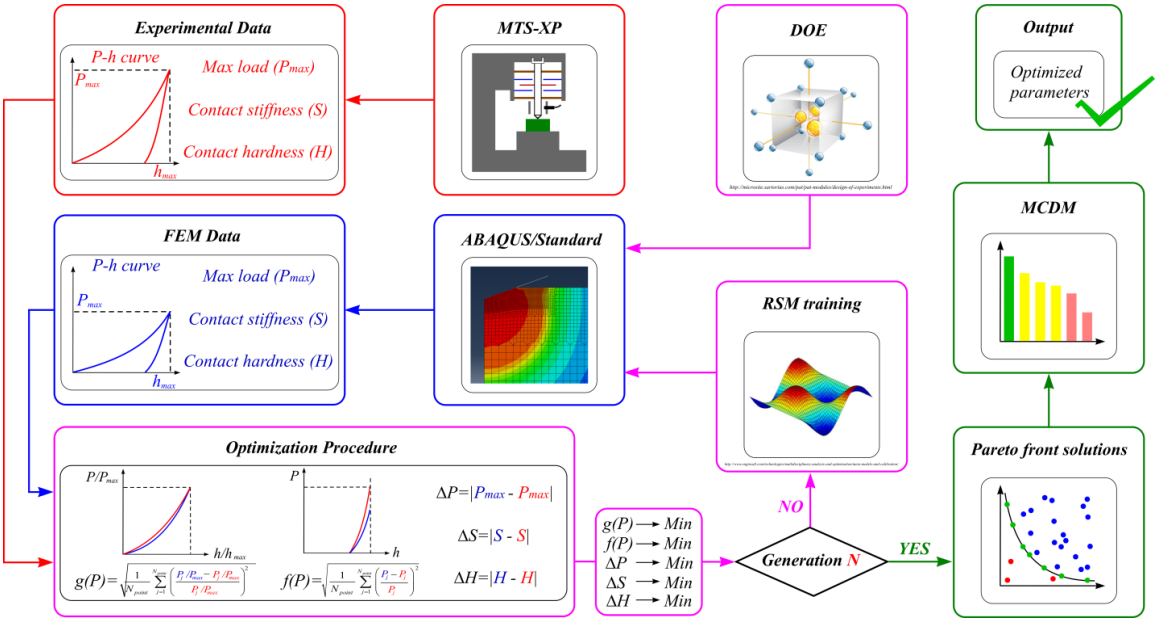


**Fig. 3-24. The schema of the inverse investigating process.**

### 3.7.2 Indenter shape optimization

For making the tip-shape optimization, the first important thing is determine a proper objective. When performing IIT simulations, we occasionally found that the shape of the loading part of the normalized *P-h* curve might be a good choice, because it seems to be only sensitive to the variation of tip shape but relatively insensitive to other factors. For better understand the shape of the normalized loading *P-h* curve, a series of IIT simulations with different material properties and various friction coefficients were conducted with two types of tip (one is the ideal equivalent conical tip with a 70.3° apex angle, the other is the "calibrated tip"). All the cases and the corresponding parameters are listed in Table 3-4.

**Table 3-4 Experimental and simulated cases for investigating the tip-shape affecting factor.**

| | | Copper [123] | A | B | C | T40 grade 2 CPT | | | |
|---|---|---|---|---|---|---|---|---|---|
| FEM simulations | Young's modulus $E$ (GPa) | 122 | 122 | 122 | 122 | 119 | 119 | 119 | 119 |
| | Poisson's ratio $\upsilon$ | 0.33 | 0.33 | 0.33 | 0.33 | 0.34 | 0.34 | 0.34 | 0.34 |
| | Yield strength $\sigma_y$ (MPa) | 240 | 800 | 240 | 800 | 280 | 280 | 280 | 280 |
| | Hardening coefficient $K$ (MPa) | 340 | 340 | 340 | 340 | 415 | 415 | 415 | 415 |
| | Hardening exponent $n$ | 0.57 | 0.1 | 0.1 | 0.57 | 0.38 | 0.38 | 0.38 | 0.38 |
| | Friction coefficient $f$ | 0.15 | 0.15 | 0.15 | 0.15 | 0 | 0.15 | 0.25 | 0.5 |
| | Tip | Ideal equivalent conical tip ($A_c$=24.56$h_c^2$)<br>Calibrated equivalent conical tip ($A_c$=24.3514$h_c^2$+4968.34$h_c$) | | | | | | | |
| Experiments | Sample | Reference T40 grade 2 CPT sample (electrolytic polishing)<br>Common T40 grade 2 CPT IIT sample (carefully mechanical polishing) | | | | | | | |
| | Tip | Berkovich tip | | | | | | | |

Results confirmed our former observation and showed that the normalized loading *P-h* curve obtained on the T40 grade 2 CPT reference sample stay in the middle of the curve obtained with the ideal tip and that obtained with the calibrated tip, as shown in Fig. 3-27, which will be discussed in detail in the later section. The simplest way for making tip shape optimization is controlling the tip shape with a function, as same as building the calibrated tip with the calibrated tip area function. However, from Fig. 3-27 we can see that the difference between experimental result and simulated results is not uniform on the whole curve. Thus, we can imagine that the tip shape, which covers the middle part of loading curve, might change much more than the tip shape in the others parts during the optimization process. Controlling tip shape with a single function might be impossible to handle this kind of non-uniform variation of tip shape. In fact, since the tip in the FEM model is represented by a 2D axisymmetric analytical rigid body, it is discretized into a series of coordinate points in X-Y space in job file (*.inp) of ABAQUS®. Thus, every single point on the tip can be optimized individually. In present study, the tip is discretized into 36 points, except the start point which is superposed with the ideal tip. The X coordinates of these 36 points will be respectively set as the input variables for the optimization process, as shown in Fig. 3-25.

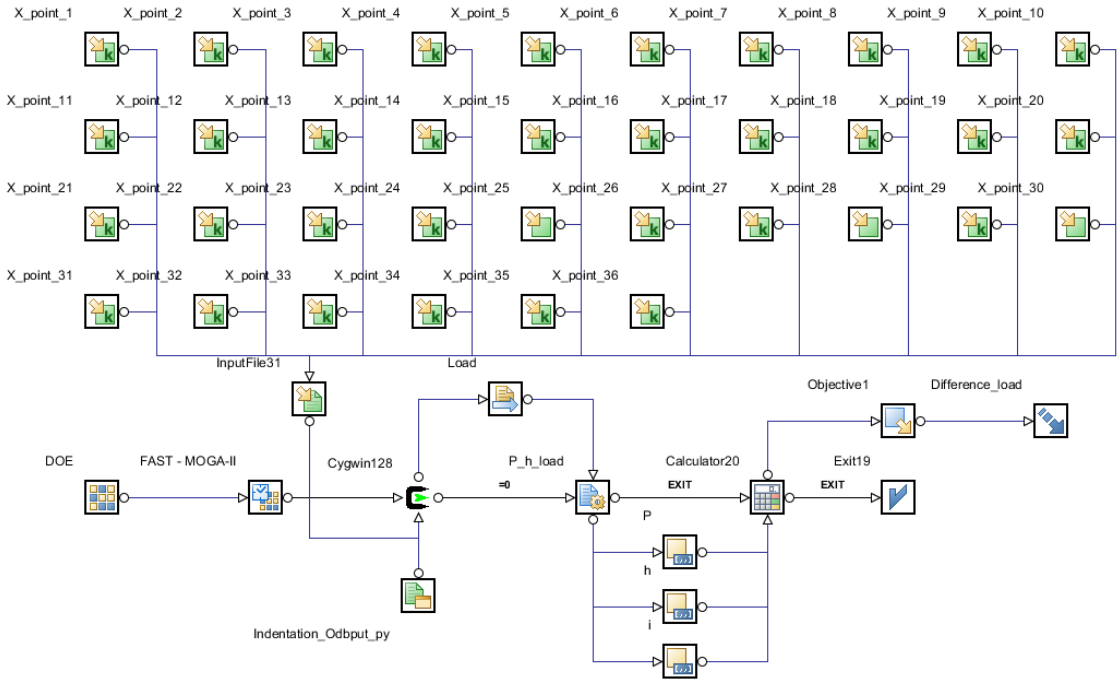


**Fig. 3-25. Workflow of the tip-shape optimization procedure.**

One thing need to be explained is about the boundaries of the input variables. Considering the big difference between the ideal tip and the calibrated tip, if these two tips are directly set as the up and the low boundary, localized sever change of the tip shape may occur when optimizing with the FMOGA II algorithm, as sketched in Fig. 3-26(a). This may directly lead to misconvergence of the FEM simulations. In order to avoid this problem, multi-step optimization will be conducted. The gap between the ideal tip and the calibrated tip will be uniformly divided into 10 parts, as shown in Fig. 3-26(b). In step 1, the right and left boundary of the rightmost part will be set as the up and the low boundary of the input variables. In step 2, the gap between the ideal tip and the firstly optimized tip will be divided into 10 parts as well, and the rightmost part will also be set as the boundaries. The following steps can be done in the same way, until the tip shape variation localizes in the middle part after a few steps. Then, the localized tip shape optimization steps will be performed by setting the localized input variable boundaries. This is because that we can image the points near the apex and the bottom should reach the best solution earlier than the points in the middle of tip.

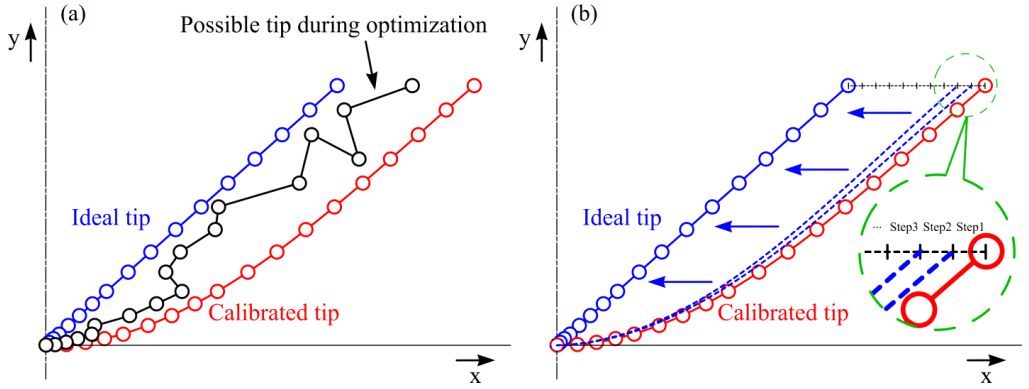

**Fig. 3-26. The strategy of setting limits of input variables: (a) if ideal tip and calibrated tip are respectively set as the low and up limits of the input variables, sever tip distortion, which can directly cause the failure of the FEM simulation, may occur during optimization process, because the range between the two limits is too large; (b) a step-by-step optimization strategy can effectively avoid the former problem by dividing the whole range into 10 equal divisions.**

As a rule of thumb, the initial DOE size is recommended to be 16 at least for using MOGA II algorithm. Considering the number of our input variables, 36 DOE designs were set. For most engineering problems, at least 10 generations are needed to get good evolution [156]. Thus, the total design number for an overall tip-shape optimization step will be 360. Design number in a localized tip-optimization step will depend on how many points will remain as the input variables.

### 3.7.2.1 Determining the objective of indenter shape optimization

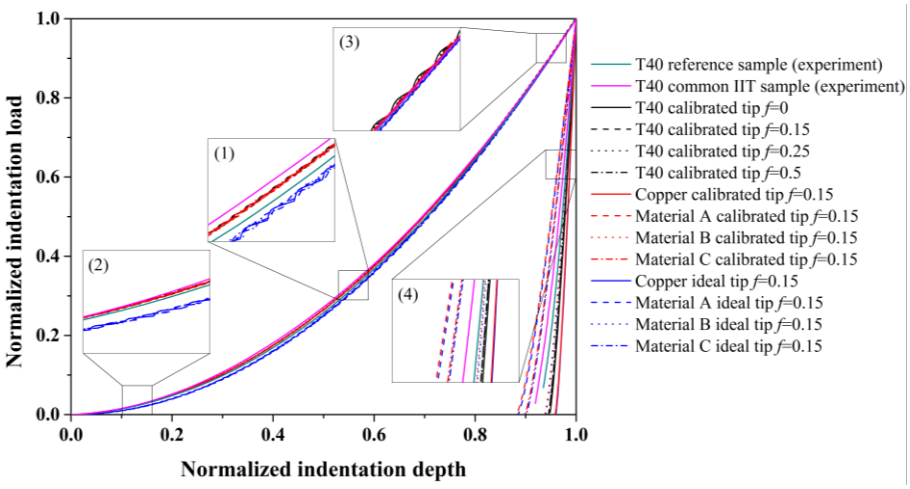


**Fig. 3-27. Normalized *P-h* curves obtained from experiments and simulations.**

The normalized *P-h* curves obtained from all the cases listed in Table 3-4 were plotted in Fig. 3-27. From zoom-in (1) it can be seen that all the normalized loading *P-h* curves are clearly divided into four groups. The loading curves obtained from the simulations have confirmed our former occasional discovery that shape of the normalized loading *P-h* curve only depends on the geometric shape of the indenter. It is quite insensitive to other factors, such as material properties and friction coefficient. Because for all the five materials and the four friction coefficient values which are quite different from each other, exactly the same normalized loading *P-h* curve can be obtained. Thus, the shape of the normalized loading *P-h* can be used as the index for optimizing the shape of the indenter.

Zoom-in (2) and (3) in Fig. 3-27 showed that near the beginning and the end of the loading curve, experimental curves are quite close to the simulated curves obtained with the calibrated tip, which indicated that during the optimization process, tip profile near the apex and the bottom may reach the best tip shape earlier than the tip profile in the middle. Considering this kind of phenomenon, localized tip optimization is quite possibly need to be done after a few steps of overall tip shape optimization. This has been proved by our optimization results which will be shown later.

One interesting thing is the difference between the two normalized loading *P-h* curves acquired from experiments. Based on the conclusion got from the simulations, these two curves should be completely superposed, because the same Berkovich tip was used on the two samples. However, experimental results did not follow our conclusion of simulations. Were we wrong with the simulation results? The answer is negative. In fact, the sticking point comes from two aspects: the difference between Berkovich indenter and the equivalent conical indenter, and the difference between material model and the real material property. In simulations, axisymmetric tips and isotropic hardening material model were used. Thus, during the whole loading process, the contact area is always a conic section (projected contact area is a circle). Furthermore, the variation of contact area during loading process is nearly the same, as shown in Fig. 3-28(a), once the maximum indentation depth is controlled. However, for experiments, the feature of Berkovich tip makes the indentation responses around the three edges quite different from those around the three flat surfaces. Consequently, pile-up/sinking-in phenomenon will vary between the edge and the flat surfaces as well. Moreover, anisotropic material properties, misorientation of the neighbor grains, and some other material-correlated factors exist in experiments. Thus, along with the increase of penetration depth, pile-up/sinking-in phenomenon will evolve as well. For instance, as sketched in Fig. 3-28(b), when indentation depth becomes larger, pile-up phenomenon will become much more severe as well. Last but not least, different preparation procedures of the two samples makes their surface properties become quite different, although they come from the same piece of T40 grade 2 CPT. Our former research showed that even very carefully performed mechanical polishing process can still induced severe plastic deformation in the surface region ($\leq 5\ \mu$m) of the IIT sample. However, this will not happen to the electrolytic polishing process which may even etch the grain boundaries and the inclusions on the sample surface. Different surface material properties of the two samples make the pile-up/sinking-in phenomenon evolve in different ways. All these may directly cause the difference between the two experiment curves shown in Fig. 3-27.

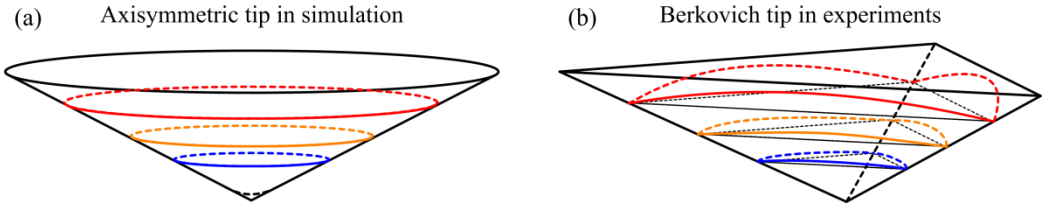


**Fig. 3-28. Normalized *P-h* curves obtained from experiments and simulations: (a) conical tip; (b) Berkovich tip.**

Analysis above indicated that only IIT simulations with axisymmetric indenter and isotropic material will show the tip-shape dependence of the shape of the normalized loading *P-h* curve. IIT experiments with Berkovich indenter showed that this kind of dependence does not exist with polycrystalline grade 2 CPT. However, this does not conflict with our tip-shape optimization, the aim of which is to make the simulations results getting close to the experimental data.

Zoom-in (4) in Fig. 3-26 showed another interesting thing that indenter shape and friction coefficient have negligible influence on the normalized unloading *P-h* curve. However, the effect of material properties is much more significant. This indicates that when we try to optimize material properties, considering contact stiffness *S* and the shape of the normalized unloading *P-h* curve might be necessary and meaningful.

### 3.7.2.2 Optimizing indenter shape

The whole process of tip shape optimization contents three steps (two overall tip-shape optimization steps and one localized tip-shape optimization step) following the strategy being explained above. Setting of the input variables and their corresponding boundaries were listed in Table 3-5.

**Table 3-5 Input variable limits and the corresponding optimized ranges of each step.**

| | Up boundary | Low boundary | Input variables |
|---|---|---|---|
| Step 1 | Calibrated tip | Calibrated tip–(Calibrated tip-ideal tip)*0.1 | X_point_1 ~ X_point_36 |
| Step 2 | No.360 tip | No.360tip–(No.360 tip-ideal tip)*0.1 | X_point_1 ~ X_point_36 |
| | | No.714 tip | X_point_1 ~ X_point_19 |
| | | No.714tip–(No.714 tip-ideal tip)*0.05 | X_point_20 ~ X_point_21 |
| Step 3 | No.714 tip | No.714tip–(No.714 tip-ideal tip)*0.1 | X_point_22 ~ X_point_27 |
| | | No.714tip–(No.714 tip-ideal tip)*0.05 | X_point_28 ~ X_point_30 |
| | | No.714 tip | X_point_31 ~ X_point_36 |

The history chart of the tip shape optimization objective *g*(*P*) is shown in Fig. 3-29. We can see that the objective keep decreasing along with the optimization process. There are some severe fluctuations at the beginning part of the overall tip-shape optimization step 1 and step2 because of the random choice of DOE members in the limit range. After the whole optimization process (3 steps and 830 designs), the best solution was obtained as design No.810.

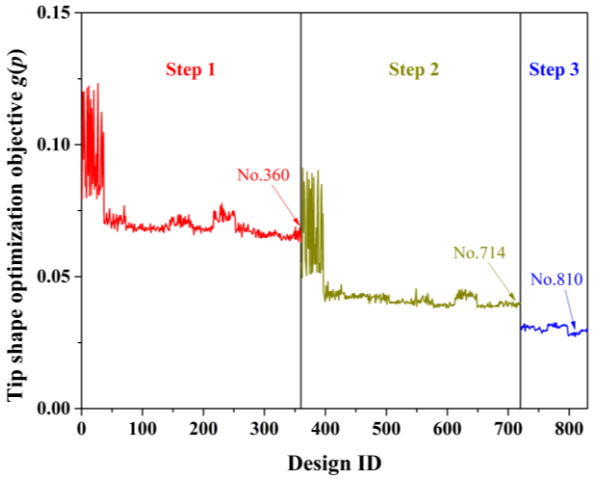


**Fig. 3-29. History chart of tip shape optimization objective *g*(*P*).**

Normalized *P-h* curves obtained from the best solution of each tip-shape optimization step are listed in Fig. 3-30. Since the points near the apex and the bottom of the indenter converged earlier without many variations, all the curves in zoom-in (2) and (3) are completely mixed together. However, zoom-in (1) showed that during the step-by-step optimization process, the

simulated curve was getting closer and closer to the experimental curve, until they are completely superposed. As the same as we observed before, the variation of tip shape nearly has no influence on the shape of the normalized unloading *P-h* curves.

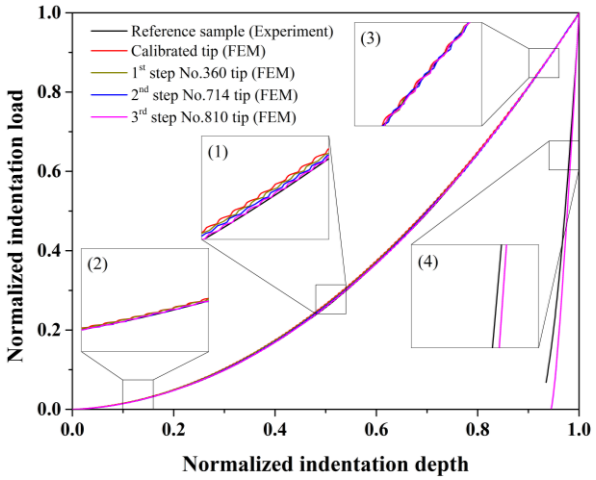


**Fig. 3-30. History chart of tip shape optimization objective *g*(*p*).**

Tip shapes for the best solution of each step are listed in Fig. 3-31. Zoom-in (2) and (3) showed that there is no big variation of the shape near the apex and the bottom of the tip, which confirmed the results shown in Fig. 3-30. Zoom-in (1) showed that during the optimization process, X coordinate of the points in the middle part of the tip profile shrunk towards the ideal tip. The maximum shrinkage, nearly 30% of the range between the ideal tip and the calibrated tip, can be reached for design No.810. Considering the possible experimental error of the tip calibration process, the optimized tip shape is considered to be reasonable.

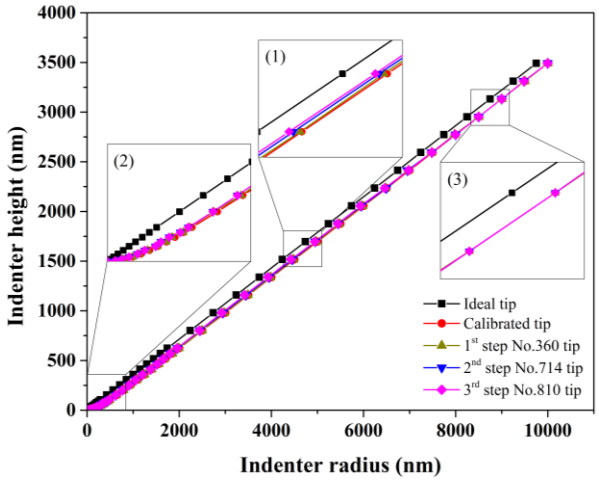


**Fig. 3-31. History chart of tip shape optimization objective *g*(*p*).**

### 3.7.3 Material parameters and friction coefficient optimization

Once the tip shape optimization is finished, other parameters will be optimized. Parameters correlated with the elastic properties of material are the Young's modulus *E* and the Poisson's ratio *v*. As for the plastic properties of material described by Ludwick model, there are three

key parameters: yield strength $\sigma_y$, hardening coefficient $K$ and hardening exponent $n$. As for the friction behavior between the indenter and the material in our FEM model, only tangent friction coefficient $f$ was considered. All of these six parameters will be taken into account as initial input variables for the second optimization process. The difference of maximum load ($\Delta P_{max}$), the difference of contact stiffness ($\Delta S$) and the difference of contact hardness ($\Delta H$) between the simulated values and the experimental values will be set as the initial objectives. Furthermore, as discussed above, the effect of material properties can significantly affect the shape of the unloading. This indicates that when we try to optimize material properties, considering contact stiffness $S$ and the shape of the normalized unloading $P$-$h$ curve should be necessary and meaningful. Thus, the square distance between the simulated and the experimental normalized unloading $P$-$h$ curves ($\Delta f(P)$) will be set as the fourth initial objective. The significations of all the four objectives are shown in Table 3-6. Constrains were set on the experimental $P_{max}$, $S$ and $H$ values with an up limit and a low limit which are equal to 105% and 95% of the average experimental values respectively.

**Table 3-6 Significations of all the initial objectives.**

| Objective | Signification |
|---|---|
| Objective 1 | $\Delta f(P)$ |
| Objective 2 | $\Delta P_{max}$ |
| Objective 3 | $\Delta S$ |
| Objective 4 | $\Delta H$ |

The necessity and feasibility of the initial input variables and the objectives will be checked through a preliminary selection process. An initial range which can cover all the possible input variable values was firstly chosen, as shown in Table 3-7. Uniform Latin Hypercube method [157] will be used for constructing an initial DOE contenting 100 groups of input variables. Uniform Latin Hypercube algorithm allows a regular equally-spaced sample distribution throughout the whole possible range to attain the most information in the range with minimum number of design evaluations.

**Table 3-7 Possible ranges of the input variables.**

| Input variable | Possible range |
|---|---|
| Young's modulus $E$ (GPa) | 90 - 150 |
| Poisson ratio $\nu$ | 0.3 – 0.5 |
| Yield stress $\sigma_y$ (MPa) | 200 - 400 |
| Hardening coefficient $K$ (MPa) | 200 - 500 |
| Hardening exponent $n$ | 0.1 – 0.6 |
| Friction coefficient $f$ | 0.0 – 0.5 |

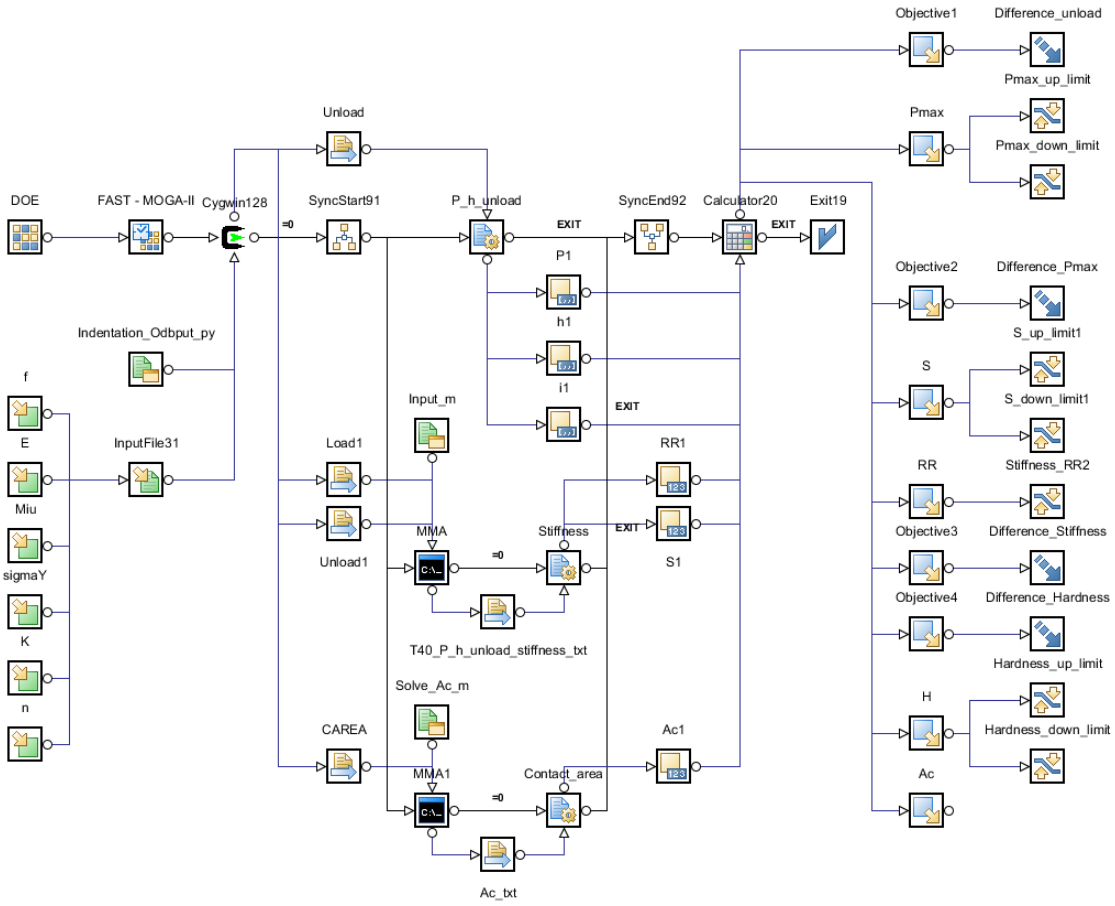


**Fig. 3-32. Workflow of the material properties and friction coefficient optimization procedure.**

The inverse investigation of the material properties and friction coefficient is much more complex than the former optimization process of indenter shape, as shown in Fig. 3-32. All the six input parameters, as illustrated above, are directly defined in the input file (*.inp) of ABAQUS®. However, they are linked with some dedicated data nodes to specify their boundaries. The input file will be sent to ABAQUS® for simulation. A Python script (*.py) was written for extracting reaction force (RF2), vertical displacement (U2) and total contact nodal area (CAREA) data from the result files of the simulations (*.odb and *.dat) as the indentation load ($P$), the penetration depth ($h$) and the contact area ($A$) respectively. Since large numbers of simulations need to be done to achieve the optimized solution, a Unix server with 24 CPUs and 120 GB RAM was used. A Cygwin code was set up for exchanging data between local PC and the server. DOE and the optimization algorithm were set in the scheduler node connected with the Cygwin node. Three result files (*.txt), which contain the loading $P$-$h$ curve, the unloading $P$-$h$ curve and the contact area data respectively, will be transported to the local PC once a simulation was finished on the server. The $P_{max}$ and $S$ will be extracted from the unloading curve. As for the contact area data, it needs to be converted into the projected contact area ($A_c$). Two Mathematica® scripts were written for fulfilling these two tasks. All the extracted data will be sent to a calculator code for calculating $H$ value and constructing all the

objectives discussed above. Constraints were set on $P_{max}$, $S$ and $H$ respectively for selecting feasible designs. In order to reach the optimal solution, all the objectives need to be minimized as much as possible.

### 3.7.3.1 Preliminary selection of the input variables and the objectives

After the best tip shape had been determined, optimization of material properties and friction coefficient was conducted. In order to determine a proper design space for the input variables, the preliminary selection process was carried out. The Pearson Correlation Coefficient (PCC) of each input variable group, shown in the Scatter Matrix chart was used to evaluate the performance of the Uniform Latin Hypercube DOE algorithm. The range of the PCC varies from -1(inverse linear relationship) to +1 (direct linear relationship) which represents the linear dependency among the variable in each group [158]. For our DOE, the PCC for each group of input variables was almost zero, as shown in Fig. 3-33(a), which indicated that the input variables in the 100 groups were uniformly distributed throughout the whole possible ranges.

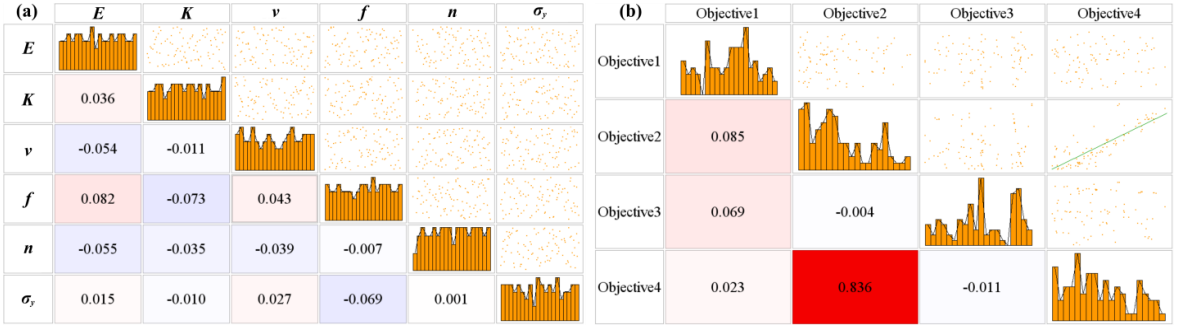


**Fig. 3-33. Scatter Matrix charts of the Uniform Latin Hypercube DOE: (a) Scatter Matrix chart of all the input variable groups; (b) Scatter Matrix chart of all the objective groups, in which objective 1 is $\Delta f(P)$, objective 2 is $\Delta P_{max}$, objective 3 is $\Delta S$ and objective 4 is $\Delta H$.**

Similarly, Scatter Matrix chart for all the objectives can be plot as well for reducing objectives number. Highly correlated two objectives (the PCC is close to 1 or -1) can be reduced as one. From Fig. 3-33(b) we could see that for most of the groups, their PCC is close to 0, except the group of objective 2 (difference of $P_{max}$) and objective 4 (difference of $H$), for which the PCC is 0.836. This indicated that these two objectives are highly linearly correlated. Therefore, one of them can be neglected for reducing the complexity of the optimization without loss of quality of results. Since $H$ is calculated from $P_{max}$, thus, objective 4 was eliminated.

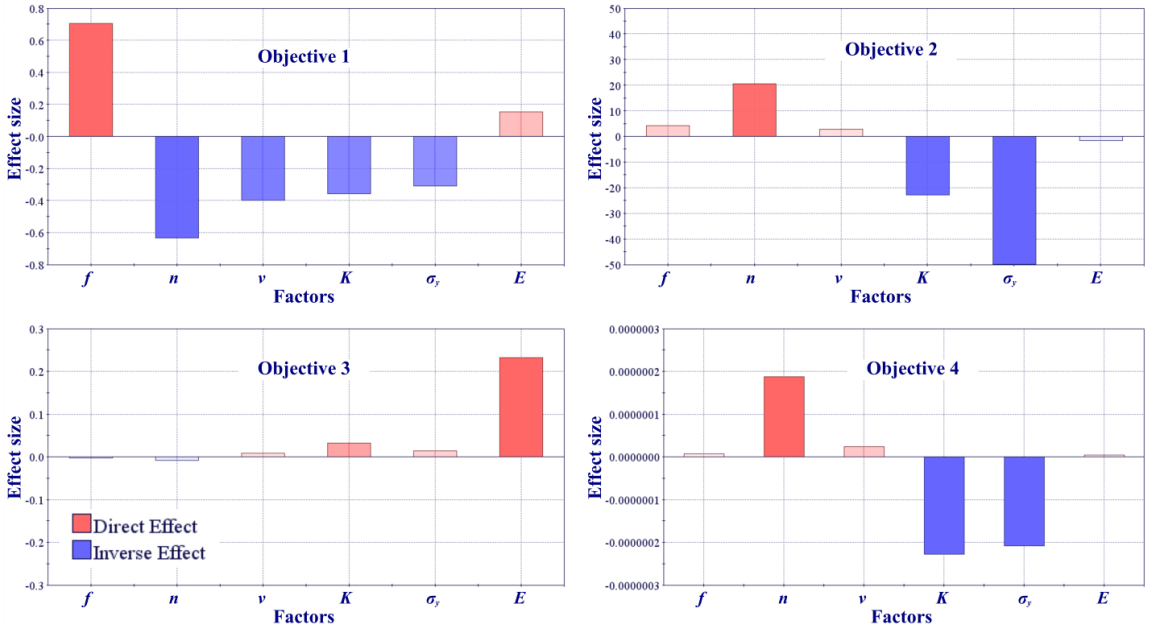


**Fig. 3-34. T-student charts for all the objectives, in which objective 1 is $\Delta f(P)$, objective 2 is $\Delta P_{max}$, objective 3 is $\Delta S$ and objective 4 is $\Delta H$.**

After the determination of objectives, sensitivity analysis was conducted with t-student charts [159], as shown in Fig. 3-34, for analyzing the effects of input variables on outputs. We could see that all the six input variables have significant effects on objective 1 (difference of the shape of the unloading curve). However, only Young's modulus ($E$) has strong influence on objective 3 (difference of $S$). As for objective 2 and objective 4, their t-student charts are quite similar that the impacts of friction coefficient ($f$), Poisson's ratio ($\upsilon$) and Young's modulus ($E$) are negligible, which confirmed the result above that objective 4 can be neglected. Considering objective 1, 2 and 3, all of the six input variables are necessary for the optimization process.

### 3.7.3.2 Optimization on the optimal cluster with FMOGA II algorithm.

When input variables and objectives were confirmed, optimization of material properties and friction coefficient was conducted. A new DOE contents 16 random designs was used as the beginning design set and the FMOGA II were evolved for 10 generations. Since several constrains have been set on the outputs, all the designs were mainly divided into two groups (the feasible designs in the constraint ranges and the unfeasible designs out of the ranges). Several tools and methods, such as Self Organizing Maps (SOM) method [160], Parallel Coordinate chart analysis [161], Clustering chart analysis [162] and so on, were integrated in modeFRONTIER for analyzing the feasible designs. The Pareto Frontier set analysis was conducted here, which can give a set of optimized solutions called as the Pareto Frontier designs [163, 164]. Pareto Frontier means there are no solutions with better values for all the objectives. This is explained in detail in the literature [165]. All the designs listed in the space of the three objectives are shown in Fig. 3-35.

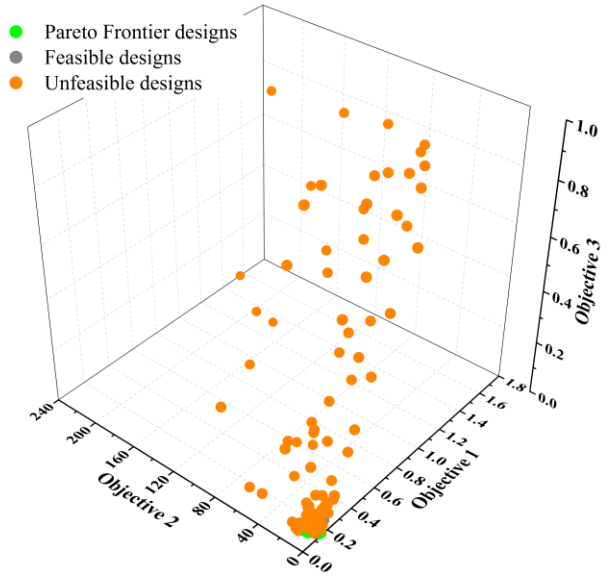


**Fig. 3-35. 3D Scatter chart of all the designs.**

The History charts of all the three objectives were listed in Fig. 3-36. Since the aim of the present work is to minimize the differences between experimental IIT responses and simulated ones, objectives are expected to decrease all with the process of optimization. From Fig. 3-36 we can see that all the three objectives decrease obviously after about three or four generations.

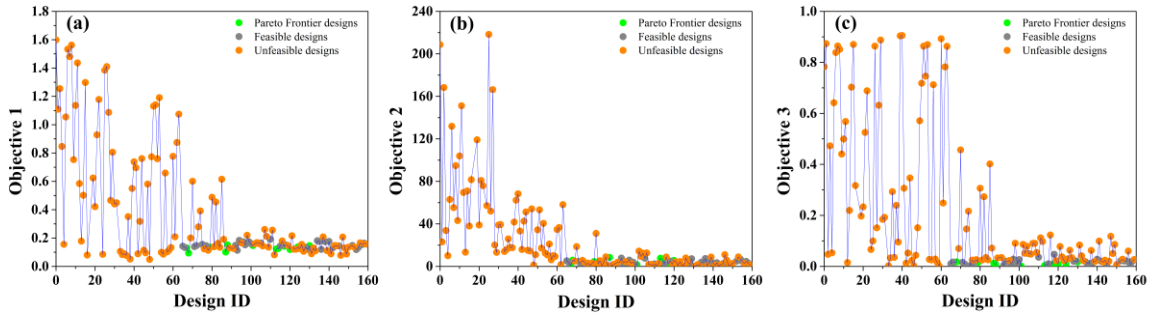


**Fig. 3-36. History charts of all the three objectives: (a) objective 1; (b) objective 2; (c) objective 3.**

The Pareto frontier designs can be considered as a set of optimized solutions performing differently on different objectives. However, for this study, only one “best solution” is needed. How to rank the Pareto frontier designs and find out the best solution is a delicate issue. In order to facilitate the choice of a good compromise between objectives from the Pareto frontier, a Multi-Criteria Decision Making (MCDM) [166] technique was used. There are four kinds of MCDM algorithms packaged in modeFRONTIER. In present study, GA-MCDM was used. Since it was hard to define the weights of the utility function precisely, this algorithm can provide a full ranking without specifying the function parameters, indicating the importance of one criterion with respect to others [167]. Various weight configurations of the three objectives were tried, however, all of them gave the same best solution (design No.113) with the highest ranking. The ranking bar chart of the equal weight configuration (0.33 for each objective) is shown in Fig. 3-37.

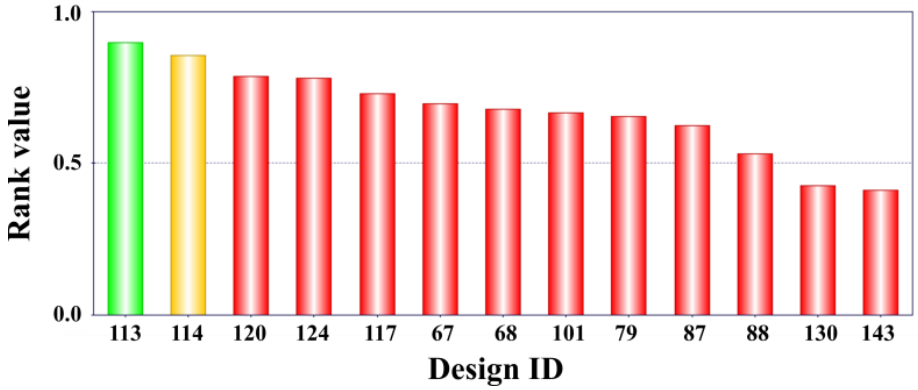


**Fig. 3-37. Scatter chart of all the designs.**

The main IIT responses for different cases were listed in Fig. 3-38 and Table 3-8 for making comparison. Fig. 3-38 showed that with the initial parameters, simulated *P-h* curves with both the ideal tip and the calibrated tip are much lower than the experimental curve. Large differences also exist in $P_{max}$, $S$ and $H$, as shown in Table 3-8. We can see that the tip calibration procedure has improved the quality of the IIT responses a bit, however, far from enough. This big difference is also the original reason for the optimization work in the present study. As for the best design No.113 obtained from the optimization process, the quality of all the IIT responses has been greatly improved, which clearly showed the efficiency of the optimization process.

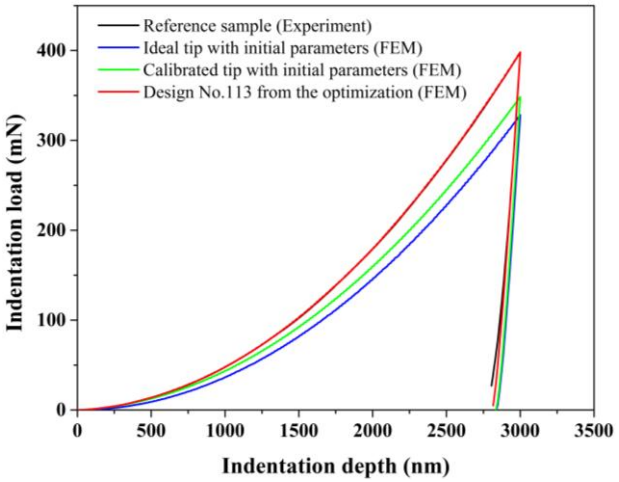


**Fig. 3-38. *P-h* curves obtained from IIT experiment and the FEM simulations.**

**Table 3-8 IIT responses from experiment and the FEM simulations.**

| Indentation response | Reference sample (Experimental) | Ideal tip with initial parameters (FEM) | Calibrated tip with initial parameters (FEM) | Design No.113 from the optimization (FEM) |
|---|---|---|---|---|
| Maximum indentation load $P_{max}$ (MPa) | 398.0 ±20.3 | 328.2 | 348.4 | 398.2 |
| Contact stiffness $S$ (mN/nm) | 2.542 ±0.036 | 2.710 | 2.608 | 2.541 |
| Contact hardness $H$ (GPa) | 1.67 ±0.13 | 1.37 | 1.38 | 1.63 |

The rationality of the optimized tip shape was discussed above. Whether the optimized material properties and the friction coefficient are reasonable or not will be discussed

subsequently. Comparison between the experimental and the optimized parameters were listed in Fig 3-39 and Table 3-9. The original value of the friction coefficient f was obtained from the literature, because there is no effective experiment to characterize the friction behavior between the indenter tip and the target material. Considering the complexity and the possible variation range of the friction between diamond and metal, the optimal value should be acceptable. The original values of Young's modulus *E* was obtained from uniaxial tensile test, and the original Poisson's ratio *v* was estimated from the possible range in literature [168, 169]. Seeing the uncertainty of uniaxial tensile test and the Poisson's ratio range of grade 2 CPT in literature, the two optimal values are reasonable as well.

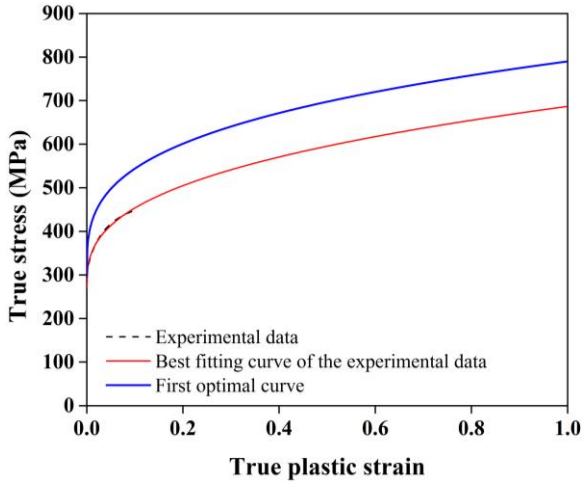


**Fig. 3-39. Uniaxial tensile true stress vs true plastic strain curve, the corresponding best-fitting curve and the optimal curve.**

**Table 3-9 Comparison between the experimental parameters and the optimal parameters.**

| Material parameters | Original values | Optimal values |
|---|---|---|
| Young's modulus *E* (GPa) | 119.0 | 119.5 |
| Poisson's ratio *v* | 0.34 | 0.36 |
| Yield stress $\sigma_y$ (MPa) | 279.6 | 295.2 |
| Hardening coefficient *K* (MPa) | 415.4 | 494.8 |
| Hardening exponent *n* | 0.38 | 0.30 |
| Friction coefficient *f* | 0.15 | 0.36 |

### 3.7.4 Checking the rationality of the optimal parameters

The biggest difference came from the plastic properties. From Fig. 3-39 we could see, the optimized curve has an upshift about 100 MPa (about 20%) as compared with the original curve. Uniaxial tensile test stress-strain curve has been broadly used in various simulations for describing the constitutive behavior of metallic materials not only because it is simple and convenient but also because of its quite good efficiency and feasibility. The difference between the original material parameters (obtained from the best fitting curve of the uniaxial tensile data) and our optimized parameters is significant. So, further discussion is necessary to find out the possible sources of this kind difference and to explain if it is reasonable.

### 3.7.4.1 The influence of friction coefficient *f*

The first possible source is friction coefficient *f*. In order to clarify the influence of *f* on the IIT responses of T40 grade 2 CPT, indentation simulations with both the original and the optimal parameters and two different *f* values (0.15 and 0.36) were performed. And all the IIT reponses are shown in Fig. 3-40 and Table 3-10. From Fig. 3-40 we could see that, for both the two groups of material parameters, the corresponding *P-h* curves obtained with different *f* values are almost totally superposed. Data listed in Table 3-10 showed similar results that the differences of all the IIT responses are less than 1%. This is far from in charge of the big difference shown in Fig. 3-39.

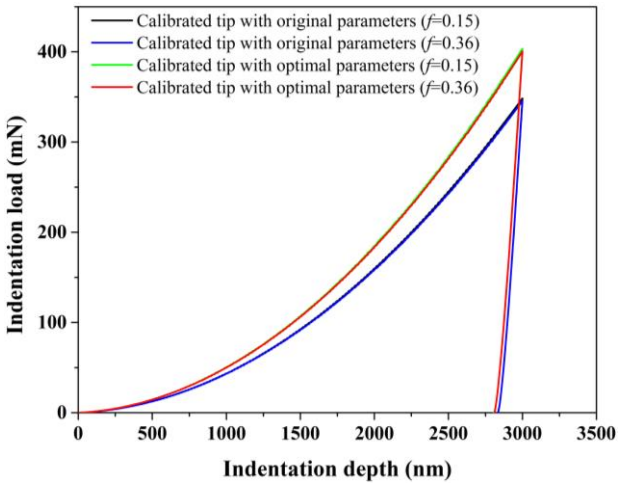


**Fig. 3-40. *P-h* curves of simulations on both the original and the optimal material parameters with different *f* values.**

**Table 3-10 IIT responses of simulations with both the original and the optimal material parameters and different *f* values.**

| Indentation response | *f*=0.15 (original parameters) | *f*=0.36 (original parameters) | Difference | *f*=0.15 (optimal parameters) | *f*=0.36 (optimal parameters) | Difference |
|---|---|---|---|---|---|---|
| $P_{max}$ (MPa) | 348.4 | 345.6 | 0.8% | 403.4 | 400.5 | 0.7% |
| *S* (mN/nm) | 2.606 | 2.614 | 0.3% | 2.583 | 2.591 | 0.3% |
| *H* (GPa) | 1.38 | 1.39 | 0.7% | 1.63 | 1.64 | 0.6% |

### 3.7.4.2 The influence of tip geometric shape

The second possible source should be the difference between the 3D Berkovich indenter used in the experiment and the 2D axisymmetric equivalent conical indenter used in the simulations. A conical indenter with a 70.3° apex angle is called the equivalent conical tip of the Berkovich indenter because both of them are self-similar, and theoretically, they can get the same the projected contact area at the same depth. However, indentation response is not only a matter of projected area but also depends on the actual local plastic flow under the indenter. Since the geometric difference between the Berkovich tip and its equivalent conical tip, their indentation responses will vary accordingly.

Several investigations have been conducted to study the difference between these two types of tip [118, 123, 170-172]. Some people used perfect Berkovich tip and its equivalent conical

tip to do FEM simulation and showed that both of them fit well the experimental result [123, 170]. However, their results are questionable. First, the constitutive behaviors invested in these studies are quite limited, which is not enough to realize a comprehensive comparison between the two tips. Otherwise, shapes of *P-h* curves are normally the only factor which was used by them to make comparison between experimental and simulated results. This is quite unilateral as well. As shown in our former researches, even if the shapes of *P-h* curves are nearly the same, the differences of other indentation responses, such as contact stiffness, contact hardness, pile-up/sinking-in values, etc., still might be significant. By comparing these two tips through FEM simulations and experiments, Moore *et al.* [172] noticed that the maximum equivalent plastic strain value induced by the indenter is demonstrated to be 20% lower for an equivalent conical indenter than for a Berkovich indenter. This leads that lower localized plastic strains would result in higher resistance to indentation by the material. Their results reveal that the use of a 70.3° conical indenter to approximate a Berkovich indenter is not valid for all materials. However, Moore *et al.* [172] only mentioned this in their conclusion but didn't make any further study.

Systematic investigation between these two types of tips with a wide range of material properties was conducted by Sakharova *et al.* [171] and Swaddiwuhipong *et al.* [118]. Sakharova *et al.* [171] not only compared the *P-h* curves, buy they also established the correlation between $h_f/h_{max}$ ($h_f$ is the final depth after unloading) and normalized indentation responses (such as $H_{Conical}/H_{Berkovich}$) and the geometric correction factor $\beta$. However, there is a main shortcoming of the study of Sakharova *et al.* [171]: they did not directly build the relationship between material properties and indentation responses. Even if they mentioned that the values of $h_f/h_{max}$ are different along with the variation of material properties. Swaddiwuhipong *et al.* [118] made a big progress. Through a larger number of simulations, they constructed the relationship between material properties (hardening exponent $n$ and ratio of effective Young's modulus and yield stress $E^*/\sigma_y$) and indentation response ($C_{Berkovich}/C_{Conical}$ where $C$ is the constant curvature in Kick's law: $P=Ch^2$), as shown in Fig. 3-41.

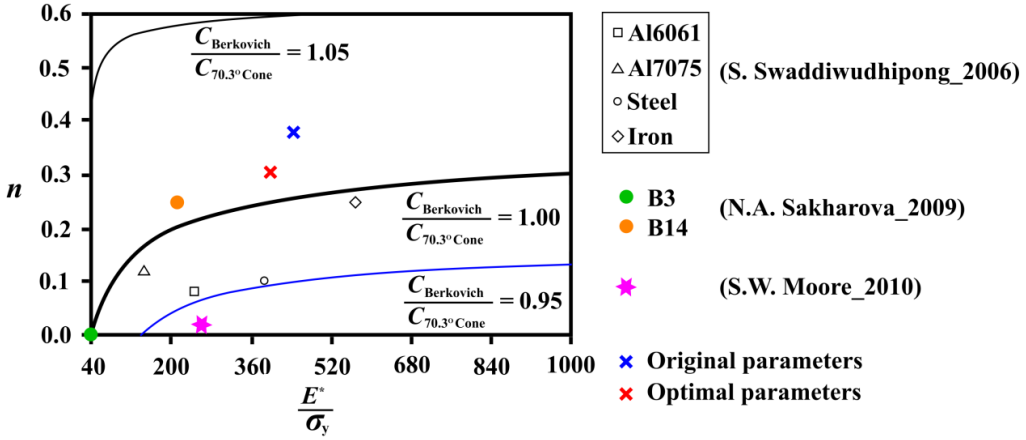


**Fig. 3-41. The isolines of $C_{Berkovich}/C_{Conical}$ with different combinations of $n$ and $E^*/\sigma_y$ constructed by Swaddiwuhipong *et al.* [118]. Results obtained from other studies and our own study can be localized on these isolines as well.**

Since few researches have focused on the difference between the two indenters from contact hardness, contact stiffness and even the shape of normalized *P-h* curve, a 3D FEM model, with a Berkovich indenter, was built for making comparison with 2D axisymmetric FEM model. The calibrated tip shape is also considered here, which means that the triangular pyramid was built according to $A_c=24.3514h_c^2$ and the same tip roundness as the 2D calibrated indenter was corrected near the summit.

The mesh of the 3D FEM model is shown in Fig. 3-42. This model was built according to the same principles as the original 2D model (such as size of the model, boundary conditions, displacement-controlled load, etc.), but in 3D space. Considering the accuracy and the convergence of the model, elements near the tip summit and the center part of the target material were particularly refined. 100549 eight-node linear brick, reduced integration with hourglass control, hybrid with constant pressure elements (C3D8RH) were used in the target material and the Berkovich indenter was represented by a discrete rigid body.

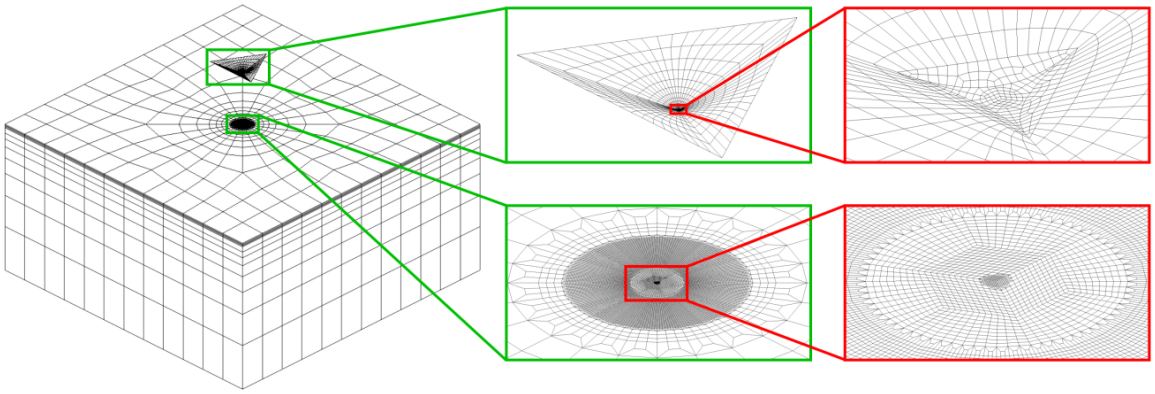

**Fig. 3-42. 3D FEM model with the Berkovich indenter.**

Simulations with both the original and the optimal parameters were conducted on both the two FEM models. All the corresponding IIT responses were then extracted and shown in Fig. 3-43 and Table 3-11. Fig. 25 showed that for both the two groups of parameters, *P-h* curve obtained from the 3D FEM model shifted downwards a little bit compared with that obtained from the 2D axisymmetric FEM model. According to the Kick's law, this directly caused the $C_{Berkovich}/C_{Conical}$ values in Table 3-11 become smaller than one. This is different from the results derived by Swaddiwuhipong *et al*. [118]. However, since the research of Swaddiwuhipong *et al*. [118] concerns with power-law constitutive material model, but not Ludwick model, this kind of difference is not surprising.

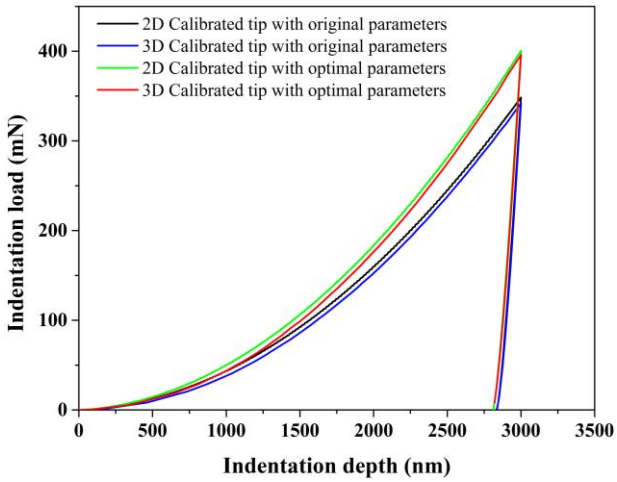


**Fig. 3-43. *P-h* curves obtained from simulations with different FEM models with various parameters.**

**Table 3-11 Results of the instrumented indentation tests and the simulation with optimal parameters.**

| Indentation response | 2D calibrated tip with original parameters | 3D calibrated tip with original parameters | Difference | 2D calibrated tip with optimal parameters | 3D calibrated tip with optimal parameters | Difference |
|---|---|---|---|---|---|---|
| $P_{max}$ (MPa) | 348.4 | 341.9 | 1.9% | 400.5 | 396.0 | 1.1% |
| $S$ (mN/nm) | 2.606 | 2.655 | 1.9% | 2.591 | 2.644 | 2.0% |
| $H$ (GPa) | 1.38 | 1.37 | 0.7% | 1.64 | 1.66 | 1.2% |
| $C_{Berkovich}/C_{Conical}$ | 0.99325 | | - | 0.99410 | | - |

The differences of all the IIT responses listed in Table 3-11 show that the discrepancy between the 3D Berkcovich indenter and the 2D equivalent conical indenter is quite limited (≤ 2%). This can only explain a little part of the big gap between the original and the optimal plastic parameters, which is not sufficient.

### 3.7.4.3 The influence of the plastic deformation mechanisms of titanium alloys

For metals with cubic crystal structure, the basic plastic deformation mechanism is slip. Because slip is independent of the sign of the shear stress, they can operate both forward and backward and the tensile compressive yield stresses are equal. So, the yield functions are symmetric about the origin in the stress space. As for metals with hexagonal close packed (hcp) crystal structure such as T40, plastic deformation can occur through both slip and twinning. As opposed to slip, twinning is an asymmetric shear mechanism: shear in one direction can cause twinning, but shear in the opposite direction cannot [173]. This directly leads to the fact that hcp crystal has different strength upon load inversion, which is normally called strength differential (SD) effects.

The cold rolled hcp metal sheets exhibit strong basal textures (*c*-axis oriented predominantly perpendicular to the thickness direction or the radial direction), a pronounced anisotropy in yielding is observed in pure $\alpha$-phase titanium [173]. It is generally agreed that pronounced yield anisotropy is associated with the activation of twinning [174]. Twinning plays two important roles in $\alpha$-phase titanium. On one hand, this plastic deformation mechanism is a main contributor to texture evolution by reorienting the twinned areas [174,

175], even for the simplest monotonic loading path. On the other hand, twinning drastically influence the strain-hardening behavior [174, 176].

The comprehensive effects caused by twinning (together with slip) is that both SD effects and the anisotropy will occur during the plastic deformation process of $\alpha$-phase titanium [173, 177]. In order to develop accurate and realistic model to describe these behavior of $\alpha$-phase titanium, several studies have been made by different researchers [174, 178-181]. Among these studies, the work of Nixon *et al.* [174] can be distinguished. By doing quasi-static uniaxial tensile and compressive tests on a cross-rolled high purity polycrystalline $\alpha$ titanium disk, the SD effects and the anisotropy were investigated in detail in all the three typical directions of the material. Comparisons between the compression and tension responses in all the three directions are respectively shown in Fig. 3-44.

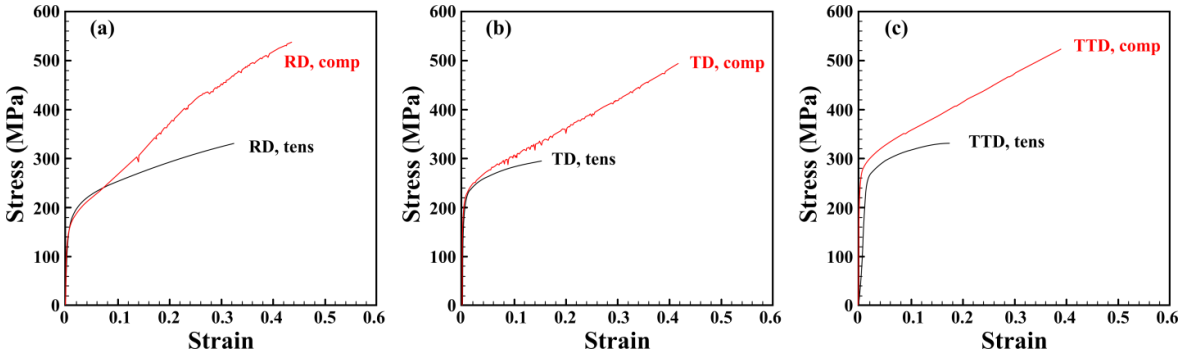


**Fig. 3-44. Comparisons between the compression and tension responses in all the three directions: (a) rolling direction (RD); (b) transverse direction (TD); (c) through-thickness direction (TT) [174].**

Fig. 3-44(a) showed the comparison between tensile and compressive stress-strain curve along rolling direction. We can see that although initially there is no significant difference in yielding behavior, a very pronounced tension-compression asymmetry is observed after 10% strain. The hardening evolutions are quite different. As for tension, the material hardened gradually until the onset of necking at about 30% strain. However, in compression, strongly non-linear work hardening with a very high hardening rate occurs. Comparison in transverse direction is shown in Fig. 3-44(b). The highly nonlinear work hardening behavior shown in the rolling direction does not exist. The hardening rate in both tension and compression seems to be constants, which may be indicative of minimal deformation twinning. Fig. 3-44(c) showed the comparison in the through-thickness direction. A strong tension-compression asymmetry in initial yielding can be observed whereas the asymmetry in hardening evolution is less pronounced. The difference among the tensile (or compressive) stress-strain curves in all the three directions are attributed to anisotropy of rolling process. While, the tension-compression difference in the same direction is believed due to twinning.

Study of Nixon *et al.* conclude that the mechanical response of cold rolled highly pure polycrystalline $\alpha$ titanium disk is non-symmetric (tension-compression asymmetry). Specifically, the hardening rate is strongly dependent on the loading direction and the sense of the applied load. Similar results are confirmed by the study of Nemat-nasser *et al.* [182]

performed on extruded grade 2 CPT rod and the work of Ahn *et al.* [183] conducted on the extruded TB340H grade 2 CPT bar.

Since it can be obtained easily and conveniently, the stress-strain relation from uniaxial tensile test is broadly used to simulate many mechanical processes. Thus, it also becomes the first choice for identifying material constitutive behavior in the simulation of instrumented indentation process as well [123, 184-186]. However, during indentation test, target material beneath the indenter will go through a process which is much more complex than uniaxial tension. Some researchers are prone to use uniaxial compressive responses to describe the material behavior in indentation simulations [182, 183, 187, 188]. Seeing the strong tension-compression asymmetry and SD effects exist in pure titanium, the consideration of uniaxial compression test seems to be much more reasonable.

The results of Nixon *et al*. [174], Nemat-nasser *et al*. [182] and Ahn *et al*. [183], showed that in the first 10% plastic strain range, the tension-compression asymmetry is about 20 MPa. Although it is still far away from the difference in this study (about 100 MPa), it showed an important and possible direction to explain the difference. Moreover, indentation test is still not as same as uniaxial compression. The material behavior in the former process is much more complex. This might be one part of the difference as well. However, further investigations need to be performed to explore which kind of constitutive behavior identification process is suitable for indentation simulations. This is still an open question which is beyond the scope of this study.

Finally, we cannot thoroughly explain the difference between the original material parameters and the optimal parameters. However, we found out some possible explanations which at least showed some possibilities. So, we decided to continue with the optimal parameters in following studies.

## 3.8 Extracting RS and PP with the firstly optimized FEM model

In Section 3.5.7, the large gap between the simulated result and the experimental result on the T40 grade 2 CPT reference specimen was successfully reduced to an acceptable range. Thus, we suppose that our model with the new optimal parameters is now suitable for describing indentation process. So, in this section we will use our new FEM model to perform a series of simulations, with various levels of PP and RS, to build the functions of all the three normalized key indentation responses ($P_{max}/P_{max0}$ $S/S$ and $H/H$). Then, by combining the functions with the normalized experimental indentation results, we will try to characterize RS and PP simultaneously induced by the shot-peening process.

The strategy for separating RS and PP used here is as the same as proposed in Section 2.7. However, considering the true plastic strain profiles along with depth extracted in Section 3.4.2, the PP levels were extended until 70% (0%, 1%, 5%, 10%, 15%, 20%, 30%, 40%, 50%, 60% and 70%) for covering the whole possible true plastic range. The corresponding RS levels were started from 0 MPa with an interval of -100 MPa until reaching the yield stress of each PP level. $P_{max}$, $S$ and $H$ values at each discrete point were derived from the $P$-$h$ curve and projected

contact area $A_c$ which were extracted from all the simulation results. The $P_{max}/P_{max0}$, $S/S_0$ and $H/H_0$ values at all the discrete points were used to build the functions. Then, contour plots of all the three functions were then obtained by projecting each of them onto the plane of RS and PP, as shown in Fig. 3-45.

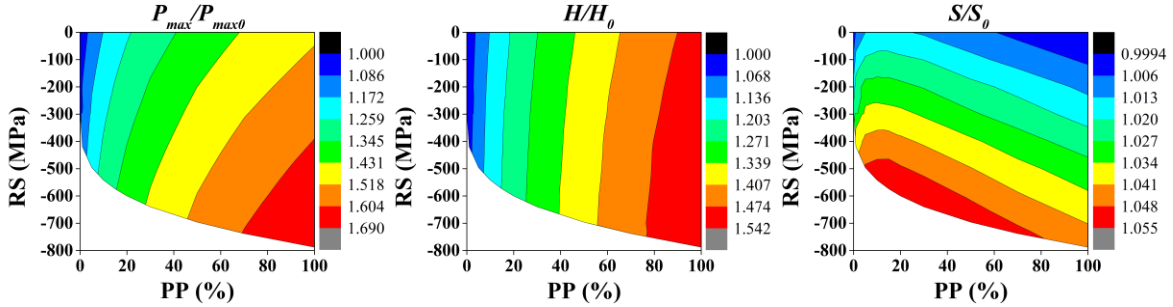


**Fig. 3-45. Contour plots of normalized parameters (vs RS and PP) obtained with the first optimized FEM model of T40: (a)$P_{max}/P_{max0}$; (b)$H/H_0$; (c)$S/S_0$.**

The trends of the contour plots shown in Fig. 3-45 are favorable for extracting RS and PP values, for the isolines of the plots are obviously different from each other. Especially for $S/S_0$ and $H/H_0$, the isolines of one are nearly perpendicular to each other.

**Table 3-12. Results obtained on the sample No.3 by instrumented indentation and X-ray diffraction tests.**

| Depth | $P_{max}$ | $S$ | $H$ | $P_{max}/P_{max0}$ | $S/S_0$ | $H/H_0$ | RS* | PP* |
|---|---|---|---|---|---|---|---|---|
| $\mu$m | mN | mN/nm | GPa | - | - | - | MPa | % |
| 20 | 617.39 | 2.155 | 2.69 | 1.5502 | 0.85 | 1.61 | -303.9 | 0.6288 |
| 50 | 599.56 | 2.035 | 2.63 | 1.5054 | 0.80 | 1.57 | -331.0 | 0.5417 |
| 80 | 575.03 | 1.961 | 2.49 | 1.4438 | 0.77 | 1.49 | -345.2 | 0.413 |
| 140 | 542.62 | 2.198 | 2.32 | 1.3625 | 0.86 | 1.39 | -296.0 | 0.1821 |
| 200 | 508.07 | 2.154 | 2.26 | 1.2757 | 0.85 | 1.35 | -226.5 | 0.0675 |
| 280 | 489.87 | 2.179 | 2.09 | 1.2300 | 0.86 | 1.25 | -156.5 | 0.0213 |
| 360 | 453.27 | 2.061 | 1.97 | 1.1381 | 0.81 | 1.18 | -109.4 | 0.0041 |
| 440 | 459.17 | 2.238 | 2.03 | 1.1529 | 0.88 | 1.21 | -67.3 | 0.0002 |
| 520 | 478.49 | 2.169 | 2.10 | 1.2014 | 0.85 | 1.26 | -92.2 | 0 |
| 600 | 457.12 | 2.128 | 2.05 | 1.1478 | 0.84 | 1.23 | -39.7 | 0 |
| 700 | 486.48 | 2.287 | 2.16 | 1.2215 | 0.90 | 1.29 | -44.4 | 0 |
| 900 | 436.37 | 2.243 | 1.87 | 1.0957 | 0.88 | 1.12 | - | - |
| Reference | 398.26 | 2.542 | 1.67 | 1.0000 | 1 | 1 | -46.5 | 0 |

* The RS and PP values are obtained from the interpolation of X-ray diffraction results shown in Fig. 3-4.

Unfortunately, three severe problems were encountered. First, from Fig. 3-18(b) we could see that the contact stiffness value obtained from the reference is higher than that obtained from that of any other sample, which means that the results of the normalization should be less than 1. However, the simulation results are on the contrary all the $S/S_0$ values are larger than 1. Second, Fig. 3-18(b) also showed that along with the decrease of RS and PP (we can roughly suppose that RS and PP will decrease with increasing depth), contact stiffness was increasing. However, simulation results nearly showed an opposite phenomenon, as shown in Fig. 3-45(c). It means that the contour plot map of $S/S_0$ is not suitable. Third, by comparing the information in Table 3-12 with Fig. 3-45(b) we could notice that the $H/H_0$ values (1~1.61) obtained from experiments has extended the range set by the simulation contour plot map (1~1.542). However,

the combination of RS and PP, set in the model, should have already covered all the possible range.

The three problems mentioned above severely obstructed the application of the simultaneous function method from real experiments. But, there still is one thing not so bad. The contour plot map of $P_{max}/P_{max0}$ covered all the possible experimental data range. Furthermore, a more limited, exploitation of the results might be to use the contour plot map of $P_{max}/P_{max0}$ and the RS profile obtained with X-RD to obtain the PP profile. If this method works, it can save time by avoiding the calibration of integral peak width vs PP and also to allow measurements beyond the range achievable by a tensile test. PP profiles obtained with this limited method and X-ray diffraction are shown in Fig. 3-46, from which it can be seen that there is an obvious discrepancy between the two curves. The PP values extracted from the limited method are generally 10% higher than the corresponding values obtained with X-ray diffraction. Since the limited method is based on the contour plot map of $P_{max}/P_{max0}$, thus, this kind of discrepancy means that a PP level, which is higher than the X-ray diffraction extracted PP value, is need to obtained the same $P_{max}/P_{max0}$ value as what is obtained from experiments. It is quite possibly that the present FEM model has underestimated the work hardening behavior of T40 grade 2 CPT from some aspects, even if inverse method investigation has been performed.

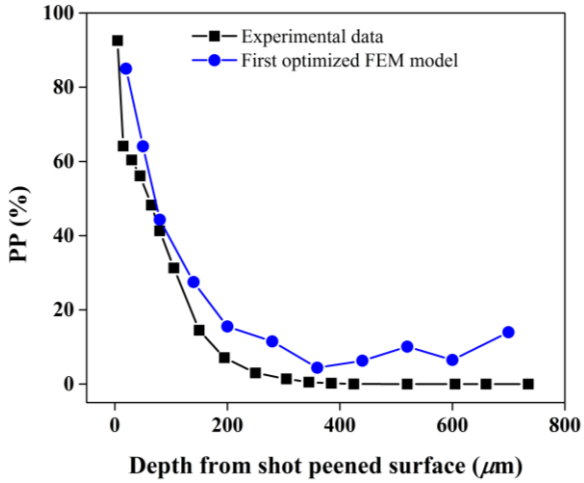


**Fig. 3-46. Comparison between the PP profile obtained from experiments and that obtained with the limited method.**

A not perfect PP profile was obtained with a limited method based on the contour plot map of $P_{max}/P_{max0}$. However, this is not our original intention. Thus, in order to characterizing RS and PP simultaneously, some further efforts need to be made.

## 3.9 Disturbance induced by the polishing process

Results in Section 3.5.6 showed that combining the simultaneous function method with experimental data cannot provide the correct RS and PP profiles along the depth. However, results in Section 3.5.5 indicated that the FEM model fits quite well with the experimental data after the modification with inverse method. The experimental data for the inverse method came

from the indentation tests on the reference which was prepared through an electrolytic polishing process. However, the tests for characterizing RS and PP were conducted on the sample (No.3) which was prepared with a careful mechanical polishing process. The X-ray diffraction data (with standard $\sin^2\Psi$ configuration), in Fig. 3-15, showed that the RS and PP level of the mechanical polished sample is quite close to the reference, however, indentation results in Fig. 3-18 proved that there still are some differences between the two samples. According to Eq.(3-1), the average penetration depth of X ray on pure titanium is about 5 $\mu$m, which means that the X-ray diffraction data shown in Fig. 3-15 can only approximately reflect the RS and PP states around the depth of 5 $\mu$m. As for the layer shallower than this value, sample disturbances induced by the polishing process are probably quite severe, especially for the material in the very top layer. Furthermore, comparing with the $h_{max}$ of 3 $\mu$m for our indentation tests, the impact of the disturbances induced by the polishing process in the top 5-$\mu$m layer cannot be ignored.

Recently, much attention has been paid on the characterization of residual stress and accumulated plastic strain by IIT. One big challenge which occurs during this process is the preparation of a test surface that minimizes both sample disturbance (such as unwanted extra residual stresses and plastic deformation gradients) and surface roughness. Another challenge is to understand how this disturbance can affect the results of IIT. Although surface preparation is of great importance to IIT process, only a few researches focused on this part of study. Furthermore, nearly all of them concentrated on the surface roughness and topography of testing samples. Little attention was paid to the mechanical origin of sample disturbance induced by surface preparation.

Considering this fact, indentation sample disturbance that might be introduced by the polishing process will be studied in detail, with grazing incidence X-ray diffractions, in this part of work, to further improve the feasibility and accuracy of our model.

### 3.9.1 The grazing incidence X-ray diffraction method

The grazing incidence X-ray diffraction (GIXRD) [189, 190] is a modification of the symmetrical Bragg-Brentano geometry for the standard $\sin^2\Psi$ method, introduced in Section 1.4.2.2, by reducing the penetration depth of the X-rays into the surface of the material. The investigation of the stress gradients by changing the incidence angle can be obtained on a 4-circle goniometer set up in low-incidence mode. The idea is to set $\omega$ at a fixed angle of $\alpha$ (the angle between the incident beam and $S_1$ direction) typically 2°-5°, and the $\chi$ and $\varphi$ rotations are used to vary the measurement direction as shown in Fig. 3-47.

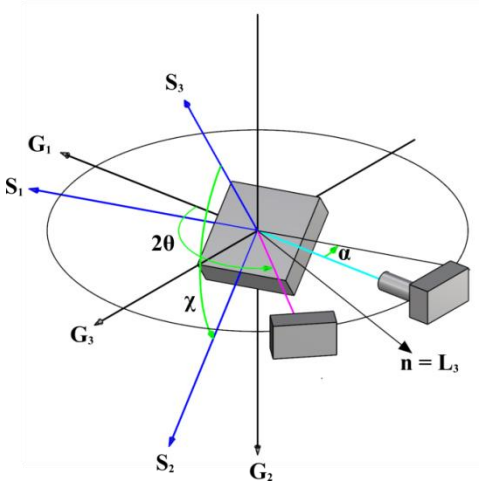


**Fig. 3-47. Scheme of the geometric configuration of the low-incidence mode (combined tilt mode (mixed mode)) [50].**

Considering a conventional $\chi$-mode tilting, for a plane specimen with infinite thickness, the average penetration depth $\tau$ is given as a function of the goniometric and diffractometric angles:

$$\tau = \frac{\cos\chi \sin(2\theta-\alpha)\sin\alpha}{2\mu \sin\theta \cos(\theta-\alpha)} \tag{3-9}$$

where $\mu$ is the linear absorption coefficient. Eq.(3-9) shows that each $\alpha$ angle yields a particular value of the average penetration depth $\tau$ that is defined as the depth from which the diffracted intensity has a value of $1/\mu$ of the incident intensity [34]. This means that the usage of a low $\alpha$ angle allows the penetration depth to remain small (near the surface), even for $\chi$=0.

In the classical $\sin^2\Psi$ method, the $\Psi$ and $\Phi$ angles that occur in Eq.(1-4) are obtained through one of the two acquisition modes: the $\chi$-mode, where $\Psi=\chi$ and $\Phi=\varphi+\pi/2$, or the $\omega$-mode, where $\Psi=\omega-\theta$ and $\Phi=\varphi$. In grazing incidence, the $\Psi$ and $\Phi$ angles are given by:

$$\cos\Psi = \cos\chi\cos(\omega-\theta) \tag{3-10}$$

$$\Phi = \varphi + \Delta\varphi \tag{3-11}$$

$$\tan\Delta\varphi = \sin\chi / \tan(\omega-\theta) \tag{3-12}$$

Where $\alpha=\omega$. As was shown in [191], when $\alpha$ angle is lower than 10 °, the penetration depth $\tau$ given by Eq.(3-9) is almost constant versus $\Psi$ angle, for a given value of $\alpha$. This means that the depth at which the surface is analyzed can be easily controlled through the choice of $\alpha$.

By keIIng $\Phi$ angle constant (which means varying the goniometer angle $\varphi$ through Eq.(3-10) the stress components $\sigma_{11}$ and $\sigma_{13}$ can be obtained with:

$$\varepsilon_{\Phi\Psi}(\{hkl\},\tau) = F_{ij}(\{hkl\},\tau)\sigma_{ij} + F_{ij}(\{hkl\},\tau)\sigma_{ij} \tag{3-13}$$

### 3.9.2 The grazing incidence X-ray diffraction tests

As mentioned in Section 3.4, X-ray diffraction peak broadening can be used to characterize true plastic strain by combining with a series of uniaxial tensile test. Here, the same principle was used with grazing incidence X-ray diffraction. Nearly all of the testing situations are the same as we used in Section 3.3, but with only a few variations. Considering the features of the grazing incidence X-ray diffraction, a scintillation counter was used with 0.4 ° Soller slits

mounted in front of it to limit unwanted peak broadening due to instrumental effects. The counting time is 55 s/step and the step size is 0.02 °2$\theta$.

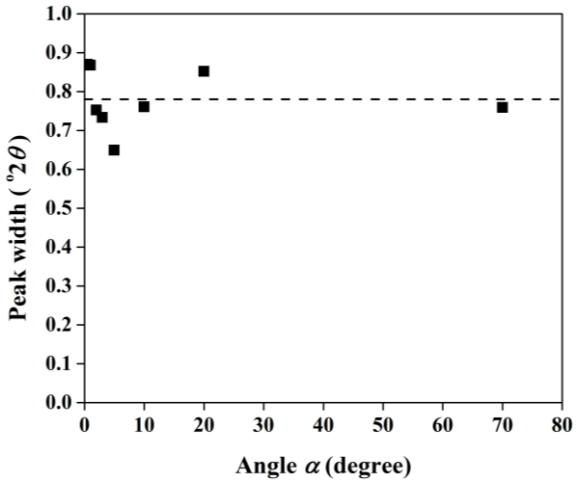


**Fig. 3-48. Peak width value for each incidence angle ⍺ on a standard silicon powder.**

In order to investigate the instrumental broadening under the configuration of low-incidence mode, acquisitions on a standard stress-free silicon powder were conducted with different incidence angles $\alpha$: 0.5°, 1°, 2°, 3°, 5°, 10°, 20° and 70°. The {444} diffracting plane was used and the scanning range was from 132° to 141°. All the integral peak width values stayed in range 0.75°±0.12°, as shown in Fig. 3-48, which shows that the instrumental broadening caused by the decrease of the incidence angle ⍺ is acceptable, at least until $\alpha$=0.5°. X-ray diffraction acquisitions on both the polished and the reference samples, were conducted with different angles $\alpha$ (0.5°, 1°, 2°, 3°, 5°, 10°, 20° 40°, 50°, 60° and 70°) and angles $\chi$ (-60°, -40°, -20°, 20°, 40° and 60°). After removal of a linear background, peak positions and width were obtained by fitting a pseudo-Voigt function on the diffraction patterns, taking into account the $K_{\alpha1}$-$K_{\alpha2}$ doublet through Rachinger's assumptions.

In Section 3.4.2, the relationship between integral peak width and the true plastic strain was calibrated, and the results were shown in Fig. 3-13. Since the peak width obtained with PSD and the scintillation counter are quite close to each other, the plastic strain vs depth relathionship in this part of study will be obtained with the same calibrated results in Section 3.4.2. All the results obtained with X-ray diffraction tests were listed in Table 3-13. One thing need to be explained is the reason why only residual stresses for low incidence angles were obtained (0.5°-5°). Under the configuration of grazing incidence X-ray diffraction, as shown in Fig.3-47, the angles $\alpha$, $\chi$ and $\omega$ are correlated. Seeing that 90° and -90° are the up limit and low limit of the angle $\omega$. High incidence angle $\alpha$ (larger than 5° in this study) will make the $\omega$ angles beyond these limits, which is impossible in reality.

**Table 3-13 Material properties considered in the numerical simulation**

| | Incidence angle $\alpha$ (°) | Penetration depth) ($\mu$m) | Residual stress (MPa) | Peak width (°2$\theta$) | Plastic strain % |
|---|---|---|---|---|---|
| | 0.5 | 0.093 | -81.1 ±39.9 | 2.45 | 69.755 |

| | | | | | |
|---|---|---|---|---|---|
| Carefully polished specimen | 1 | 0.184 | 8.4 ±56.7 | 2.26 | 53.194 |
| | 2 | 0.357 | -45.8 ±62.2 | 2.06 | 39.464 |
| | 3 | 0.521 | -69.1 ±46.2 | 1.70 | 20.080 |
| | 5 | 0.827 | 13.6 ±37.8 | 1.45 | 11.103 |
| | 10 | 1.497 | - | 1.47 | 11.844 |
| | 20 | 2.590 | - | 1.37 | 8.840 |
| | 40 | 4.169 | - | 1.12 | 3.848 |
| | 50 | 4.698 | - | 0.83 | 0.732 |
| | 60 | 5.050 | - | 0.78 | 0.485 |
| | 70 | 5.220 | - | 0.54 | 0.003 |
| Reference sample* | 72-77 | 5.238 | -46.5 ±17.7 | 0.50 | 0 |

*The reference sample was characterized with standard $\sin^2\Psi$ method.

Table 3-13 shows that in the surface layer, the residual stress levels are low (several tens MPa), even if the error range is quite large as compared with the mean value. This means that the careful polishing procedure mentioned above can effectively reduce the influence of residual stresses induced during polishing process. As for the plastic strain levels, the situation is totally different. Even if the quantitative relation shown in Fig. 3-13 is debatable, there is no doubt that a significant plastic strain obviously exists in the surface layer. Especially in the top layer (the thickness is about 350 nm), the plastic strain levels are considerably high. It can even reach more than 60% at the extreme surface. And, the influence of plastic strain will only fade away when the depth reaches about 5 $\mu$m which is even deeper than maximum penetration depth (3 $\mu$m) of the instrumented indentation test.

### 3.9.3 IIT simulations with surface plastic strain

In fact, an influencing depth of 5$\mu$m cannot be neglected even for micro indentation tests, let along conventional nanoindentation test. The influence can be seen clearly from the results of the instrumented indentation tests. Instrumented indentation tests were conducted on both the reference raw material specimen and the carefully polished specimen for comparison. 10 tests were made on each specimen and the results were averaged. The most important three parameters for both instrumented tests and FEM simulations were listed in Table 3-14. Table 3-14 showed that the influences of the polishing process, even if it is carefully conducted, obviously increased the maximum indentation load ($P_{max}$) and the contact hardness ($H$), and, on the opposite, decreased the contact stiffness ($S$). The same trend was observed for $P_{max}$ and $H$ with FEM simulations (described below).

**Table 3-14. Results of IIT experiment and simulations.**

| Indentation response | Reference sample | Carefully polished specimen | FEM | FEM with surface plastic strain |
|---|---|---|---|---|
| $P_{max}$ (MPa) | 398.0 ±20.3 | 435.8 ±51.8 | 398.1 | 406.3 |
| $S$ (mN/nm) | 2.542 ±0.036 | 2.280 ±0.031 | 2.556 | 2.545 |
| $H$ (GPa) | 1.67 ±0.13 | 1.87 ±0.32 | 1.63 | 1.73 |

Through FEM simulations, similar results were obtained as well. By using the keywords * INITIAL CONDITIONS in ABAQUS® to different sets of elements in the top surface, plastic strain were introduced into the finite element model, as shown in Fig. 3-49. Plastic strain was

assumed to be linear in each layer. Residual stresses could be induced in the same way. However, they were not considered in this model, for their amplitudes are not so high.

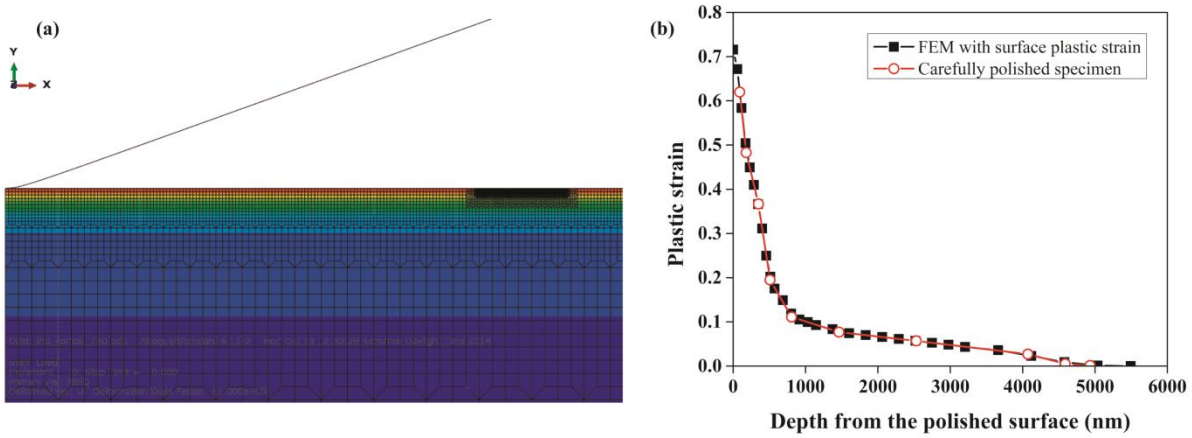


**Fig. 3-49. Plastic indentation imposed in the FEM model: (a) equivalent plastic strain (PEEQ) contour plot, (b) plastic strain gradient from both the experiment and induced in the numerical simulation.**

The way we used for imposing residual stress and plastic strain fields into our FEM model and the configuration of the corresponding boundary condition were introduced in Section 2.1. Actually, this kind of configuration can be used not only to introduce uniform plastic strain and residual stress fields into the FEM model, but also to introduce plastic strain and residual stress gradients as well. Similar as the instrumented indentation tests, indentation simulations were performed on both models with and without the high plastic strain in the surface region for comparison. Load vs depth (*P-h*) curves of both the experiment and the simulation were listed in Fig. 3-50. The *P-h* curve of the experiment is a mean curve averaged from the *P-h* curves of all the 10 tests. The uncertainty on the experimental loading curve equals to the standard deviation observed on all the 10 tests. It goes from almost zero at low loads to about 50 mN at $P_{max}$. The *P-h* curve of the FEM model without high plastic strain in the surface region (the green curve) fitted well with that of the reference specimen (the black curve), which proved that the numerical model was reliable. When high plastic strain in the surface region was induced into the FEM model, there is an upward shift of the *P-h* curve, which is consistent with the experimental results. This kind of shift, caused by the existence of plastic strain, was observed in our former research as well [8, 9]. The upward shift in this study is not so obvious in the range of 3 $\mu$m, however, if we enlarge the first 1-$\mu$m range, the shift caused by the high plastic strain in the surface region becomes much more obvious. In the zoom-up of Fig. 10, the green and the black curves are still superposed and stay in a lower position, which proves that our original model is still reliable in the first 1-$\mu$m range. While, the blue and the red curves are superposed as well and stay in a higher position, which confirms that the FEM model with surface plastic strain can represent the upward shift of the carefully polished sample very well in the first 1-$\mu$m range. The coincidence between experiment and simulation in the 1-$\mu$m depth range is much better than that in 3-$\mu$m depth range might because that 3-$\mu$m maximum indentation depth is too large to capture the effects of the high plastic strain in the surface region.

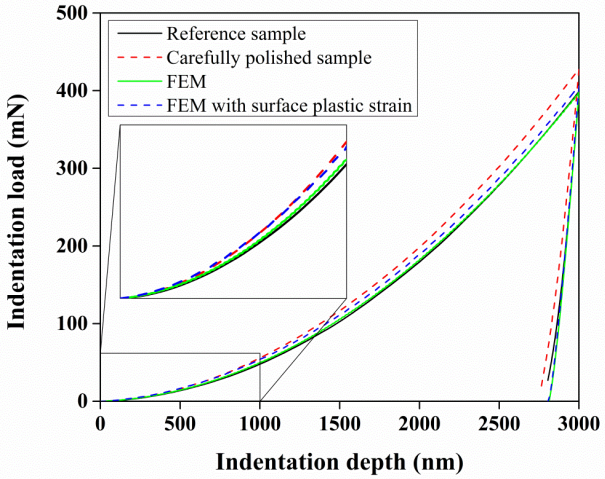


**Fig. 3-50. *P-h* curves for the experimental comparison group and the numerical comparison group.**

The influences of the plastic strain induced by the polishing process could be seen clearly in both experiments and simulations, especially in the first 1-$\mu$m range. However, considering the average *P-h* curve of the carefully polished specimen and the corresponding uncertainty, the simulation result with 3-$\mu$m indentation depth is still on the lower side. There are several possible reasons for this.

First, using an equivalent conical indenter to represent a Berkovich indenter was shown to be accurate in common situations. When high plastic strain in the surface region is taken into account, it may not be suitable any more. Literature showed that the plastic depths, plastic volumes and plastic strain levels influenced by a Berkovich indenter and an equivalent conical indenter are not the same [171].

Second, the non-homogeneity among the neighbor grains could be reinforced by the mechanical polishing process and be weakened by the electrolytic polishing process, because the former will increase the density of dislocations or produce intergranular stresses due to deformation incompatibilities, while the later will etch defects (such as grain boundaries, sub grain boundaries, dislocations, etc) in the material and thus induce a mechanical relaxation.

Third, by observing the indentation dimples on the carefully polished specimen, a slight sample tilt was found, as shown in Fig. 3-51. The nominal contact area (pile-up/sinking-in are not taken into account) corresponding to a $h_{max}$ value of 3 $\mu$m was represented by a blue dashed triangle. Normally, pile-up/sinking-in phenomenon occurs on the surface of the indenter. Since the sharpness of the indenter edges, pile-up/sinking-in phenomena on the edges are negligible. By supposing that there is no pile-up/sinking-in on the indenter edges, the three edges of the contact dimple could be used to approximately calculate the actual nominal contact area of the experiment, as shown with the red solid triangle in Fig. 3-51. It could be seen that there is an obvious difference between the two triangles. One contact edge of the red triangle is longer and the other two are shorter than the corresponding edges of the blue triangle. This kind of difference is normally caused by the fact that the axis of the indenter tip was not perfectly perpendicular to the sample surface. However, discrepancy of material or mechanical

properties of the neighbor grains can lead to this kind of difference as well. But another phenomenon shows the existence of sample tilt. As shown in the enlarged view of Fig. 3-51, there was a declination between the contact edge of the red triangle and that of the blue triangle, however, the other two pair of contact edges are all superposed. The inhomogeneity due to the neighboring grains cannot cause this kind of deflection. Literature showed that sample tilt will make the *P-h* curve shift upwards for all of the studied materials to different extents considerably. For metal materials, this kind of effect is even more obvious than for fused silica. [192-194]. Kashani *et al*. [193] also showed that the influence of sample tilt is more severe with Berkovich indenter than with equivalent conical indenter.

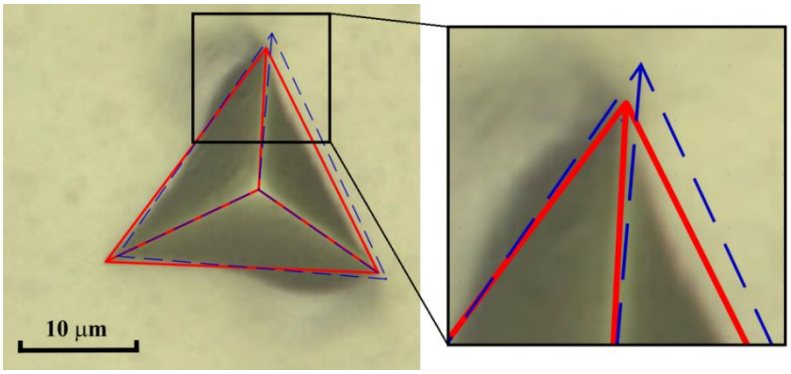


**Fig. 3-51. The evidence of the existence of sample tilt.**

Fianlly, in this part of simulation, the role of residual stresses is neglected. As, in the average, they are compressive, it would increase slightly the load values. Rough simulation showed that a residual stress of -50 MPa will probably increase the $P_{max}$ value about 1.5%. And, the influence of residual stress may vary along with the increase of indentation depth.

### 3.9.4 Extracting RS and PP with FEM model considering surface plastic strain

In above sections, disturbance induced by sample preparation process which may affect the results of the IIT process were investigated. Thus, in present part of work, high plastic strain induced by the polishing process will be considered in our FEM model for modifying the simultaneous method.

The way for introducing high plastic strain in the surface region, as shown in Section 3.8.3, will be used for all the FEM models with various combinations of PP and RS. The thing need to be explained is that we suppose that the shot-peening induced plastic strain and the sample preparation induced plastic strain will accumulated together. By performing series of simulations, the normalized contour plot map obtain from the functions were listed in Fig. 3-52. The reference of the normalization is still the data from the FEM model optimized with the inverse method in Section 3.6.3.

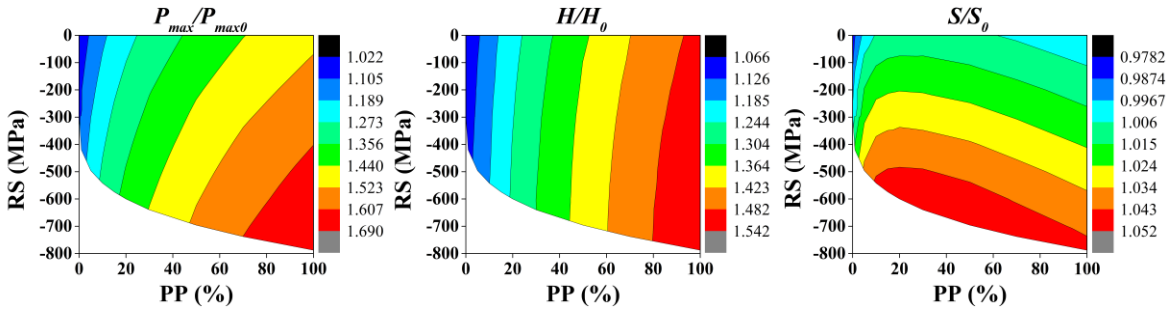


**Fig. 3-52. Contour plot maps of normalized parameters (vs RS and PP) obtained with the FEM model of T40 considering the high plastic strain in the surface region: (a) $P_{max}/P_{max0}$; (b) $H/H_0$; (c) $S/S_0$.**

Comparing with Fig. 3-45, contour plot maps shown in Fig. 3-52 do not change a lot, no matter from the trend of the isolines or from the range of the color scales. Especially, the problem of the contour plot maps of $S/S_0$ and $H/H_0$ obtained with the optimized FEM model, as mentioned in Section 3.7, still exist. So, we do not expect that considering the high plastic strain in the surface region can significantly improve the quality of the FEM model. This can be confirmed by the results of the limited method, as shown in Fig. 3-53. This might be reasonable if the discrepancy does come from the under estimation of the work hardening behavior of T40 grade 2 CPT, because considering the surface high plastic strain cannot solve problems caused by this kind of undervaluation.

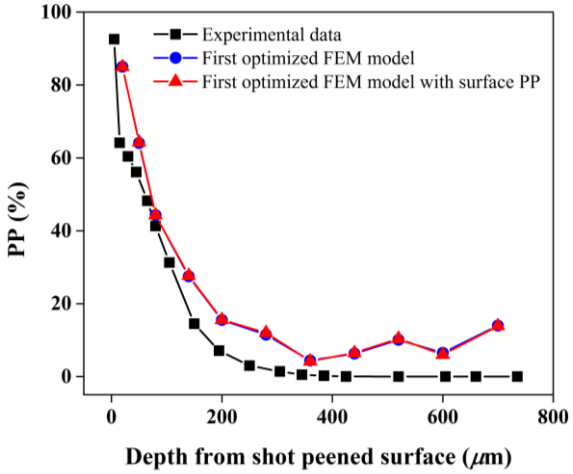


**Fig. 3-53. Comparison between the PP profile obtained from experiments and those obtained with the limited method.**

## 3.10 Further modification of the FEM model

### 3.10.1 Second optimization

In Section 3.8, the possible disturbances which may be introduced by the carful mechanical polishing process have been studied. Results showed that even very carefully performed mechanical polishing procedure still can induce sever plastic strain into the surface region of the IIT sample. By taking this kind of surface high plastic strain into consideration, the optimized FEM model was modified again. However, results of the simulation of 3-$\mu$m IIT

process showed that the improvement of this kind of modification is limited. The gap between the experimental *P-h* curve and the simulated one is still quite large. Thus, the performance of the limited method has not been obviously promoted. The reason must be that the modification we made on the optimized FEM model is not sufficient to represent the real situation. This kind of insufficiency particularly appeared when applicate the simultaneous function method and the limited method.

All the things we did before are based on the precondition that considering the electrolytic-polished sample as reference, which gave us a big problem that we need to figure out the difference between the electrolytic-polished sample and the careful mechanically polished sample. In fact, our optimization of the FEM model can bypass this problem by directly using the part (on the careful mechanically polished sample) which is far away enough from the shot-peened surface as the reference. This is reasonable, because that effect of the shot-peening process at such a large distance from the surface should be negligible. In this way, the electrolytic-polished sample does not need to be considered any more.

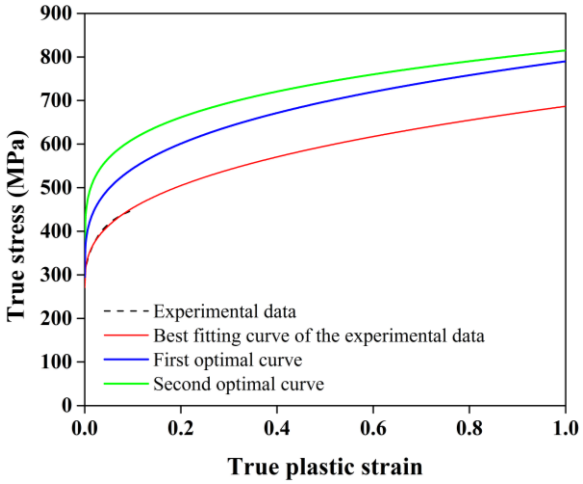


**Fig. 3-54. Comparison among the true stress vs true plastic strain curves obtained from various situations.**

**Table 3-15 Comparison between the experimental parameters and the optimal parameters.**

| Material parameters | Original values | Optimal values |
|---|---|---|
| Young's modulus *E* (GPa) | 119.0 | 108.7 |
| Poisson's ratio *v* | 0.34 | 0.34 |
| Yield stress $\sigma_y$ (MPa) | 279.6 | 319.5 |
| Hardening coefficient *K* (MPa) | 415.4 | 495.5 |
| Hardening exponent *n* | 0.38 | 0.23 |
| Friction coefficient *f* | 0.15 | 0.21 |

Following this way, a second optimization process was performed. Fig. 3-30 showed that the normalized loading *P-h* curve obtained from the carefully mechanically polished sample is different from the one obtained from the electrolytic-polished sample. Thus, the first procedure of the second optimization process is still the indenter shape optimization. This part of work has been conducted similarly as the procedure discussed in Section 3.7.2.2. After the optimal tip shape had been determined through a multi-step tip shape optimization process, the material parameters and the friction coefficient were then optimized with FMOGA II algorithm, similar as what had been done in Section 3.7.3. The best solution was obtained from the design No.124.

The optimal parameters of the second optimization process were listed in Fig. 3-54 and Table 3-15. From Table 3-14 we can see that the Young's modulus value obtained from the second optimization process becomes 10 GPa lower than the original value. Nothing strange has happened to the Poisson's ratio and the friction coefficient. The biggest difference still comes from the plastic parameters, which can be seen clearly from Fig. 3-54. The stress-strain curve obtained from the second optimization process is higher than the one obtained from the first optimization.

Here, we do not want to get to the bottom of the difference between the original parameters and the optimal ones any more. The aim of this part of work is just to try to testify that if our thinking of changing the reference sample can improve our simultaneous function method or at least the limited method. After all, one final goal of this thesis is to explore a new way to characterize shot-peening induced residual stress and work hardening. As for the influences of various sample preparation methods and the reasons behind them are far beyond the scope of this thesis, and they can be investigated and discussed in the future work.

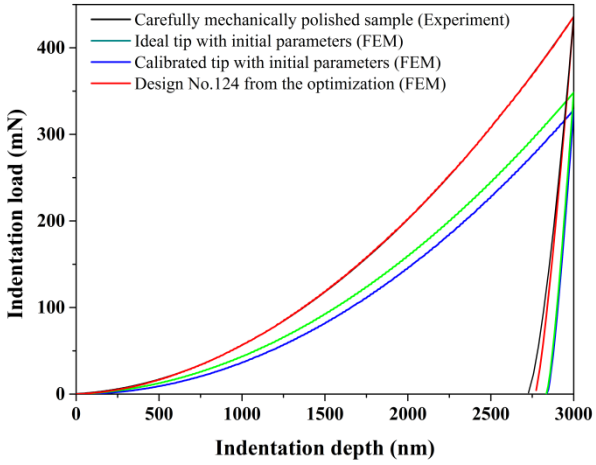


**Fig. 3-55. *P-h* curves obtained from experiment and simulations with various FEM models.**

**Table 3-16 IIT responses obtained from experiment and simulation with optimized parameters.**

| Indentation responses | Carefully mechanically polished sample (900 $\mu$m) | Design No.124 from the second optimization |
|---|---|---|
| $P_{max}$ (MPa) | 435.8±51.8 | 435.4 |
| $S$ (mN/nm) | 2.280±0.031 | 2.252 |
| $H$ (GPa) | 1.87±0.32 | 1.83 |

The indentation responses obtained with the optimal parameters were listed in Fig. 3-55 and Table 3-16, which showed that the quality of the second optimization process is fairly good. Thus, a series of simulations with various RS and PP levels were performed, similar as what bad been done in Section 3.8 and Section 3.9.4, by using the optimal parameters from the second optimization. Contour plot map of all the normalized indentation responses were shown in Fig. 3-56.

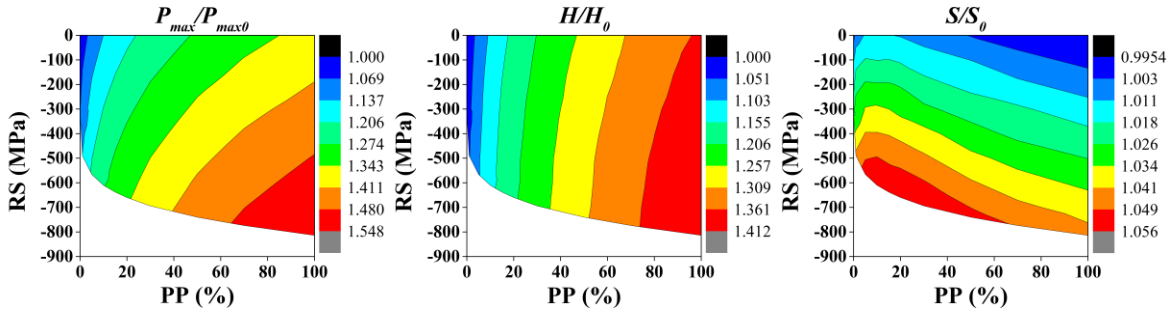


**Fig. 3-56. Contour plot maps of normalized parameters (vs RS and PP) obtained with the FEM model considering the high plastic strain in the surface region: (a) $P_{max}/P_{max0}$; (b) $S/S_0$; (c) $H/H_0$.**

Simultaneous function method was tried to be constructed once more. The problems mentioned in Section 3.8 have been relieved, which showed the effects of the second optimization process. However, this kind of relief is still not enough for the application of simultaneous function methods, because no function pair can be consistent with experimental results. Thus, the limited method was used again. The extracted PP profile was shown in Fig. 3-57. Comparing the profiles obtained before, the PP profile obtained from the second optimized FEM model got much closer to the experiment calibrated profile, especially for depths larger than 100 $\mu$m.

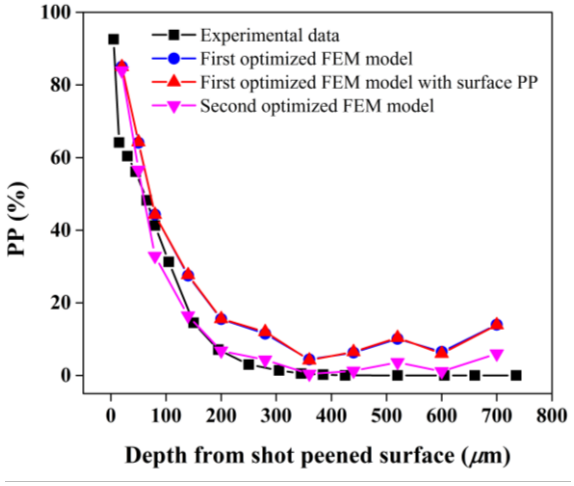


**Fig. 3-57. Accumulated plastic strain (PP) profile obtained from experiments and various FEM models.**

## 3.6 Conclusion

In Chapter 2, it was found that the simultaneous function method worked quite well from a pure numerical point of view. In the present chapter we tried to verify its accuracy and adaptability with experiments.

A piece of T40 grade 2 CPT was shot-peened. Metallographic observation on the cross section of the shot-peened sample showed that there is no grain refining on the treated surface, which indicated that the treatment process is conventional shot-peening.

Both the residual stress and the accumulated plastic strain profiles along the depth were extracted from X-ray diffraction (X-RD) measurements. The residual stresses were obtained

from diffraction peak displacement while the plastic strain was obtained from peak broadening. The calibration of the peak widths versus the plastic strain was performed with uniaxial tensile tests. Results showed that the maximum value of the compressive residual stress can reach -340 MPa, and the depth influenced can reach about 450 $\mu$m. Shot-peening process can induce a high plastic strains in a significant depth. At the extreme surface, the plastic strain level can reach even more than 70%.

Instrumented indentation tests were conducted on three mechanically polished samples (with different conditions) and on an electrolytic polished reference sample which is supposed to be free from the influence of shot-peening. Results showed that even if a very careful mechanical polishing process is applied, there were still some polishing-induced factors which will influence the indentation responses on the sample. Results of the instrumented indentation tests on the carefully polished sample also showed a decrease of contact stiffness along with depth from the shot-peened surface, which is on the opposite of our former simulated results in Chapter 2. One possible reason of this phenomenon is the free-edge effect. By inducing the correction of free-edge effect, the contact stiffness values tend to be a constant along with depth.

By using the Ludwick type isotropic hardening constitutive model to describe the uniaxial tensile stress-strain relationship of T40 grade 2 CPT, numerical simulations of the instrumented indentation process were conducted. However, significant difference existed between the experimental results and the simulated results. Considering that several factors can affect the accuracy of IIT simulations, an inverse method was used to optimize the indenter shape, material parameters and the friction coefficient for improving the quality of our initial FEM model. Results showed that the indentation responses obtained from the optimized model fit fairly well with those from the experiments. When performing the indenter shape optimization, we also found out that the shape of the normalized loading *P-h* curve obtained from the simulations with the 2D axisymmetric FEM model only depends on the shape of the indenter. This may supply a new way for calibrating the indenter shape and tip area.

However, when using the simultaneous function method with the modified model, new problems occurred: the contour plot maps of $S/S_0$ and $H/H_0$ cannot cover the actual range of experimental data. Even so, a limited method was proposed to obtain the plastic strain profile along the depth. The results are overall higher than experimental profile.

With grazing incidence X-ray diffraction (GIXRD) technique, residual stress and plastic strain gradient induced by the polishing process were examined. Results showed that residual stresses (supposed to be constant in each layer) in the polished specimen did not show much variation comparing with the residual stresses in the reference sample. This proved that this polishing process can effectively reduce the levels of residual stresses induced by the mechanical polishing process.

However, the GIXRD technique showed that the plastic strain levels in the surface region are significant. Through the combination of GIXRD and uniaxial tensile tests the relationship between the peak width and plastic strain was characterized. Results showed that plastic strain

caused by the polishing process can affect the depth until 5 $\mu$m, which is even deeper than the $h_{max}$ (3 $\mu$m ) value of the indentation tests. In the near surface layer (in the range of depth about 350 nm), the plastic strain levels are fairly high. In the layer closest to the surface, the plastic strain can reach more than 60%. Considering both the sample disturbance induced by the mechanical polishing process, our FEM model was modified again. However, the results showed that there is no obvious improvement.

Several kinds of influencing factors were checked, and the corresponding modifications were performed as well. However, the simultaneous function method still cannot be used with experimental data. Since this method works very well from a pure numerical point of view, there must be some other factors that should be incorporated in our model to better describe the experimental indentation responses. For instance, the constitutive model used is too simple (kinematic hardening was not taken into account), the equivalent conical indenter cannot fully represent the real Berkovich indenter (especially considering the existence of residual stress), the residual stress state cannot simply be substituted by a biaxial stress state which has the same hydrostatic stress state, and so on. Considering all of these possible problems, a 3D FEM model which takes the possible components of residual stress tensor and a more realistic and suitable constitutive model into account need to be built in the near future. If possible, comprehensive constitutive model and friction model both correlated with stress state need be developed for a better description of the indentation responses of material.

# Chapter 4

# The evolution of shot-peening induced RS and WH during low cycle fatigue process

Many studies showed that residual stresses and work hardening induced through the shot peeing process can significantly influence the fatigue performance of materials and components. Besides, both residual stresses and work hardening will change continuously during the whole fatigue process. Especially for low cycle fatigue (LCF), the cyclic deformation can always reach the plastic range. Thus, investigating the evolution of residual stresses and work hardening during low cyclic fatigue process becomes quite meaningful in the study on the application of shot-peening process for improving fatigue resistance performance of materials.

As a new member of high-strength near $\beta$-phase titanium alloy, Ti-18 alloy was developed aiming at the replacement and improvement of Ti-5553 alloy which is mainly used for the fabrication of the landing gear of jumbo jets, like Boeing 777. Low cycle fatigue property is of great importance to it.

In Chapter 2 and Chapter 3, from both a pure numerical point of view and a combination with experimental data, a semi-experimental method has been proposed for simultaneously characterizing residual stresses and work hardening induced by the shot-peening process with instrumented indentation test. Although, the accuracy on the two quantities may not be sufficient in practice when they are determined simultaneously, the limited method still can help us to obtain the profile of the accumulated plastic strain which can be directly correlated with work hardening.

In this chapter, a series of strain-controlled low cycle fatigue tests will be performed on several Ti-18 specimens treated with different procedures, including shot-peening, prestrain, and prestrain & shot-peening. Both instrumented indentation and X-ray diffraction techniques will be used to characterize the residual stresses and work hardening imposed in the specimens. Finally, the evolution of residual stresses and work hardening during low cycle fatigue process will be investigated.

## 4.1 Material characterization

### 4.1.1 Preparation of the material

A quarter of an ingot ($\Phi$ = 250 mm) of high-strength near $\beta$-phase Ti-18 alloy was supplied by TIMET (Valley Creek Blvd, USA). Vacuum arc remelting (“VAR”) was used to prepare the ingot [195]. The chemical composition of it is listed in Table 4-1.

**Table. 4-1 The chemical composition ofTi-18 alloy.**

| Elements | Al | Mo | V | Cr | Fe | O | C | N | Ni | $Mo_{eq}$ | Ti |
|---|---|---|---|---|---|---|---|---|---|---|---|
| Wt% | 5.5 | 5.0 | 5.0 | 2.3 | 0.8 | 0.15 | <0.1 | <0.1 | <0.1 | 13.6 | Balance |

Final forging and rolling of the ingot specimen was performed below the beta transformation temperature (beta transus). The ingot specimen was then solution heat treated at a subtransus temperature (816 ℃) for 2 hours and air cooled. Then, it was precipitation hardened at 621 ℃ for 8 hours and air cooled as well.

### 4.1.2 Uniaxial tensile test

Uniaxial tensile tests were firstly carried out to investigate the basic mechanical properties of the ingot specimens. Millet [196] had already made uniaxial tensile tests on the Ti-18 specimens from different part of the ingot and the results are listed in Table 4-2. The uniaxial tensile test results are quite consistent which shows that the ingot is homogeneous. The standard deviation for the yield stress is 4.8 MPa and for the ultimate tensile stress, it is 8.8 MPa. For obtaining more details on the tensile properties of the Ti-18, a uniaxial tensile test on a specimen was performed as well. The dimension of the specimen and test situation are as the same as used in Section 3.4.1. The true stress vs true strain curve until necking point were plot in Fig. 4-1. Considering the difference between engineering stress (used by Millet) and true stress, our results are consistent with Millet's results.

**Table. 4-2 Uniaxial tensile properties of Ti-18 specimen from different parts of the ingot [196]**

| Position | UTS (MPa) | TYS (MPa) | Elongation (%) | RA (%) |
|---|---|---|---|---|
| Outer | 1338 | 1277 | 8.7 | 20 |
| Mid-Radius | 1340 | 1285 | 7.2 | 17 |
| Center | 1345 | 1274 | 9.6 | 21 |
| Center | 1356 | 1276 | 9.3 | 18 |
| Mid-Radius | 1335 | 1274 | 8.9 | 18 |
| Outer | 1331 | 1271 | 8.6 | 21 |

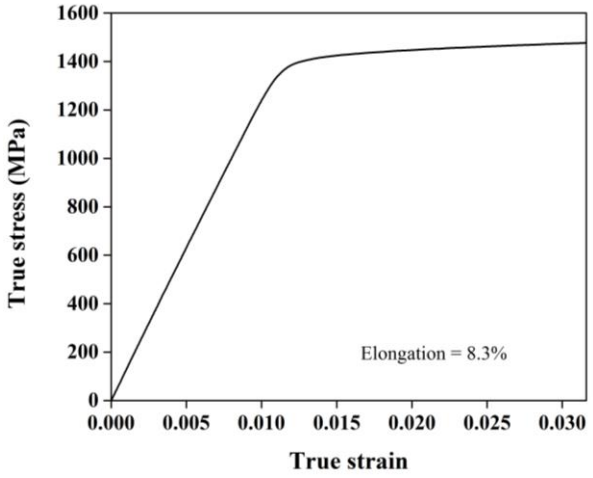


**Fig. 4-1. Uniaxial tensile true stress vs true strain curve of Ti-18.**

Comparing with conventional near $\beta$-phase high-strength titanium alloys, this Ti-18 alloy exhibits superior tensile strength and similar ductility. This is due to the unique combination

of elements in the preferred weight percentages. This produces a yield strength ($\sigma_{0.2}$) of 1407 MPa (Fig. 4-1). The curve in Fig. 4-1 indicates a small capacity for strain hardening in this material and a possibility for early microcrack formation upon loading to plastic deformation regime including cycling deformation [197].

### 4.1.3 Microstructure

Two small pieces of materials were cut off from the ingot. They were respectively polished on transverse section and longitudinal section on a Vector® LC 250 automatic lapping and polishing unit (BUEHLER An ITW International, Lake Bluff, USA) using 800-grit and 1200-grit silicon carbide abrasive disc films, (ESCIL, Ltd., Chassieu, FR) followed by 10-$\mu$m suspension diamond abrasive paste and 0.05-$\mu$m silica powder (ESCIL, Ltd., Chassieu, FR) on special tissues. After being polished to a mirror-like surface, they were respectively etched with a mixed solution (5% perchloric acid, 3% nitric acid and 92% distilled water) for 10 s and then washed with running cold water. After polishing and etching, microstructures of Ti-18 alloy were observed and tested under the SU 8030 ultra-high resolution cold field emission scanning electrical microscope (FE-SEM) (HITACHI, Ltd., Tokyo, JP). In order to identify and distinguish the $\alpha$ phase and the $\beta$ phase, Energy-dispersive X-ray spectroscopy (EDXS) was used for checking the chemical components in different parts of one piece of specimen. Results of EDXS, as shown in Fig. 4-2, show that the particles are $\alpha$ phase and the matrix is $\beta$ phase, because that the peaks of Mo and Cr (two typical and important $\beta$ phase stabilizing alloy elements) are only present at point 2.

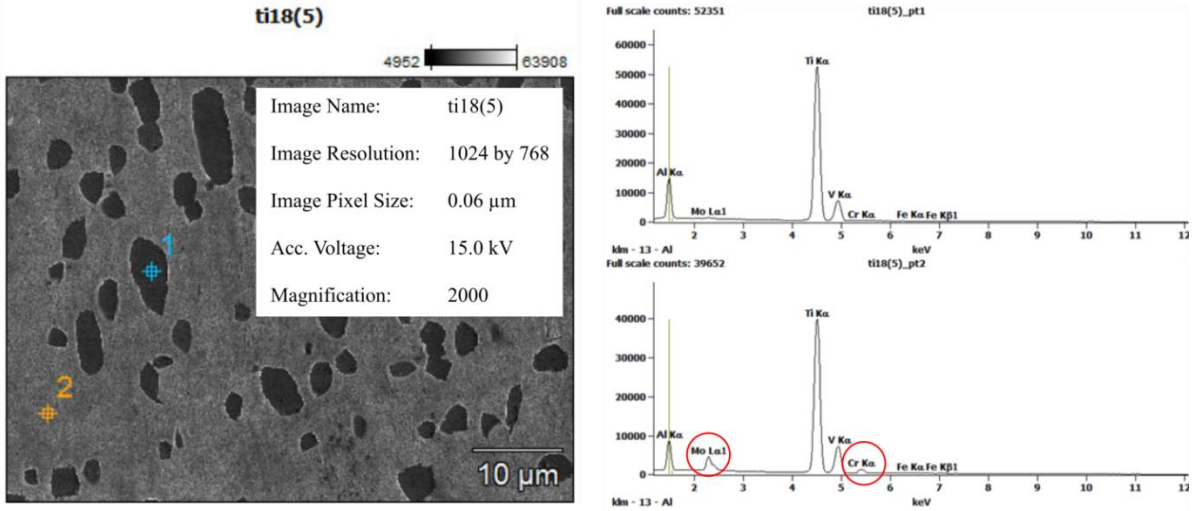


**Fig. 4-2. EDXS results of Ti-18 alloy.**

Fig. 4-3 and Fig. 4-4 show the SEM images of Ti-18 on both the transverse and the longitudinal sections. It can be seen that the heat treatment process generated a typical bimodal microstructure of titanium alloys: many discrete globular primary $\alpha_p$ phase grains

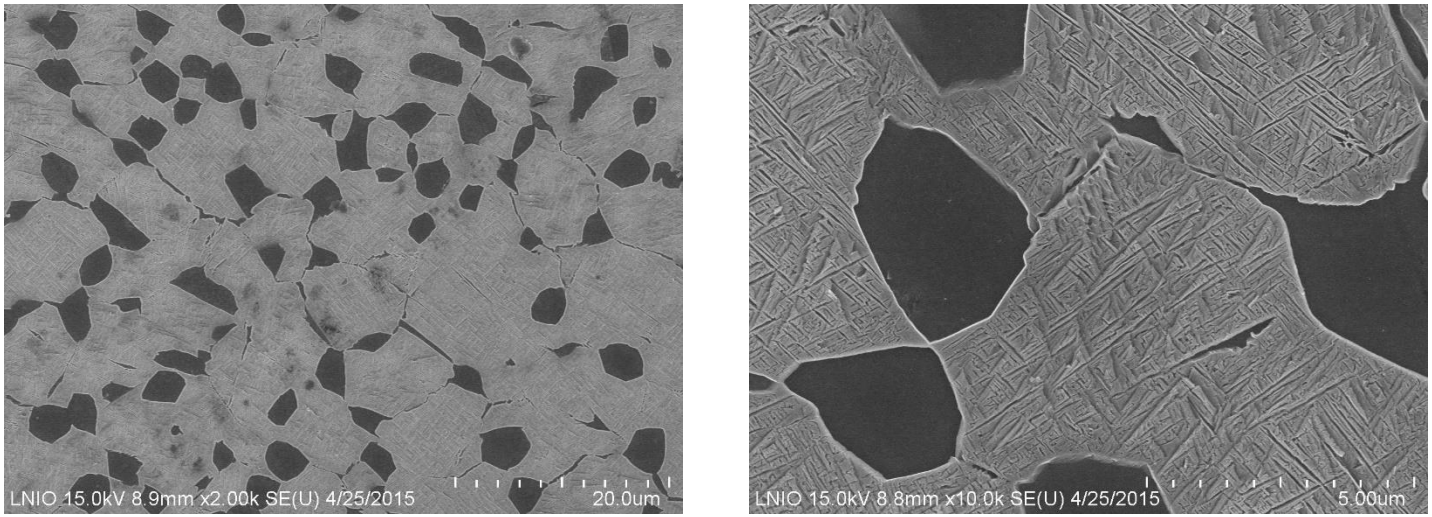


**Fig. 4-3. SEM images of the microstructure of Ti-18 alloy (transverse section): (a) A low-magnification image, showing a typical bimodal microstructure with uniformly distributed globular $\alpha_p$ particles embedded in the transformed $\beta$ matrix; (b) A higher magnification image showing that the lenticular $\alpha_s$ precipitates formed inside the retained $\beta$ during precipitation hardening.**

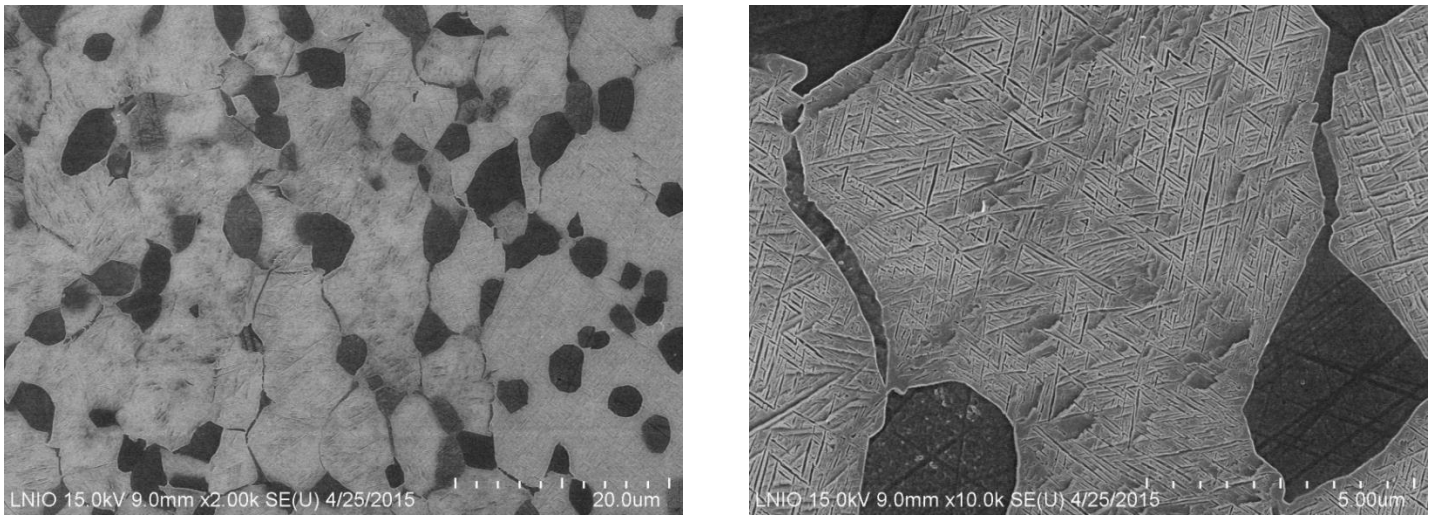


**Fig. 4-4. SEM images of the microstructure of Ti-18 alloy (longitudinal section): (a) A low-magnification image; (b) A higher magnification image.**

are surrounded by the transformed $\beta$ matrix which includes the retained $\beta$ phase and the precipitated $\alpha_s$ phase. The grain size and volume fraction of globular primary $\alpha_p$ phase were estimated by using image processing technique, and the results are listed in Table 4-3. Note that there is no apparent aspect ratio of the grains and texture structure can be seen on the transverse section [197].

**Table. 4-3 The microstructure morphology of the heat-treated Ti-18 alloy.**

| Texture (section) | Average size of $\alpha_p$ ($\mu$m) (range) vol% | Average size of retained $\beta$ ($\mu$m) (range) | Lenticular $\alpha_s$ in transformed $\beta$ ($\mu$m) |
|---|---|---|---|
| Transverse | 2.4 (1.5-4.5) 17.8% | 8.0 (3.0-14) | Width. 0.05-0.2 Length 0.2-3.5 |
| Longitudinal | 3.5 (2.0-5.5) 17.8% | 9.5 (3.0-16) | Width. 0.02-0.1 Length 0.2-2.5 |

## 4.2 Preparation of fatigue specimens

### 4.2.1 Manufacture of specimens

In order to perform series of fatigue tests, several fatigue specimens were prepared. According to the standard ASTM E466-07 [2], the smallest dimensions of specimen, as shown in Fig. 4-5(d), were chosen for saving as much material as possible. One piece of material was cut off from the center of the ingo. Then, 18 cylinders were cut off from it by wire-cutting electric discharge machining (WEDM). These cylinders were finally treated with fine turning for reaching the desired dimensions. The whole process is shown in Fig. 4-5.

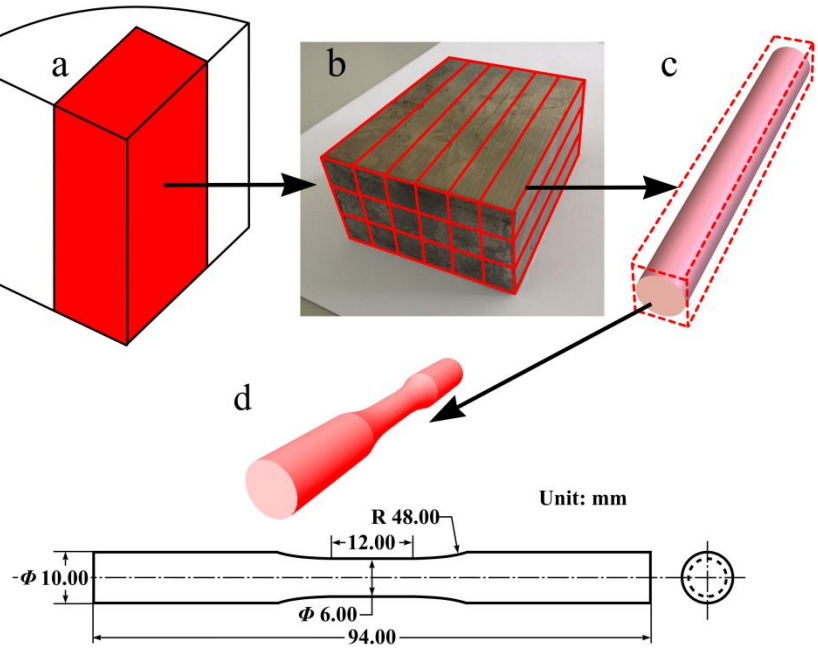


**Fig. 4-5. The whole process for preparing the fatigue specimens.**

### 4.2.2 Surface roughness test

Fatigue facture of metallic materials is normally a surface-sensitive damage form. So, checking the surface roughness of specimens before performing fatigue test is important. In

this study, it was analyzed with Taylor-Hobson Surtronic 3+ Roughness gage (Taylor Hobson Ltd., Leicester, UK) which is a 1D testing system. Considering the length of the calibration part of the fatigue specimens and the difficulty of surface roughness measurement with 1D equipment, $\lambda_c$=0.8 mm and $L_m$=4.0 mm were chosen. The results were listed in Table 4-4 and an expecimen roughness profile was shown in Fig. 4-6.

**Table 4-4 Surface roughness of the Ti-18 fatigue specimens.**

| | Ra ($\mu$m) | Rp ($\mu$m) | Rv ($\mu$m) | Rt ($\mu$m) |
|---|---|---|---|---|
| Mean value | 0.946 | 2.485 | 1.973 | 5.351 |
| Standard deviation | 0.067 | 0.262 | 0.320 | 1.021 |

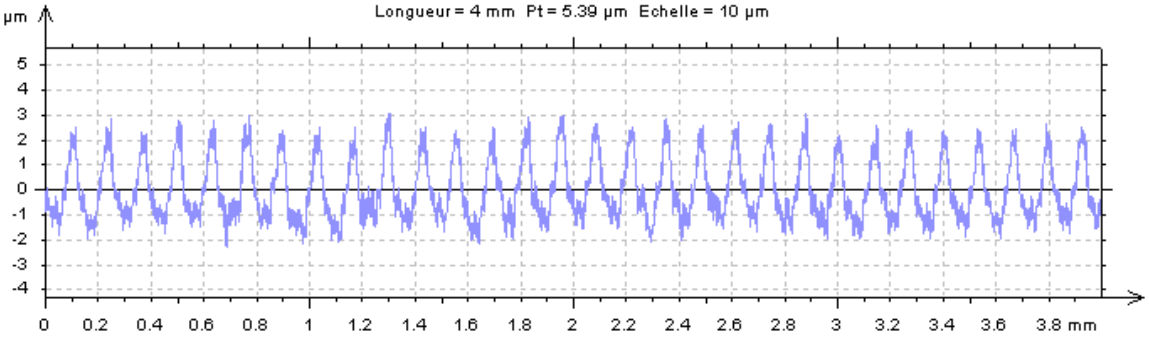


**Fig. 4-6. Surface roughness profile of the Ti-18 fatigue specimen (No.2).**

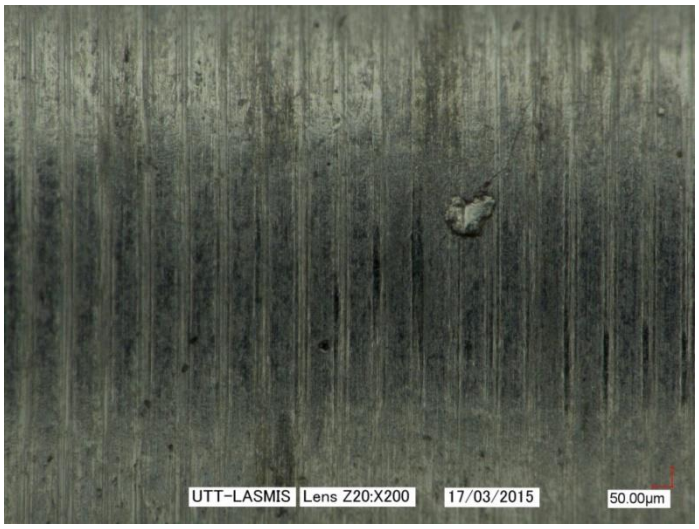


**Fig. 4-7. Surface observation of the Ti-18 fatigue specimen (No.2) under numerical microscope.**

Under numerical microscope, surface topography of the fatigue specimens was observed, as shown in Fig. 4-7. The tread-like texture caused by the fine turning process can be seen very clearly, which is consistent with the surface roughness results. One thing need to be mentioned is that the standard ASTM E466-07 [2] recommends that removing the final 0.025 mm on the top surface by polishing longitudinally to impart a maximum surface roughness of 0.2-$\mu$m Ra in the longitudinal direction. However, considering that there is no very proper way to polish the specimen longitudinally and maintain the dimensional accuracy of the specimen, we did not make any further surface treatment on the raw fatigue specimens.

## 4.3 Pretreatment of fatigue specimens

In order to study the influences of both residual stress and work hardening on low cycle fatigue responses, a simple Design Of Experiment (DOE) was conducted. Twelve specimens, with four different mechanical states were considered:

A) Raw specimens from turning (Raw);
B) Raw specimens + tensile plastic prestrain (Prestrain);
C) Raw specimens + shot-peening (SP);
D) Raw specimens + tensile plastic prestrain +shot-peening (Prestrain & SP).

Specimens in C) and D) will exhibit significant compressive residual stress gradient in the surface region due to shot-peening. Specimens of state A may have some residual stresses owing to turning. However, residual stresses induced by turning process in specimens of state B should be fully eliminated. The comparison between C and A, and between D and B, can show the effects of both residual stress and work hardening due to peening. The contrast between B and A, and between D and C, can indicate the influences of a homogeneous plastic strain. The comparison between D and A, and between C and B can reveal interaction between shot peeing and prestraining.

Another ideal state would have been to generate compressive residual stresses without work hardening, but, this is not feasible in practice. One possible substitute would be using laser shock peening to introduce compressive residual stresses accompanied with a relatively low accumulated plastic strain. However, this was not available for the present study.

For each of these 4 mechanical states, tensile cyclic tests, in strain control mode will be performed with 3 total strain amplitudes: 0.7%, 1.0% and 1.4% ($\Delta\varepsilon/2$) with a loading ratio $R_\varepsilon=0$, in order to follow the relaxation of the applied mean stress and of the residual stress

### 4.3.1 Prestraining

In order to investigate the effects of homogeneous plastic strain during fatigue tests, six specimens need to be prestrained. An ideal situation would be to achieve an accumulated plastic strain of the same magnitude as obtained during shot-peening process. However, during a tensile test, the specimen will break long before reaching the desired strain level. Furthermore, the cyclic test will also introduce an accumulated plastic strain. In order to guarantee that the fatigue specimens can reach a number of cycles high enough to induce a significant relaxation of residual stresses and applied mean stress, a total strain of 3.2% (plastic strain 1.8%) was chosen as the loading condition for the pre-strain procedure. Comparing with the possible plastic strain level that can be induced by the shot-peening process, this amount of prestain value is not so much. However, shot-peening induced high plastic strain only distributes in the surface region, while prestrain induced plastic strain uniformly distributes on the whole cross section. Considering this, the impacts of 1.8% prestrain might be comparable with the effects of shot-peening process.

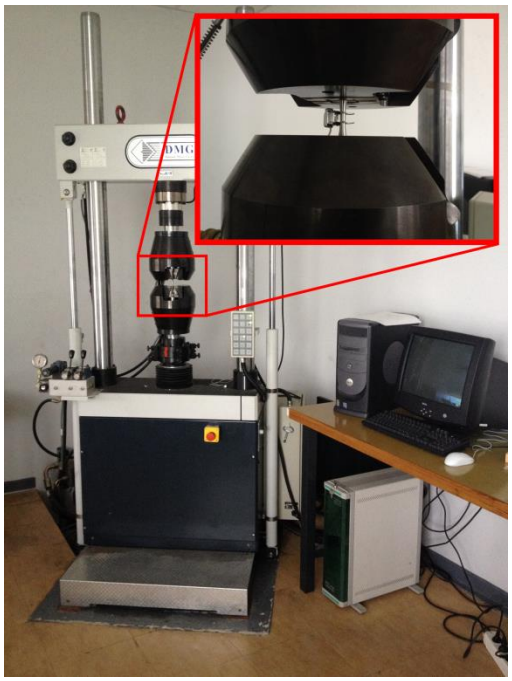

**Fig. 4-8. Denison Mayes Group (DMG) 100 kN hydraulic fatigue frame.**

The tensile pre-strain process was conducted on a Denison Mayes Group (DMG) 100 kN hydraulic fatigue frame (Denison Mayes Group Ltd., Beeston, UK), as shown in Fig.4-8, under monotonic loading module.

The tensile true stress vs true strain curves of all the prestrained specimens are listed in Fig. 4-9. All the 6 specimens came from the center part of the ingot and prestrained under exactly the same condition, however, their tensile responses are not exactly the same. From the up-right zoom-up of Fig. 4-9 it could be seen clearly that the strengths are divided into 3 groups. The strength of No.8 and No.11 are highest, the strength of No.5 and No.10 are lowest, and the strength of No.6 and No.9 stay in the middle. The same sequence can also be observed in the elastic range, as shown in the down-left zoom-up of Fig. 4-9. Even if all the specimens were taken from the ingot center, a slight heterogeneity may still be present. This is one way to explain the difference among these curves. However, the exact reason is hard to say. In order to figure this out, further investigations on Ti-18 alloy need to be conducted in the future. However, it is still worthy to pay attention to this kind of difference in is study, because this kind of difference can directly affect the cyclic behavior of the specimens which will be shown later on.

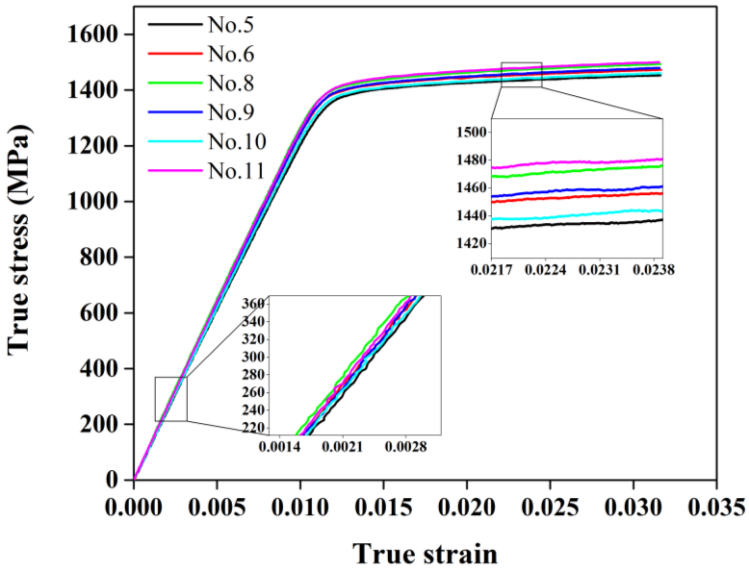


**Fig. 4-9. True stress-true strain curve of the tensile pre-strain process.**

## 4.3.2 Shot-peening

### 4.3.2.1 Determination of treating parameters

For the purpose of comparing the shot-peening process on cylindrical specimens of Ti-18 with what had been done on the flat specimen of T40, some simulations were made for determining proper treatment parameters which can approximately give the same impact density for the two cases.

These simulations are based on a model developed by Badreddine *et al*. [198]. Fig.4-10 presents the geometric model for the simulation on both the flat and the cylindrical specimens. Cylindrical chambers are modelled according to the actual dimension of the equipments. The sonotrode is positioned at the bottom of the chamber and its vibration is modeled with a triangular signal characterized with a frequency F and amplitude A. A number N of rigid spheres of diameter D represents the spheres that compose the shot. The total mass of the shot is 20 g. The flat specimen is fixed on the top of the chamber, whereas the cylindrical specimen is positioned in the center of the chamber.

The aim of these simulations is to find out the power and the time which give approximately the same impact density for cylindrical specimens as the parameters in Table 3-2 had given on the flat specimen. Two things need to be explained. The first thing is that for the flat specimen, the impact density is calculated from the whole shot-peened surface. However, the impact density of the cylindrical fatigue specimen is calculated only from the surface of the calibrated part (the red cylinder shown in the zoom-up of Fig 4-10(b)), because that only this part is meaningful and important for fatigue tests. The second thing is that the flat specimen is fixed on the top of the chamber during shot-peening process, while the cylindrical specimen is rotated with a constant speed (0.5 rotation per second) in the center part of the chamber in order to make sure that all the calibrated part is treated uniformly. The shot-peening parameters for

the cylindrical specimens determined by simulations are listed in Table 4-5 for making comparison with the parameter in Table 3-2.

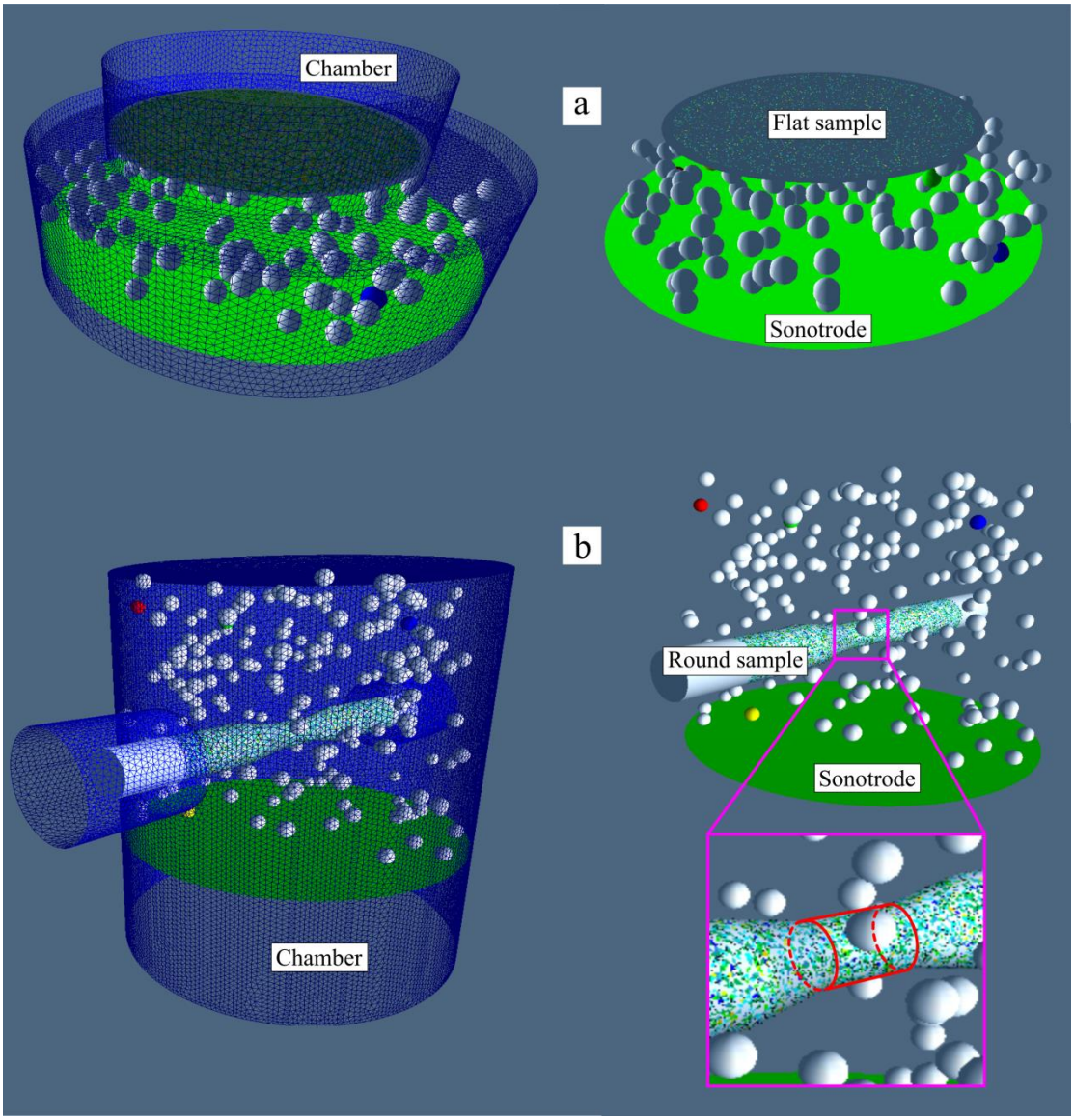


**Fig. 4-10. Geometric model used in the shot-peening simulations.**

**Table 4-5 comparison between the shot-peening parameters of the flat specimen and the cylindrical specimen**

| Parameters | Flat specimen | Cylindrical specimen |
|---|---|---|
| Diameter of shot (mm) | 3 | 3 |
| Mass of shot (g) | 20 | 20 |
| Material of shot | 100Cr6 | 100Cr6 |
| Distance between specimen and sonotrode (mm) | 15 | 15 |
| Power (%) | 27 | 37% |
| Duration (min) | 10 | 22 |
| Impact numbers | 747074 | 94334.4 |
| Impact densities (impacts/mm$^2$) | 421.8 | 417.3 |

#### 4.3.2.2 Shot-peening treatment

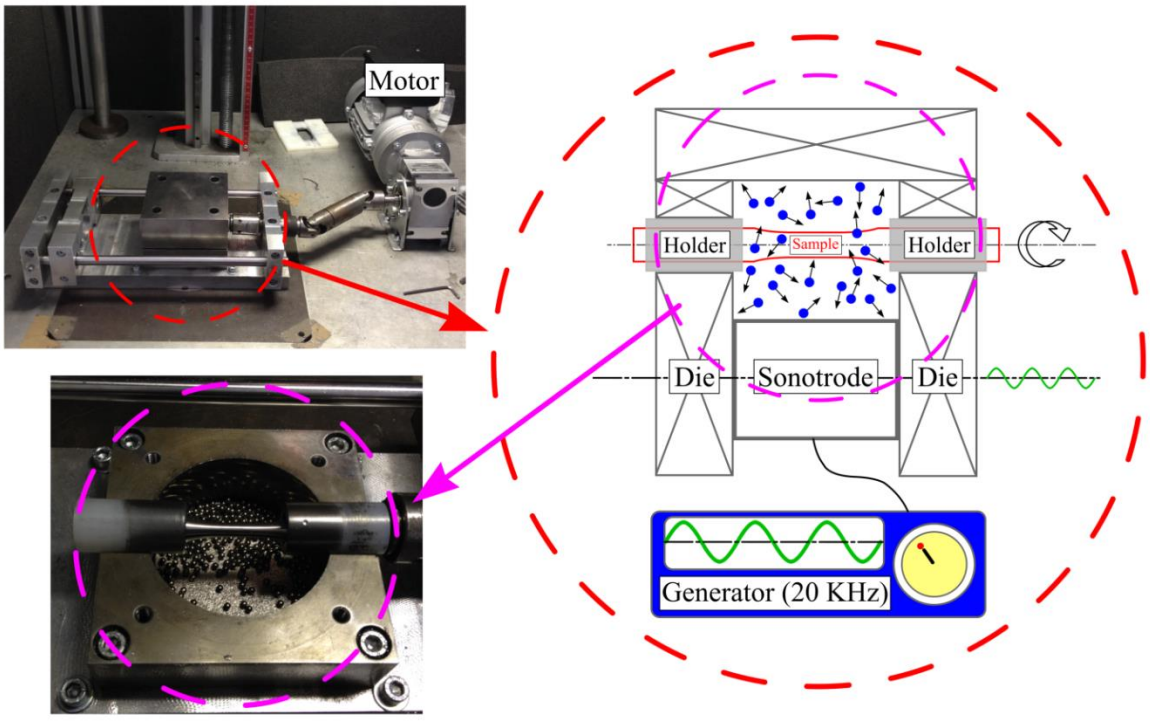


**Fig. 4-11. Set-up of the shot-peening equipment for Ti-18 fatigue specimens.**

After the treating parameters were determined through simulations, shot-peening is performed on Ti-18 specimens. The set-up of the shot-peening equipment is shown in Fig.4-11. One end of the fatigue specimen is fixed on one side of a Hooke's joint. The other end of the Hooke's joint is fixed on a motor for rotating the specimen during shot-peening. Then, the two grip ends of the fatigue specimen are held by two plastic holders to help the rotation of the specimen and the closeness of the chamber. After putting the shots into the lower half of the chamber, the two parts of the chamber are screwed together tightly to form a closed space, together with the plastic holders and the sonotrode. After launching the motor and sonotrode, the specimens are shot-peened with the power of 37% for 22 minutes.

Eight specimens were shot-peened. Four of them are raw specimens and the other four are prestrained specimens. Shot-peening can severely affect the surface roughness of specimens. Thus, the surface roughness values of the shot-peened specimens are checked as well. The results are listed in Table 4-6 and an example of roughness profile is shown in Fig. 4-12. The observation of the shot-peened surface was performed under numerical microscope, as shown in Fig. 4-13.

**Table 4-6 Surface roughness of the shot-peened Ti-18 fatigue samples.**

| | Ra ($\mu$m) | Rp ($\mu$m) | Rv ($\mu$m) | Rt ($\mu$m) |
|---|---|---|---|---|
| Mean value | 0.547 | 1.601 | 1.537 | 3.750 |
| Standard deviation | 0.041 | 0.173 | 0.122 | 0.295 |

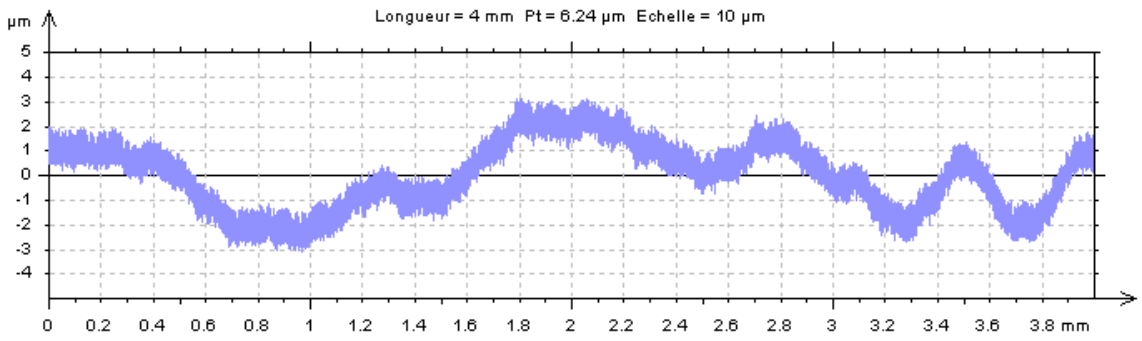


**Fig. 4-12. Surface roughness profile of the Ti-18 fatigue specimen after shot-peening (No.2).**

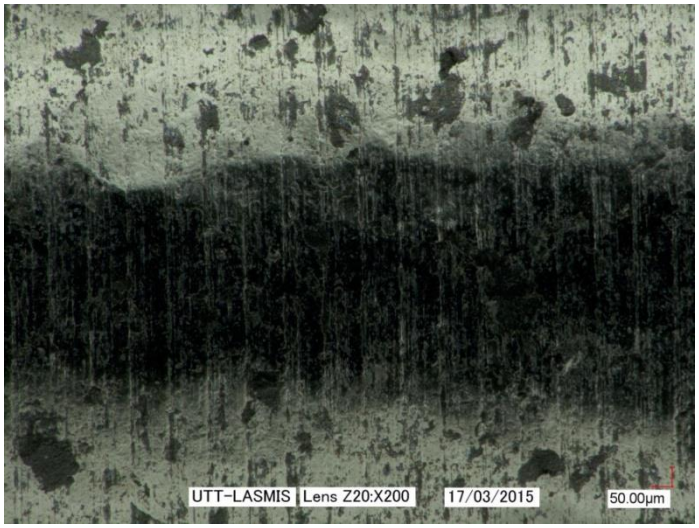


**Fig. 4-13. Surface observation of the shot-peened Ti-18 fatigue specimen (No.2) under numerical microscope.**

From Fig. 4-13 we can see that the shot-peening process has erased most of the screw-like texture on the surface of the fatigue specimen. This could be one factor which can improve the fatigue performance of the specimens. Both Table 4-6 and Fig. 4-12 supported the microscope observation results that surface roughness has been obviously improved by shot-peening.

## 4.4 Fatigue tests

### 4.4.1 Determination of experimental condition

In this study, we mainly focus on the evolutions of the surface residual stress and plastic strain induced by shot-peening process during low cycle fatigue tests. As mentioned in Chapter 1, in order to understand the similarity and the difference between the relaxation behavior of the mean stress and that of the surface residuals stress, strain controlled alternative fatigue tests ($R_\varepsilon$=0) will be performed and discussed in this chapter.

As shown in Fig. 1-9, along with the increase of strain amplitude, the relaxation behavior of mean stress (probably even of the surface residuals stress) will vary. In order to observe this kind of variation clearly, LCF test under several typical strain amplitudes need to be performed. However, since only 18 specimens were manufactured, it is impossible to choose proper

loading conditions by attempting with several specimens with various conditions. In order to overcome the shortcoming of specimen numbers, a special procedure was used for the selection of loading conditions.

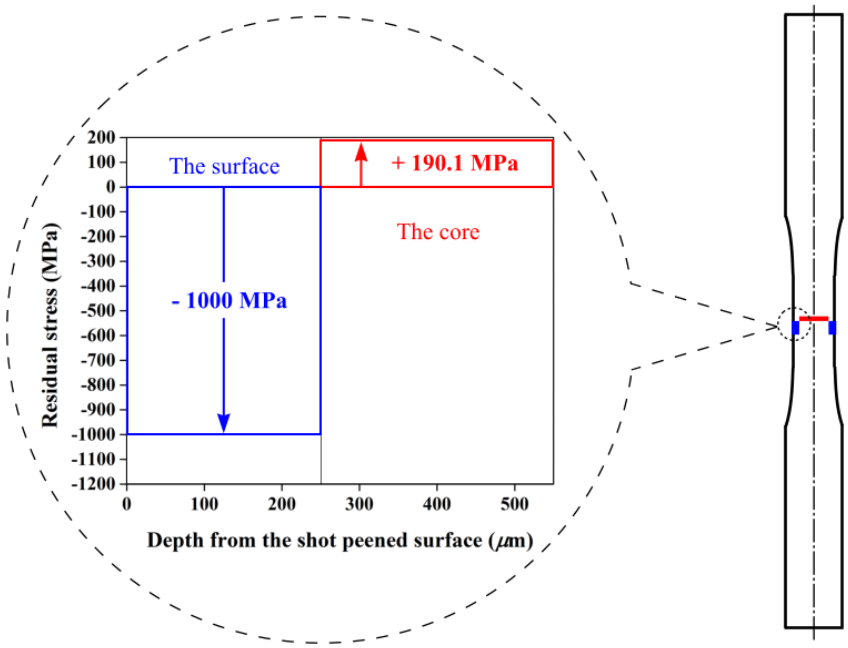


**Fig. 4-14. Schema of the simplification of the residual stress profiles in the shot-peened cylindrical fatigue samples.**

Research in Chapter 3 showed that shot-peening process with the parameters listed in Table 3-2 can produce a maximum compressive stress the absolute value of which is even higher than the yield stress of T40 grade 2 CPT. In fact, this is quite normal considering the work hardening behavior of T40 grade 2 CPT. Seeing this and the uniaxial tensile property of Ti-18 alloy, we can make a simplified assumption that shot-peening will respectively induce a uniform compressive residual stress and a uniform tensile residual stress , which are balanced over the cross section of a Ti-18 fatigue specimen. The compressive residual stress value is supposed to be -1000 MPa in the surface 250-$\mu$m layer. Considering the stress equilibrium inside the calibrated part of the fatigue specimen, the uniform tensile residual stress value can be calculated to be +190.1 MPa, as sketched in Fig 4-14.

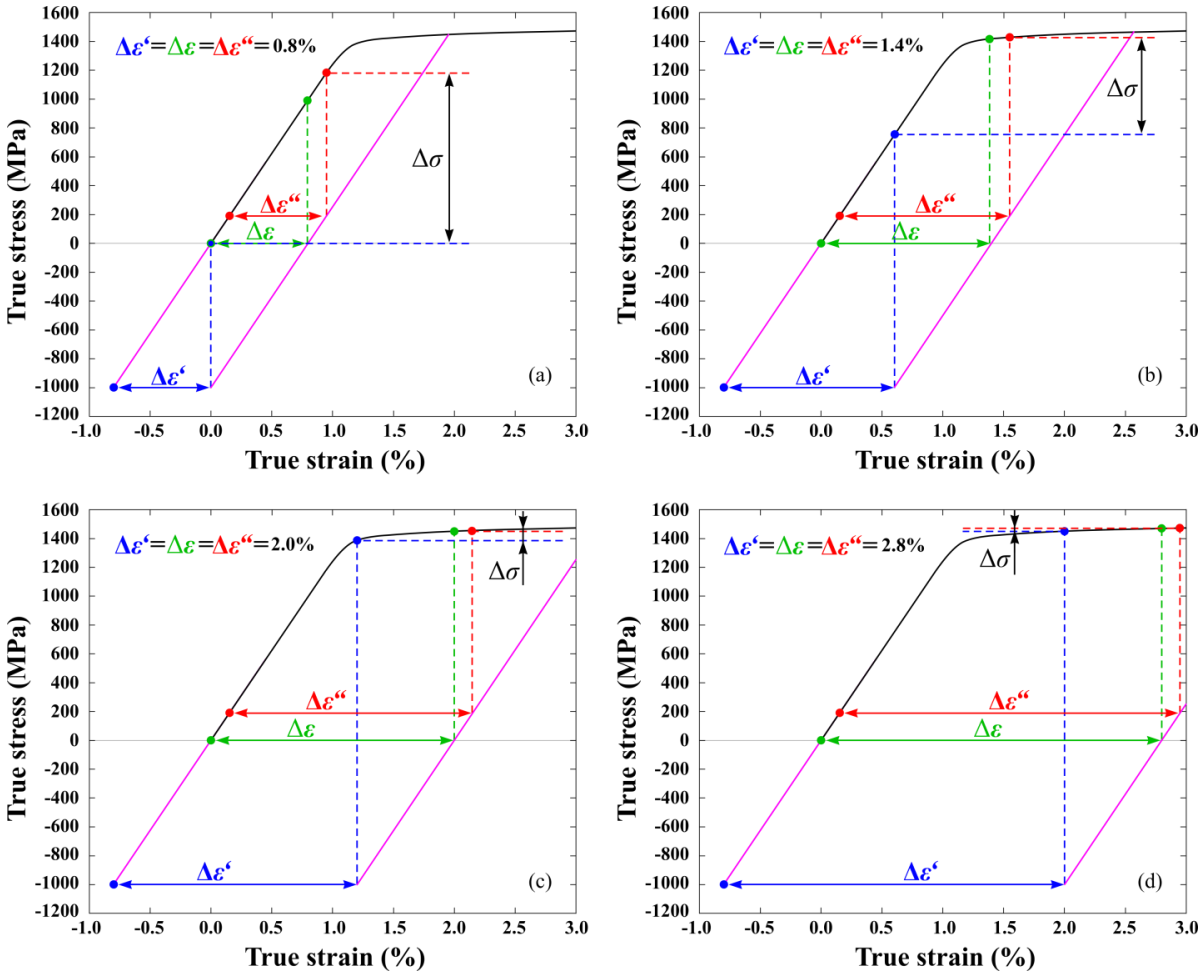


**Fig. 4-15. Choosing various loading condition from the pure structural point of view: (a) 0.8% tensile strain (stress in the surface region will become zero); (b) 1.4% tensile strain (only the core and the overall specimen is plastified a bit but the surface region is still in elastic range); (c) 2.0% tensile strain (the surface region is plastified a little bit, while the core and the overall specimen are highly plastified); (d) 2.8% tensile strain (all parts of the whole specimen are highly plastified). Δ$\sigma$ is the difference between the stress in the core and in the shot-peened layer after the first half of loading cycle.**

With the simplification and assumption above, we can approximately extract some key information with the uniaxial tensile stress-strain curve of Ti-18 from a pure structural point of view (the possible effects of material properties are not taken into account), which can help us to decide the load conditions. When the specimen goes through the tensile stage of a fatigue cycle, the deformation should be uniform (if the cross sections remain plane), which means that all the points on the radial cross section of the calibration part should have the same strain value. If we set the strain in the surface layer (with compressive residual stress) as $\Delta\varepsilon$', the strain in the core region (with tensile residual stress) as $\Delta\varepsilon$'' and the averaged strain on the whole cross section as $\Delta\varepsilon$, then we should have $\Delta\varepsilon'=\Delta\varepsilon=\Delta\varepsilon''$. Taking the residual stress values we estimated before into the uniaxial tensile curve of Ti18, with various tensile loads, stress levels in different parts of the specimen can be estimated as shown in Fig. 4-15.

Considering the results shown in Fig. 4-15, three different strain amplitudes (0.7%, 1.0% and 1.4%) were determined as our loading conditions. In order to understand this determination well, we firstly need to know that how residual stress relaxation happens during low cycle fatigue test. There are mainly two kinds of relaxation mechanisms. First, there is a structural relaxation linked to the global equilibrium of the cross section. Plastification in the core region will reduce the incompatibility between the shot-peened layer and the core. Sequentially, compressive residual stresses induced by shot-peening will relax even if the surface region has remained purely elastic. Only one cycle of loading is necessary for this process. Second, there is a relaxation linked to a local plasticity in the surface region which diminishes the incompatibility among different layers progressively. This process will require several cycles to accumulate enough microplasticity to show its effect at the global scale.

In our case, $\Delta\varepsilon/2$=0.7% is expected to exhibit the smallest relaxation of residual stress because only a bit of plastic deformation in the core, but the surface region is still in the elastic range. Since the surface region with compressive residual stresses will be plastified a bit with $\Delta\varepsilon/2$=1.0%, it is expected to exhibit moderate relaxation at this loading level. As for $\Delta\varepsilon/2$=1.4%, owing to the relatively large plastic deformations that will occur in all parts of the specimen, the relaxation of residual stress should be the most severe one. By choosing these various strain amplitudes, we expect to be able to observe and study the relationship between strain amplitude and the relaxation of residual stress. The amount of relaxation can be represented by the quantity $\Delta\sigma$, as shown in Fig. 4-15, which is the stress difference between the core and the surface region after the first half of loading cycle. If the unloading

Seeing the possible specimen states and loading conditions, all the fatigue test situations are summarized in Table 4-7.

**Table 4-7 All the fatigue test situations determined with possible sample states and loading conditions.**

| | $\Delta\varepsilon/2$ | | | |
|---|---|---|---|---|
| | 0.0% | 0.7% | 1.0% | 1.4% |
| Raw | - | No.15 | No.1 | No.18 |
| SP* | No.14 | No.2 | No.4 | No.3 |
| Prestrain | - | No.8 | No.6 | No.5 |
| Prestrain & SP | No. | No.11 | No.10 | No.9 |

## 4.4.2 Fatigue tests

Fatigue tests were performed on the same DMG hydraulic fatigue framework as shown in Fig. 4-8. An extensometer with a 10-mm gauge length was used for controlling the fatigue tests under controlled stain amplitudes. A triangular waveform (with R=0) was used to apply the load with a constant strain rate of $10^{-3}$. Since we are mainly interested in the relaxation of residual stress, which can be approximately represented by the relaxation of mean stress ($\sigma_{mean}$), the specimens do not have to be broken. Once the relaxation of $\sigma_{mean}$ is stabilized, the test will be terminated. Observation showed that for 0.7% and 1.4% strain amplitudes conditions will be stopped at 100 cycles. As for $\Delta\varepsilon/2$=0.7%, number of cycles will be

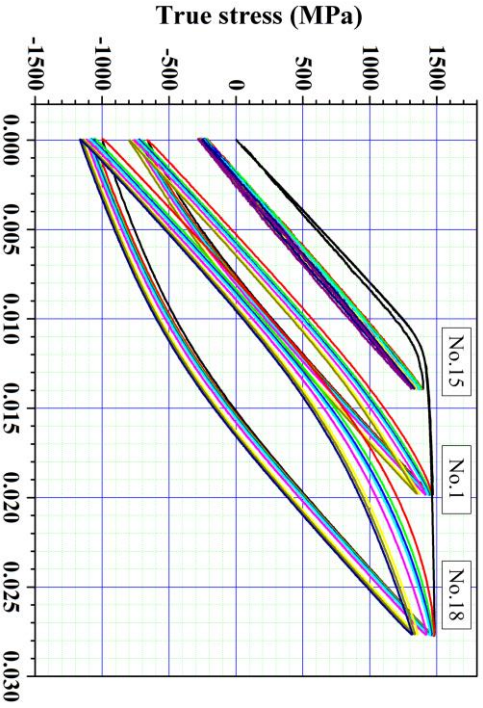


**Fig. 4-16. Cyclic stress-strain curves of raw Ti18 specimens: No.15 ($\Delta\varepsilon/2$=0.7%), No.1 ($\Delta\varepsilon/2$=1.0%) and No.18 ($\Delta\varepsilon/2$=1.4%).**

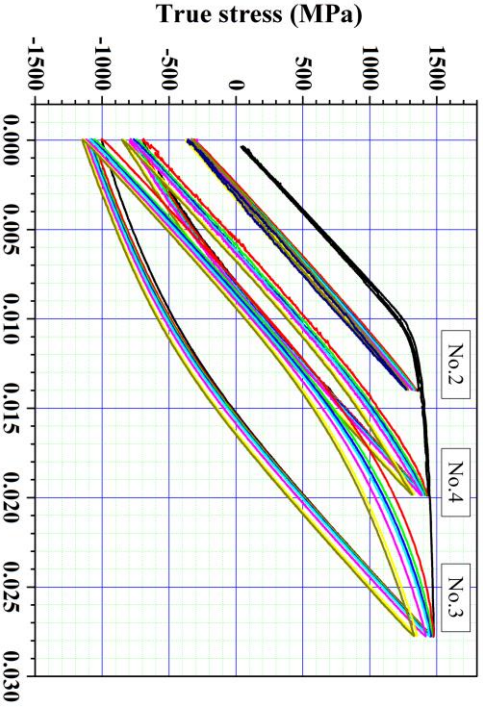


**Fig. 4-17. Cyclic stress-strain curves of shot-peened Ti18 specimens: No.2 ($\Delta\varepsilon/2$=0.7%), No.4 ($\Delta\varepsilon/2$=1.0%) and No.3 ($\Delta\varepsilon/2$=1.4%).**

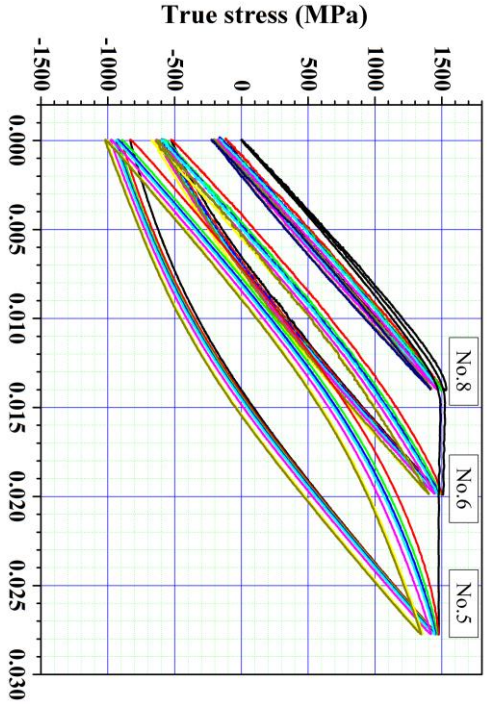


**Fig. 4-18. Cyclic stress-strain curves of pre-strained Ti18 specimens: No.8 ($\Delta\varepsilon/2$=0.7%), No.6 ($\Delta\varepsilon/2$=1.0%) and No.5 ($\Delta\varepsilon/2$=1.4%).**

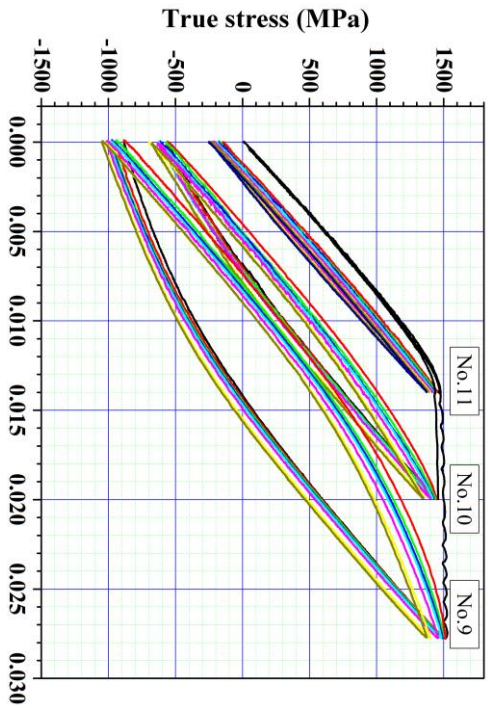


**Fig. 4-19. Cyclic stress-strain curves of pre-strained and shot-peened Ti18 specimens: No.11 ($\Delta\varepsilon/2$=0.7%), No.10 ($\Delta\varepsilon/2$=1.0%) and No.9 ($\Delta\varepsilon/2$=1.4%).**

increased to 140 cycles, because the stabilization is a bit more difficult to decide.

#### 4.4.2.1 Cyclic true stress vs true strain curves

Cyclic true stress vs true strain curves of all the fatigue tests were listed in Fig. 4-16, Fig. 4-17, Fig. 4-18 and Fig. 4-19. For all the four material states, along with the increase of imposed strain amplitudes, the opening of the hysteresis loops (cyclic plastic strain values) increases as well.

Theoretically, for each material state with different strain amplitudes, the tensile part of the first cycles should be superposed, because all the specimens are of the same material state. However, slight heterogeneity exists in the response of some specimens, such specimen No.15 in Fig. 4-16, specimens No.8, No.6 and No.5 in Fig. 4-18 and specimen No.10 in Fig. 4-19. The reason of this kind of difference is probably the variance of material properties among specimens as well, which will directly affect the values of several key fatigue responses, such as maximum stress ($\sigma_{max}$), minimum stress ($\sigma_{min}$) and so on. Furthermore, comparison between Fig. 4-16 and Fig. 4-18 showed that the introduction of prestrain decreases the stress amplitude obviously. No obvious cyclic hardening or softening can be directly observed from these cyclic true stress vs true strain curves. To obtain cyclic hardening or softening information, some further treatments of the data need to be done, which will be discussed latter.

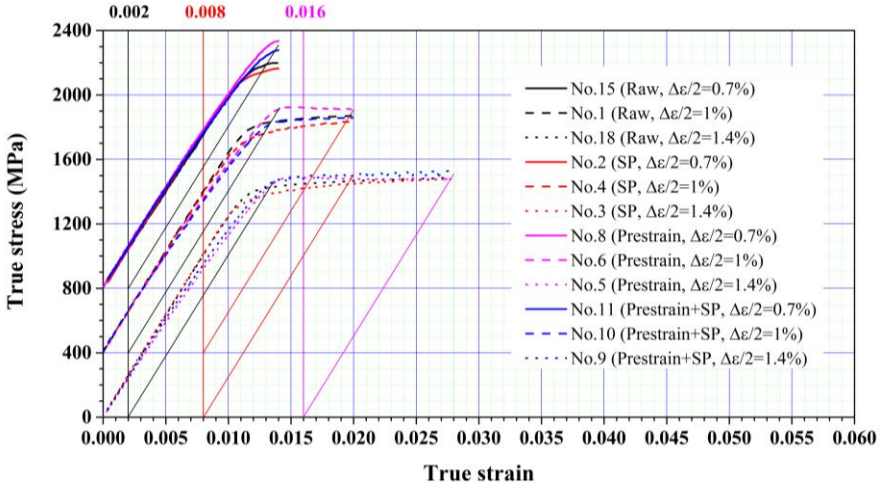


**Fig. 4-20. Tensile part of the 1st cycle of all the fatigued specimens.**

As for the tensile part of the first cycles, observation of Fig. 4-16, Fig. 4-17, Fig. 4-18 and Fig. 4-19 can only show the variance in each material state. In order to analyze it better, the tensile part of the first cycle of all the specimens were picked up and divided into three groups according to their strain amplitude, as shown in Fig. 4-20. A global feature of the first half-cycle of loading is that the treatment influences the hardening/softening behavior of the specimens.

- The raw specimen hardens weakly (~100 MPa) and is saturated at 2.5% total strain around 1500 MPa.

- The prestrained specimen begins softening almost immediately after the onset of plastification.

- The shot-peened specimen is work-hardened significantly (~250 MPa) and is also saturated at 2.5% total strain, around 1500 MPa.

- The prestrained & shot-peened specimen has a rather "flat" response, as if it had an intermediate behavior between the shot-peened and prestrained specimens. This behavior can be interpreted in the following way. The shot-peening did not really affect the "true" yield stress (~1250 MPa) but produced a longer elastoplastic transition as the different zones of the cross section plastify one after another (starting with the core exhibiting a tensile residual stress and followed by the surface region with compressive residual stress). Once the whole cross section is plastified, the two responses meet (for a plastic strain above 1% as can be seen in Fig. 4.15(c)).

After a prestrain of 1.8% of plastic strain, the material has almost reached its maximum hardening and starts to soften. For the prestrained & shot-peened specimen, this softening cannot occur before the elastoplastic transition is finished, which leads to the observed "flat" behavior.

The group of $\Delta\varepsilon/2=0.7\%$ showed clearly that the introduction of prestrain can obviously increase the yield stresses (elastic limit). This is because of the work hardening behavior exhibited by Ti-18, although it is not so high. On the opposite, shot-peening treatment will decrease the yield stresses a little bit (several tens of MPa). This is reasonable as well. Considering a simplified situation as shown in Fig. 4-14, when tensile load applied, the whole calibration part should stretch uniformly. Along with the elongation, because of the existence of tensile residual stress, the core will yield first. Similarly, compressive residual stress makes the surface region yield later than the core. The direct result of this kind of successive yielding makes the overall yield stress of the specimen decrease. As for the exact amount of the decrease, it highly depends on the magnitude and the distribution of residual stresses induced by shot-peening.

Similar phenomenon can be observed from the group $\Delta\varepsilon/2=1.0\%$ and $\Delta\varepsilon/2=1.4\%$ as well, however, with some difference. The curves of specimens No.6 and No.5 in Fig. 4-21 showed that slight necking (the decrease of plastic flow stress) has emerged after the prestrain process. However, the yield-decreasing phenomenon caused by shot-peening weakened the performance of necking, as shown by the curves of specimens No.10 and No.9. Furthermore, the curves of specimens No.5 and No.10 are a little bit abnormal: the former is mixed with the curve of specimen No.9 and the latter is mixed with the curve of specimen No.1. In order to know what happened, we have to look back to Fig. 4-9 which showed that the strengths of specimens No.5 and No.10 are about 20 MPa lower than the average strength. Thus, low strengths of specimens No.5 and No.10 should be the main reason of their abnormality shown in Fig.4-20.

Another strange thing in Fig.4-20 is that the introduction of prestrain changes the elastic part of the curves for the groups $\Delta\varepsilon/2=1.0\%$ and $\Delta\varepsilon/2=1.4\%$. However, there is no similar

phenomenon for group $\Delta\varepsilon/2$=0.7%. One possible reason is that the prestrain process changed the creep property of Ti-18. And, the variation of creep property became more obvious under higher strain amplitude. In addition, strength differential (SD) effects and the yield anisotropy of $\alpha$-phase titanium might be another explanation as well. And, this is why the shot-peening process showed some influences as well.

#### 4.4.2.2 Key fatigue responses

In order to analyze the stress and strain variation during fatigue process better, several critical fatigue responses, including maximum stress ($\sigma_{max}$), minimum stress ($\sigma_{min}$), mean stress ($\sigma_{mean}$) stress amplitude ($\sigma_a$) and cyclic plastic strain amplitude (half of the opening of the hysteresis loops, $\Delta\varepsilon_p/2$), were extracted from the cyclic true stress vs true strain curves, as shown in Fig. 4-16, Fig. 4-17, Fig. 4-18 and Fig. 4-19. Thereinto, $\sigma_{mean}$ has a role on the mean hydrostatic pressure and thus on fatigue crack initiation. The lower it is, the more difficult for the appearance of a crack. As for $\sigma_a$, it usually gives information on the cyclic hardening/softening behavior of the structure. Moreover, $\sigma_{mean}$ and $\sigma_a$ are independent quantity. They are calculated from $\sigma_{max}$ and $\sigma_{min}$. Once fatigue crack initiated, its propagation process is the accumulation of many sharpen-blunt cycles. Crack sharpening is correlated with $\sigma_{max}$ and crack blunting is correlated with $\sigma_{min}$. The original fatigue responses vs accumulated plastic strain were respectively divided into three groups according to their strain amplitude and plot in Fig. 4-21, Fig. 4-23, Fig. 4-25, Fig. 4-27 and Fig. 4-29. For the convenience of making comparison in each group, all the data were normalized by the corresponding values of the first cycle. All the normalized curves were plot in Fig. 4-22, Fig. 4-24, Fig. 4-26, Fig. 4-28 and Fig. 4-30.

Fig. 4-21 showed that $\sigma_{max}$ decreases during fatigue tests. Prestrained specimens have higher $\sigma_{max}$ values than those non-prestrained specimens. This is consistent with the fact that tensile prestrain process strengthened the specimens. While, along with the increase of $\Delta\varepsilon/2$, $\sigma_{max}$ of the non-prestrained specimens became higher. On the opposite, $\sigma_{max}$ of the prestrained specimens went lower. Finally, they went to nearly the same level, as shown in Fig. 4-21(c). This is because that slight necking had already happened to the prestrained specimens, which could be observed clearly from Fig. 4-20. Thus, increasing of $\Delta\varepsilon/2$ can continuously strengthen the non-prestrained specimens, but "soften" a little bit the prestrained specimens. Furthermore, shot-peening process made the $\sigma_{max}$ values become lower. Shot-peening process introduces compressive residual stresses in the surface and tensile residual stresses in the core of the specimen. When tensile load was applied, the surface will yield earlier than the core, the comprehensive effect of which is the overall yield strength of the shot-peened specimen will become lower, as shown in Fig. 4-20. However, this kind of yield stress decreasing can only happen in small plastic strain range. Once the plastic deformation in the specimen is large enough, the effects of shot-peening induced residual stresses will be covered. This is way the shot-peened and non-shot-peened curves in Fig. 4-20 converged with each other when $\Delta\varepsilon/2$=1.4%. Thus, along with the increase of $\Delta\varepsilon/2$, the gap between the

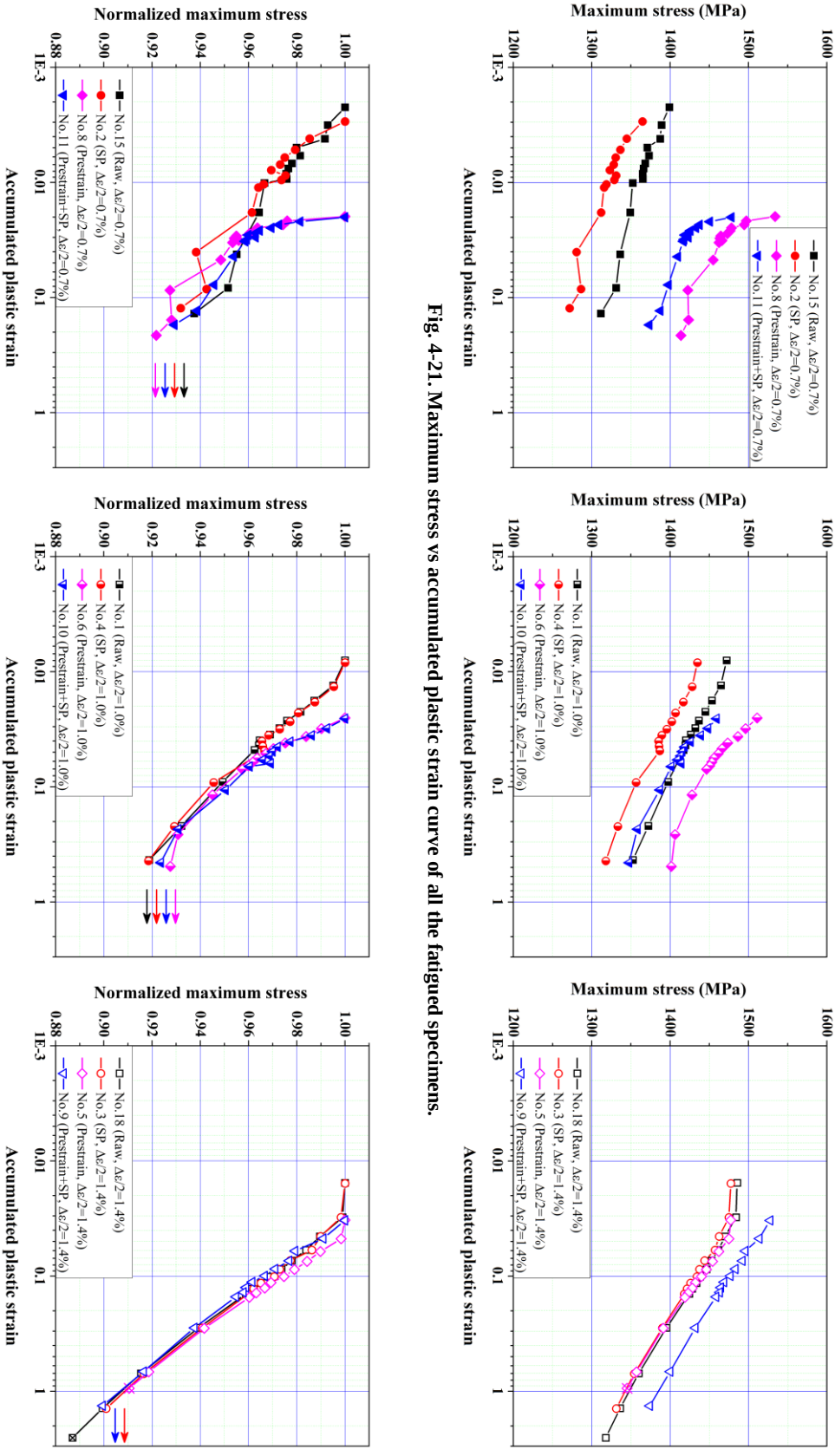


**Fig. 4-21. Maximum stress vs accumulated plastic strain curve of all the fatigued specimens.**




**Fig. 4-22. Normalized maximum stress vs accumulated plastic strain curve of all the fatigued specimens.**

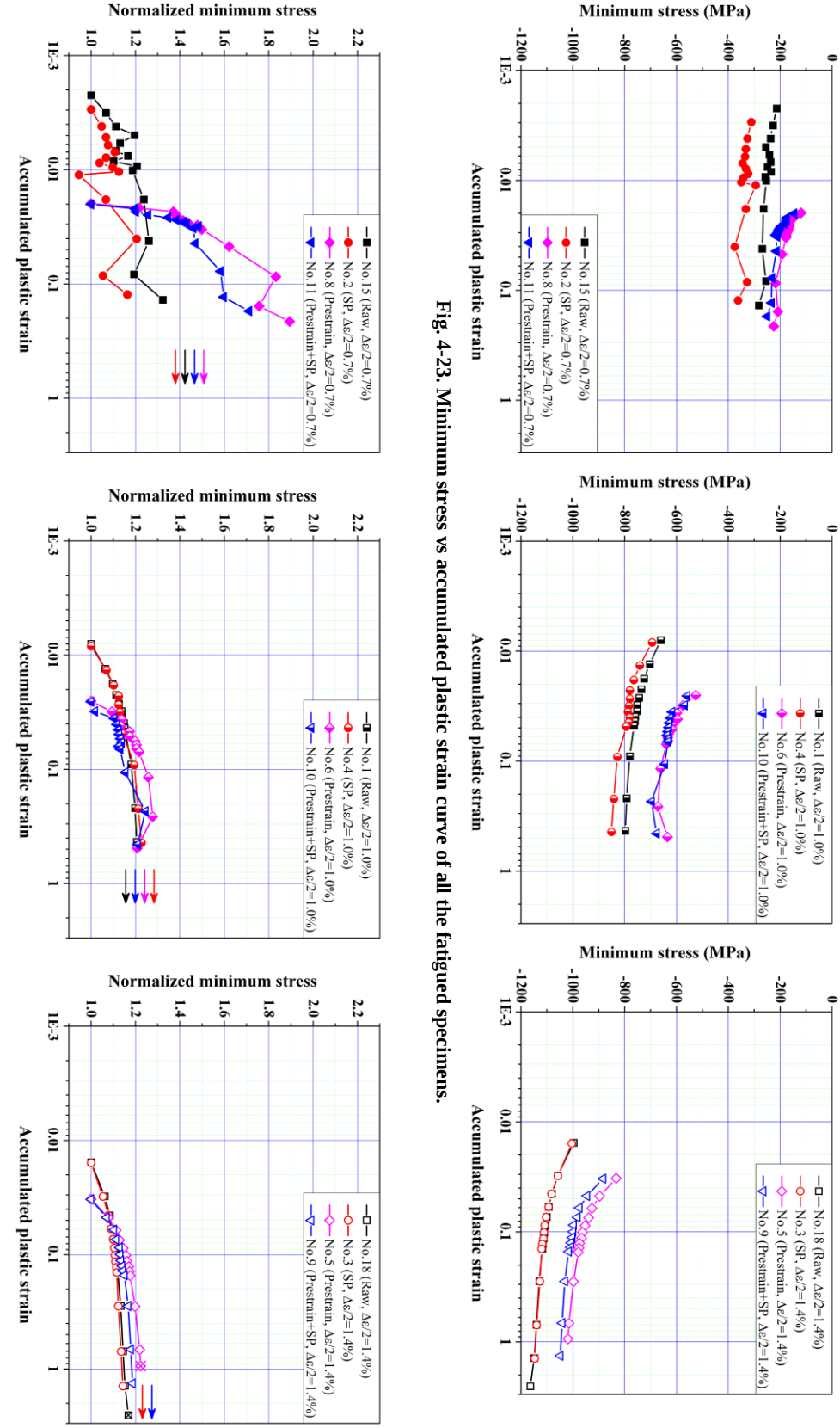


**Fig. 4-23. Minimum stress vs accumulated plastic strain curve of all the fatigued specimens.**




**Fig. 4-24. Normalized minimum stress vs accumulated plastic strain curve of all the fatigued specimens.**

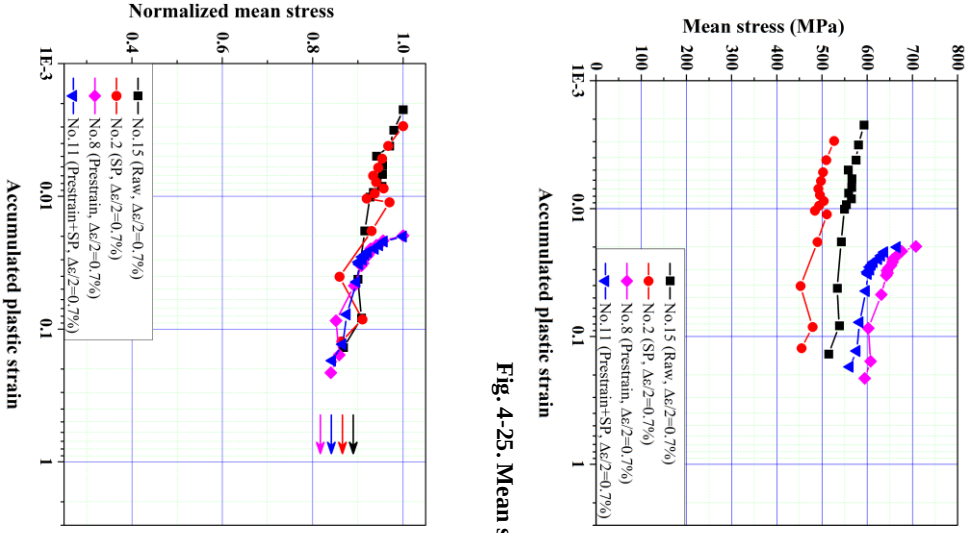


**Fig. 4-25. Mean stress vs accumulated plastic strain curve of all the fatigued specimens.**




**Fig. 4-26. Normalized mean stress vs accumulated plastic strain curve of all the fatigued specimens.**

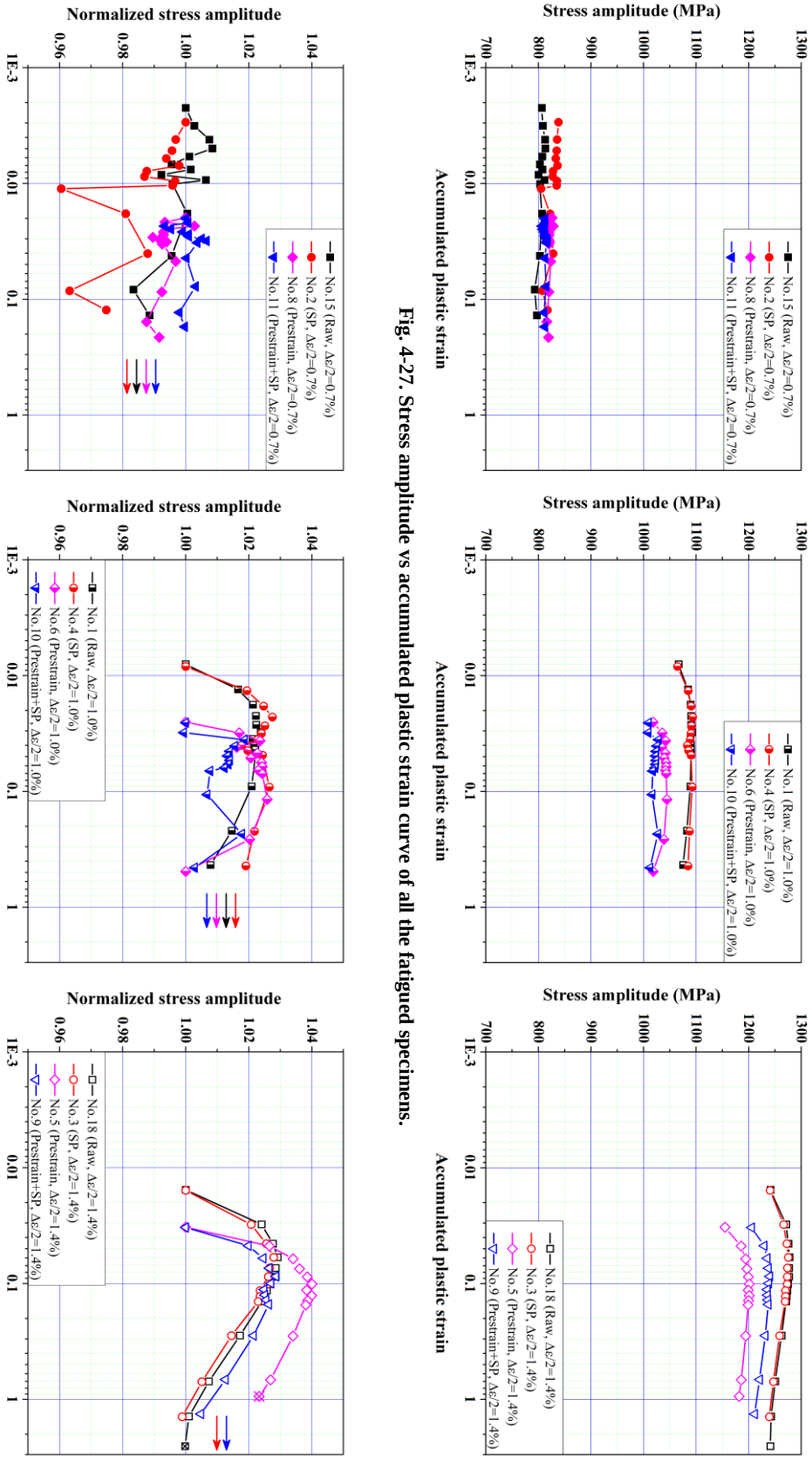


**Fig. 4-27. Stress amplitude vs accumulated plastic strain curve of all the fatigued specimens.**




**Fig. 4-28. Normalized stress amplitude vs accumulated plastic strain curve of all the fatigued specimens.**

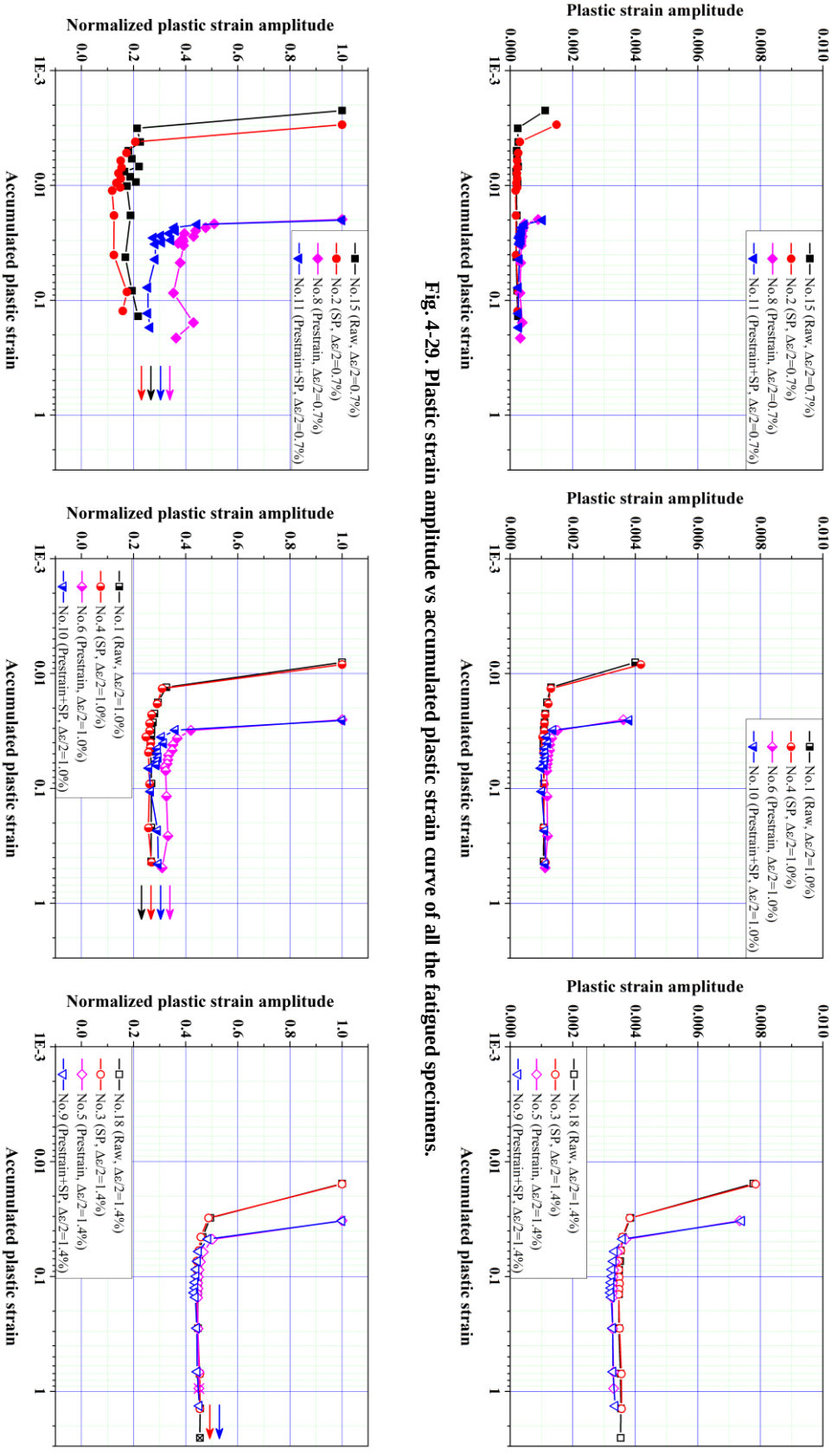


**Fig. 4-29. Plastic strain amplitude vs accumulated plastic strain curve of all the fatigued specimens.**




**Fig. 4-30. Normalized plastic strain amplitude vs accumulated plastic strain curve of all the fatigued specimens**

shot-peened and non-shot-peened specimens shrank, as shown in Fig. 4-21. Specimen No.9 is an exception which is hard to be explained. However, some clues can be obtained from Fig. 4-9 which showed that specimen No.9 is originally stronger than specimen No.5. Fig. 4-22 showed that shot-peening process can hardly influence the decreasing rate of the $\sigma_{max}$. However, prestrain process increased the decreasing rate of the $\sigma_{max}$ at the beginning. While, finally, decreasing rate of the prestrained and non-prestrained specimens still became the same. The effect of prestrain process became smaller along with the increase of $\Delta\varepsilon/2$.

Fig. 4-23 showed that $\sigma_{min}$ has the opposite phenomenon as $\sigma_{max}$, with only two exceptions. First, along with the increase of $\Delta\varepsilon/2$, $\sigma_{min}$ of all the specimens increased. Second, the gap between the prestrained and non-prestrained specimens did not decrease but increased. This is because that the tensile half-cycle (before the compressive half-cycle) had intensified the necking phenomenon introduced by the prestrain process. In addition, this kind of intensification will increase along with the increase of $\Delta\varepsilon/2$. Fig. 4-24 showed that when $\Delta\varepsilon/2$=0.7%, the increasing rate of $\sigma_{min}$ for the prestrained specimens are much higher than that for the non-prestrained specimens. However, along with the increase of $\Delta\varepsilon/2$, this kind of difference trend to disappear. This is because that shot-peening process can reduce both the overall tensile and the compressive yield stress of the specimen. However, $\Delta\varepsilon/2$ value large enough can cover the effect of shot-peening induced residual stresses.

The relaxation of $\sigma_{mean}$ is of great importance, for it can approximately represent the relaxation of residual stress. As expected, relaxation of $\sigma_{mean}$ occurred in all the three groups, and the higher strain amplitude exhibits the more relaxation, as shown in Fig. 4-25. Shot-peening process did not show obvious effects on the relaxation of $\sigma_{mean}$, no matter from the amount or from the rate. However, the influences of prestrain process are much more obvious. This is not so strange. The magnitude of compressive residual stress (several hundred MPa) and plastic strain (tens percent) induced by shot-peening can be quite high, however, the layer influenced by them is quite limited (only hundreds $\mu$m). While, prestrain can affect the whole cross section, which means that its effects should be significant even if its magnitude is relative low. The introduction of prestrain made the relaxation rate of $\sigma_{mean}$ at the initial stage for all the three groups increase severely. But, the finial relaxation rates of all the specimens in each group trended to be stable. This stable relaxation rate seemed to be correlated with $\Delta\varepsilon/2$. Higher $\Delta\varepsilon/2$ value made this stable relaxation rate higher as well, which can be seen from Fig. 4-26 more obviously. In addition, Fig. 4-26 also showed that prestrain decreased this stable relaxation rate, which means that for Ti-18 alloy, proper tensile prestrain process can effectively retard the relaxation of $\sigma_{mean}$ during low cycle fatigue tests, even if $\Delta\varepsilon/2$ reached as high as 1.4%.

The variations of $\sigma_a$ are important as well, because they can reflect the cyclic hardening/softening behavior of the specimens. Fig. 4-28(a) showed that specimens of all the four material stats are softened a bit during fatigue process without obvious differences. However, for the other two groups, all the specimens go through a hardening-to-softening process. For the groups $\Delta\varepsilon/2$=1.0% and 1.4 in Fig. 4-27(b) and Fig. 4-27(c), specimens without

prestrain exhibit more hardening than the specimens prestrained. This is reasonable, because the hardening behavior of Ti-18 tends to be saturated along with the increase of strain, as shown in Fig. 4-1. Thus, the prestrained specimen should have a lower hardening property. However, the difference between No.6 and No.10 and that between No.5 and No.9 in Fig. 4-27 are not normal. If we recall the prestrain stress vs strain curves shown in Fig. 4-9, this kind of abnormality might also be attributed to the difference of material properties. However, the normalized $\sigma_a$ curves of these specimens might still be useful. The curve of No.5 in Fig. 4-27 showed that prestrain & shot-peening can effectively keep the hardening in the specimen.

Fig. 4-29 showed that $\Delta\varepsilon_p/2$ decreased drastically at the beginning and became stable after only a few cycles. From the group $\Delta\varepsilon/2$=0.7% in Fig. 4-24 we could see that shot-peening will aggravate the cyclic softening a little bit. However, prestrain and prestrain & shot-peening can effectively inhibit the softening, especially the latter. However, the increase of strain amplitude can distinctly weaken the effects of prestain and shot-peening. For the group $\Delta\varepsilon/2$=1.4%, all the curves are superposed together, which means that the strain amplitude is high enough to thoroughly eliminate the effects of prestain and shot-peening.

## 4.5 X-Ray diffraction

For better understanding the influence of strain amplitude on the variations of residual stress and work hardening, X-ray diffraction tests were conducted as well. All the X-ray diffraction tests were performed on a 4-circle Seifert PTS-3000 X-ray diffractometer (now GE Inspection Technologies GmbH, Hürth, DE), equipped with a copper anode tube (40 kV and 30 mA, $K_\beta$ line is filtered by a Ni filter). {302} planes of $\alpha$ phase, with peak position at $2\theta_0$ =149.05°, was selected as the target peak for this study. A Position Sensitive Detector (PSD) which covers 11° was used to collect the diffracted signal. The scanning range was selected from 144° to 154°. The counting time is 220 s/step and the step size is 0.27 °2$\theta$.

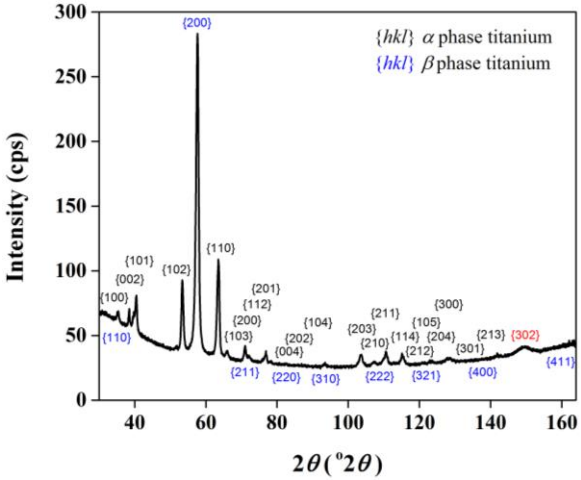


**Fig. 4-31. The X-ray diffraction pattern of Ti18 alloy.**

Two things need to be explained. The first thing is the reasons why the peak of {302} planes of $\alpha$ phase was selected. First, diffraction peaks with higher angle will be more sensitive

to residual stress and lattice distortion. Second, Ti-18 is a bi-phase titanium alloy, while, most of the peaks of $\alpha$ phase are mixed together with the peaks of $\beta$ phase as shown in Fig. 4-31 (especially at high angles), which arouses many troubles when extracting residual stresses from diffraction pattern. Actually, we tried to extract residual stresses with several peaks together (both $\alpha$ phase and $\beta$ phase), however, the results are terrible. Finally, we decided to use the peak of {302} planes of $\alpha$ phase, even if there is still some interferences caused by its neighbor peaks.

The second thing is that, as we mentioned in Chapter 1, measuring residual stresses with X-ray diffraction on the surface of a cylindrical part with small diameter is not a simple task. If not, we don't have to explore the new characterizing way with instrumented indentation. In order to reduce the problem caused by the dimension of the cylindrical part, black scotch tape, as we used in Chapter 3, was used again for covering most part of the specimen surface. Only a 3-mm narrow gap along the axial direction was opened for making diffraction, as shown in Fig. 4-32. In fact, literature suggested that the largest width of the gap should be ¼ of the diameter, which should be 1.5 mm for our case. However, the quality of the diffraction signal is so poor. Thus, did not have any other choice, we had to enlarge the gap a bit.

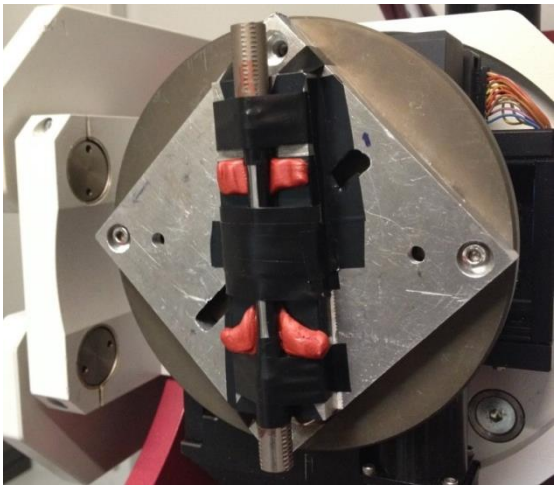

**Fig. 4-32. Protection of the Ti18 specimens for X-ray diffraction tests.**

For using $\sin^2\Psi$ method introduced in Chapter 1, 9 $\Psi$ angles (-60°, -45°, -30°, -15°, 0°, 7.5°, 22.5°, 37.5° and 52.5°) were selected. Since shot-peening usually produces an equibiaxial stress state, for the purpose of measuring residual stress in both axial and hoop direction, two $\Phi$ ($\Phi$=0° and 90°) directions were necessary. In order to avoid the unwanted diffraction caused by the specimen holder, all parts around the specimen were covered with black scotch tape. All the 12 fatigued specimens were measured with X-ray diffraction. Furthermore, another four specimens (one for each material state) without fatigue were tested as well for using as controls.

All the diffraction data were treated with a Wolfram Mathematica® script to obtain residual stress and peak broadening information. In fact, because of the geometric shape of specimens, disturbance of the neighbor peaks and the size of the gap, residual stress and peak width values

extracted in the hoop direction are quite abnormal. So, only the results in axial direction are selected in this study. Moreover, considering the number of specimens and the complexity and time of the electrolytic polishing procedure, only the residual stress and peak width information on the specimen surfaces are obtained, but not the whole profiles along depth. All the axial residual stresses obtained with X-ray diffraction tests were listed in Fig. 4-33.

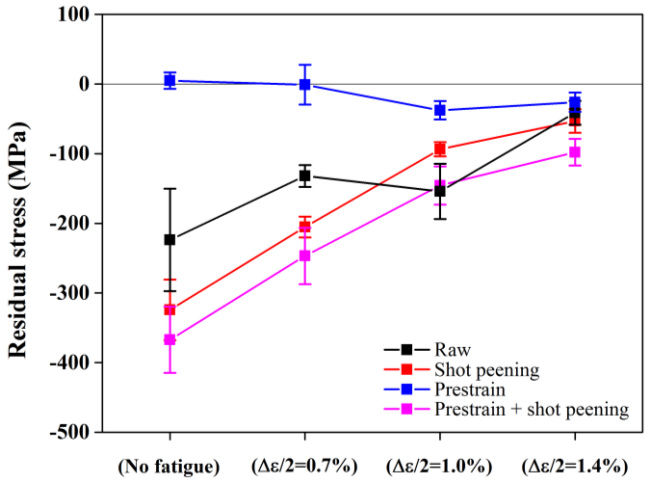


**Fig. 4-33. Axial residual stress of all the specimens obtained through X-ray diffraction.**

The black curve in Fig. 4-33 showed that about -200 MPa of residual stress, which might be induced by the manufacturing process, exists in the surface region of raw material. Along with the increase of strain amplitude, the pre-existed residual stress is relaxed more and more, which means that surface residual stresses can be obviously relaxed under cyclic loading. When $\Delta\varepsilon/2=1.4\%$, it is nearly completely relaxed. Only the point of $\Delta\varepsilon/2=1.0\%$ (specimen No.1) has a little bit rebound, which is kind of strange. The blue curve indicated that prestrain procedure can effectively relax pre-existed surface residual stresses. And this effect can hardly be affected by the subsequent fatigue procedures.

Things worthy to be noticed are the red (shot-peening) and the magenta (prestrain & shot-peening) curves. It is clear that shot-peening procedure conducted in Section 4.3.2 can induce significant compressive residual stress into the specimen surfaces, even if the magnitude is much lower than we expected in Section 4.4.1. Actually, it is possible that the residual stress in the subsurface region can be much higher than the surface value. Higher strain amplitude can cause more relaxation of the surface residual stress. For $\Delta\varepsilon/2=1.4\%$, the shot-peening induced residual stress is relaxed to the same level as the pre-existed residual stress in the raw specimen. Difference between the magenta and the red curve showed that the same shot-peening procedure can produce higher compressive surface residual stress in the prestained specimen. This is reasonable, because that the specimen is work hardened in the prestrain process. Interesting thing is that prestrain can keep the higher residual stress under fatigue loading, even if strain amplitude reach 1.4%. This is quite meaningful, which indicated that tensile prestain can effectively suppress the relaxation of shot-peening induced compressive

surface residual stress under cyclic loading, even if the amount of prestrain is quite limited and the material shows only slight work hardening characteristic.

Integral peak widths obtained with X-ray diffraction tests were listed in Fig. 4-34. The trends of the black and the blue curves means that, on the surface, the raw and the prestrained specimens are hardened a little bit when $\Delta\varepsilon/2=0.7\%$ and then keep softening along with the increase of strain amplitude. As for the shot-peened specimens (red curve) and the presstrained & shot-peened specimens (the magenta curve), they keep softening along with the increase of strain amplitude. However, the Fig. 4-27 and Fig.4-28 showed different phenomena that specimens will be softened a little bit when $\Delta\varepsilon/2=0.7\%$ and the subsequent increase of strain amplitude did not show any softening. For some cases, hardening even happed, such as specimens No.1, No.4 and No.5. But, these differences do not mean that our peak width results are wrong. In fact, results in Fig. 4-27 and Fig.4-28 showed the cyclic hardening or softening behavior of the whole specimen. While, the phenomena showed in Fig. 4-34 reflected the cyclic hardening or softening behaviors in the surface region of the specimens. Furthermore, when extracting the first points of the black and the blue curves from X-ray diffraction data, the disturbance caused by the neighbor peaks are much more severe than other cases. This may be one reason which caused the low value of these two points. Moreover, seeing that the influences of the shot-peening and the fine turning processes are localized in the specimen surface, the differences between the results in this part and those in Section 4.4.2.2 are acceptable. Actually, the surface cyclic softening behavior observed here may have important meaning for analyze the instrumented indentation results, which will be discussed in detail latter on.

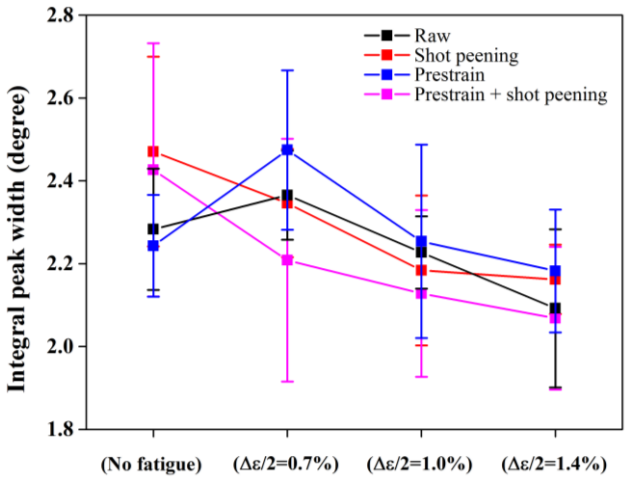


**Fig. 4-34. Integral peak width of all the specimens obtained through X-ray diffraction.**

## 4.6 Instrumented indentation tests on Ti-18

As investigated in Chapter 2 and Chapter 3, instrumented indentation test (IIT) is sensitive to both residual stress and accumulated plastic strain (which can be used to represent the amount of work hardening). Although, our original goal, characterizing shot peeing induced residual stress and work hardening with IIT, cannot be realized very well as discussed in

Chapter 3, IIT still can supply lots of meaningful and important information which can greatly help us to better understand mechanical properties of target material and their evolutions. Thus, in this part of work, IIT will be conducted on Ti18 specimens to investigate fatigue responses.

### 4.6.1 Specimen preparation

After fatigue tests, the calibration parts of the specimens are cut off into small pieces using a metallographic cut off saw Secotem-15 (Struers International, Ballerip, DK) with a low feeding speed (0.01 mm/s) to minimize the influences of the cutting process. According to strain amplitude values (no fatigue, 0.7%, 1.0% and 1.4%), these little pieces are divided into 4 groups. Then hot mounting (heating at 180°C for 10 min and then water cooling for 10 min) was conducteded on the LaboPress-3 hot mounting machine (Struers International, Ballerip, DK) with resin polyester SODY 33 (ESCIL Ltd, Chassieu, FR) for fixing and organizing the specimen pieces in each group. Mounted specimens are shown in Fig. 4-35. Two things need to be explained. First, in order to save specimens, there are only 2 specimens (SP_No.14 and Prestrain & SP_No.12) in the group “no fatigue”. One each of these 2 specimens, the center parts, which are far enough from the shot-peened surface, will be considered as the “Raw_no fatigue” and “Prestrain_no fatigue” specimens respectively. This plan should be reasonable if assuming that the influences caused by the fine turning process are negligible. Second, owning to some specific reasons, fatigue test on specimen No.1 was performed lately. Thus, the piece of specimen No.1 is cold mounted individually.

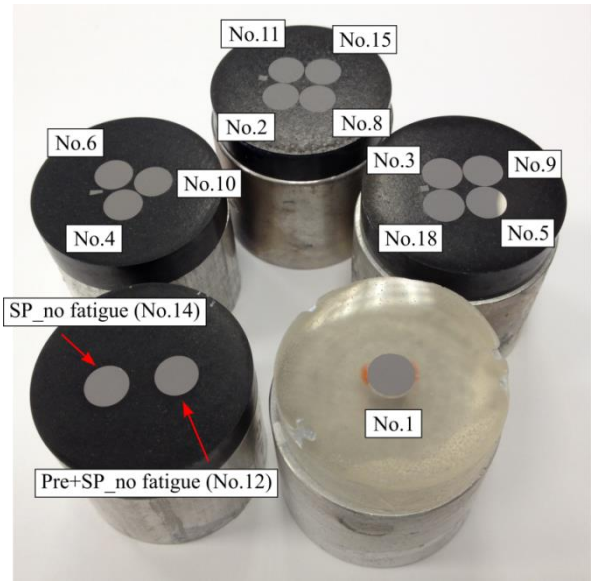


**Fig. 4-35. Instrumented indentation specimens of Ti18 alloy.**

Based on our former experiences in Chapter 3, even if carefully conducted mechanical polishing still can induced high plastic strain in the surface of IIT specimen. Thus, self-weights of these specimens are strictly controlled between 6.9 g and 7.7 g to minimize the pressure during polishing. All the specimens were then polished to mirror flatness on Vector® LC 250

automatic lapping and polishing unit (BUEHLER An ITW International, Lake Bluff, USA) using abrasive discs of 800-grit and 1200-grit silicon carbide abrasive disc films, (ESCIL Ltd, Chassieu, FR) followed by 10-$\mu$m suspension diamond abrasive paste and 0.05-$\mu$m silica powder (ESCIL Ltd, Chassieu, FR). After that, they were polished on the VibroMet®2 vibratory polisher (BUEHLER An ITW International, Lake Bluff, USA) with the 0.05-$\mu$m silica powder (ESCIL Ltd, Chassieu, FR). During the whole polishing process, only self-weight of the specimens was used for applying pressure, without any other external pressure applied. In Chapter 3, it was mentioned that the material removal speed is quite low with this kind polishing procedure on T40 grade 2 CPT. Seeing that the strength and hardness of Ti18 are much higher than those of T40 grade 2 CPT, the polishing time here should be even longer than before for guaranteeing the layer affected by previous polishing steps were fully removed. Polishing time for each polishing step is 3 hours (abrasive discs of 800-grit and of 1200-grit respectively), 4 hours (10-$\mu$m diamond abrasive paste), 24 hours (0.05-$\mu$m silica powder) and 144 hours (vibration polishing with 0.05-$\mu$m silica powder) respectively.

Considering the dimension and the arrangement of the specimens in the resin, it is impossible to make X-ray diffraction on the polished surface. Furthermore, there is not electrolytic polished specimen as reference. So, unlike what we did in Chapter 3, we cannot check the peak with values on these specimens here. However, based on our former experiences, the quality of the polishing should be sufficient for making IIT.

### 4.6.3 Instrumented indentation

A series of instrumented indentation tests were performed on all the 14 specimens at various depth from the shot-peened surface (50 $\mu$m, 80 $\mu$m, 140 $\mu$m, 200 $\mu$m, 280 $\mu$m, 360 $\mu$m, 440 $\mu$m, 520 $\mu$m, 600 $\mu$m, 700 $\mu$m, and 900 $\mu$m) following the standard ASTM E 2546-07 [142]. 5 tests were made at each depth for and their results were averaged. As for specimens No.14 and No.12, 10 more tests were conducted at the depth 2500 $\mu$m on each of them for representing the specimens “Raw no fatigue” and “Prestrain no fatigue” respectively. The maximum penetration depth is 3 $\mu$m as well to overcome the effects in the surface region induced by the polishing procedure. All the instrumented indentation tests were performed on the Nano indenter®XP (MTS systems corporation, Eden Praire, USA) with a Berkovich indenter.

All the indentation results are listed as follows, after the corrections of frame stiffness and free-edge effects. For the convenience of analysis, the results are organized in two different ways. First, they are organized according to the variation of strain amplitude. Then, they are organized with different material states. This kind of differential organization can help us to understand the influences of prestrain, shot-peening and strain amplitude better and easier.

### 4.6.4 IIT responses analysis

As discussed in Chapter 2 and Chapter 3, there are mainly there IIT responses which are of great importance: maximum indentation load ($P_{max}$), contact hardness ($H$) and contact stiffness ($S$). Each of them will be discussed in detail in the following sections.

One troublesome thing for analyzing the IIT responses is the significant scatter of the data, which makes some profiles mixed together with some other profiles, as shown in Fig. 4-36, Fig. 4-38 and Fig. 4-40. It is difficult to clearly distinguish the differences among groups with various strain amplitudes. In order to overcome this kind of problem, data points and their error bars on each profile are averaged in the whole depth range according to formulas as follows:

$$\bar{x} = \frac{\sum_{i}^{m} n_i \bar{x}_i}{\sum_{i}^{m} n_i} \tag{4-1}$$

$$\sigma = \sqrt{\frac{\sum_{i}^{m} n_i (\sigma_i^2 + (\bar{x}_i - \bar{x})^2)}{\sum_{i}^{m} n_i}} \tag{4-2}$$

where $\bar{x}_i$ is the data point on each profile (which is a mean value of $n_i$ indentation tests), $\bar{x}$ is the mean value of the whole profile, $\sigma_i^2$ is the standard deviation corresponding to each data point, $\sigma$ is the combined standard deviation of the whole profile. The averaged indentation responses are shown in Fig. 4-37, Fig. 4-39 and Fig. 4-41. In this way, the comparison between each profile will become clear and easy.

#### 4.6.4.1 Maximum indentation load ($P_{max}$)

The profiles of $P_{max}$ along depth for the raw and prestrained specimens are shown in Fig. 4-36(a) and Fig. 4-36(c), from which we could see that there is no obvious gradient for all the profiles. Some of the points near the surface seem to be kind of different from the points in the core, which might be caused by slight influences induced by the fine turning process when manufacturing the specimens. However, the overall trends of the profiles are rather flat, which means that our testing plan on specimens No.14 and No.12, as discussed in Section 4.6.3, is reasonable.

Gradient occurred on the profiles of shot-peened and prestrained & shot-peened specimens, as shown in Fig. 4-36(b) and Fig. 4-36(d). However, the $P_{max}$ gradient is quite different from the results we obtained on T40 grade2 CPT, as shown in Fig. 3-18(a). Fig. 3-18(a) showed that getting close to the shot-peened surface, $P_{max}$ will increase, which is

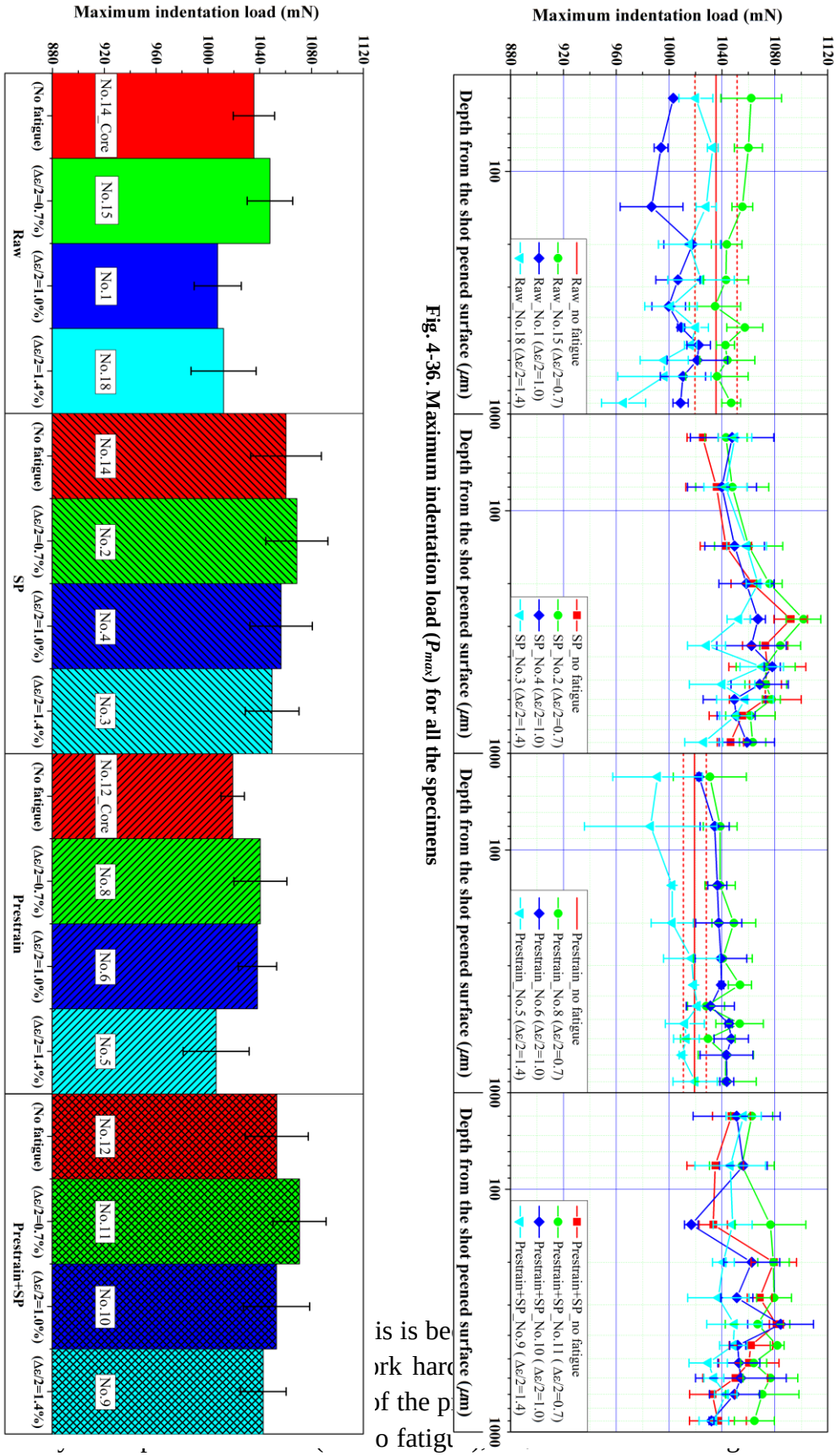


**Fig. 4-36. Maximum indentation load ($P_{max}$) for all the specimens**




**Fig. 4-37. Maximum indentation load ($P_{max}$) averaged on the whole depth profile for all the specimens.**

consistent wit is is be e,
the level of c ork hard ill
become highe of the p en
decreased dra o fatigu en

low than that in the core. Seeing that the residual stress in the shot-peened surface region must be higher than that in the core, the only explanation of the abnormal $P_{max}$ profiles should be that the surface regions of Ti-18 specimens were softened during the shot-peening process. Although X-ray diffraction tests along the whole depth has not been performed, the rationality of this speculation still can be indirectly proved by the results of the $\sigma_a$ showed in Fig. 4-27 and Fig. 4-28. If look back into Fig. 4-27 and Fig. 4-28, we could see that under high strain amplitude, the material will only be hardened a little bit in the first few cycles. After that, it will keep softening. We can imagine that, after 100 cycles, if cyclic loading is keep going on, it is quite possible that the material will become softer than its original state. Different from monotonic loading process, shot-peening process will make the surface material go through a very complex loading path and history, which should be more similar as a cyclic loading path and history. Considering the severe surface deformation and the repeat impacts of the shots during shot-peening process, it is quite possible that the surface region of the specimen has already been severely cyclic softened. However, in the subsurface region, the softening effect is not so severe. In the deeper layer, the material might still stay in the hardening stage. Thus $P_{max}$ value in this range becomes higher along with the increase of the depth. From Fig.4-36(b) and Fig.4-36(d), we can also see that the for the cases $\Delta\varepsilon/2$=1.4%, the whole profiles became quite flat. This is quite reasonable, because that under the strain amplitude high enough, the effects of the shot-peening process will be completely covered by the cyclic softening caused by the fatigue loading.

By doing the averaging operation mentioned above, each profile can be represented by one $P_{max}$ value with an error bar, as shown in Fig. 4-37. Although this method cannot reflect the local variations of each profile, it is still meaningful because that an overall situation of each profile can give us some information about the influences of strain amplitude. Fig.4-37(a) showed that along with the increase of strain amplitude, maximum indentation load will first increase and then decrease. In fact, this is not occasional. Fig.4-37(b), Fig. 4-37(c) and Fig.4-36(d) showed the similar phenomenon as well. Results in Fig. 4-27 showed that, for $\Delta\varepsilon/2$=0.7%, all the specimens are softened a bit. While for $\Delta\varepsilon/2$=1.0% and 1.4%, after 100 cycle, some of the specimens are hardened a little bit, while some others are nearly neither hardened not softened, such as specimens No.3, No.6, No.10 and No.18. Although the results of our former simulations showed that the increase of compressive residual stress and work hardening can cause the increase of $P_{max}$, it does not mean what we observed here is abnormal. The constitutive model used in our former simulations is too simple, which did not take material softening, kinematic hardening, etc. into account. In fact, even if material is softened, $P_{max}$ might increase as well, which is because that the contact area might increase.

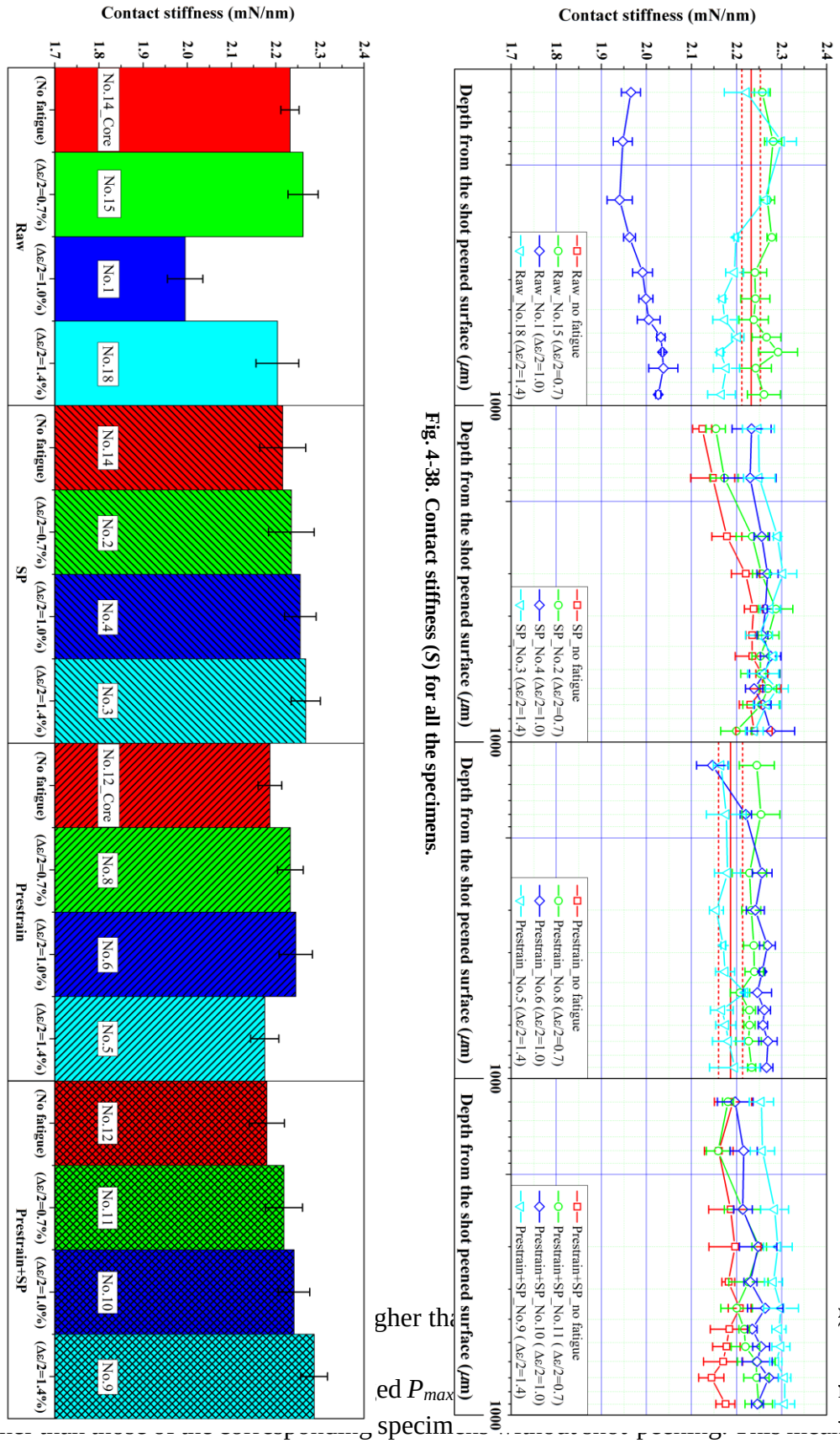


**Fig. 4-38. Contact stiffness (S) for all the specimens.**




**Fig. 4-39. Contact stiffness (S) averaged on the whole depth profile for all the specimens.**

So, the averag gher th %
and 1.4% is n
From Fig. ed $P_{max}$ is
are always hig specim is

that shot-peening can effectively obstruct the softening of Ti-18 alloy under low cycle fatigue loading. However, the effects of prestrain process on $P_{max}$ seem to be quite limited. Considering the fairly flat monotonic hardening behavior of Ti18, this is normal.

#### 4.6.4.2 Contact stiffness (*S*)

In Fig. 4-38(a) and Fig. 4-38(c), for the raw and the prestrained specimens, most of the *S* profiles are rather flat. Few exceptions showed variation of *S*. The most strange one is specimen No.1 (Raw, $\Delta\varepsilon/2$=1.0%), the stiffness of which is much lower than all other specimens. Specimen No.1 was polished individually, as shown in Fig. 4-35. Although the polishing procedure was strictly controlled, the existence of unexpected mistakes was still possible. Another possible reason is that the material property of specimen No.1 may be different from others. Result shown in Fig. 4-33 has confirmed this from one aspect. However, the abnormality of specimen No.1 and the stiffness decrease phenomenon did not affect the averaged *S* value so much. As for the variations of *S* occurred in the surface regions of specimens No.18 and No.6, they might be caused by the fine turning process of the specimens.

From Fig.4-38(b) we can see that for all the four shot-peened specimens, *S* decreased when getting close to the surface. However, along with the increase of strain amplitude, the *S* decrease phenomenon in the surface region became more and more gentle. Since the correction of free-edge effects has already been done, there must be some other reasons for these variations. According to Eq.1-X, contact stiffness is directly correlated with Young's modulus and projected contact area. Since Young's modulus is an eigen material constant, thus the decrease of *S* in the shot-peened surface region should be attributed to the decrease of projected contact area. However, our former simulations in Chapter 2 and Chapter 3 showed that shot-peening process induced residual stresses and work hardening will increase projected contact area, which is opposite to our observation here. In order to know the variation of contact stiffness in the shot-peened surface region, further investigations need to be performed in the future.

Fig. 4-38(d) showed that similar *S* variations in the surface region also existed in the prestrained & shot-peened specimens, however, the extents are much lower. This means that the prestrain process effectively obstructed the variation of *S*. In addition, the effect of strain amplitude became fairly unobvious that all the profiles were quite similar.

Fig. 4-39(b) and Fig. 4-39(d) showed that for all the shot-peened specimens, the averaged *S* values tend to increase along with the increase of strain amplitude. This might because that IIT test of fatigue specimen with higher strain amplitude can produce a larger projected contact area.

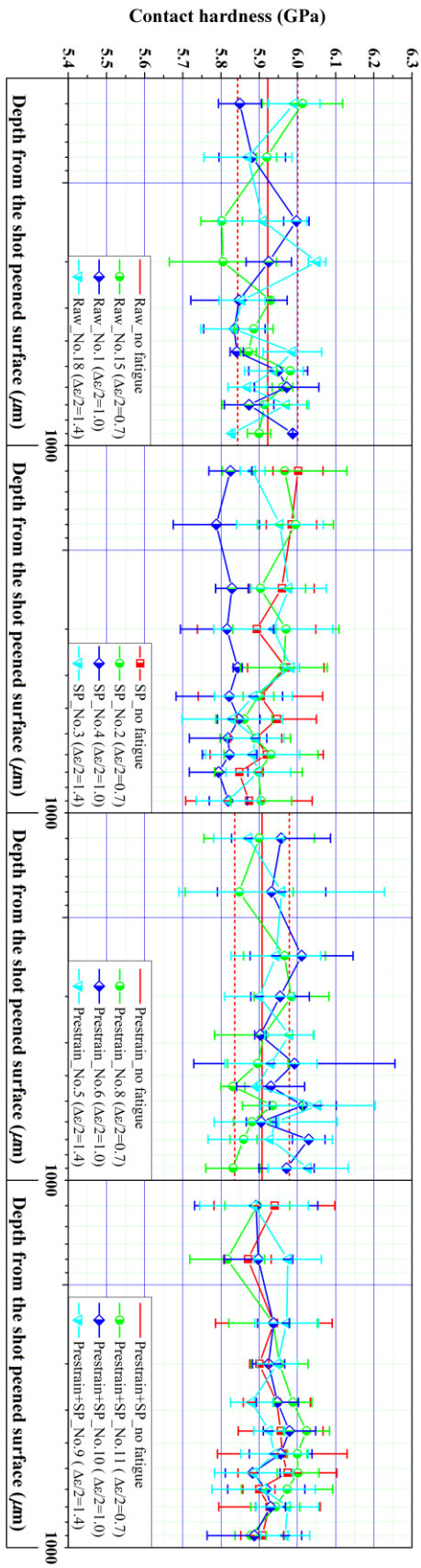


**Fig. 4-40. Contact hardness (*H*) for all the specimens.**

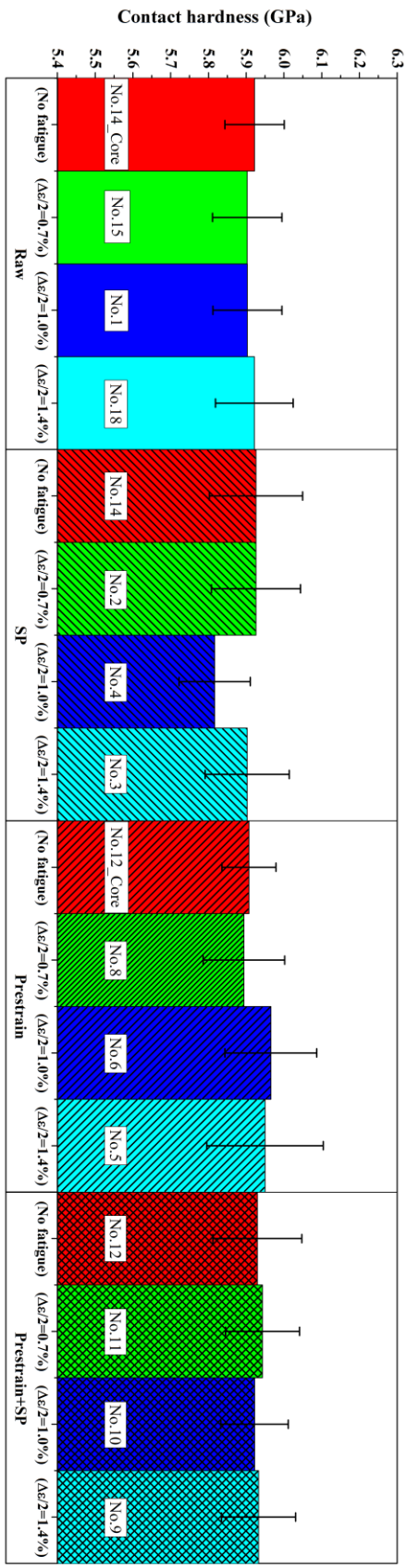


**Fig. 4-41. Contact hardness (*H*) averaged on the whole depth profile for all the specimens**

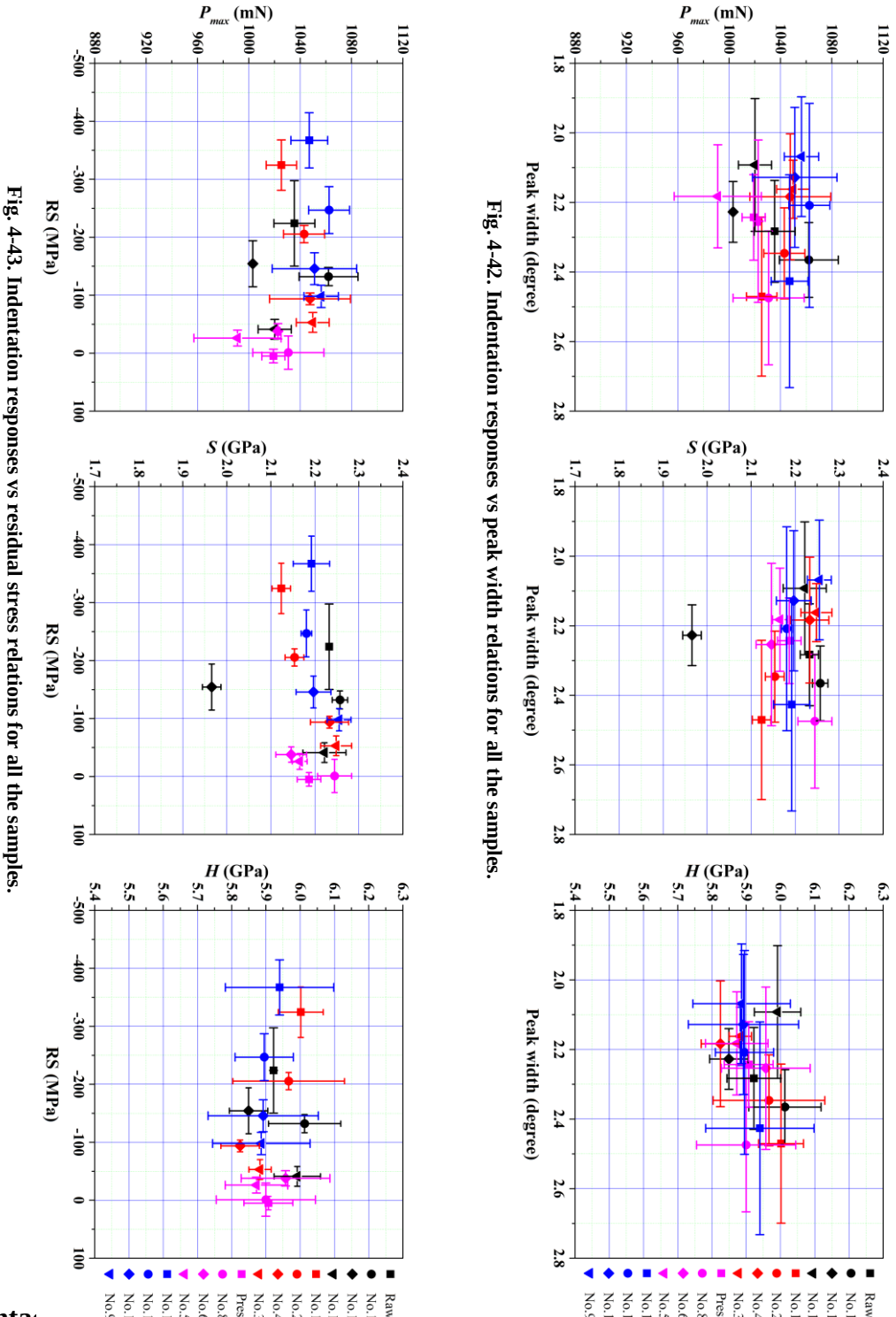


**Fig. 4-42. Indentation responses vs peak width relations for all the samples.**




**Fig. 4-43. Indentation responses vs residual stress relations for all the samples.**

### 4.6.4.3 Conta

As for con rofiles i at
*H* seems to be veraged lar
results, which ain amp act
hardness as w n No.4 bit

lower than all other specimens. For raw and prestraiend specimen, unchanged contact hardness is quite normal and logical. While, for the shot-peened and prestrained & shot-peened specimens, this is strange. In Chapter 3, obvious gradient of contact hardness was observed on the shot-peened T40 grade 2 CPT specimen, as shown in Fig. 3-18(c). However, considering the possibility of softening discussed above, the invariance of contact hardness in shot-peened specimen becomes explainable from one aspect.

#### 4.6.4.4 Correlating IIT responses with residual stresses and peak width

All the IIT responses showed and discussed above are either profiles along depth or averaged value over the whole depth, which is difficult to be compared and correlated with the results obtained from X-ray diffraction tests which was performed on the surface of the specimens. However, our information about residual stresses and peak broadening was obtained from X-ray diffraction.

In order to correlate the IIT responses with residual stresses and peak width information obtained with X-ray diffraction, the data were treated in a special way. All the IIT responses of the first point (depth = 20 $\mu$m) of each profile were selected as the IIT data on the shot-peened surface. Then, IIT responses vs residual stresses and peak widths were plot in Fig. 4-42 and Fig. 4-43. Although the IIT responses of "Raw no fatigue" and "Prestrain no fatigue" are represented by the data on specimens No.14 and No.12 at 2500 $\mu$m depth, they still will be plot for making comparison.

Considering the whole variation range of peak widths, their scatters are considerably larger. Thus, there is no relationship between any IIT response and peak width can be concluded very clearly. It is interesting to note that peak width is not correlated to hardness.
Both quantities could be seen as linked to dislocation density variation due to plasticity (coming from shot-peening, prestrain or cyclic loading). However, the global variations of H are smaller than 3% which is smaller than the dispersion which means that plasticity does not induce any hardening. This is consistent with the very flat tensile curve. On the other hand, the global variations of peak width are about 19% which is significant. Indeed, Fig. 4-31 shows meaningful evolutions of peak width versus loading amplitude. It can be concluded that, on some materials, both hardness and peak width can be used to follow the evolutions due to plasticity but for Ti-18 alloy, only peak widths give information.

Much smaller dispersion of residual stress makes it possible to observe some trends of IIT responses from Fig. 4-43. Along with increase of compressive residual stress, $P_{max}$ decreases slightly, which is totally different from the results on T40 grade 2 CPT. This might be attributed to the fact that cyclic softening had happed in the surface region on the specimens. Similar regular can also be observed from $S$ which increases when RS decreases. This means that projected contact area, which is closely correlated with pile-up/sinking-in phenomenon, increases. However, this is contrast to what we obtained from the simulations on material A in Chapter 2. The correlation between RS and $H$ is faint but perceptible. $H$ decreases when the absolute value of RS decreases. This is consistent with the results observed by Tsui's [124] on

aluminum alloy 8009. As compared to Tsui's classical results in Fig. 4-44, the variation of our case is about 0.1 GPa between -400 MPa and 0 (a 1.5% variation), while for Tsui's research on aluminum alloy, the variation is 0.05 GPa between -400 MPa and 0 (a 3.5% variation). Furthermore, for both aluminium and Ti-18 alloys, the dispersions are fairly large.

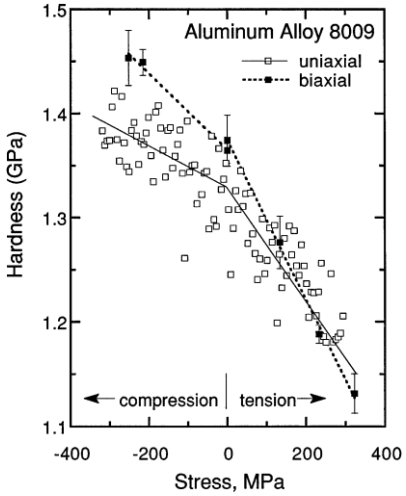


**Fig. 4-44. Classic correlation between hardness and residual stress obtained by Tsui *et al*. [124].**

## 4.7 Conclusion

Because of its great mechanical properties, such as high specific strength, good ductility, etc., a recently developed new type of high-strength bi-phase titanium alloy, Ti-18, has a great potential to be used for the landing gear as an improved alternative to conventional $\beta$ phase high-strength alloys. Since it is still quite new, investigations on the material properties of Ti-18 are still lacking in many aspects. Thus, it was chosen as the target material in this chapter.

Uniaxial tensile test showed that the yield strength of Ti-18 alloy is higher than 1300 MPa and its elongation is about 8.3%. Observation under scanning electrical microscope (SEM) showed that Ti-18 has a typical bimodal microstructure of titanium alloys: many discrete globular primary $\alpha_p$ phase grains are surrounded by the transformed $\beta$ matrix including the retained $\beta$ phase and the precipitated $\alpha_s$ phase.

Several fatigue test specimens of Ti-18 alloy were manufactured and pretreated with shot-peening, prestraining and prestraining & shot-peening. According to the uniaxial tensile responses of Ti-18 alloy, a 3.2% total strain (1.8% plastic strain) was introduced into 7 specimens. A shot-peening condition, which can generate approximately the same impact density as the shot-peening process performed on T40 grade 2 CPT, was obtained through series of specific simulations. 4 raw specimens and 4 prestrained specimens were then shot-peened under this condition. From a pure structural view point, three different strain amplitudes (0.7%, 1.0% and 1.4%) were decided as the loading conditions of fatigue tests.

After prestaining and shot-peening treatments, strain controlled low cycle fatigue tests were conducted on 12 specimens of four different material states (raw, shot-peened, prestrained and prestrained & shot-peened) under all the three strain amplitudes respectively.

Another two specimens (one is shot-peened and the other one is prestrained & shot-peened) without fatigue were used for refence. Prestrain and fatigue test results showed that a certain level of scatter of material strength (several tens of MPa) exist among these specimens.

Fatigue test results showed that mean stress relaxation happened for all the three strain amplitudes. Along with the increase of strain amplitudes, both the amount and the speed of the mean stress relaxation become larger. Stress amplitude results showed that when $\Delta\varepsilon/2=0.7\%$, specimen of all the four material states will cyclically softened a little bit. As for $\Delta\varepsilon/2=1.0\%$ and 1.4%, all the 8 specimens went through a "first hardening and then softening" process. However, since the fatigue tests were terminated after only 100 cycles, 4 of the specimens were still hardened a little bit than their original states. Another 4 specimens came back to the same level as their original states. None was cyclically softened.

X-ray diffraction tests performed on the specimen surfaces showed that the increase of strain amplitude can increase the relaxation of shot-peening induced compressive surface residual stresses. Cyclic softening was also observed on the surface of the shot-peened and prestrained & shot-peened specimens. As for the raw and prestrained specimens, along with the increase of strain amplitude, material was firstly hardened a little bit and then softened.

Instrumented indentation tests were performed on the fatigued and reference specimens as well. For the shot-peened specimens, getting close to the surface, decrease of $P_{max}$ happened, which is different from our former observations on T40 grade 2 CPT. The reason of this phenomenon might because that the surface region were softened during shot-peening. Contact hardness showed kind of invariance. For most of the specimens, the variation of contact stiffness is limited except specimen No.1. Considering the complex cyclic hardening and softening behavior of Ti-18 and the possibilities of other impacting factors, it is hard to say the exact reason of the variance of contact stiffness.

In order to better understand the evolutions of residual stress and work hardening during the low cycle fatigue processes of Ti-18 alloy, some further investigations need to be done in the future. First, the whole residual stress and peak width profiles need to be characterized, because this can show the relaxation residual stress relaxation behavior in the whole depth direction. Second, the relationship between X-ray diffraction peak width and accumulated plastic strain needs to be characterized, which can help us to qualitatively understand the cyclic hardening/softening behavior of Ti-18 alloy.

# Chapter 5

# Conclusions and perspectives

Nearly all of the manufacturing and mechanical processes, such as shot-peening, rolling, deep drawing, cutting, etc. can simultaneously introduce residual stresses (RS) and work hardening into metallic components. Shot-peening, as a highly mature surface treatment technique, has been broadly used in many fields for improving the performance, especially the fatigue resistance, of components. In the past decades, several conventional characterizing methods of residual stresses (such as hole-drilling method, splitting method, X-ray diffraction, etc.) and work hardening (such as hardness indentation, electron back scatter diffraction, X-ray diffraction, etc.) had been developed and consummated. However, there are still some limitations of these techniques. For instance, they cannot be applied in small volume, are always complex in practice, cannot quantitatively measure work hardening, etc. Aiming at these insufficiencies, the present thesis tried to propose a new approach, based on instrumented indentation test (IIT), for simultaneously measuring shot-peening induced residual stresses and work hardening in a localized volume. Furthermore, the relaxation of residual stresses and the evolution of work hardening during low cycle fatigue process can severely influence the fatigue resistance of components. Thus, in the present thesis, relevant investigations were also performed on Ti-18, a newly developed high-strength near $\beta$-phase titanium alloy.

First, a systemic review was made on a series of critical conceptions involved in this thesis, including shot-peening, residual stress, work hardening, measuring methods of residual stress, characterizing approaches of work hardening, fatigue process, evolution of residual stresses and work hardening during fatigue, titanium alloy and so on. Through the review, current situation and background in relative researching fields have been clarified, and the motivation and necessity of present study have been demonstrated.

After the review, our attention was firstly paid to the exploration of the new approach to qualitatively characterize residual stresses and work hardening in small volume. Since instrumented indentation test is a localized technique, which is sensitive to both residual stresses and work hardening, it became our idea candidate. Seeing that there is a direct relationship between work hardening and accumulated plastic strain (PP), the later was used to represent the former. A series of finite element method (FEM) simulations were firstly performed on four targets materials (copper and 3 virtual materials), which were described by a Ludwick type isotropic hardening constitutive behavior, to study the influences of RS and PP on IIT process. A cylinder representative volume element (RVE) under the shot-peening the surface was set as the investigating domain and the problem with a 3D Berkovich identer was simplified into a 2D axisymmetric problem with an equivalent conical indenter. For receiving high accuracy with low computing costs, the FEM model was locally refined in the

zone beneath the indenter. Mesh convergence and model adequacy studies showed the performance of the FEM model is good enough.

The Suresh method and the approach of differentiating shapes of load vs depth (*P-h*) curves were then studied. However, both of the two methods were failed in measuring RS and PP, because none of them can separate the two factors. Thereinto, study of the second approach showed that certain levels of PP and RS can produce nearly the same *P-h* curve. Fortunately, topography analysis of the indentation dimple showed that the pile-up/sinking-in values for different cases are influenced differently by magnitudes of the RS and PP. However, this difference, which varies from few nanometers to several tens nanometers on different materials, is too small to be measured experimentally. Since the pile-up/sinking-in value is directly correlated with the projected contact area ($A_c$) and the Young's moduls ($E$), which are two basic factors to extract contact hardness ($H$) and contact stiffness ($S$), it is possible that $H$ and $S$ can show some larger differences. Then, a series of FEM simulations concerning with various RS and PP levels in the possible elasto-plasto range of a virtual material were conducted. Results showed that three functions $P_{max}/P_{max0}=f$(RS, PP), $H/H_0=g$(RS, PP) and $S/S_0=k$(RS, PP) could be built, where $P_{max}$, $H$ and $S$ are respectively the maximum load, the contact hardness and the contact stiffness of material with arbitrary RS and PP, while $P_{max0}$, $H_0$ and $S_0$ are respectively the maximum load, the contact hardness and the contact stiffness of reference sample which is supposed to be the raw material without any RS and PP. Since the common solution of each two functions can directly give the RS and the PP values, this new approach is called simultaneous function method. Simulations with two arbitrary combinations of RS and PP showed the fairly high accuracy of this method from a purely numerical view point.

Next, the accuracy and adaptability of the simultaneous function method were investigated together with IIT experiments and simulations on a T40 grade 2 CPT specimen which had been shot-peened. Both the RS and PP profiles along the depth were extracted by X-ray diffraction (X-RD) measurements. Thereinto, RS values were obtained from diffraction peak shift, while PP values were derived from integral peak width. The relationship between PP and peak width was calibrated with a series of uniaxial tensile tests on a specially prepared specimen, which is supposed to be free from the influence of extra RS and PP. Results showed that the maximum value of the compressive residual stress can reach - 340 MPa, whereas the influenced depth is about 450 $\mu$m. Shot-peening process can induce a high plastic strains in a significant depth. At the extreme surface, the plastic strain level can reach even more than 70%.

Several indentation specimens were cut off from the shot-peened T40 sample along the cross section and carefully polished. Indentation tests at various depth from the shot-peened surface on three specimens (No.1, No.2 and No.3), which are mechanically polished under different conditions, were conducted. All the indentation responses were corrected from the free-edge effects. Results showed that polishing procedure can severely influence the values of the IIT responses. Then, another 10 indentation tests were performed on an electrolytic polished raw reference sample which is supposed to be free of the influences of extra RS and PP. IIT responses ($P_{max}$, $S$ and $H$) on the carefully mechanically polished specimen (No.3) were

normalized by the corresponding data ($P_{max0}$, $S_0$ and $H_0$) derived from the averaged values on the reference sample.

The constitutive behavior of T40 was extracted from uniaxial tensile test and put into the FEM model. However, simulation IIT responses, without any RS and PP, were far away from the corresponding values obtained from indentation tests on the reference raw material. In order to reduce the gap between simulated and experimental results, the indenter shape was modified by considering the tip defect.

Simulations with various RS and PP levels were conducted for deriving functions of the normalized IIT responses. However, when using the simultaneous function method together with the normalized IIT responses obtained from experiments, the contour plots of $S/S_0$ (1~1.057) and $H/H_0$ (1~426) are not sufficient to cover the range of the corresponding experimental data (0.85~1 and 1~1.61). A limited method was proposed to extract the PP profile, however, the result is generally higher than the profile obtained with X-RD. Once possible reason for these problems is that some extra effects had been introduced by the mechanical polishing process, even if it was carefully performed.

In order to improve the capability to use the simultaneous function method in practice, several modifications were made. First, disturbance introduced by the carefully mechanical polishing procedure was investigated. Grazing incidence X-ray diffraction (GIXRD) tests were conducted. Results showed that residual stresses (supposed to be constant in each layer) in the surface of specimen No.3 did not show much variation, comparing with the residual stresses in the reference raw sample, which indicated that the carefully mechanical polishing procedure used here can effectively reduce the levels of the extra induced residual stresses. However, drastically increased peak width showed that fairly high plastic strain exists in the surface region of specimen No.3. The relationship between peak width and plastic strain calibrated before showed that the polishing process can induce plastic strain into an approximate depth of 5 $\mu$m, which is even deeper than the $h_{max}$ (3 $\mu$m ) value of the indentation tests. In the layer near the surface (in the range of depth about 350 nm), the plastic strain levels are significantly high, which can even reach more than 60% in the very top layer. The surface high plastic strain levels were taken into account to modify the FEM model as well. However, there was no obvious improvement with both the simultaneous function method and the limited method.

In order to bypass the difference between electrolytic-polished sample and the carefully mechanically polished sample, a secondary optimization process was then conducted by using one part on the carefully mechanically polished sample, which is far away enough (900 $\mu$m) from the shot-peened surface, as the new reference. Because X-ray diffraction results showed that the material should be free from the effects of the shot-peening process at such a depth. The newly optimized parameters were then set into the FEM model for further modification. Although simultaneous method still does not work, the plastic strain profile obtained with the limited method was still greatly improved. This demonstrated one possibility of extracting shot-peening induced plastic strain profile in practice, which is closely correlated with work hardening.

Afterwards, the relaxation of residual stress and the evolution of work hardening during low cycle fatigue process were studied. A recently developed high-strength near $\beta$-phase titanium alloy, T-18, was used as the target material. Because of its excellent mechanical properties, such as high specific strength, good ductility, etc., Ti-18 has a great potential to be used for the landing gear as an improved alternative to conventional $\beta$ phase high-strength alloys. Its great properties and fine microstructure were shown by uniaxial tensile test and scanning electrical microscope (SEM) observation.

Several fatigue specimens were manufactured through wire-cutting electric discharge machining (WCDM) and fine turning, and further prepared by various pretreatments for obtaining different material states, including raw, shot-peened, prestrained and prestrained & shot-peened. Thereinto, the prestraining condition was determined from uniaxial tensile test, and the shot-peening condition, which can generate approximately the same impact density as the shot-peening process performed on T40 flat sample, was calculated through series of multibody dynamics simulations. Three different strain amplitudes (0.7%, 1.0% and 1.4%) were decided from a pure structural view point to study different levels of plasticity. The low cycle fatigue tests at room temperature, controlled under stain amplitude, were performed on twelve specimens of the four different material states (three for each state). Another two specimens (one is shot-peened and the other one is prestrained & shot-peened) that were not submitted to fatigue loading were used as references.

Both prestraining and fatigue stress-strain curves showed that scatters of several tens of MPa exist among these specimens. The fatigue tests were stopped after only 100 cycles ($\Delta\varepsilon/2$=1.0% and 1.4%) or 140 cycles ($\Delta\varepsilon/2$=0.7%) to permit the comparison of the relaxation of the mean stress and the residual stress on the four states, except for two specimens which were broken. Fatigue results showed that relaxation of mean stress, which is supposed to be correlated with residual stress relaxation, occured under all the three strain amplitudes. Moreover, along with the increase of strain amplitudes, both the amount and the speed of the mean-stress relaxation became larger. Stress amplitude results showed that when $\Delta\varepsilon/2$=0.7%, specimen of all the four material states will cyclically softened a little bit (about 20 MPa). As for $\Delta\varepsilon/2$=1.0% and 1.4%, all the eight specimens went through a “first hardening and then softening” process. Thereinto, four specimens were still hardened a little bit (several tens MPa) than their original states. The other four specimens came back to the same level as their original states. None was cyclically softened after about 100 cycles.

X-ray diffraction tests on the surface of the specimens showed obvious relaxation of shot-peening induced compressive residual stresses. Meanwhile, the variation of peak width showed that cyclic softening happened to the surfaces of all the shot-peened and prestrained & shot-peened specimens. As for the raw and the prestrained samples, along with the increase of strain amplitude, the material was firstly hardened a bit and then softened. Instrumented indentation tests on the cross section of the fatigue samples showed that the $P_{max}$ profiles on Ti-18 is different from that on T40, which showed that shot-peening may not work harden but soften the surface regions on the samples. There is no obvious correlation between critical indentation

responses and peak with, which is different from T40 as well. However, contact hardness increased slightly along with the increase of compressive residual stress, which confirmed the classic observation obtained in the literature.

Although lots of work has been done and many problems have been discussed in the present thesis, there is still much work that needs to be done in the future.

One of our original goals is to explore and establish a new approach, based on instrumented indentation test, for characterizing shot-peening induced residual stress and work hardening simultaneously. Meanwhile, we hope this new method can be easily used in practice and insensitive to constitutive model. However, investigation of the present thesis showed that the critical IIT responses ($P_{max}$, $S$ and $H$) are sensitive to constitutive model, especially contact stiffness $S$. For better describing instrumented indentation process on metallic materials, kinematic hardening (or maybe mixed hardening) behavior and cyclic constitutive equations together with specific identifications need to be taken into account in the future. Precisely describe the IIT process with FEM model is of great importance to the application of the simultaneous function method proposed in the present work.

Furthermore, based on the results of the literature, we used a simplified way to introduce residual stress and work hardening into the RVE by only considering the hydrostatic pressure, which transformed the problem into a 2D axisymmetric one. However, this way of constructing RVE is still questionable. In the future, 3D FEM model considering the all the components of stress tensor need to be built for better investigating the effects of residual stresses on IIT process with a Berkovich indenter. In addition, IIT experiments and simulations with spherical indenter also deserve to be studied in the future. Since spherical indenter is axisymmetric, it can prevent the problem between 2D and 3D models caused by the difference of indenter shapes.

Although our simultaneous function method met a big problem when trying to be applied in practice, it is still worthy to be further explored and modified in the future. Since high accuracy has already been achieved from a pure numerical view point, it means that there is no fatal problem with this method. Reducing the gap between numerical results and the experimental data through inverse method by considering residual stress and accumulated plastic strain will be one possible direction for improving the performance of simultaneous function method. Our former simulations showed that the normalized unloading $P$-$h$ curve, which is also correlated with contact stiffness $S$, is sensitive to all the material parameters in our FEM model. Thus, it may supply one possible direction to analyze the dispersion on IIT process caused by the material parameters. This might be important to thoroughly figure out the difference between electrolytic polished sample and the mechanically polished sample. Further tests with the limited method on other materials are also necessary, because it is still meaningful, even if only the profile of accumulated plastic strain can be extracted.

Concerning the tests on Ti-18 alloy, some further investigations need to be completed as well. Because of the limitation of time and equipment, the whole residual stress and peak width profiles along the depth have not been characterized. In the future, a new electrolytic-polishing

instrument will be installed and tested for realizing precise layer removal on the cylindrical fatigue specimens. In addition, the relationship between peak width and accumulated plastic strain on Ti-18 need to be calibrated as well, which will be significant important to study the hardening/softening behavior of this alloy. Of course, trying to apply the simultaneous function method and the limited method on Ti-18 will be conducted as well.

In the long term, simultaneous function method will be modified to be maturely used for the quantitative characterization of the shot-peening induced residual stresses and work hardening in fatigue samples. With this method, the cyclic relaxation of residual stresses and mean stress, and the cyclic evolution of work hardening in more metallic materials will be studies. The corresponding results can be used to guide the optimization of shot-peening parameters and the improvement of the efficiency of the shot-peeing process. Our final goal is to develop a code which can link the fatigue performance of components with the shot-peeing parameters. By considering the material properties of the components, the cyclic evolution of residual stresses and work hardening and so on, this code should be able to predict a set of shot-peeing parameters which can produce a best fatigue performance of the components.

# Résumé en français

Deux questions se posent lorsqu'on étudie les effets du procédé de grenaillage sur la fatigue oligocyclique (FO) des composants. En effet, le grenaillage peut introduire simultanément des contraintes résiduelles (CR) et de l'écrouissage dans les composants. La première question est comment les séparer et puis les caractériser quantitativement dans l'épaisseur de matériau traitée. La seconde est la relaxation des CR et l'évolution de l'écrouissage au cours du cyclage, ce qui peut diminuer l'efficacité du grenaillage.

L'analyse de l'écrouissage introduit lors d'un essai de traction est bien maîtrisée, mais, à ce jour, il n'existe pas de méthode universelle pour caractériser quantitativement l'écrouissage introduit par un procédé de mise en forme ou de traitement.

La caractérisation des CR a été étudiée par beaucoup de scientifiques dans les dernières décennies [3]. Des techniques comme la méthode du perçage incrémental, la diffraction des rayons X, la propagation des ultrasons, etc. ont été développée et améliorées et présentent aujourd'hui une bonne fiabilité [4]. Les limites de ces méthodes pour déterminer un profil de contraintes résiduelles sont bien connues et elles pourraient être utilement complétées par l'essai d'indentation instrumentée. Cet essai est, en effet, sensible simultanément aux contraintes et à l'écrouissage [5, 6] et permet, par ailleurs, une caractérisation locale aisée sur une coupe droite de l'éprouvette traitée. L'un des objectifs de cette thèse est de discuter de sa pertinence dans le cas des couches grenaillées.

Dans cette thèse, nous voulons étudier l'influence du grenaillage sur la résistance des alliages de titane à la fatigue oligocyclique. En particulier la relaxation des CR, l'évolution de l'écrouissage et les effets d'un traitement de pré-déformation. Dans la bibliographie, certains chercheurs ont proposé que le rôle des CR dans le processus de fatigue est tout à fait similaire à celui de la contrainte moyenne [7]. Ainsi, la relaxation de contrainte moyenne sera un des points abordés dans la présente thèse. En outre, l'écrouissage local introduit par le grenaillage peut également avoir un rôle sur la fatigue et notamment modifier le durcissement ou l'adoucissement du matériau sous l'effet de la déformation plastique cumulée à chaque cycle de sollicitation.

# Chapitre 1

# Contexte et état de la recherche

## Les concepts de base concernés

### Grenaillage

Le grenaillage de précontrainte est un procédé de traitement à froid utilisé pour produire une couche de contraintes de compression et modifier les propriétés mécaniques des métaux [9]. Pendant le processus de grenaillage, chaque bille frappe les couches superficielles de la surface de la pièce provoquant une déformation plastique localisée. Après avoir été martelée

de nombreuses fois, la surface va être plastifiée de manière relativement uniforme ce qui produit une couche en compression, équilibrée par une sous-couche en traction. Simultanément, un écrouissage est induit dans la couche en compression. Le grenaillage de précontrainte est utilisé pour augmenter les performances en fatigue des composants soumis à de fortes sollicitations mécaniques [10].

## Contraintes résiduelles (CR)

D'une manière générale, les contraintes résiduelles sont des contraintes auto-équilibrées existants dans un composant ou une structure libre sans aucune charge externe appliquée. En fait, le mécanisme essentiel de formation de contraintes résiduelles est l'inhomogénéité de déformations inélastiques produites dans un composant. Cette inhomogénéité est produite par exemple par le procédé de mise en forme ou de traitement du matériau. Selon l'échelle de l'hétérogénéité, les contraintes résiduelles sont divisées en trois catégories, appelées CR d'ordre I (à peu près homogènes dans une zone relativement grande, macroscopique), d'ordre II (presque homogènes dans les constituants microscopiques, un grain ou une phase) et d'ordre III (non homogènes dans les zones microscopiques, sur quelques distances inter-atomiques) [11]. Dans cette thèse, nous nous concentrerons sur les contraintes d'ordre I.

## Écrouissage

L'écrouissage est un phénomène de durcissement d'un métal ductile quand il est déformé plastiquement [14]. Le mécanisme de l'écrouissage est étroitement lié aux dislocations. Dans les métaux, la déformation plastique se produit par le mouvement des dislocations. Lorsque les dislocations se déplacent, elles sont plus susceptibles de rencontrer et d'interagir avec d'autres dislocations ou défauts cristallins, produisant ainsi une résistance à la poursuite du mouvement. En outre, le nombre de dislocations dans un métal au cours de la déformation augmente considérablement, ce qui augmente encore la probabilité d'interaction. Cela se traduira une diminution de la mobilité des dislocations et un renforcement du métal [15].

## Fatigue dans les matériaux métalliques

La fatigue ou la rupture par fatigue est définie comme une modification des propriétés des matériaux en raison de l'application de contraintes ou de déformations cycliques, dont la répétition peut conduire à la fissuration ou à la rupture [16]. Les premiers travaux effectués par August Wöhler ont montré qu'un chargement unique, très en dessous de la résistance statique d'une structure, ne provoque pas de dommages. Cependant, si la même charge est répétée de nombreuses fois, elle peut provoquer une défaillance complète. Selon les variations de taux de charge (le rapport entre la charge minimale et la charge maximale) et le nombre de cycles, les essais de fatigue peuvent être classés en plusieurs types, tels que la fatigue alternée, la fatigue ondulée, etc. Les essais de fatigue peuvent également être classés en fatigue sous contrainte contrôlée ou en fatigue sous déformation contrôlée selon la manière de commander les essais. Les ruptures par fatigue se produisent en plusieurs phases qui sont généralement divisées en phase d'amorçage de la fissure, en phase de propagation et en rupture finale. On peut généralement considérer que le comportement en relaxation cyclique des CR induites par grenaillage se produit principalement pendant la phase d'amorçage.

## Influence des CR et de l'écrouissage sur la fatigue

### Influence des CR

De nombreux travaux ont confirmé que la présence de CR de compression à la surface des composants chargés cycliquement est bénéfique pour améliorer la durée de vie de fatigue [12]. Par conséquent, pour les pièces soumises à des sollicitations de fatigue, de nombreux concepteurs préconisent des techniques générant des CR de compression au niveau de la surface.

### Influence de l'écrouissage

Des expériences ont montré que le durcissement ou l'adoucissement des aciers joue un rôle sur la stabilité des contraintes. En effet, l'écrouissage, en augmentant la densité des dislocations rend plus difficile le mouvement de ces mêmes dislocations et augmente la résistance à la plastification [18]. Ceci est utile pour maintenir les CR de compression initiales induites par le grenaillage et améliore la résistance à la fatigue du métal. L'écrouissage (usuellement par l'application d'une surcharge) peut produire une zone plastique en pointe des microfissures de fatigue, ce qui peut retarder leur croissance [20].

## Evolution des CR et de l'écrouissage au cours du processus de fatigue

### Relaxation cyclique des CR

Pour les échantillons qui sont grenaillés, la relaxation se produit à tous les niveaux de chargement et est la plus rapide dans les premiers stades de fatigue. Dans une éprouvette grenaillée soumise à une sollicitation ondulée, les CR peuvent même changer de signe et devenir de la traction. Il existe principalement deux types de mécanismes de relaxation des CR. Tout d'abord, il y a une relaxation de structure lié à l'équilibre global de la section. Une plastification dans la région du cœur permet de réduire l'incompatibilité entre la surface grenaillée et le cœur. Ainsi, les CR de compression induites par grenaillage seront relaxées, même si la région de la surface est restée purement élastique. Un seul cycle de chargement est nécessaire pour ce processus. Ensuite, il peut y avoir une relaxation liée à une plasticité locale dans la région de la surface qui diminue l'incompatibilité entre les différentes couches progressivement. Ce processus nécessitera plusieurs cycles pour accumuler suffisamment de microplasticité pour se manifester à l'échelle mondiale.

### Relaxation cyclique de la contrainte moyenne

Dans les composants mécaniques soumis à un chargement cyclique asymétrique en déformation imposée, la plupart des matériaux présentent une relaxation de la contrainte moyenne. La bibliographie montre que l'amplitude de déformation a une forte influence sur le comportement de relaxation cyclique de la contrainte moyenne [29]. Une étude sous une sollicitation telle que $R_\varepsilon=0$ peut être intéressante pour analyser les relaxations de la contrainte moyenne et de la CR en surface. Elle peut nous aider à mieux comprendre la similitude et la divergence entre le comportement de relaxation de la contrainte moyenne et celui de la CR de surface introduite par grenaillage. Cela signifie que la relaxation en contrainte peut également

se produire dans un matériau durcissant cycliquement [32], bien que les mécanismes à l'origine de cette relaxation ne soient pas très clairs.

## Caractérisation des CR

Beaucoup d'expériences ont montré que des déformations structurelles se produisent lorsque les CR sont libérées par la coupe ou l'enlèvement de matière. Lorsque ces relaxations se produisent de manière purement élastique, il existe une relation linéaire entre la contrainte relâchée et les déplacements ou les déformations induites. Ceci est à la base des méthodes dites « de relaxation » pour caractériser les CR [34-36]. Il existe de nombreuses méthodes de relaxation, et la méthode du trou est probablement la plus largement utilisée [38-45].

## Caractérisation de l'écrouissage

Le fait que l'écrouissage augmente la valeur de la dureté mesurée a été montré expérimentalement dans la bibliographie [80, 81]. Des simulations numériques ont également montré un phénomène similaire [84]. L'essai de dureté est simple et facile à réaliser. Cependant, la dureté est sensible à la fois à l'écrouissage et aux contraintes résiduelles, ce qui a limité son utilisation pour évaluer l'écrouissage.

Il est possible de quantifier le niveau d'écrouissage dans les composants en corrélant les largeurs des pics de diffraction des rayons X à la déformation plastique équivalente [95-97]. Si le niveau d'écrouissage est assimilé à la déformation plastique équivalente, alors il est cumulatif et indépendant du mode de déformation [96]. Puis, en étalonnant la relation entre la largeur de pic et la déformation plastique cumulée, écrouissage peut être mesuré [94].

## Le titane et ses alliages

Le titane pur et la majorité des alliages de titane, cristallisent à basse température selon une structure hexagonale compacte (hcp) appelée titane $\alpha$. À des températures élevées, cependant, la structure cubique centrée (bcc) est stable et est appelé titane $\beta$. La température de transformation entre ces deux phases est 882ºC dans le matériau pur [107]. Des alliages de titane commerciaux sont classés en trois catégories différentes (alliages $\alpha$, $\alpha + \beta$ et $\beta$) en fonction de leur proportion de phase $\beta$ [107]. Dans le présent travail de thèse, deux alliages ont été étudiés, le T40 et le Ti-18.

### Titane pur de grade 2 commercial-T40

Le titane pur commercial (TPC) a un contenu minimum en titane allant d'environ 98,635 à 99,5 % en poids. Selon les normes ASTM B 348 [110] et ASTM B 265 [111], le titane pur de grade 2 doit présenter les compositions chimiques indiquées dans le Tableau 1-1. Ses propriétés de traction répondent aux exigences indiquées dans le Tableau 1-2.

**Tableau. 1-1 composition chimique nominale du T40 [110, 111].**

| Éléments | C | Fe | N | O | H | Ti |
|---|---|---|---|---|---|---|
| % masse | ≤0,08 | ≤0,20 | ≤0,03 | ≤0,18 | ≤0,015 | Bal |

**Tableau. 1-2 performances en traction du T40 [110, 111]. T est l'épaisseur de la tôle.**

| Résistance à la traction | Limite élastique (0.2% offset) | | Allongement dans 50 mm | Essai de pliage (Rayon de Mandrin) | |
|---|---|---|---|---|---|
| min | min | max | min | Sous 1,8 mm | 1,8-4,75 mm |
| MPa | MPa | MPa | % | d'épaisseur | d'épaisseur |
| 345 | 275 | 450 | 20 | 2T | 2,5T |

A température ambiante, le titane de pureté commerciale est typiquement une structure cristalline 100% $\alpha$. Il a une excellente résistance à la corrosion, une haute résistance spécifique et une bonne ductilité [113]. C'est un matériau standard en génie chimique où il est placé en contact avec de nombreux milieux corrosifs [107].

### Alliage de titane quasi $\beta$ à haute résistance Ti-18

Le TIMETAL 18 (Ti-18) a récemment été conçu comme un nouvel alliage de titane bimodal, visant à fournir une combinaison améliorée de la ductilité et la résistance mécanique, une capacité de refroidissement supérieure et moins de sensibilité à la chaleur des paramètres de traitement par rapport à l'alliage Ti-555 [116]. En considérant la table périodique des éléments, les éléments d'alliage du Ti-18 ont été définis comme: Ti-5,5Al-5Mo-5V-2.3Cr-0,8Fe-0,15O (% masse). Le Ti-18 a déjà montré des améliorations significatives des propriétés par rapport aux alliages actuels [116].

# Chapitre 2

# Caractérisation par indentation des CR et de l'écrouissage induits par le processus de grenaillage, étude par la méthode des éléments finis.

Dans le Chapitre 1, nous avons expliqué que l'écrouissage peut difficilement être mesuré directement. Compte tenu de la relation étroite entre l'écrouissage et la déformation plastique cumulée, cette dernière sera utilisée comme paramètre pour représenter le premier dans cette étude. Les contraintes résiduelles et la déformation plastique cumulée seront introduites dans un modèle par éléments finis (MEF) de l'indentation. Ensuite, les réponses d'indentation seront analysées pour construire une méthode permettant d'obtenir les valeurs des contraintes résiduelles et de la déformation plastique cumulée à partir du signal d'indentation.

### Modèle MEF

Le processus de grenaillage va générer une distribution des CR et de PP (Plastic Prestrain, déformation plastique) selon la profondeur. Afin de simplifier le problème, l'étude est effectuée sur un élément de volume représentatif. Les résultats de la bibliographie ont montré

que pendant le processus de simulation de l'indentation en présence de CR, c'est la contrainte hydrostatique dans la région sous la pointe de pénétrateur qui va influencer de manière significative le résultat, mais pas chaque composante individuelle du tenseur des contraintes [63]. Nous prenons un élément de volume représentatif (EVR) cylindrique en supposant que les valeurs des CR et des PP dans un tel volume sont homogènes. Ensuite, le pénétrateur Berkovich est représenté par un pénétrateur conique rigide avec un angle au sommet égal à 70,3° [118].

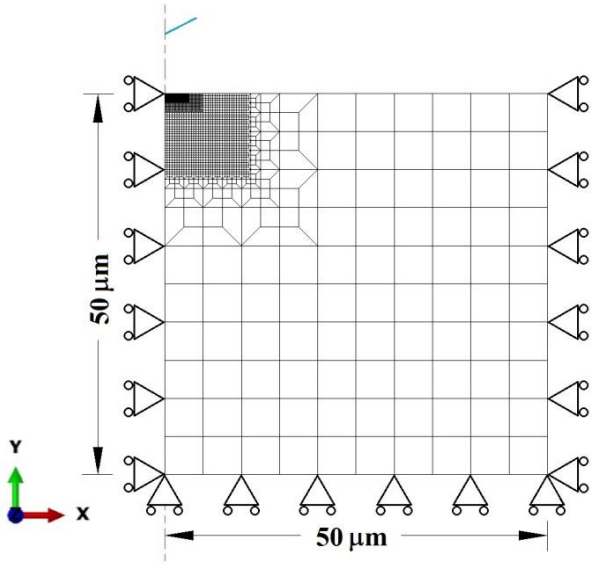


**Fig. 2-1. Le modèle axisymétrique utilisé dans cette étude.**

L'EVR axisymétrique en deux dimensions a été construit et maillé dans le code MEF commercial ABAQUS®6.11.2, comme le montre la Fig. 2-1. Les champs de contrainte et d'écrouissage initiaux sont ajoutés dans le modèle en utilisant le mot-clé *INITIAL CONDITION [120]. L'interaction entre la pointe de l'indenteur et le matériau cible est modélisée par un frottement de Coulomb avec un coefficient de frottement de 0,15, selon la bibliographie [122]. Un modèle d'écrouissage de type isotrope Ludwick est utilisé pour décrire le matériau cible, comme suit:

$$\sigma = \sigma_y + K(PP)^n \tag{2-1}$$

Tous les paramètres du modèle constitutif et leurs valeurs sont présentés dans le Tableau 2-1. Nous avons essentiellement étudié le rôle de la limite d'élasticité et du coefficient d'écrouissage, avec un niveau haut et un niveau bas pour chacun. Le comportement de référence étant celui du cuivre.

**Tableau 2-1 Propriétés des matériaux utilisés dans la simulation numérique.**

| | Cuivre [123] | A | B | C |
|---|---|---|---|---|
| Module d'Young $E$ (GPa) | 122 | 122 | 122 | 122 |
| Coefficient de Poisson $v$ | 0,33 | 0,33 | 0,33 | 0,33 |
| Limite d'élasticité $\sigma_y$ (MPa) | 240 | 800 | 240 | 800 |
| Coefficient d'écrouissage $K$ (MPa) | 340 | 340 | 340 | 340 |
| Exposant d'écrouissage $n$ | 0,57 | 0,1 | 0,1 | 0,57 |

Avec le comportement constitutif du matériau A, la convergence du maillage et le type de maille ont été étudiés. Un maillage raffiné localement est construit et testé afin de converger avec un coût de calcul minimal. Une validation a été effectuée en comparant le modèle MEF avec des solutions théoriques.

## Mesure des CR à l'aide d'un étalonnage par MEF

Avant d'essayer de caractériser simultanément par indentation les CR et la PP induites par le processus grenaillage, nous avons d'abord tenté de mesurer les CR seules. Comme mentionné dans le Chapitre 1, plusieurs stratégies ont été construites pour caractériser CR par indentation instrumentée au cours des dernières décennies.

La bibliographie montre que les CR dans la surface du matériau, de traction ou de compression, entraîneront des changements de la courbe de charge en fonction de la profondeur (courbe *P-h*) [63, 125]. Si l'indentation est effectuée en déplacement contrôlé afin d'atteindre une profondeur de pénétration maximale donnée, des CR de compression décaleront la courbe *P-h* vers le haut, c'est à dire pour les forces de pénétration plus élevées, et des CR de traction vont induire le comportement inverse. Sur cette base, nous avons essayé d'étalonner les CR à l'aide de la courbe *P-h* à la charge. Cependant, nous avons pu montrer que les courbes *P-h* pour un certain PP et cela pour une CR donnés sont presque complètement superposées, ce qui signifie que les CR et les PP ne peuvent pas être séparées à l'aide la forme des courbes *P-h*.

## Principes de la méthode des fonctions simultanées

Bien que les courbes *P-h* soient superposées, une différence sur les valeurs de bourrelet (pile-up) a été observée ce qui peut nous donner une autre possibilité pour séparer CR et PP. Pour mieux comprendre cela, une série de travaux a été menée. Un travail sur les lois de comportement a montré qu'une limite d'élasticité plus élevée augmente la charge maximale ($P_{max}$) et la dureté de contact ($H$). Une augmentation du coefficient d'écrouissage donne une valeur plus élevée du bourrelet et la raideur de contact ($S$).

D'autres travaux ont montré que les CR et les PP vont influencer $P_{max}$, $S$, $H$ et le bourrelet, ce dernier étant très sensible aux CR, mais insensible à la PP. Alors maintenant, les inconnues sont CR et PP et les entrées possibles sont $P_{max}$, $S$, $H$ et le bourrelet. Du fait que $H$ et $S$ sont corrélés avec le bourrelet, mais beaucoup plus facile d'obtention, nous avons décidé d'éliminer le bourrelet de la mesure. $P_{max}$, $S$ et $H$ peuvent alors être normalisés par $P_{max0}$, $S_0$ et $H_0$ qui sont les réponses d'indentation obtenues à partir d'un échantillon de référence sans CR et PP. Bien que CR et PP puissent affecter $P_{max}/P_{max0}$, $S/S_0$ et $H/H_0$, la manière et le niveau de variation de chaque paramètre peut ne pas être la même. Ainsi, il est possible d'obtenir trois fonctions mathématiques individuelles, tels que $P_{max}/P_{max0}=f$(CR, PP), $S/S_0=g$(CR, PP) and $H/H_0=h$(CR, PP). En combinant simultanément deux de ces fonctions ou même les trois, on doit être en mesure d'obtenir les valeurs de CR et PP. Cette méthode est appelée la "méthode des fonctions simultanées".

## Caractérisation de CR et PP avec la méthode des fonctions simultanées

Le matériau A a été choisi comme matériau cible, parce qu'une étude préalable a montré la sensibilité aux CR et à PP. Si la méthode des fonctions simultanées fonctionne bien sur le matériau A, il devrait bien fonctionner pour les trois autres matériaux également. En outre, la limite d'élasticité du matériel A étant relativement élevé, on peut explorer des niveaux élevés de contraintes résiduelles comme ceux observés dans grenaillage pour des applications pratiques. Une série de simulations de l'indentation sur le matériau A avec différents niveaux de CR et PP a été effectuée. Les niveaux de PP sont respectivement de 0%, 1%, 5%, 10%, 15% et 20%. Les niveaux de CR correspondants sont 0 MPa, -200 MPa, -400 MPa, -600 MPa, -800 MPa -1000 MPa et $-\sigma_y$, où $\sigma_y$ est la limite d'élasticité obtenue pour un écrouissage correspondant à chaque niveau de PP imposée et calculée selon l'Eq.(2-1). Une simulation numérique a été effectuée pour chaque combinaison possible de CR et PP. Précisons que les valeurs de rigidité de contact (S) sont obtenues par ajustement linéaire du début de la décharge de la courbe *P-h*, mais pas avec le modèle d'Oliver et Pharr car cela donne des résultats plus cohérents.

Afin d'illustrer la méthode d'un point de vue purement numérique, des simulations de deux combinaisons arbitraires de CR et PP sont effectuées. La combinaison 1 (C1) est PP=11,5% et CR=-830 MPa , et la combinaison 2 (C2 ) est PP=16,5% et CR=-450 MPa. Les valeurs de CR et PP dérivés de la méthode des fonctions simultanées sont présentées dans le Tableau 2-2. On constate que, d'un point de vue numérique, les résultats sont cohérents.

**Tableau 2-2 Les valeurs de RS et PP dérivées de la méthode des fonctions simultanées.**

| | $C_1$ (PP=11,5%, CR=-830MPa) | | | $C_2$ (PP=16,5%, CR=-450MPa) | | |
|---|---|---|---|---|---|---|
| | $P_{max}/P_{max0}$ -$S/S_0$ | $P_{max}/P_{max0}$ -$H/H_0$ | $S/S_0$ -$H/H_0$ | $P_{max}/P_{max0}$ -$S/S_0$ | $P_{max}/P_{max0}$ -$H/H_0$ | $S/S_0$ -$H/H_0$ |
| CR (MPa) | -837,9 | -838,3 | -837,6 | -453,4 | -453,1 | -453,8 |
| PP (%) | 11,62 | 11,61 | 11,61 | 16,51 | 16,60 | 16,59 |

Afin d'étudier la stabilité de la méthode par rapport à un bruit sur les valeurs d'entrée, une fluctuation de ±0,5% a été ajoutée sur chaque paramètre d'indentation $P_{max}/P_{max0}$, $S/S_0$ et $H/H_0$. Les résultats montrent que la sensibilité de la méthode varie de façon significative avec l'intervalle (PP-CR) et l'espace exploré avec la paire de fonctions ($P_{max}/P_{max0}$ et $S/S_0$, ou $P_{max}/P_{max0}$ et $H/H_0$, ou $S/S_0$ et $H/H_0$) choisis. Cela signifie que, en fonction du comportement du matériau constitutif et l'amplitude attendue de la contrainte résiduelle et la déformation plastique, les fonctions utilisées doivent être choisies avec soin.

# Chapitre 3

# Caractérisation expérimentale de la CR et de l'écrouissage induits par le processus de grenaillage

Les simulations numériques ayant montré une bonne faisabilité et la qualité de la méthode des fonctions simultanées pour la séparation des CR et des PP, l'étape suivante consiste à appliquer cette méthode dans des cas réels. Dans le présent chapitre, nous allons mettre l'accent sur comment caractériser les CR et la PP induites simultanément par le processus de grenaillage.

## Grenaillage

Tout d'abord, un morceau de T40 TCP, avec une épaisseur d'environ 12 mm, a été coupé à partir d'une barre ($\Phi$=50 mm). Il a été poli avec des disques abrasifs de 800 grains pour enlever la couche affectée par le processus de coupe et obtenir une bonne planéité et rugosité. Ensuite, l'échantillon a été grenaillé sur un système de grenaillage par ultrasons. L'observation de la microstructure de la section transversale de l'échantillon grenaillé est tout à fait typique du grenaillage.

## Diffraction des rayons X (DRX)

Des essais de DRX ont été effectués pour mesurer les profils de CR et la largeur des pics de diffraction. Le diffractomètre est équipé d'un tube à anode de cuivre (40 kV et 30 mA). Les mesures ont été effectuées sur les plans {302} de la phase $\alpha$ du titane, à $2\theta_0$=149,05°. Un détecteur à localisation linéaire (PSD) qui couvre 11° a été utilisé pour recueillir le signal diffracté. La gamme de balayage est 144° à 154°. Le temps de comptage est de 220 s/pas, et la taille de pas est de 0,05 °$2\theta$. Pour utiliser méthode des $\sin^2\Psi$, 13 valeurs des angles $\Psi$ ont été choisies. La procédure de polissage électrolytique, avec une tension de 50 V et un courant de 16 mA pendant 30 s chaque fois dans une solution de type D11 (70% d'éthanol, 20% de l'acide perchlorique et 10% de *l'éthylène glycol éther monobutylique*), a été utilisée pour réaliser l'enlèvement de couches successives sur l'échantillon grenaillé. L'épaisseur de la couche enlevée a été mesurée par un capteur laser de distance présentant une incertitude de 3 $\mu$m. Un script de Wolfram Mathematica® a été écrit pour extraire les CR et l'élargissement de pics des données de DRX. Les profils obtenus sont présentés dans la Fig. 3-1. Le profil de CR a déjà été corrigé des effets d'enlèvement de matière à l'aide du formalisme des eigenstrains.

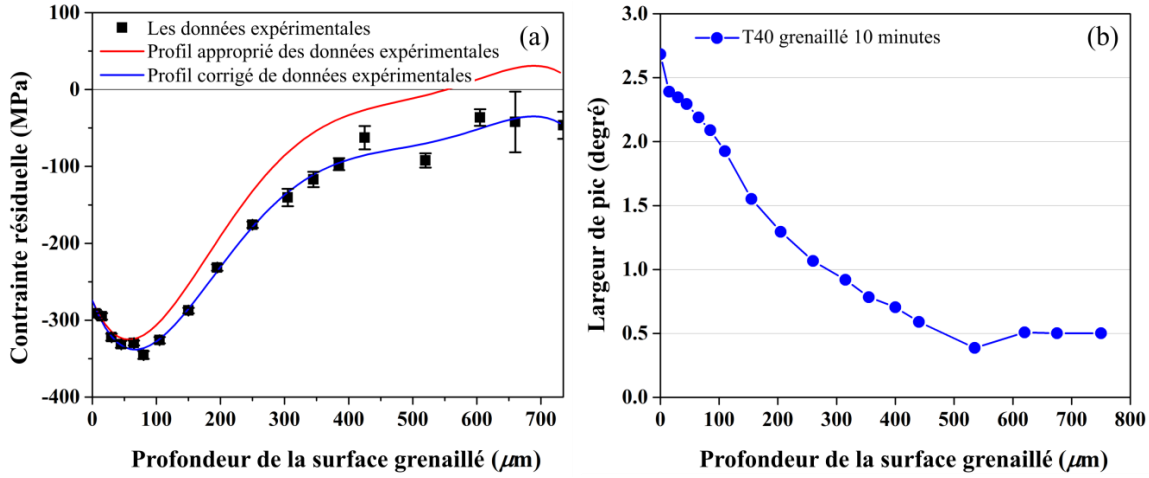

**Fig. 3-1. Les résultats des essais de DRX: (a) le profil des CR; (b) le profil de largeur de pic.**

## Caractériser l'écrouissage par DRX

La méthode consistant à quantifier le niveau d'écrouissage en corrélant la largeur d'un pic de diffraction des rayons X à la déformation plastique équivalente a été étudiée et discutée dans la bibliographie [95-97]. Afin de réaliser ce type d'étalonnage, plusieurs étapes sont nécessaires, y compris la préparation de plusieurs échantillons de traction uniaxiale, la réalisation de tests de traction à différents niveaux de déformation plastique et des essais de diffraction des rayons X après chaque essai de traction pour obtenir les largeurs des pics correspondantes.

Les éprouvettes de traction ont été conçues selon la norme ASTM E8/E8M-09 [135], et fabriquées par électroérosion à fil. Afin d'éliminer les perturbations introduites par l'électroérosion, des protocoles de polissage spécifiques ont été menés. Premièrement, une étape de polissage mécanique commune à tous les échantillons a été menée. À la fin de la phase de polissage mécanique commune, le polissage par vibrations a été utilisé avec une pression de contact la plus faible possible. Si cette étape ne peut toujours pas offrir une surface sans déformation plastique, un polissage électrolytique est finalement effectué, au cours duquel les échantillons seront sous protection particulière pour maintenir la précision dimensionnelle. La DRX sera également utilisée pour vérifier la variation de la largeur de pic pendant toute la procédure de polissage. Sur la Fig. 3-1 nous pouvons voir que la largeur de pic à l'état initial est d'environ $0.5^{o}$. Cependant, nos résultats ont montré que, même pour un polissage vibratoire très doux et très long, on ne peut atteindre une largeur de pic inférieure à $0.9^{o}$, ce qui signifie qu'il y a encore une certaine déformation plastique externe introduite par la procédure de polissage mécanique. Ainsi, le polissage électrolytique, avec une tension de 45 V et un courant de 15 mA pendant 15 s chaque fois dans une solution de D11, a ensuite été effectuée. Comme cette procédure est encline à arrondir les bords, une protection particulière doit être appliquée sur l'échantillon, qui ne laisse exposée que la partie calibrée.

Après la préparation des échantillons, des essais de traction uniaxiale ont été menés jusqu'à atteindre le point de striction autour de PP=15%. Comme cette valeur est petite par rapport au niveau de PP induit par grenaillage, les données ont été extrapolées à l'aide d'une loi de puissance qui est, bien sûr, discutable. Les résultats de la Fig. 3-2(a) montrent que la qualité de l'ajustement est bonne. Avec cet ajustement, le profil d'écrouissage introduit par le processus de grenaillage peut être estimé, comme le montre la Fig. 3-2(b). Nous pouvons voir que, près de la surface grenaillée, le niveau d'écrouissage peut dépasser 60%. Ensuite, elle diminue rapidement et s'estompe lorsque la profondeur est supérieur à 400 $\mu$m.

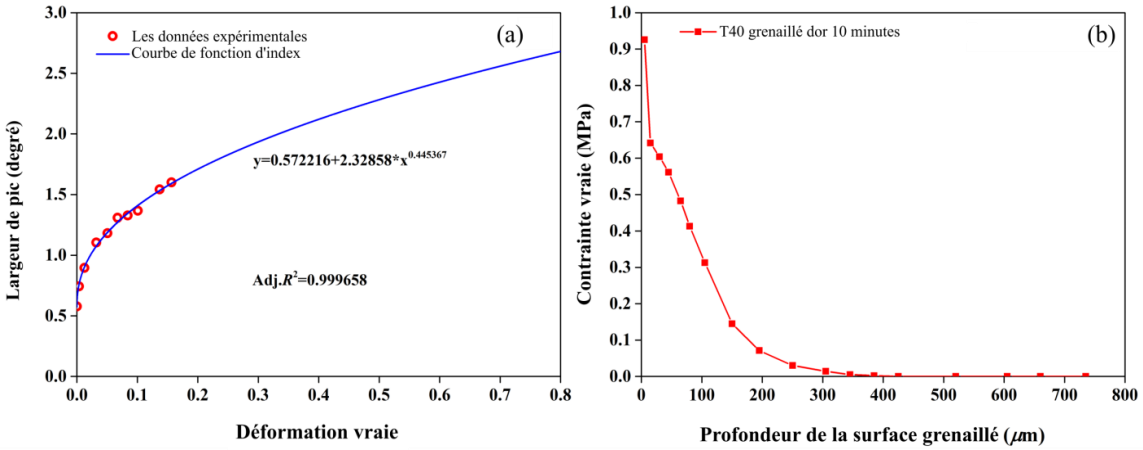


**Fig. 3-2. Relation entre la largeur de pic et la déformation plastique équivalente et le profil de la déformation plastique équivalente selon la profondeur: (a) points de données expérimentales et l'indice fonction d'ajustement de largeur de pic contre déformation plastique équivalente; (b profil de la déformation plastique équivalente selon la profondeur extrait de (a).**

Jusqu'à présent, les valeurs de CR et PP dans l'échantillon de T40 grenaillé ont été obtenus. Ceci donne une référence pour les parties ultérieures de l'étude consistant à caractériser les CR et l'écrouissage par indentation instrumentée.

## Indentation instrumentée

Dans la présente section, la méthode des fonctions simultanées est testée expérimentalement. Premièrement, un échantillon est préparé par polissage mécanique minutieux. Après le polissage, il présente une largeur de pic assez faible (0.52°) ce qui permet de le considérer comme bien préparé. Puis, suite à la norme ASTM E 2546-07 [142], une série d'essais de pénétration instrumentée a été effectuée sur l'échantillon à différentes distances de la surface de grenaillé selon la profondeur (50 $\mu$m, 80 $\mu$m, 140 $\mu$m, 200 $\mu$m, 280 $\mu$m, 360 $\mu$m, 440 $\mu$m, 520 $\mu$m, 600 $\mu$m, 700 $\mu$m, et 900 $\mu$m). La partie qui est assez loin (900 $\mu$m) de la surface grenaillée sur l'échantillon est utilisée comme référence, parce qu'à une telle profondeur, les effets du processus de grenaillage sont censés être inexistants.

Les résultats d'indentation ont montré que lorsqu'on se rapproche de la surface grenaillée, $H$ et $P_{max}$ augmentent, ce qui est conforme à nos résultats de simulation. Cependant, la valeur de $S$ diminue significativement. Même en corrigeant l'effet de bord libre, la raideur S dans la zone grenaillée reste inférieure à la valeur loin de la surface grenaillée.

## Simulations par éléments finis de l'indentation instrumentée sur T40

Dans cette partie du travail, avant de l'appliquer la méthode des fonctions simultanées sur le T40, des simulations par éléments finis sans CR et PP sont d'abord effectuées et discutées. Le modèle construit dans le Chapitre 2 est utilisé avec deux pénétrateurs (un idéal et un calibré) et la loi de comportement obtenue par un essai de traction uniaxiale sur le T40. Tous les

résultats des courbes *P-h*, $P_{max}$, *S* et *H* ont montré une grande différence entre l'expérience et les simulations.

Grâce à l'examen de la pointe calibrée dans le modèle MEF, la qualité de toutes les réponses d'indentation pourrait être améliorée, mais pas encore assez, ce qui signifie qu'il doit y avoir certains facteurs qui n'ont pas été pris en compte correctement. En analysant les configurations du modèle, plusieurs aspects ont été considérés. Ils sont respectivement la forme de pénétrateur, les paramètres du comportement mécanique du matériau et le coefficient de frottement (*f*). En fait, de nombreux autres facteurs pourraient également introduire des décalages dans le modèle. Cependant, ils ne sont pas pris en compte ici, parce qu'ils dépassent le cadre de la présente thèse.

Afin de réduire la différence entre les données expérimentales et les résultats simulés, une méthode inverse est utilisée. La forme du pénétrateur est d'abord optimisée, car elle est la base d'autres optimisations. Ensuite, les paramètres du matériau et le coefficient de frottement (*f*) sont optimisés. À l'origine, il y a six variables d'entrée, qui sont les deux paramètres élastiques (module d'Young *E* et coefficient de Poisson *v*), trois paramètres plastiques (limite d'élasticité $\sigma_y$, coefficient d'écrouissage *K* et l'exposant d'écrouissage *n*) et le coefficient de frottement (*f*). Ensuite, il y a quatre objectifs, qui sont la différence de charge maximale ($\Delta P_{max}$), la différence de raideur de contact ($\Delta S$) entre les valeurs simulées et les valeurs expérimentales, et le carré de la distance entre la courbe *P-h* à la décharge normalisée simulée et expérimentale ($\Delta g(P)$).

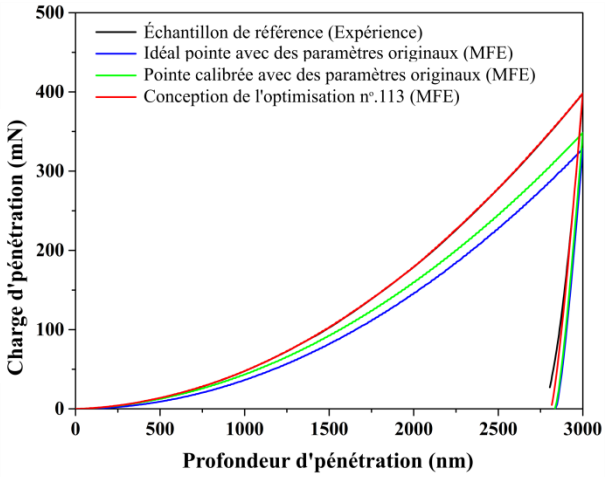


**Fig. 3-4. Courbes *P-h* obtenues à partir d'indentation expérimentale et simulée par MEF.**

Après l'optimisation des paramètres du matériau et du coefficient de frottement (*f*), la différence entre les données expérimentales et les résultats simulés sont évidemment diminués, comme représenté sur la Fig. 3-4. Mais, les paramètres plastiques optimisés sont très différents de ceux d'origine, comme représenté sur la Fig. 3-5, ce qui doit être examiné en détail.

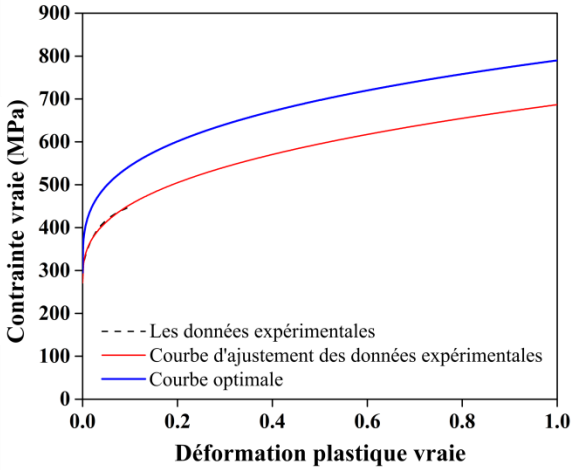


**Fig. 3-5. Courbe de la contrainte en fonction de la déformation plastique vraie en traction uniaxiale, la courbe correspondante qui est mieux adaptée et la courbe optimale.**

Trois raisons possibles sont étudiées. Ce sont le coefficient de frottement (*f*), la différence entre un pénétrateur Berkovich 3D et le pénétrateur conique équivalent en 2D et les mécanismes de déformation plastique des alliages de titane. Les résultats ont montré que l'influence des deux premiers facteurs est assez limitée. L'effet de la différence entre comportement en traction et en compression et l'anisotropie d'écoulement de la phase $\alpha$-du titane peuvent expliquer beaucoup plus.

## Extraction de CR et PP avec la méthode des fonctions simultanées

Dans cette section, le modèle MEF avec les paramètres optimisés est utilisé pour effectuer une série de simulations avec différents niveaux de la PP (0%, 1%, 5%, 10%, 15%, 20%, 30%, 40%, 50%, 60% and 70%) et de la CR (commencé de 0 MPa avec un intervalle de -100 MPa jusqu'à atteindre la limite d'élasticité de chaque niveau de la PP). Ensuite, les valeurs de $P_{max}/P_{max0}$, $S/S_0$ et $H/H_0$ à tous les points discrets ont été utilisés pour construire les fonctions. En combinant les fonctions avec les réponses normalisées qui sont obtenues à partir d'indentations expérimentales sur l'échantillon, nous essayons de caractériser les CR et la PP induites simultanément par le processus de grenaillage. Malheureusement, deux problèmes critiques ont été rencontrés. Tout d'abord, la variation de $S/S_0$ avec l'augmentation de PP et CR qui est obtenue par les simulations est à l'opposé des résultats expérimentaux. Deuxièmement, la gamme des valeurs de $H/H_0$ obtenus par simulation ne suffisent pas à couvrir la gamme des données expérimentales. Ces deux problèmes ne permettent pas l'application de la méthode des fonctions simultanées dans le cas du grenaillage. Toutefois, la gamme de $P_{max}/P_{max0}$ simulé couvre toutes les données obtenues expérimentalement, ce qui offre la possibilité de construire une méthode limitée qui peut être utilisée pour extraire le profil de PP, connaissant le profil de CR, comme le montre la Fig. 3-6.

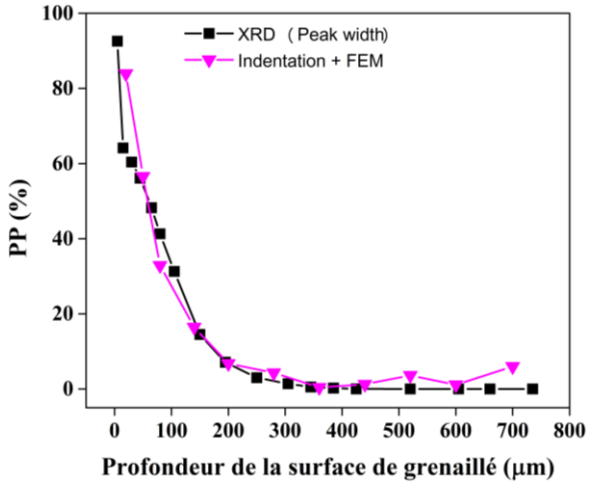


**Fig. 3-6. Les PP profils obtenus avec différentes méthodes.**

# Chapitre 4

# Evolution des CR et de l'écrouissage induits par grenaillage durant la fatigue oligocyclique

Dans ce chapitre, le Ti-18, un alliage quasi β haute résistance nouvellement développé a été choisi. Une série de tests de fatigue à faible nombre de cycles en déformation contrôlée a été effectuée sur plusieurs éprouvettes traitées mécaniquement par des procédures différentes : grenaillage, prédéformation plastique et prédéformation plastique + grenaillage. Les techniques de diffraction des rayons X et l'indentation instrumentée ont été utilisées pour caractériser les contraintes résiduelles et l'écrouissage du matériau. Enfin, l'évolution des contraintes résiduelles et de l'écrouissage au cours du cyclage a été étudié.

## Caractérisation du matériau

Un quart d'un lingot ($\Phi$=250 mm) de l'alliage Ti-18 a été utilisé. Un essai de traction uniaxiale a été effectué pour étudier les propriétés mécaniques de base et a donné des résultats cohérents avec la bibliographie [196].

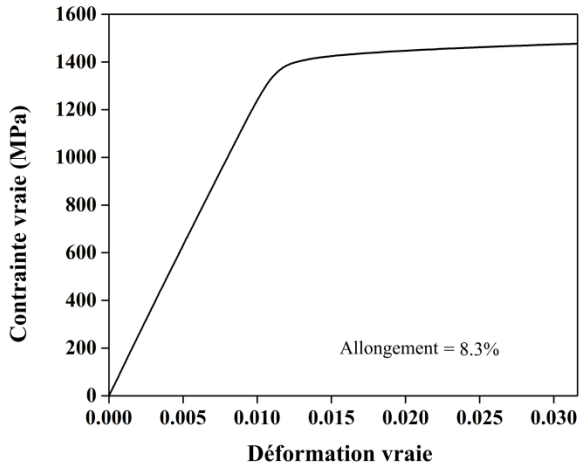


**Fig. 4-1. Courbe de la contrainte vraie en fonction de la déformation vraie en traction uniaxiale du Ti-18.**

## Préparation et prétraitement des éprouvettes de fatigue

Plusieurs éprouvettes de fatigue ont été préparées selon la norme ASTM E466-07 [2]. Les échantillons ont d'abord été découpés dans le lingot par électroérosion puis tournés pour atteindre la forme désirée.

Afin d'étudier les influences de la CR et de l'écrouissage sur les réponses en fatigue oligocyclique, un plan d'expériences simple a été mené. Douze éprouvettes, avec quatre états mécaniques différents ont été utilisées:

A) Eprouvettes brutes de tournage;

B) Eprouvettes brutes + pré déformation plastique en traction;

C) Eprouvettes brutes + grenaillage;

D) Eprouvettes brutes + pré déformation plastique en traction + grenaillage.

Afin d'étudier les effets d'une déformation plastique homogène sur les essais de fatigue, six spécimens doivent être pré déformés. L'idéal serait d'atteindre une déformation plastique cumulée similaire à celle obtenue en grenaillage, ce qui n'est pas possible en pratique. Compte tenu de la courbe contrainte-déformation de la Fig.4-1, une déformation totale de 3,2% (déformation plastique de 1,8%) a été choisie.

Afin de comparer le processus de grenaillage sur des échantillons cylindriques de Ti-18 avec ce qui avait été fait sur l'éprouvette plate de T40, des simulations ont été faites pour déterminer les paramètres de traitement appropriés qui peuvent donner environ la même densité d'impact pour les deux cas. Ces simulations utilisent le modèle et le logiciel développés par Badreddine *et al*. [198]. Six échantillons (trois bruts et trois pré déformés) ont été grenaillé sur un système de grenaillage par ultrasons. Les mesures de rugosité et l'observation au microscope optique ont montré que le grenaillage a effacé une partie importante de la topographie (stries) induite par le tournage. Ce facteur peut influer sur les performances en fatigue des éprouvettes.

## Essais de fatigue

Afin de comprendre la relaxation de la contrainte moyenne et des CR en surface, des essais de fatigue en déformation totale contrôlée ($R_\varepsilon$=0) ont été réalisés. Pour choisir les amplitudes de déformation imposées aux éprouvettes, 3 niveaux ont été considérés vis-à-vis du grenaillage, en supposant que les sections planes restent planes :

- Légère plastification du cœur, en contrainte résiduelle de traction
- Plastification franche du cœur et légère plastification de la couche grenaillée, en compression
- Plastification franche de l'ensemble de la section

Ces critères nous donnent trois amplitudes correspondantes : $\Delta\varepsilon/2$= {0,7%, 1,0%, 1,4%}.

Les essais de fatigue ont été effectués sur une machine hydraulique de fatigue (100 kN) du Denison Mayes Group (DMG). Tous les essais ont été arrêtés lorsque la contrainte moyenne est à peu près stabilisé (pour $\Delta\varepsilon/2$=1,0% et $\Delta\varepsilon/2$=1,4%, il est après 100 cycles, et pour $\Delta\varepsilon/2$=0,7%, il est après 140 cycles).

L'observation des cycles de contrainte-déformation a montré que lorsque l'amplitude de déformation imposée augmente, l'ouverture des boucles d'hystérésis (déformation plastique cyclique) augmente également. L'influence du traitement des éprouvettes peut être observée à partir de ces courbes ainsi, par exemple l'échantillon n°15 dans la Fig. 4-3.

En outre, la prédéformation diminue ce taux stable de relaxation, ce qui signifie que pour le Ti-18, une prédéformation en traction appropriée peut effectivement retarder la relaxation de la contrainte moyenne pendant les essais de fatigue oligocyclique, même pour une amplitude de déformation est aussi élevée que 1,4%. Les variations de l'amplitude de contrainte pour $\Delta\varepsilon/2$=0,7% montrent que les échantillons sont légèrement adoucis. Pour $\Delta\varepsilon/2$=1,0% and $\Delta\varepsilon/2$=1,4%, tous les spécimens passent par un stade de durcissement suivi par un stade d'adoucissement.

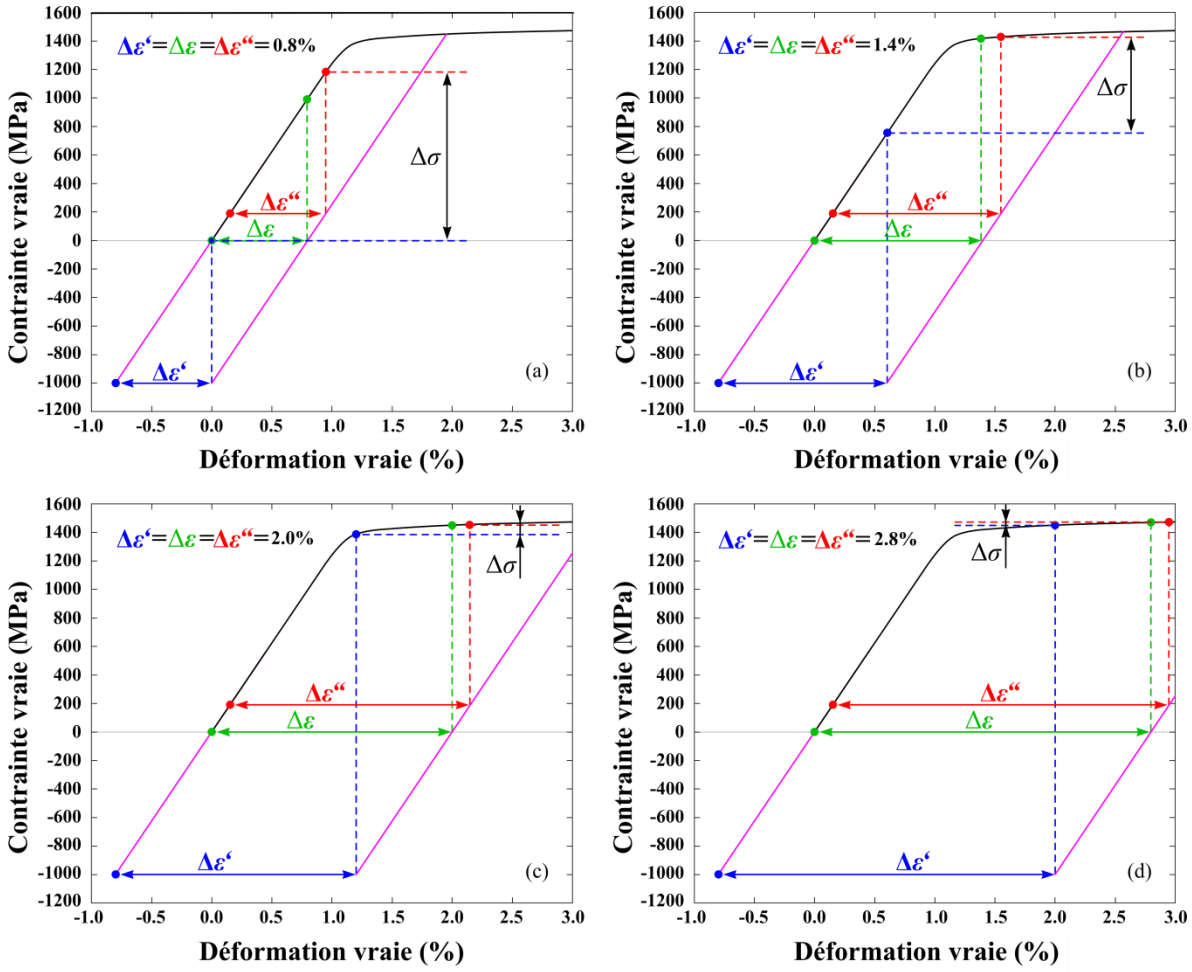


**Fig. 4-2. Choix des conditions de chargement du point de vue structurel: (a) 0,8% d'amplitude de déformation de traction (b) 1,4% d'amplitude (c) 2,0% d'amplitude (d) 2,8% d'amplitude. Δ$\sigma$ est la différence de contrainte entre le coeur (CR de traction) et la surface grenaillée (CR de compression) après la première moitié du cycle de chargement.**

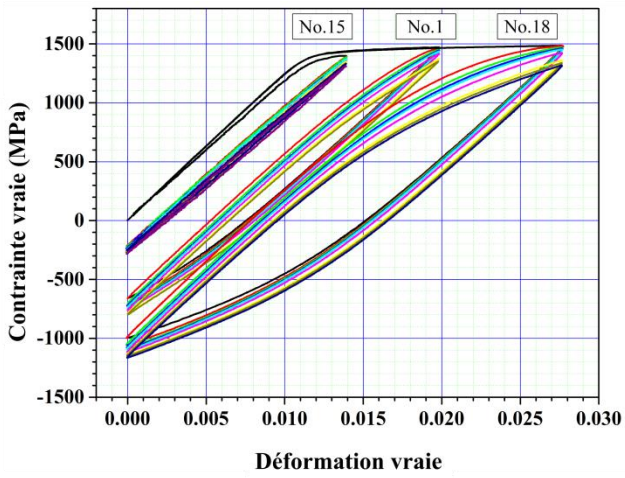


**Fig. 4-3. Courbes de traction cycliques pour les éprouvettes en Ti-18 prédéformées: No.8 (Δε/2=0.7%), No.6 (Δε/2=1.0%) et No.5 (Δε/2=1.4%).**

# Diffraction des rayons X (DRX)

Des essais de DRX ont été effectués pour mesurer les profils de CR et la largeur des pics à la surface des éprouvettes. Le plan {302} de la phase $\alpha$ du titane, avec un angle de diffraction à $2\theta_0$=149,05°, a été choisi pour cette étude. Un détecteur à localisation linéaire qui couvre 11° été utilisé pour recueillir le signal diffracté. L'intervalle de mesure est 144° à 154°. Le temps de comptage est de 220 s/pas, et la taille de pas est de 0,27 °2$\theta$. Pour utiliser méthode des $\sin^2\Psi$, 9 $\Psi$ angles ont été choisis entre -60 ° et +60 °.

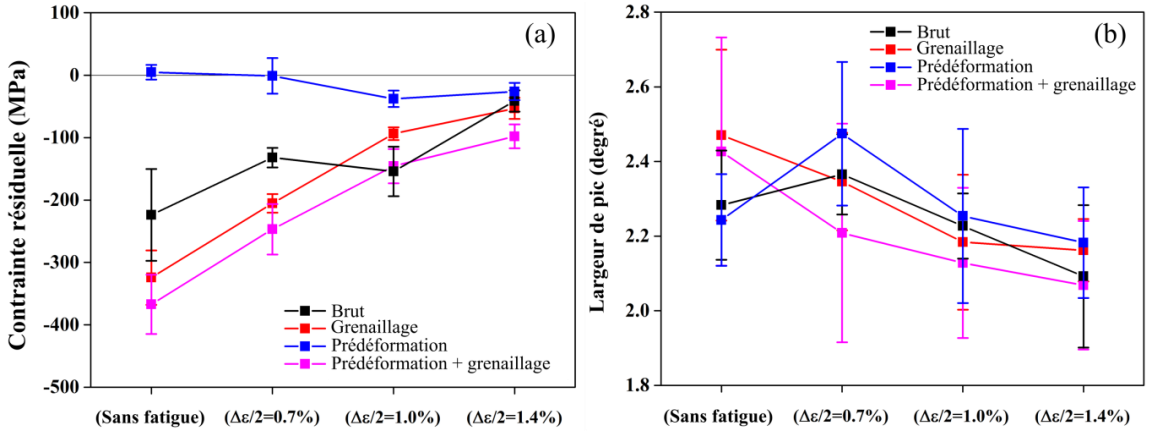


**Fig. 4-4. (a) Contraintes résiduelles axiales obtenues par diffraction des rayons X; (b) largeurs de pic par diffraction des rayons X. Valeurs obtenues en surface avant fatigue ou après 100 cycles pour l'amplitude de déformation indiquée.**

La Fig. 4-4(a) montre que le grenaillage ou une prédéformation suivie d'un grenaillage peuvent induire des CR de compression significatives à la surface des éprouvettes. En outre, amplitude de déformation plus élevée peut causer davantage de relaxation de la CR de surface. Les éprouvettes grenaillées relaxent plus fortement que l'éprouvette non traitée (CR dues à l'élaboration par tournage). L'éprouvette prédéformée ne présente pas de contrainte significative. Fig. 4-4(b) montre qu'un adoucissement cyclique se produit dans les éprouvettes grenaillées (avec ou sans prédéformation). Cet adoucissement est d'autant plus prononcé que l'amplitude de déformation est élevée. Pour les deux autres éprouvettes (brute d'usinage ou prédéformée), on observe une augmentation de la largeur des pics pour une faible amplitude de déformation et une diminution pour de plus fortes amplitudes.

## Indentation instrumentée

Sur les éprouvettes après fatigue, des essais d'indentation instrumentée ont été effectués sur une section transverse. La surface analysée a été soigneusement polie avec la même procédure que pour le T40 mais avec une durée à chaque étape plus élevée. Tous les échantillons du II sont soigneusement polis dans la même procédure de l'échantillon n°3 du T40 mais avec plus de temps de chaque étape. Les mesures ont été effectuées sur les 14 éprouvettes à différentes profondeurs depuis la surface grenaillée (50 $\mu$m, 80 $\mu$m, 140 $\mu$m, 200 $\mu$m, 280 $\mu$m, 360 $\mu$m, 440 $\mu$m, 520 $\mu$m, 600 $\mu$m, 700 $\mu$m, and 900 $\mu$m) en suivant les préconisations de la norme ASTM E 2546-07 [142].

Les échantillons grenaillés et prédéformés + grenaillés montrent des valeurs moyennes de $P_{max}$ plus élevées que les échantillons bruts et simplement prédéformés. Les valeurs de $P_{max}$ diminuent lorsqu'on se rapproche de la surface grenaillée, ce qui peut indiquer que le grenaillage a induit un adoucissement et non un durcissement de la surface. Ce fait est à rapprocher du comportement du matériau qui présente un écrouissage saturant très rapidement.

Pour tous les échantillons grenaillés et prédéformés + grenaillés, les valeurs moyennes de $S$ ont tendance à augmenter avec l'augmentation de l'amplitude de la déformation.

Il n'y a pas de variation de $H$ significatives pour toutes les éprouvettes, ce qui est surprenant et peut être également rapproché du comportement « très plat » du matériau.

# Chapitre 5

# Conclusions

Lors de l'étude du comportement en fatigue oligocyclique de matériaux grenaillés, deux points doivent être abordés. Tout d'abord, comment caractériser simultanément les contraintes résiduelles et l'écrouissage, localement sous la surface grenaillée et notamment pour des pièces de géométrie complexe. Ensuite, on souhaite suivre l'évolution de ces deux quantités au cours des essais de fatigue.

L'indentation instrumentée a été choisie pour répondre au premier point. En effet, cette technique permet d'analyser très localement l'état mécanique du matériau avec une grande finesse. Toutefois, les contraintes résiduelles de compression et l'écrouissage peuvent tous deux introduire des changements similaires sur les courbes de la force d'enfoncement en fonction de la pénétration.

Une modélisation numérique par éléments finis a permis d'analyser l'effet conjoint des contraintes et de l'écrouissage sur les mesures par indentation. Les deux grandeurs (contrainte et écrouissage) n'ayant pas le même effet sur le développement du bourrelet autour de l'indenteur, cela nous a permis de proposer une méthode pour les séparer à l'aide de la mesure de deux des trois paramètres : dureté, raideur de contact et force de pénétration maximale. La méthode a été testée numériquement avec succès, y compris en introduisant un bruit sur les valeurs mesurées.

La méthode a été testée expérimentalement sur un alliage de titane de pureté commerciale, le T40 qui a été grenaillé par ultrasons. Elle a été toutefois mise en défaut par deux aspects : les variations de dureté observées expérimentalement sont plus élevées que celles obtenues par éléments finis et la raideur de contact expérimentale est plus faible dans l'épaisseur grenaillée que sur le matériau non traité, ce qui ne peut pas être reproduit par le modèle. Le même phénomène a été observé sur l'alliage Ti18. La force maximale de pénétration peut toutefois être utilisée pour mesurer la déformation plastique cumulée avec une bonne précision lorsque les valeurs de contraintes résiduelles sont connues, par exemple par diffraction des rayons X.

L'évolution des contraintes résiduelles de surface et l'évolution des largeurs de pics de diffraction a été observée au cours de la fatigue oligocyclique d'un alliage de titane Ti18 de

structure α+β. Quatre états de traitement ont été étudiés : brut d'usinage, prédéformé plastiquement, grenaillé et prédéformé puis grenaillé. Trois amplitudes de déformation ont été appliquées sur une centaine de cycles avec $R_\varepsilon = 0$. On a pu constater que la contrainte moyenne ainsi que la contrainte résiduelle de surface sont relaxées de manière plus forte lorsque l'amplitude de déformation appliquée augmente. L'introduction d'une prédéformation peut retarder efficacement la relaxation de la contrainte moyenne et de la contrainte résiduelle introduite par grenaillage. Par ailleurs, les différentes caractérisations effectuées par indentation instrumentée et diffraction des rayons X montrent que le grenaillage introduit plutôt un adoucissement du matériau qu'un durcissement.

# Reference


1. Ratti, G., et al., *Effect Of Residual Stresses From Shot Peening On Fatigue Strength And Threshold To Crack Propagation Of Al 7475 Alloy Components*, in *ICAF 2009, Bridging the Gap between Theory and Operational Practice*, M.J. Bos, Editor. 2009, Springer Netherlands. p. 859-870.
2. International, A., *ASTM B466-07, Standard Specification for Titanium and Titanium Alloy Strip, Sheet, and Plate, ASTM International, West Conshohocken, PA, 2007, www.astm.org*. 2007: West Conshohocken.
3. Nascimento, M.P., et al., *Effect of a Shot Peening Pre Treatment on the Fatigue Behaviour of Hard Chromium on Electroless Nickel Interlayer Coated AISI 4340 Aeronautical Steel.* Materials Research, 2002. **5**: p. 95-100.
4. Schajer, G.S., *Practical residual stress measurement methods*. 2013: John Wiley & Sons.
5. Oliver, W.C. and G.M. Pharr, *Measurement of hardness and elastic modulus by instrumented indentation: Advances in understanding and refinements to methodology.* Journal of materials research, 2004. **19**(01): p. 3-20.
6. Jang, J., *Estimation of residual stress by instrumented indentation: A review.* J. Ceram. Process. Res, 2009. **10**(391): p. 1996-1944.
7. Morrow, J. and G. Sinclair, *Symposium on Basic Mechanisms of Fatigue*. 1958, ASTM, Boston.
8. Liu, Z., et al., *The effect of cumulative large plastic strain on the structure and properties of a Cu–Zn alloy.* Materials Science and Engineering: A, 1998. **242**(1): p. 137-140.
9. Niku-Lari, A., *Advances in Surface Treatments: Technology—Applications—Effects*. Vol. 5. 2013: Elsevier.
10. Schijve, J., J. Schijve, and J. Schijve, *Fatigue of structures and materials*. 2001: Springer.
11. Vöhringer, O., *Advances in Surface Treatments: Technology, Applications Effects*. 1987, Pergamon Press, Oxford.
12. Totten, G.E., *Handbook of residual stress and deformation of steel*. 2002: ASM international.
13. Hauk, V., *Structural and residual stress analysis by nondestructive methods: Evaluation-Application-Assessment*. 1997: Elsevier.

14. Paglietti, A., *Plasticity of cold worked metals: a deductive approach*. 2007: Wit Press.

15. Cubberly, W.H., *Metals Handbook: Properties and Selection: Irons and Steels*. 1978: American Society of Metals.

16. Bathias, C. and A. Pineau, *Fatigue of materials and structures*. 2013: John Wiley & Sons.

17. Schreiber, R., H. Wohlfahrt, and E. Macherauch, *Effect of Shot-Peening on the Bending Fatigue Strength of the Case-Hardened Steel 16 MnCr 5.* Arch. Eisenhuttenwes., 1978. **49**(1): p. 37-41.

18. Syren, B., H. Wohlfahrt, and E. Macherauch. *Influence of Residual Stresses and Surface Topography on Bending Fatigue Strength of Machined CK 45 in Different Heat Treatment Conditions*. in *Second International Conference on Mechanical Behavior of Materials. ASM, Metals Park, Ohio. 1976, 807-811*. 1976.

19. Macherauch, E., *Introduction to residual stress.* Advances in surface treatments, 2014: p. 1.

20. Gallagher, J.P., *USAF damage tolerant design handbook: guidelines for the analysis and design of damage tolerant aircraft structures*. 1984.

21. Quesnel, D., M. Meshii, and J. Cohen, *Residual stresses in high-strength low alloy steel during low cycle fatigue.* Materials Science and Engineering, 1978. **36**(2): p. 207-215.

22. Noyan, I. and J. Cohen, *The nature of residual stress and its measurement*. In Residual Stress and Stress Relaxation, Edited by E. Kula and V. Weiss, 1982: Springer, New York.

23. McClinton, M. and J. Cohen, *Changes in residual stress during the tension fatigue of normalized and peened SAE 1040 steel.* Materials science and engineering, 1982. **56**(3): p. 259-263.

24. TAIRA, S., T. ABE, and T. EHIRO, *X-ray study of surface residual stress produced in fatigue process of annealed metals.* Bulletin of JSME, 1969. **12**(53): p. 947-957.

25. Taira, S., T. Abe, and T. Ehiro. *X-ray investigation on surface residual stress produced in fatigue process*. in *Proc*. 1968.

26. James, M.R. and W.L. Morris, *The relaxation of machining stresses in aluminium alloys during fatigue.* Residual stress for designers and metallurgists, ASM, 1981: p. 169-188.

27. Potter, J. and R. Millard. *The effect of temperature and load cycling on the relaxation of residual stresses*. in *Paper from" Proc. Conf. on Advances in X-Ray Analysis", 1977, 20, 309-319.* 1977.

28. Rosenthal, D., *Influence of residual stress on fatigue*, in *Metal Fatigue*, G. Sines and J.L. Waisman, Editors. 1959, McGraw-Hill: New York. p. 170.

29. G., H., *Propagation des fissures à haute température dans le superalliage N18 pour disques de turbomachine.*, in *Interactions entre la nature des sollicitations mecaniques et des effets d'oxydation.* 1994, France: Ecole des Mines de Paris: Paris.

30. FLAVENOT, J. *Prediction of the Fatigue life Taking into Account Residual Stress Relaxation Under Cyclic Loading*. in *ECF7, Budapest 1988*. 2013.

31. Chassaigne, J.C., *Fissuration à hautes températures du superalliage base nickel N18 élaboré par métallurgie des poudres: Etude du couplage mécanique-environnement en pointe de fissure*. 1997.

32. Sandor, B.I., *Fundamentals of cyclic stress and strain*. 1972: Univ of Wisconsin Pr.

33. Kettunen, P. and U. Kocks, *On a possible relation between work hardening and fatigue failure.* Scripta Metallurgica, 1967. **1**(1): p. 13-17.

34. Lu, J., *Handbook of measurement of residual stresses*. 1996: Egully. com.

35. Schajer, G., *Residual stresses: measurement by destructive methods.* Section 5a in "Encyclopedia of Materials: Science and Technology". Elsevier, Oxford, 2001.

36. Schajer, G., *Relaxation methods for measuring residual stresses: techniques and opportunities.* Experimental mechanics, 2010. **50**(8): p. 1117-1127.

37. E837-08, A., *Standard Test Method for Determining Residual Stresses by the Hole Drilling Strain Gage method*. 2008, ASTM Intrenational Conshohocken, PA.

38. Walton, H., *Deflection methods to estimate residual stress.* ASM International, Member/Customer Service Center, Materials Park, OH 44073-0002, USA, 2002., 2002: p. 89-98.

39. Shadley, J., E. Rybicki, and W. Shealy, *Application guidelines for the parting out step in a through thickness residual stress measurement procedure.* Strain, 1987. **23**(4): p. 157-166.

40. Treuting, R. and W. Read Jr, *A mechanical determination of biaxial residual stress in sheet materials.* Journal of Applied Physics, 1951. **22**(2): p. 130-134.

41. Leggatt, R., et al., *Development and experimental validation of the deep hole method for residual stress measurement.* The Journal of Strain Analysis for Engineering Design, 1996. **31**(3): p. 177-186.

42. DeWald, A.T. and M.R. Hill, *Improved data reduction for the deep-hole method of residual stress measurement.* The Journal of Strain Analysis for Engineering Design, 2003. **38**(1): p. 65-77.

43. Prime, M.B., *Residual stress measurement by successive extension of a slot: the crack compliance method.* Applied Mechanics Reviews, 1999. **52**(2): p. 75-96.

44. Cheng, W. and I. Finnie, *Residual stress measurement and the slitting method*. 2007: Springer Science & Business Media.

45. Prime, M.B., *Cross-sectional mapping of residual stresses by measuring the surface contour after a cut.* Journal of Engineering Materials and Technology, 2001. **123**(2): p. 162-168.

46. *Residual Stress Measurement by X-ray Diffraction: HS-784*. 2003: SAE International.

47. Reimers, W., et al., *The use of high-energy synchrotron diffraction for residual stress analyses.* Journal of Materials Science Letters, 1999. **18**(7): p. 581-583.

48. Hayaski, M., et al. *Residual stress distribution measurement in plastically bent carbon steel by neutron diffraction*. in *The Fifth International Conf. on Residual Stresses*. 1997.

49. Root, J., R. Hosbons, and T. Holden, *Neutron Diffraction Measurements of Residual Stress near a Pin Hole in a Solid-Fuel Booster Rocket Casing.* Practical Applications of Residual Stress Technology, 1991: p. 83-86.

50. Francois, M., *Unified description for the geometry of X-ray stress analysis: proposal for a consistent approach.* Journal of Applied Crystallography, 2008. **41**(1): p. 44-55.

51. He, B.B., *Two-dimensional X-ray diffraction*. 2011: John Wiley & Sons.

52. Jiles, D., *Review of magnetic methods for nondestructive evaluation.* NDT international, 1988. **21**(5): p. 311-319.

53. Leon-Salamanca, T. and D. Bray, *Residual stress measurement in steel plates and welds using critically refracted longitudinal (LCR) waves.* Journal of Research in Nondestructive Evaluation, 1996. **7**(4): p. 169-184.

54. Oliver, W.C. and G.M. Pharr, *An improved technique for determining hardness and elastic modulus using load and displacement sensing indentation experiments.* Journal of materials research, 1992. **7**(06): p. 1564-1583.

55. Field, J. and M. Swain, *Determining the mechanical properties of small volumes of material from submicrometer spherical indentations.* Journal of Materials Research, 1995. **10**(01): p. 101-112.

56. Swain, M., *Mechanical property characterisation of small volumes of brittle materials with spherical tipped indenters.* Materials Science and Engineering: A, 1998. **253**(1): p. 160-166.

57. Dao, M., et al., *Computational modeling of the forward and reverse problems in instrumented sharp indentation.* Acta materialia, 2001. **49**(19): p. 3899-3918.

58. Jang, J.-i. and G. Pharr, *Influence of indenter angle on cracking in Si and Ge during nanoindentation.* Acta Materialia, 2008. **56**(16): p. 4458-4469.

59. Kokubo, S., *On the change in hardness of a plate caused by bending.* Science Reports of the Tohoku Imperial University 1932. **1**(21): p. 256-267.

60. Sines, G. and R. Carlson, *Hardness measurement for determination of residual stresses.* ASTM Bulletin, 1952. **180**: p. 35-37.

61. Li, Y.G., P. Kanoute, and M. Fran ̧ois. *Characterization of Residual Stresses and Accumulated Plastic Strain Induced by Shot Peening through Simulation of Instrumented Indentation*. in *Advanced Materials Research*. 2014. Trans Tech Publ.

62. LaFontaine, W., et al., *Residual stress measurements of thin aluminum metallizations by continuous indentation and X-ray stress measurement techniques.* Journal of materials research, 1991. **6**(10): p. 2084-2090.

63. Suresh, S. and A. Giannakopoulos, *A new method for estimating residual stresses by instrumented sharp indentation.* Acta Materialia, 1998. **46**(16): p. 5755-5767.

64. Jang, J.-i., et al., *Assessing welding residual stress in A335 P12 steel welds before and after stress-relaxation annealing through instrumented indentation technique.* Scripta Materialia, 2003. **48**(6): p. 743-748.

65. Lee, Y.-H. and D. Kwon, *Measurement of residual-stress effect by nanoindentation on elastically strained (100) W.* Scripta Materialia, 2003. **49**(5): p. 459-465.

66. Carlsson, S. and P.-L. Larsson, *On the determination of residual stress and strain fields by sharp indentation testing.: Part I: theoretical and numerical analysis.* Acta Materialia, 2001. **49**(12): p. 2179-2191.

67. Carlsson, S. and P.-L. Larsson, *On the determination of residual stress and strain fields by sharp indentation testing.: Part II: Experimental investigation.* Acta Materialia, 2001. **49**(12): p. 2193-2203.

68. Swadener, J., B. Taljat, and G. Pharr, *Measurement of residual stress by load and depth sensing indentation with spherical indenters.* Journal of Materials Research, 2001. **16**(07): p. 2091-2102.

69. Chen, X., J. Yan, and A.M. Karlsson, *On the determination of residual stress and mechanical properties by indentation.* Materials Science and Engineering: A, 2006. **416**(1): p. 139-149.

70. Xu, Z.-H. and X. Li, *Estimation of residual stresses from elastic recovery of nanoindentation.* Philosophical Magazine, 2006. **86**(19): p. 2835-2846.

71. Hay, J.C., A. Bolshakov, and G. Pharr, *A critical examination of the fundamental relations used in the analysis of nanoindentation data.* Journal of Materials Research, 1999. **14**(06): p. 2296-2305.

72. Love, A., *Boussinesq's problem for a rigid cone.* The Quarterly Journal of Mathematics, 1939(1): p. 161-175.

73. Love, A.E.H., *The stress produced in a semi-infinite solid by pressure on part of the boundary.* Philosophical Transactions of the Royal Society of London. Series A, Containing Papers of a Mathematical or Physical Character, 1929: p. 377-420.

74. Harding, J. and I. Sneddon. *The elastic stresses produced by the indentation of the plane surface of a semi-infinite elastic solid by a rigid punch*. in *Mathematical Proceedings of the Cambridge Philosophical Society*. 1945. Cambridge Univ Press.

75. Sneddon, I.N., *The relation between load and penetration in the axisymmetric Boussinesq problem for a punch of arbitrary profile.* International Journal of Engineering Science, 1965. **3**(1): p. 47-57.

76. Bolshakov, A., W. Oliver, and G. Pharr, *Influences of stress on the measurement of mechanical properties using nanoindentation: Part II. Finite element simulations.* Journal of Materials Research, 1996. **11**(03): p. 760-768.

77. Troyon, M. and L. Huang, *Correction factor for contact area in nanoindentation measurements.* Journal of materials research, 2005. **20**(3): p. 610-617.

78. Tabor, D., *The Hardness of Metals*. 1951: ClarendonP.

79. Westbrook, J.H., H. Conrad, and A.S.f. Metals, *The Science of hardness testing and its research applications*. 1973: American Society for Metals.

80. Johnson, K., *The correlation of indentation experiments.* Journal of the Mechanics and Physics of Solids, 1970. **18**(2): p. 115-126.

81. Gerk, A., *The effect of work-hardening upon the hardness of solids: minimum hardness.* Journal of Materials Science, 1977. **12**(4): p. 735-738.

82. Pramudia, M. and K. Mubarok. *The Effects of the Degree of Deformation in the Work Hardening Process on Microstructure, Hardness, and Phase Transformation of the Material Structure of Nickel-Free Austenitic Stainless Steel*. in *International Journal of Engineering Research and Technology*. 2014. ESRSA Publications.

83. Milad, M., et al., *The effect of cold work on structure and properties of AISI 304 stainless steel.* Journal of Materials Processing Technology, 2008. **203**(1): p. 80-85.

84. Sonmez, F.O. and A. Demir, *Analytical relations between hardness and strain for cold formed parts.* Journal of materials processing technology, 2007. **186**(1): p. 163-173.

85. Remy, L., *Kinetics of fcc deformation twinning and its relationship to stress-strain behaviour.* Acta Metallurgica, 1978. **26**(3): p. 443-451.

86. Remy, L., *The interaction between slip and twinning systems and the influence of twinning on the mechanical behavior of fcc metals and alloys.* Metallurgical Transactions A, 1981. **12**(3): p. 387-408.

87. Allain, S., *Caractérisation et modélisation thermomécaniques multi-échelles des mécanismes de déformation et d'écrouissage d'aciers austénitiques à haute teneur en manganèse: application à l'effet TWIP*. 2004, Vandoeuvre-les-Nancy, INPL.

88. Bouaziz, O., S. Allain, and C. Scott, *Effect of grain and twin boundaries on the hardening mechanisms of twinning-induced plasticity steels.* Scripta Materialia, 2008. **58**(6): p. 484-487.

89. Barbier, D., et al., *EBSD for analysing the twinning microstructure in fine-grained TWIP steels and its influence on work hardening.* Journal of microscopy, 2009. **235**(1): p. 67-78.

90. Wilkinson, A.J., G. Meaden, and D.J. Dingley, *Mapping strains at the nanoscale using electron back scatter diffraction.* Superlattices and Microstructures, 2009. **45**(4–5): p. 285-294.

91. Yoda, R., T. Yokomaku, and N. Tsuji, *Plastic deformation and creep damage evaluations of type 316 austenitic stainless steels by EBSD.* Materials characterization, 2010. **61**(10): p. 913-922.

92. Child, D., G. West, and R.C. Thomson, *Assessment of surface hardening effects from shot peening on a Ni-based alloy using electron backscatter diffraction techniques.* Acta Materialia, 2011. **59**(12): p. 4825-4834.

93. Tosha, K. *Influence of residual stresses on the hardness number in the affected layer produced by shot peening*. in *Second Asia–Pacific Forum on Precision Surface Finishing and Deburring Technology, Seoul, Korea*. 2002.

94. Prevéy, P.S., *The effect of cold work on the thermal stability of residual compression in surface enhanced IN718*. 2000, DTIC Document.

95. Prevey, P.S., *X-ray diffraction residual stress techniques.* ASM International, ASM Handbook., 1986. **10**: p. 380-392.

96. Prevéy, P.S., *The measurement of subsurface residual stress and cold work distributions in nickel base alloys.* Residual Stress in Design, Process & Materials Selections, ed. WB Young, Metals Park, OH: Am. Soc. For Metals, 1987: p. 11-19.

97. Ji, V., Y.-G. Zhang, and C.-Q. Chen, *The non-destructive estimation of the superficial mechanical properties of components in the INCONEL 600 alloy by X-ray diffraction peak width.* Surface and Coatings Technology, 2000. **130**(1): p. 95-99.

98. Simmons, J.A., et al., *Fundamental Aspects of Dislocation Theory: Conference Proceedings, National Bureau of Standards, April 21-25, 1969*. 1970: U.S. National Bureau of Standards.

99. Wilkens, M., *The determination of density and distribution of dislocations in deformed single crystals from broadened X-ray diffraction profiles.* Physica status solidi (a), 1970. **2**(2): p. 359-370.

100. Ungar, T., H. Mughrabi, and M. Wilkens, *An X-Ray line-broadening study of dislocations near the surface and in the bulk of deformed copper single crystals.* Acta Metallurgica, 1982. **30**(10): p. 1861-1867.

101. Warren, B.E. and B.L. Averbach, *The Separation of Cold-Work Distortion and Particle Size Broadening in X-Ray Patterns.* Journal of Applied Physics, 1952. **23**(4): p. 497-497.

102. Groma, I., T. Ungár, and M. Wilkens, *Asymmetric X-ray line broadening of plastically deformed crystals. I. theory.* Journal of applied crystallography, 1988. **21**(1): p. 47-54.

103. Ungár, T., I. Groma, and M. Wilkens, *Asymmetric X-ray line broadening of plastically deformed crystals. II. Evaluation procedure and application to [001]-Cu crystals.* Journal of applied crystallography, 1989. **22**(1): p. 26-34.

104. Yang, Y., et al. *Quantitative measurement of plastic strain field at a fatigue crack tip*. in *Proceedings of the Royal Society of London A: Mathematical, Physical and Engineering Sciences*. 2012. The Royal Society.

105. Sarkar, A., P. Mukherjee, and P. Barat, *X-ray diffraction studies on asymmetrically broadened peaks of heavily deformed zirconium-based alloys.* Materials Science and Engineering: A, 2008. **485**(1): p. 176-181.

106. Lütjering, G. and J.C. Williams, *Titanium*. 2013: Springer Berlin Heidelberg.

107. Leyens, C. and M. Peters, *Titanium and Titanium Alloys: Fundamentals and Applications*. 2006: Wiley.

108. International, A., A.I.A.P.D. Committee, and A.I.H. Committee, *ASM Handbook, Volume 2, ASM International. Handbook Committee*. 1992: ASM International.

109. Froes, F.H., D. Eylon, and H.B. Bomberger, *Titanium technology: present status and future trends*. 1985: Titanium Development Association.

110. International, A., *ASTM B348-06, Standard Specification for Titanium and Titanium Alloy Strip, Sheet, and Plate, ASTM International, West Conshohocken, PA, 2006, www.astm.org*. 2006: West Conshohocken, PA.

111. International, A., *ASTM B265-07, Standard Specification for Titanium and Titanium Alloy Strip, Sheet, and Plate, ASTM International, West Conshohocken, PA, 2007, www.astm.org*. 2007, PA: West Conshohocken.

112. Committee, A.I.H., *ASM Handbook, Volume 13, ASM International. Handbook Committee*. 2005: ASM International.

113. Sun, Q. and H. Gu, *Tensile and low-cycle fatigue behavior of commercially pure titanium and Ti–5Al–2.5 Sn alloy at 293 and 77 K.* Materials Science and Engineering: A, 2001. **316**(1): p. 80-86.

114. Speidel, M., et al., *Advances in corrosion science and technology*. Vol. 2Plenum, New York, 1972: p. 115-335.

115. Speidel, M. *Effect of shot peening on stress corrosion cracking and corrosion fatigue*. in *Proceeding of the 1st international conference on shot peening*. 1981.

116. Lebrun, E., et al. *Phase Transformations of TIMETAL-18 as a New Titanium Alloy with Bimodal Microstructure*. in *Advanced Materials Research*. 2014. Trans Tech Publ.

117. Fanning, J., *Recent developments in high-strength near-beta Titanium alloys*. 2011, TIMET: San Diego, California.

118. Swaddiwudhipong, S., et al., *Equivalency of Berkovich and conical load-indentation curves.* Modelling and Simulation in Materials Science and Engineering, 2006. **14**(1): p. 71.

119. Jha, K.K., et al., *Work-of-indentation as a means to characterize indenter geometry and load–displacement response of a material.* Journal of Physics D: Applied Physics, 2013. **46**(41): p. 415501.

120. Simulia, D., *ABAQUS/Standard user's manual; ABAQUS/CAE user's manual; ABAQUS keywords manual; ABAQUS theory manual.* 2011.

121. Chen, Z. and S. Diebels, *Nanoindentation of soft polymers: modeling, experiments and parameter identification.* Tech. Mech, 2014. **34**(3-4): p. 166-189.

122. Bowden, F. and E. Freitag. *The friction of solids at very high speeds. I. Metal on metal; II. Metal on diamond*. in *Proceedings of the Royal Society of London A: Mathematical, Physical and Engineering Sciences*. 1958. The Royal Society.

123. Celentano, D.J., et al., *Numerical simulation and experimental validation of the microindentation test applied to bulk elastoplastic materials.* Modelling and Simulation in Materials Science and Engineering, 2012. **20**(4): p. 045007.

124. Tsui, T., W. Oliver, and G. Pharr, *Influences of stress on the measurement of mechanical properties using nanoindentation: Part I. Experimental studies in an aluminum alloy.* Journal of Materials Research, 1996. **11**(03): p. 752-759.

125. Menčík, J., *Uncertainties and errors in nanoindentation.* Nanoindentation in Materials Science, InTech, Rijeka, 2012: p. 53-86.

126. Li, Y., P. Kanouté, and M. François, *Influence of residual stress and work hardening on instrumented indentation.* Matériaux & Techniques, 2013. **101**(3): p. 306.

127. Dean, J., G. Aldrich-Smith, and T. Clyne, *Use of nanoindentation to measure residual stresses in surface layers.* Acta Materialia, 2011. **59**(7): p. 2749-2761.

128. Bolzon, G. and V. Buljak, *An indentation-based technique to determine in-depth residual stress profiles induced by surface treatment of metal components.* Fatigue & Fracture of Engineering Materials & Structures, 2011. **34**(2): p. 97-107.

129. Karthik, V., et al., *Finite element analysis of spherical indentation to study pile-up/sink-in phenomena in steels and experimental validation.* International Journal of Mechanical Sciences, 2012. **54**(1): p. 74-83.

130. Lee, J.H., et al., *Numerical approaches and experimental verification of the conical indentation techniques for residual stress evaluation.* Journal of Materials Research, 2010. **25**(11): p. 2212-2223.

131. Giannakopoulos, A., *The influence of initial elastic surface stresses on instrumented sharp indentation.* Journal of applied mechanics, 2003. **70**(5): p. 638-643.

132. Doerner, M.F. and W.D. Nix, *A method for interpreting the data from depth-sensing indentation instruments.* Journal of Materials Research, 1986. **1**(04): p. 601-609.

133. Hochstetter, G., A. Jimenez, and J.L. Loubet, *Strain-rate effects on hardness of glassy polymers in the nanoscale range. Comparison between quasi-static and continuous stiffness measurements.* Journal of Macromolecular Science, Part B, 1999. **38**(5-6): p. 681-692.

134. Tong, W., et al., *Nitriding iron at lower temperatures.* Science, 2003. **299**(5607): p. 686-688.

135. Roland, T., et al., *Enhanced mechanical behavior of a nanocrystallised stainless steel and its thermal stability.* Materials Science and Engineering: A, 2007. **445–446**: p. 281-288.

136. International, A., *ASTM E8/E8M-09, Standard Specification for Titanium and Titanium Alloy Strip, Sheet, and Plate, ASTM International, West Conshohocken, PA, 2009, www.astm.org*. 2009: West Conshohocken.

137. Wang, Z., *Influences of sample preparation on the indentation size effect and nanoindentation pop-in on nickel.* 2012.

138. Wong, M.F. and K. Zeng, *Mechanical Polishing Effects Toward Surface Domain Evolution in Pb (Zn1/3Nb2/3) O3–PbTiO3 Single Crystals.* Journal of the American Ceramic Society, 2011. **94**(4): p. 1079-1086.

139. Fu, G., et al., *A plasticity-based model of material removal in chemical-mechanical polishing (CMP).* Semiconductor Manufacturing, IEEE Transactions on, 2001. **14**(4): p. 406-417.

140. Li, Y., P. Kanouté, and M. François, *Disturbance induced by surface preparation on instrumented indentation test.* Materials Science and Engineering: A, 2015. **642**: p. 381-390.

141. Nanoindentation, X., *User's manual. version16.* Test Works, 2002. **4**.

142. International, A., *ASTM E2546-07, Standard Specification for Titanium and Titanium Alloy Strip, Sheet, and Plate, ASTM International, West Conshohocken, PA, 2007, www.astm.org*. 2007.

143. *http://www.struers.com/default.asp?doc_id=916*.

144. Gerber, C.E., *Contact problems for the elastic quarter-plane and for the quarter-space*. 1993: UMI Diss. services.

145. Jakes, J.E., et al., *Experimental method to account for structural compliance in nanoindentation measurements.* Journal of materials research, 2008. **23**(04): p. 1113-1127.

146. King, R., *Elastic analysis of some punch problems for a layered medium.* International Journal of Solids and Structures, 1987. **23**(12): p. 1657-1664.

147. Lu, C.-J. and D. Bogy, *The effect of tip radius on nano-indentation hardness tests.* International journal of solids and structures, 1995. **32**(12): p. 1759-1770.

148. Panich, N. and S. Yong, *Improved method to determine the hardness and elastic moduli using nano-indentation.* KMITL Science Journal, 2005. **5**(2): p. 483-492.

149. Calabri, L., et al., *AFM nanoindentation: tip shape and tip radius of curvature effect on the hardness measurement.* Journal of Physics: Condensed Matter, 2008. **20**(47): p. 474208.

150. Li, M., et al., *Influence of contact geometry on hardness behavior in nano-indentation.* Vacuum, 2009. **84**(2): p. 315-320.

151. Mata, M. and J. Alcala, *The role of friction on sharp indentation.* Journal of the Mechanics and Physics of Solids, 2004. **52**(1): p. 145-165.

152. Guo, W., et al., *Influence of friction in material characterization in microindentation measurement.* Journal of computational and applied mathematics, 2010. **234**(7): p. 2183-2192.

153. ESTECO, *The concept behind modeFRONTIER*. 2007.

154. Clarich, A., R. Russo, and M. Carriglio. *Multi-objective optimization with modefrontier interfaces for ansa and metapost*. in *4th ANSA & μETA International Conference. Thessaloniki, Greece*. 2011.

155. Alberto, C., et al., *Use of Multivariate-Data-Analysis Techniques in modeFRONTIER for Efficient Optimization and Decision Making*, in *13th AIAA/ISSMO Multidisciplinary Analysis Optimization Conference*. 2010, American Institute of Aeronautics and Astronautics.

156. Paredes, B.M., *OPTIMIZATION TECHNIQUES APPLIED TO ENGINEERING DESIGN IN CO2 CAPTURE PROCESS USING MODEFRONTIER*. 2013, Instituto ESSS de Pesquisa e Desenvolvimento.

157. McKay, M.D., R.J. Beckman, and W.J. Conover, *Comparison of three methods for selecting values of input variables in the analysis of output from a computer code.* Technometrics, 1979. **21**(2): p. 239-245.

158. Kendall, M.G., *A new measure of rank correlation.* Biometrika, 1938: p. 81-93.

159. Helmert, F.R., *Über die Bestimmung des wahrscheinlichen Fehlers aus einer endlichen Anzahl wahrer Beobachtungsfehler.* Z. Math. Phys, 1875. **20**: p. 300-303.

160. Kohonen, T., *Self-organization and associative memory*. Vol. 8. 2012: Springer.

161. Inselberg, A., *The plane with parallel coordinates.* The Visual Computer, 1985. **1**(2): p. 69-91.

162. Tan, P.N., M. Steinbach, and V. Kumar, *Introduction to Data Mining*. 2014: Pearson Education, Limited.

163. Wood, E., *Multiobjective Decision Analysis With Engineering and Business Applications.* Eos, Transactions American Geophysical Union, 1983. **64**(31): p. 486-486.

164. Szidarovszky, F., M.E. Gershon, and L. Duckstein, *Techniques for multiobjective decision making in systems management*. 1986: Elsevier.

165. Primavera, V., *Modeling and Optimization Workshop.* 2014.

166. Hwang, C.L. and K. Yoon, *Multiple Attribute Decision Making: Methods and Applications A State-of-the-Art Survey*. 2012: Springer Berlin Heidelberg.

167. Antunes, C.H. and C.O. Henriques, *Multi-Objective Optimization and Multi-Criteria Decision Analysis in the Energy Sector (part II –MCDA)*. 2014: European Working Group "Multiple Criteria Decision Aiding".

168. *http://www.ptsteelsm.com/FactsTiAlloy.pdf*.

169. Donachie, M.J., *Titanium: A Technical Guide, 2nd Edition*. 2000: ASM International.

170. Chen, F.Y. and R.C. Chang. *Elastic and Plastic Mechanical Properties Determined by Nanoindentation and Numerical Simulation at Mesoscale*. in *Key Engineering Materials*. 2006. Trans Tech Publ.

171. Sakharova, N., et al., *Comparison between Berkovich, Vickers and conical indentation tests: A three-dimensional numerical simulation study.* International Journal of Solids and Structures, 2009. **46**(5): p. 1095-1104.

172. Moore, S.W., M.T. Manzari, and Y.-L. Shen, *Nanoindentation in elastoplastic materials: insights from numerical simulations.* International Journal of Smart and Nano Materials, 2010. **1**(2): p. 95-114.

173. Plunkett, B., O. Cazacu, and F. Barlat, *Orthotropic yield criteria for description of the anisotropy in tension and compression of sheet metals.* International Journal of Plasticity, 2008. **24**(5): p. 847-866.

174. Nixon, M.E., O. Cazacu, and R.A. Lebensohn, *Anisotropic response of high-purity α-titanium: Experimental characterization and constitutive modeling.* International Journal of Plasticity, 2010. **26**(4): p. 516-532.

175. Chun, Y., et al., *Effect of deformation twinning on microstructure and texture evolution during cold rolling of CP-titanium.* Materials Science and Engineering: A, 2005. **398**(1): p. 209-219.

176. Salem, A.A., S.R. Kalidindi, and R.D. Doherty, *Strain hardening of titanium: role of deformation twinning.* Acta Materialia, 2003. **51**(14): p. 4225-4237.

177. Hosford, W., *Plane-strain compression of aluminum crystals.* Acta metallurgica, 1966. **14**(9): p. 1085-1094.

178. Cazacu, O. and F. Barlat, *A criterion for description of anisotropy and yield differential effects in pressure-insensitive metals.* International Journal of Plasticity, 2004. **20**(11): p. 2027-2045.

179. Cazacu, O., B. Plunkett, and F. Barlat, *Orthotropic yield criterion for hexagonal closed packed metals.* International Journal of Plasticity, 2006. **22**(7): p. 1171-1194.

180. Khan, A.S., R. Kazmi, and B. Farrokh, *Multiaxial and non-proportional loading responses, anisotropy and modeling of Ti–6Al–4V titanium alloy over wide ranges of strain rates and temperatures.* International Journal of Plasticity, 2007. **23**(6): p. 931-950.

181. Khan, A.S., Y.S. Suh, and R. Kazmi, *Quasi-static and dynamic loading responses and constitutive modeling of titanium alloys.* International Journal of Plasticity, 2004. **20**(12): p. 2233-2248.

182. Nemat-Nasser, S., W. Guo, and J. Cheng, *Mechanical properties and deformation mechanisms of a commercially pure titanium.* Acta materialia, 1999. **47**(13): p. 3705-3720.

183. Ahn, K., H. Huh, and J. Yoon, *Strain hardening model of pure titanium considering effects of deformation twinning.* Metals and Materials International, 2013. **19**(4): p. 749-758.

184. Cagliero, R. and G. Maizza. *Modeling of Vickers Indentation of TiAl Alloys*. in *Excerpt from the Proceedings of the COMSOL Conference, Paris*. 2010.

185. Monelli, B.D., *Mechanical Characterization of Metallic Materials by Instrumented Spherical Indentation Testing*. 2010, University of Trento.

186. Kang, J., *Determination of elastic-plastic and visco-plastic material properties from instrumented indentation curves*. 2013, University of Nottingham.

187. Chollacoop, N., *Computational and experimental study of instrumented indentation*. 2004, Massachusetts Institute of Technology.

188. Chollacoop, N., M. Dao, and S. Suresh, *Depth-sensing instrumented indentation with dual sharp indenters.* Acta materialia, 2003. **51**(13): p. 3713-3729.

189. Genzel, C., *X-ray residual stress analysis in thin films under grazing incidence–basic aspects and applications.* Materials science and technology, 2005. **21**(1): p. 10-18.

190. Van Acker, K., et al. *Internal stress measurement on CVD diamond coatings by X-ray diffraction and Raman spectroscopy*. in *MRS Proceedings*. 1993. Cambridge Univ Press.

191. Marciszko, M., et al., *Multireflection grazing incidence diffraction used for stress measurements in surface layers.* Thin solid films, 2013. **530**: p. 81-84.

192. Xu, Z.-H. and X. Li, *Effect of sample tilt on nanoindentation behaviour of materials.* Philosophical magazine, 2007. **87**(16): p. 2299-2312.

193. Kashani, M.S. and V. Madhavan, *Analysis and correction of the effect of sample tilt on results of nanoindentation.* Acta Materialia, 2011. **59**(3): p. 883-895.

194. Shi, C., et al., *Effects of Indenter Tilt on Nanoindentation Results of Fused Silica: an Investigation by Finite Element Analysis.* Materials Transactions, 2013. **54**(6): p. 958-963.

195. FANNING, J., *A precipitation hardened, near beta Ti-Al-V-Fe-Mo-Cr-O alloy*, in *2470613 (A)*. 2010, TITANIUM METALS: US.

196. Y., M., *Développement d'un nouvel alliage à hautes caractéristiques mécaniques : le Ti18*. 2012: Journées Titane Nantes.

197. Huang, J., Z. Wang, and K. Xue, *Cyclic deformation response and micromechanisms of Ti alloy Ti–5Al–5V–5Mo–3Cr–0.5Fe.* Materials Science and Engineering: A, 2011. **528**(29–30): p. 8723-8732.

198. Badreddine, J., et al., *Simulation of shot dynamics for ultrasonic shot peening: Effects of process parameters.* International Journal of Mechanical Sciences, 2014. **82**: p. 179-190.

# Yugang LI

## Doctorat : Systèmes Mécaniques et Matériaux

Année 2015


## Grenaillage et fatigue oligocyclique d'alliages de titane : indentation instrumentée et diffraction des rayons X


Deux problèmes surviennent lorsque nous étudions les effets du grenaillage de précontrainte sur le processus de la fatigue. Le premier est la caractérisation des contraintes résiduelles (CR) et de l'écrouissage. Le second est l'évolution de CR et de l'écrouissage pendant le cyclage.

Pour résoudre le premier problème, cette thèse propose une méthode pour mesurer les contraintes et l'écrouissage par nanoindentation. Ici, l'écrouissage est représenté par la déformation plastique cumulée (PP). A l'aide d'une série de simulations par éléments finis (MEF) en supposant le comportement du matériau connu, les réponses obtenues par indentation permettent d'obtenir simultanément contrainte et déformation plastique. Bien que satisfaisante d'un point vue numérique, les performances expérimentales obtenues sur un alliage de titane temps T40 restent insuffisantes. Cependant, si le profil de contrainte est connu, on peut toutefois obtenir le profil de déformation plastique. Les biais induits par la préparation de la surface ont été analysés en détail.

Pour le second problème, une série d'essais de fatigue ont été effectués sur un alliage Ti-18. Quatre traitements ont été testés sur 100 cycles sous 3 amplitudes différentes de déformation. Des mesures par diffraction des rayons X ont montré que la relaxation des contraintes et l'adoucissement cyclique augmentent avec l'amplitude de déformation. Les essais d'indentation ont montré un adoucissement de la couche grenaillée.



Mots clés : grenaillage de précontrainte - contraintes résiduelles - écrouissage – titane, alliages - rayons X, diffraction - nanoindentation - matériaux - fatigue.


## Shot-peening and Low-cycle Fatigue of Titanium Alloys: Instrumented Indentation and X-ray Diffraction


There are two problems when investigating the effects of shot-peening on fatigue process. The first one is characterizing residual stresses (RS) and strain hardening (WH) on the sample surface. The second one is the evolution of RS and WH during fatigue.

In order to solve the first problem, this thesis proposes a "simultaneous function method" to measure RS and WH with nanoindentation. Accumulated plastic strain (PP) is used to represent WH. Then, by establishing functions of normalized indentation responses through a series of finite element method (FEM) simulations, normalized indentation responses obtained from nanoindentation experiments can be used to extract RS and PP values, assuming that the constitutive behavior is known. Although the simultaneous function method shows fairly high accuracy from a pure numerical view point, experiments performed on T40 commercial pure titanium are not completely satisfying. However, if the residual stress profile is known, the method can be used to derive the work hardening profile.

In order to study the second problem, a series of strain-controlled fatigue tests are performed on Ti-18 alloy. Fatigue specimens of 4 material states, including raw, shot-peened, prestrained and prestrained + shot-peened, were tested under 3 different strain amplitudes over 100 cycles. X-ray diffraction tests on the sample surfaces showed that the RS relaxation and the cyclic softening increase together with the strain amplitude. IIT tests showed that shot-peening may induce a softening of the surface of Ti-18 alloy samples.



Keywords: shot peening - residual stresses - strain hardening - titanium alloys - X-rays, diffraction-nanoindentation – fatigue.


**Thèse réalisée en partenariat entre :**


utt
université de technologie
Troyes

**Ecole Doctorale** "Sciences et Technologies"